ENGINEERING APPROACHES TO STUDY LUNG MECHANOBIOLOGY

BY

ARKAPRAVA DAN

DISSERTATION

Submitted in partial fulfillment of the requirements
for the degree of Doctor of Philosophy in Chemical Engineering
in the Graduate College of the
University of Illinois at Urbana-Champaign, 2017

Urbana, Illinois

Doctoral Committee:

Professor Deborah Leckband, Chair and Director of Research
Professor Hyunjoon Kong
Associate Professor Brendan Harley
Associate Professor Amy Wagoner Johnson

Abstract

Engineering tools and techniques greatly expand the scope of biological studies, permitting investigation of the interplay between mechanical forces, and cell and tissue biology, and also enabling *in vitro* replication of the physiological environment. This dissertation describes the development of various engineering approaches to investigate the regulation of the pulmonary blood-gas barrier, and endothelial barrier function in particular. The pulmonary blood-gas barrier consists of airway epithelial cells, which are exposed to the inhaled air, and vascular endothelial cells, which line the blood vessels. In Chapter 2 of this thesis, I describe the development of a cyclic cell stretching device to mimic the mechanical environment of the pulmonary endothelium during physiological and pathological levels of cyclic stretch. I further varied the cell substrate stiffness in order to replicate the mechanics of soft and healthy tissue, or stiff, fibrotic tissue. This device also enables dynamic imaging of cells subject to mechanical stretch. Studies conducted with this device (Chapter 2) demonstrated that physiological cyclic stretch and substrate stiffness coordinately protect the pulmonary endothelium against disruption by the inflammatory mediator, thrombin. Further, quantitative immunofluorescence imaging established that cyclic stretch conditioning led to remodeling of endothelial junctions, and changes in the dynamics of cell membrane protrusions called lamellipodia (Chapter 3). These findings provided valuable insights into potential subcellular mechanisms underlying the cyclic stretch-induced protection of lung endothelial monolayers against proinflammatory signals.

The integrity of the pulmonary endothelium also depends on the force balance in the monolayer, which results from the interplay between intracellular contractile forces and cell-cell and cell-matrix tethering (adhesion) forces. In Chapter 4, I describe studies using a microfabricated platform to quantify the impact of biochemical, genetic, and matrix-based perturbations to cell-

generated mechanical forces. Results from these studies provided important insights into the distribution of forces between cell-cell and cell-matrix adhesions, and conditions under which this distribution was perturbed. Findings directly assessed the impact of genetic and biochemical perturbations on aspects of lung injury conducted in collaboration with the Komarova and Malik research teams at the University of Illinois at Chicago.

Finally, to better replicate pulmonary tissue, I developed an *in vitro* model of the pulmonary blood-gas barrier, consisting of primary airway epithelial cells exposed to air and primary pulmonary endothelial cells cultured in contact with medium on the opposite side of a porous membrane (Chapter 5). This close proximity enabled the two cell types to exchange soluble factors. I devised differentiation conditions under which epithelial cultures exhibited a polarized phenotype with rich mucociliary differentiation, as observed *in vivo*. This model constitutes a first step towards a lung-on-a-chip device being developed in collaboration with the Kenis and Murphy research teams at University of Illinois at Urbana-Champaign, in order to investigate the effects induced by exposure of the airway epithelium and pulmonary endothelium to aerosolized nanoparticles.

To my parents

Acknowledgements

A great many people have taught me, inspired me, and helped me over these five years of graduate school. First and foremost, I would like to thank my advisor and mentor, Prof. Deborah Leckband, who encouraged and enabled me to think like a scientist. She also encouraged me to apply for research fellowships, and present my work at conferences, which helped me develop my scientific communication skills. Under her mentorship, I developed my analytical skills, not only to analyze data, but also to critically think about processes and experiments and determine how to improve them. Most of all, I appreciate the fact that she was always patient, and never dissuaded me from asking questions, no matter how trivial. This, and the extremely collaborative lab environment she fosters, helped me as a graduate student who was starting out with no background in biology.

I have been fortunate enough to work with exceptional colleagues over the years, who have trained me on various techniques, provided feedback on proposals, manuscripts and talks, or simply made working in a lab more fun. A huge amount of thanks goes out to the talented postdocs of Leckband Lab. Ryan, Jun, Tae-Jin, Poonam, Roberto, Dean and Lydia have been helpful with advice, both inside and outside the lab. Ryan, Jun, Poonam and Roberto in particular lifted the spirits of Room 4. Special thanks goes out to Ryan, who kicked off the equibiaxial cell stretcher project, and also to Dean, who taught me how to use the Langmuir trough and perform Langmuir-Blodgett deposition. I also thank my fellow graduate students (and ex-graduate students who now hold Ph.D. degrees) – Sangwook, Johana, Nitesh, Sam, Jillian, Loki, Xinyu, Zainab, Ellen, Vinh, Tajin, Jason and Whitney. Sangwook taught me how to perform kymography experiments, Sam taught me how to perform AFM nanoindentation, Johana and Ellen taught me how to use a universal testing machine, Loki taught me lentivirus production and concentration, and while

Xinyu's knowledge of endothelial signaling is slightly intimidating, she is an extremely helpful reference guide whenever I had any signaling-related questions!

I am also grateful to my scientific collaborators. Dr. Steven Dudek and Prof. Yulia Komarova (both from University of Illinois, Chicago) provided significant insights into endothelial cell biology. Prof. Jianping Fu (University of Michigan, Ann Arbor) and his student, Dr. Yue Shao, helped make the mPAD studies possible. Prof. Marni Boppart (University of Illinois, Urbana-Champaign) and her student, Dr. Ziad Mahmassani, helped out with some Flexcell experiments. Profs. Paul Kenis and Catherine Murphy (University of Illinois, Urbana-Champaign) and their students, Dr. Joseph 'Joe' Whittenberg, Dr. Jeremy Schieferstein, Dr. Elissa Grzincic and Huei-Huei Chang, collaborated with me on a lung-on-a-chip project. Joe also provided valuable advice on lithography for my mPAD project.

My friends Anish, Subhro, Arun, Andy, Joe, Ankur, Vivek and Oki helped make these five years in Champaign interesting, and I am thankful for their friendship. This work would not have been possible without an incredible amount of support from my family. I thank my amazing wife, Namrata, for her patience and understanding over these years as we pursued our doctoral research in different states. She never failed to cheer me up through various obstacles and disappointments, and was always there to encourage me and celebrate the good times. My dad and sister, in Kolkata have been my bedrock, helping me keep my eyes on the goal. More than anyone else, I would like to thank my beloved mom. She passed away in 2014 and could not see me graduate, but her advice and teachings stay with me from childhood and will guide me through my life as they did during my studies. She and my dad have sacrificed a lot for me, and I dedicate this dissertation to them.

Table of Contents

Chapter 1: Introduction 1
1.1 Overview 1
1.2 External mechanical forces regulate cell and tissue function 2
1.3 Cells exert mechanical forces on their environment 3
1.4 *In vitro* models to replicate biological functions 5
1.5 Questions addressed in this dissertation 6
1.6 Figures 10

Chapter 2: Dynamic imaging reveals coordinate effects of cyclic stretch and substrate stiffness on endothelial integrity 13
2.1 Introduction 13
2.2 Materials and methods 15
2.2.1 Cell culture and reagents 15
2.2.2 Lentiviral transduction of HPAECs 16
2.2.3 Equibiaxial stretcher design 17
2.2.4 Hybrid membrane fabrication 18
2.2.5 Grafting polyacrylamide hydrogels on PDMS membranes 19
2.2.6 Strain characterization 20
2.2.7 Characterization of bulk polyacrylamide moduli and AFM nanoindentation of grafted gels 21
2.2.8 Preconditioning HPAECs to cyclic strain 22
2.2.9 Live-cell imaging of cyclically stretched monolayers 23
2.2.10 Optical comparison of commercial silicone and PDMS 23
2.2.11 Image analysis and statistical analysis 24
2.3 Results 25
2.3.1 Hybrid membranes exhibit improved image quality and durability 25
2.3.2 Homogeneity of equibiaxial substrate strain 26
2.3.3 Dynamic imaging reveals the protective effects of cyclic stretch on endothelial monolayers 26
2.3.4 Substrate rigidity alters thrombin induced gap formation in static and cyclically stretched monolayers 28
2.4 Discussion 30
2.5 Figures 34
2.6 Tables 43

Chapter 3: Cyclic stretch remodels endothelial junctions and enhances lamellipodia dynamics 47
3.1 Introduction 47
3.2 Materials and methods 49
3.2.1 Cell culture and reagents 49
3.2.2 Equibiaxial cyclic stretch of endothelial monolayers 50

3.2.3 Antibodies and immunostaining....51
3.2.4 Immunostaining analysis....52
3.2.5 Kymography analysis....54
3.2.6 Collective cell migration....55
3.2.7 Statistical analysis....56
3.3 Results....56
3.3.1 Endothelial junction areas decrease under physiological cyclic stretch....56
3.3.2 F-actin and cortactin are significantly enriched at junctions in cyclically stretched monolayers....57
3.3.3 Cyclic stretch increases tension on endothelial junctions....58
3.3.4 Endothelial cells under cyclic stretch show enhanced lamellipodia dynamics....59
3.3.5 Collective endothelial cell migration is unaffected by cyclic stretch....60
3.4 Discussion....61
3.5 Figures....66
3.6 Table....75

Chapter 4: Elastomeric micropillar arrays as a platform to quantify endothelial junction mechanics....76
4.1 Introduction....76
4.2 Materials and methods....79
4.2.1 Cell culture and reagents....79
4.2.2 Photolithographic patterning of silicon mPAD masters....79
4.2.3 Replica molding of elastomeric mPADs....82
4.2.4 Critical point drying of mPADs....85
4.2.5 Stamp fabrication for microcontact protein printing....86
4.2.6 mPAD functionalization....88
4.2.7 Cell seeding on mPADs and fixation....90
4.2.8 Immunostaining and imaging....90
4.2.9 Calculation of junction area and cell-generated traction forces....91
4.2.10 Calculation of junction tension and junction stress....97
4.2.11 Statistical analysis....98
4.3 Results....99
4.3.1 Thrombin increases tension and stress on endothelial junctions....99
4.3.2 VE-PTP knockout endothelial cells show increased stress at junctions....100
4.3.3 Endothelial cells on N-cadherin-coated substrates show increased tension at junctions relative to cells on fibronectin....101
4.4 Discussion....102
4.5 Figures....108
4.6 Table....115

Chapter 5: Towards an *in vitro* model of the human airway subjected to nanoparticle exposure....116
5.1 Introduction....116
5.2 Materials and methods....122

5.2.1 Cell culture and reagents 122
5.2.2 Lung epithelial-endothelial co-culture and differentiation....123
5.2.3 Antibodies and immunofluorescence 127
5.2.4 Alcian Blue staining of mucins 129
5.2.5 Nanoparticle library and stabilization 130
5.2.6 Nanoparticle treatment and cell metabolic activity measurements 131
5.2.7 Statistical analysis 135
5.3 Results 135
5.3.1 Establishing an *in vitro* co-culture model of the blood-gas barrier 135
5.3.2 Dose-dependent effects of NPs on cell viability 140
5.3.3 Size-dependent effects of NPs on cell viability....141
5.3.4 Effect of NP surface chemistry on cell viability 142
5.4 Discussion 146
5.5 Figures....151
5.6 Tables 165
Chapter 6: Conclusions and future work 171
6.1 Conclusions 171
6.1.1 Design of a live-cell imaging capable equibiaxial stretcher device with tunable substrate stiffness....171
6.1.2 Physiological substrate stiffness and cyclic stretch coordinately protect the lung endothelium against inflammatory mediators 171
6.1.3 Physiological cyclic stretch remodels endothelial junctions and enhances small wound healing 172
6.1.4 An elastomeric micropillar array quantifies changes in endothelial cell mechanics...173
6.1.5 Development of a primary co-culture model of the pulmonary blood-gas barrier.....174
6.2 Future work 174
References....177

Chapter 1: Introduction

1.1 OVERVIEW

Mechanical forces govern various functions in living organisms, starting from development[141,142], to disease progression[102,196], wound healing[113,226], and aging[37,172]. Cells can sense mechanical forces[60,103,182] through cell surface receptors, as a result of which mechanical forces trigger biochemical processes that govern a range of critical cell functions including gene expression[40,41], cell migration[137,175], stem cell differentiation[61,69], and cancer metastasis[123,225]. Recent efforts in the cell biology and tissue engineering communities have thus focused on the *in vitro* replication of not only the biochemical environment, but also the mechanical environment. This includes the use of devices and techniques such as fluid-cells for replicating shear flow, cyclic stretch devices, compressive stress devices to mimic bone loading, and use of substrates with tunable stiffness[32,52].

At the same time, cells also exert mechanical forces on their environment, including other cells, generated by the intracellular actomyosin apparatus and relayed to the external environment by cell surface proteins[39,70,144,175]. Multiple approaches, including atomic force microscopy, magnetic twisting cytometry, and optical traps, have been used to quantify these mechanical forces, which can be altered by biochemical stimuli, genetic mutations, or external mechanical forces[13,44,114,136,170,220]. Changes to these cell-matrix and cell-cell adhesive forces are often hallmarks of disease, including developmental disorders[102] and malignant progression of tumors[149,225].

In this dissertation, I focus on the lung – one of the most mechanically active organs in our bodies – which enables us to take approximately 21,000 breaths every day at a spontaneous

breathing rate of approximately 15 breaths per minute in adults[18]. Lungs enable the exchange of oxygen and carbon dioxide between the atmosphere and the bloodstream, through the thin blood-gas barrier present in hundreds of millions of alveoli[7,161], each of which is surrounded by a network of capillaries. The blood-gas barrier is comprised of airway epithelial cells in contact with the atmosphere, and endothelial cells that line the capillaries. These two cell layers are separated by a 0.2 – 0.3 μm thick interstitial structure consisting of fused epithelial and endothelial basement membranes[223]. Breakdown of the blood-gas barrier can result from various reasons including, for example, physical trauma, pulmonary infection, or mechanical ventilation. Barrier disruption ultimately results in protein-rich pulmonary edema in which fluid leaks from blood vessels to the alveolar airspaces[10,167,223] (Fig. 1.1), and results in pathologies such as Acute Lung Injury (ALI) and Acute Respiratory Distress Syndrome (ARDS)[59,145,167,216].

1.2 EXTERNAL MECHANICAL FORCES REGULATE CELL AND TISSUE FUNCTION

The vasculature is a mechanically active environment. On the vessel wall, endothelial cells experience fluid shear stress, as well as circumferential stress (hoop stress) due to blood pressure[86,99,138] (Fig. 1.2). Further, endothelial cells also sense the stiffness of the intima[101]. Specifically in the lung, pulmonary endothelial cells additionally sense the cyclic stretch of lung tissue, during respiration[20]. These mechanical forces variously regulate cell and tissue function – for example, shear stress causes cell realignment in the direction of flow[129], cyclic stretch regulates endothelial barrier function[20], and both stimuli regulate cell signaling and gene expression differentially[8,40,184].

The individual effects of shear stress[44,51,58,129,208], cyclic stretch[19,20,23,135], and matrix stiffness[25,122,192] on endothelial cells and tissues have been studied extensively. However, there have also been efforts to combine multiple mechanical stimuli to study the regulation of endothelial tissue integrity and barrier function. For example, endothelial cells cultured in compliant cylindrical tubes that can combine circumferential cyclic stretch (subjecting cells to hoop stress) and shear stress[152,236], have been used to demonstrate increased alignment and thickness of actin stress fibers in the direction of flow. Endothelial cells subjected to shear stress, showed increased cell alignment and increased barrier function when cultured on soft substrates, and changes in phosphorylation states of various kinases important to intracellular signaling[119].

In this dissertation, I report the development of a device that is capable of applying cyclic stretch on endothelial cells cultured on substrates of different stiffness[49]. This device can be mounted on a microscope, enabling live-cell imaging of the samples at any point during stretch. I investigated the effects of cyclic stretch and substrate stiffness on endothelial integrity, when treated by a barrier disrupting agent (thrombin). I also investigated the effects of cyclic stretch on the molecular composition of endothelial junctions, to determine stretch-induced changes which may protect against junction disruption. Further, I studied the effects of cyclic stretch on the dynamics of sheet-like cell membrane protrusions called lamellipodia, which are hallmarks of the wound healing response[33].

1.3 CELLS EXERT MECHANICAL FORCES ON THEIR ENVIRONMENT

In 1980, Harris, et al. used thin, compliant silicone sheets to elegantly demonstrate that adherent cells exert forces on their substrates[88]. Since then, deformable substrates engineered from different

materials have been used to detect and quantify mechanical forces exerted by cells through cell-matrix interactions[218]. This includes silicone substrates decorated with beads as fiduciary markers[127,162], polyacrylamide gels with embedded beads as fiduciary markers[170], silicone substrates with micropatterned fiduciary markers[11], and microfabricated force-sensing arrays employing cantilever deflection principles[77,178,199]. It has also been established that cells exert forces on neighboring cells through cell-cell contacts[147]. The intracellular actomyosin machinery is responsible for generating contractility[50,155,235], which is relayed to the environment through adapter proteins which link the actin cytoskeleton to transmembrane adhesion proteins such as integrins (for cell-matrix adhesions)[35,79] and cadherins (for cell-cell adhesions)[29,126,147].

While it is possible to directly measure traction forces exerted by cells on their substrates, by the approaches described previously, tension at junctions is not as easily measured directly. Tension at junctions must be calculated by applying mechanical force balance principles on traction forces underneath cell doublets[136,144,146] and specific arrangements of cell clusters[144,159], or must be estimated as 'stress' in the case of larger cell clusters[122,198]. Tension at endothelial cell junctions have been shown to be perturbed under various stimuli such as barrier disruptive agents (thrombin) and barrier protective agents (sphingosine 1-phosphate)[136] and even mechanical stimuli such as shear stress[44]. One model for cytoskeletal regulation of endothelial barrier function proposes that the mechanical force balance, between intracellular contractile forces and cell-cell and cell-matrix adhesion forces, controls the barrier integrity[65]. As a result, quantifying the effect of various perturbations on tension at endothelial junctions yields important information about endothelial barrier function under those perturbations.

I describe the use of elastomeric micropillar arrays as cell culture substrates to quantify traction forces exerted by cell doublets. Using mechanical force balance principles, I determined

the tension at endothelial junctions. Further, after determining the area of the junctions, I calculated the stress exerted on the endothelial junctions. Using this approach, I was able to determine the impact of biochemical stimuli, genetic perturbations, as well as changes to the matrix composition, on junction mechanics. I also describe the versatility of this platform over genetically encoded tension sensors, and over other elastomeric substrate-based traction sensing approaches which can be used to estimate tension or stress at junctions.

1.4 *IN VITRO* MODELS TO REPLICATE BIOLOGICAL FUNCTIONS

A majority of cell biology research consists of studies performed on a specific cell type, in isolation from other cell types. As cellular responses are not confounded by interactions with other cell types, this 'monoculture' setup has its merits. However, in many *in vitro* studies it is essential to capture the physiological interaction of cells, including intercellular signaling, which necessitates the use of cell co-cultures[66,68,83,115]. For example, endothelial cells and astrocytes have been co-cultured to study the blood-brain barrier[57], endothelial cells and smooth muscle cells have been co-cultured to replicate interactions in the vascular wall[72], and hepatocytes and fibroblasts or endothelial cells have been co-cultured to mimic interactions in the liver[185].

Various efforts have been made to mimic the pulmonary blood-gas barrier *in vitro*. Co-cultures of airway epithelial cells with endothelial cells show formation of tight junctions and enhanced barrier properties[91,92]. Triple co-cultures have been reported, which add macrophages in order to investigate the role of immune cells under specific stimuli[55,111]. A tetraculture has also been reported which includes mast cells in addition to epithelial cells, endothelial cells, and macrophages, to further accurately model the immune response[118]. However, the drawbacks in

these models include use of immortalized cell lines instead of primary cells, culture under submerged conditions instead of at the air-liquid interface, etc.

Significant progress has been made on these challenges in recent organ-on-chip models. The very first reported lung-on-a-chip[98] utilized immortalized epithelial cells, but subsequent reports of small airways-on-chips[17] and alveoli-on-chips[104] indicate the use of primary epithelial and endothelial cells, such that the epithelial cells can differentiate and display a polarized phenotype, as *in vivo*, while also replicating shear flow on the endothelium, and in the case of the lung-on-a-chip, physiological cyclic stretch on the epithelial-endothelial barrier.

With the goal of studying the effects of aerosolized nanoparticle exposure on the pulmonary barrier, I worked towards establishing a well-differentiated primary co-culture model of the blood-gas barrier in a macroscale transwell setup *in vitro*. I present the results of my work in this dissertation, optimizing cell culture conditions for differentiation of the small airway epithelium at the air-liquid interface. These results form the basis for establishment of similar well-differentiated air-liquid interface co-cultures in a small airway-on-a-chip setup.

1.5 QUESTIONS ADDRESSED IN THIS DISSERTATION

The broad goal of my research is to engineer tools and approaches for investigating the regulation of the pulmonary endothelial barrier. In this dissertation, I report the effects of specific external mechanical perturbations on lung endothelial integrity, a technique to measure mechanical forces exerted by endothelial cells at cell-matrix and cell-cell adhesions, and finally a co-culture model of primary lung epithelial and endothelial cells cultured at the air-liquid interface.

In Chapter 2, I describe the development of a device capable of applying physiological equibiaxial cyclic stretch to endothelial monolayer cultured on hydrogels, of stiffness matching healthy, or fibrotic lung tissue[49]. This device permits us to investigate the interplay of multiple mechanical perturbations and helped us demonstrate that physiological cyclic stretch and substrate stiffness coordinately protect the lung endothelium from disruption by inflammatory agents, by resulting in the formation of smaller gaps and quicker recovery from gap formation. This platform improves upon previously reported stretchers by the use of a 'hybrid' membrane, which uses polydimethylsiloxane (PDMS) instead of commercial silicone for the cell growth and imaging area. The excellent optical properties of PDMS, including low autofluorescence, enabled me to use endothelial cells transfected with mCherry-LifeAct in order to visualize actin cytoskeleton dynamics. As a result, I was able to demonstrate that lamellipodia initiation, a hallmark of endothelial monolayer recovery, begins earlier in disrupted monolayers on physiologically stiff substrates, subjected to physiological cyclic stretch.

Chapter 3 investigates the role of cyclic stretch in protecting the lung endothelial monolayer integrity. Immunofluorescence microscopy was used to visualize and quantify the abundance of cell-cell adhesion proteins (VE-cadherin), F-actin, and the actin-scaffolding protein cortactin at endothelial junctions, and I was able to demonstrate that monolayers preconditioned to physiological cyclic stretch exhibited junctional accumulation of F-actin and cortactin. Using antibodies against a tension-sensitive protein, α-catenin, I was able to determine that upon cyclic stretch preconditioning, a greater fraction of the junctional α-catenin molecules were in the tension-dependent open conformation. This suggested that physiological cyclic stretch might result in increased tension at the junctions. Collectively, these changes suggest reinforcement of the junctions against disruption by inflammatory mediators. I also determined that cyclic stretch

enhanced lamellipodia dynamics in endothelial cells preconditioned to physiological cyclic stretch, however, collective cell migration rates were unaffected. These results suggested that cyclic stretch may help enhance lamellipodia-driven recovery from small wounds, but did not enhance recovery from large wounds which needed collective cell migration.

Chapter 4 shifts the focus to mechanical forces generated by endothelial cells. I used a previously reported microfabricated platform[43,136] to quantify cell-generated traction forces and use mechanical force balance principles to calculate the tension at cell junctions, in endothelial cell doublets. This platform helped demonstrate that in endothelial cell doublets treated with thrombin, total traction force did not increase, while traction per unit area (stress) did increase. At the same time, the tension at the junctions increased and the junction area decreased, such that the overall stress at the junction doubled. Similarly, knocking out vascular endothelial protein tyrosine phosphatase (VE-PTP), which is hypothesized to stabilize VE-cadherin at endothelial junctions, was found to increase junctional stress, without causing any changes to the traction forces. Lastly, I was also able to establish that matrix composition could regulate the tension at endothelial cell-cell junctions. These results helped establish the versatility of this platform in investigating endothelial cell mechanics.

Lastly, Chapter 5 discusses the development of a primary co-culture model of the pulmonary blood-gas barrier, cultured at the air-liquid interface. This model was developed in order to study the effects of aerosolized nanoparticles on the blood-gas barrier, including nanoparticle transport across the barrier. The airway epithelial cells in this model are well-differentiated, into ciliated cells, and secretory cell types like goblet cells and club cells, which secrete mucins and other components of mucus. The airway epithelial cells and endothelial cells are separated only by a 10 μm thin porous membrane, which permits them to exchange soluble

factors. I also perform some preliminary experiments on the effects of nanoparticle exposure in solution, on viability of airway epithelial and endothelial cells.

1.6 FIGURES

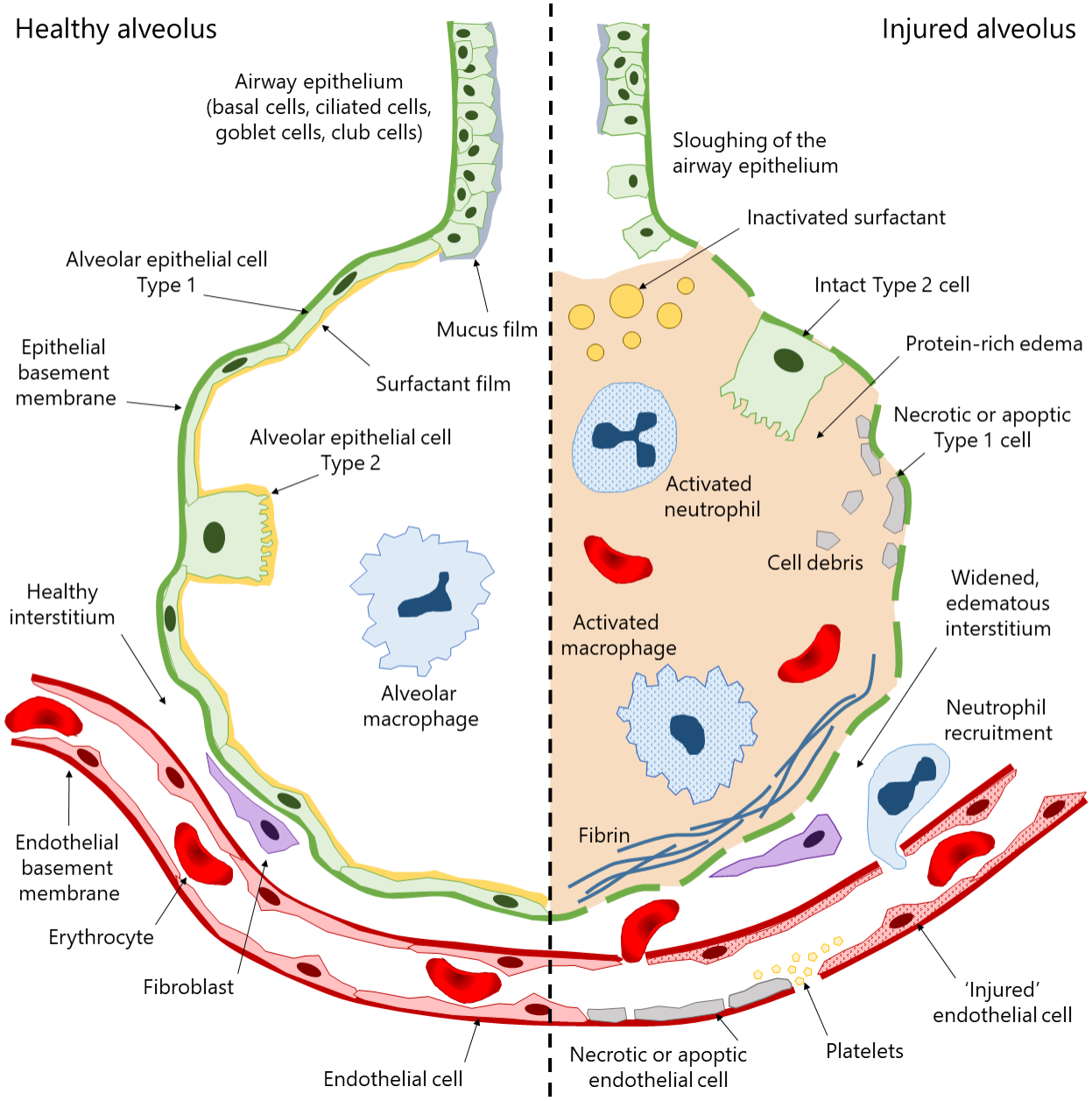

Fig. 1.1: The pulmonary blood-gas barrier is disrupted under pathological conditions. Graphical representation of the alveolus under physiological and pathological conditions shows the compromised blood-gas barrier (not to scale). In a healthy alveolus, the alveolar epithelium and capillary endothelium are both intact, with a thin interstitium in between them, comprising the blood-gas barrier. A thin surfactant film covers the epithelial cells. Alveolar macrophages in the healthy alveolus protect against pathogens. Due to pulmonary trauma, or infection, or radiation exposure etc., the blood-gas barrier can break down, often marked by epithelial and endothelial cell death, and disrupted intercellular junctions. This results in pulmonary edema – the interstitium as well as alveolus can fill up with protein-rich fluid. Alveolar macrophages, and other recruited

Fig. 1.1 (contd.): leukocytes such as neutrophils, are activated and secrete inflammatory cytokines, which can cause further damage to the integrity of the barrier. Platelets are activated and start repairing the damage. In the alveolus, type 2 alveolar epithelial cells proliferate and differentiate into type 1 cells to restore epithelial integrity and start surfactant secretion. In the capillary, endothelial cells proliferate to restore endothelial integrity. The healed tissue is typically fibrotic and thus stiffer than healthy tissue (Cabrera-Benitez, et al., *Anesthes.* 2014, 121(1):189-198). Reproduced with minor modifications, with permission from Ware, et al., *N. Engl. J. Med.* 2000, 342:1334-1349, Copyright Massachusetts Medical Society.

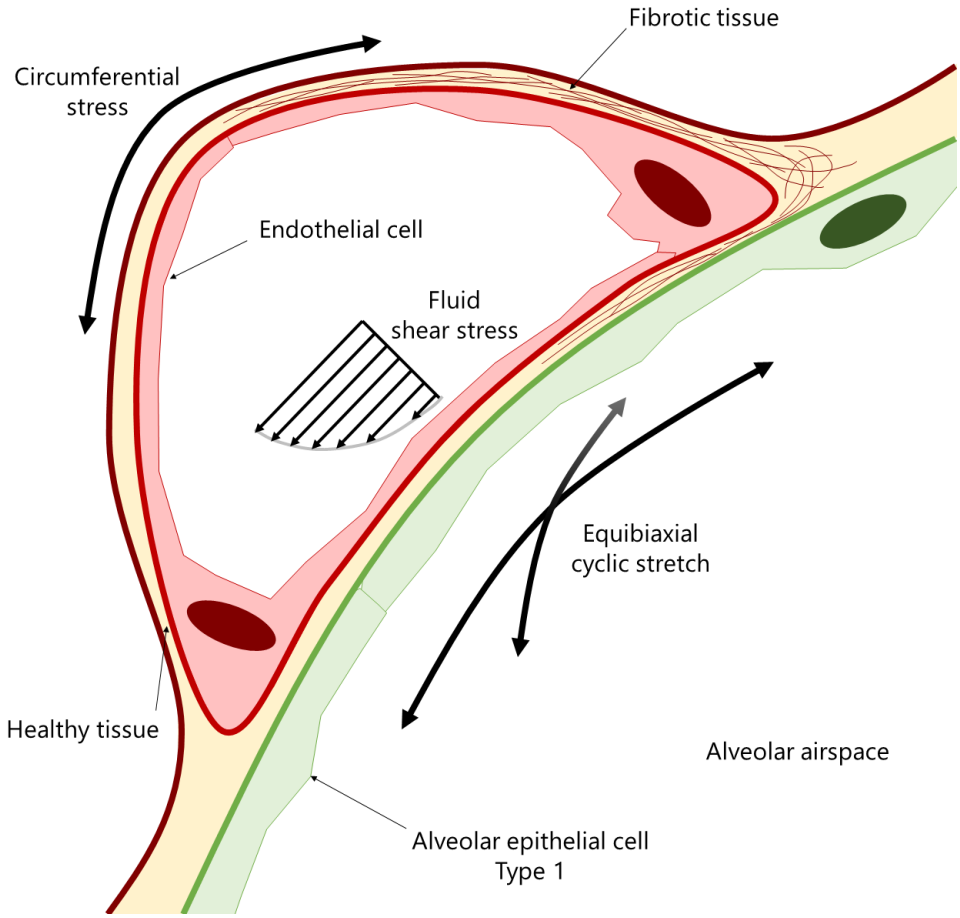

Fig. 1.2: Mechanical forces on the pulmonary vascular endothelium. Endothelial cells in capillaries on the surface of alveoli are subjected to equibiaxial cyclic stretch during respiration. Additionally, endothelial cells also sense fluid shear stress, and circumferential stress (hoop stress) due to blood pressure. In pathological cases, for example pulmonary fibrosis, cells may lie on fibrotic tissue, which is stiffer than healthy tissue.

Chapter 2: Dynamic imaging reveals coordinate effects of cyclic stretch and substrate stiffness on endothelial integrity*

2.1 INTRODUCTION

A range of mechanical cues influence vascular endothelial function, including fluid shear stress, hydrodynamic pressure and tissue stiffness[86]. The pulmonary endothelium may also experience cyclic equibiaxial strain during respiration[205,206]. The pulmonary endothelium is critical to maintaining the blood-gas barrier, and endogenous and exogenous mechanical stimuli can disrupt force balances postulated to maintain endothelial homeostasis[65]. Large-amplitude pathological cyclic strain (CS) has been shown to delay barrier recovery after treatment with inflammatory mediators like thrombin, whereas physiological CS protects against barrier failure[20-22].

In addition to cyclic strain, tissue stiffness also influences endothelial permeability[101,140]. The physiological relevance of these observations is supported by *in vivo* studies demonstrating the increased permeability of stiffer, aged arteries[101] and increased vascular permeability in fibrotic lungs[132,140]. Such observations strongly suggest that mechanotransduction signals play an important role in endothelial barrier regulation, and further suggest links between vascular stiffness and disease. However, the underlying mechanisms, their response to altered stimuli such as cyclic strain and matrix rigidity, and their broader impact on endothelial barrier properties have yet to be established. Limitations in current experimental approaches present challenges to addressing these questions.

* Adapted, with permission, from Dan, A., R. B. Huang and D.E. Leckband. Dynamic imaging reveals coordinate effects of cyclic stretch and substrate stiffness on endothelial integrity. Ann. Biomed. Eng. 44:3655-3667, 2016.

To mimic the mechanical environments of some tissues such as the lung, some *in vitro* approaches enable cell monolayer stretching, using substrates of physiologically relevant stiffness[38,165,186,202]. Common strategies for generating substrate strain involve membrane deformation techniques, such as use of positive or negative pressure, or indentation by non-flat or non-circular indenters. The latter approaches can impede dynamic cell imaging, because they move the cell monolayer out of the focal plane. These approaches also generate spatially non-uniform strain fields[180]. Alternative configurations generate uniform equibiaxial strain across a horizontal circular membrane, and avoid focal plane changes during stretch, by stretching membranes over flat cylindrical posts or drums.

Dynamic visualization of subcellular changes during continuous stretching is also a challenge. Elastic silicone membranes are conventionally used due to their biocompatibility, optical properties, and ease of use. However, not all stretching configurations permit live-cell imaging. Silicone materials, and thicknesses required for mechanical durability, can increase background fluorescence and limit resolution, thus requiring cell fixation. For example, commonly used durable, thick (~0.20-0.25 mm) commercial silicone sheeting[20,97,186,205], is translucent rather than transparent, and exhibits autofluorescence. Alternatively, polydimethylsiloxane (PDMS) membranes have superior optical properties, low autofluorescence, and can be cast in custom dimensions[38,165]. However, casting durable PDMS membranes requires compromises on membrane thinness or use of high crosslinker:elastomer base ratios, which render the membranes relatively difficult to stretch.

Silicone membranes are also typically 2-3 orders of magnitude stiffer than healthy lung tissue. Based on AFM nanoindentation studies[133], the median Young's modulus of healthy murine lung parenchyma is 1.4 kPa, with rare locations exceeding 8.4 kPa. In contrast bleomycin-treated

murine lung parenchyma, a model of pulmonary fibrosis, exhibits a higher, median Young's modulus of 8.4 kPa, with rare values exceeding 42 kPa. Rigid substrata increase intercellular tension[122,144], and likely predispose cells to junction disruption upon biochemical or mechanical perturbation.

Here I describe a cell stretcher that enables dynamic imaging of pulmonary cell monolayers under conditions that more closely mimic the physiological environment. This stretcher device i) generates homogenous, uniform equibiaxial strain, thereby mimicking deformations during respiration; ii) uses membranes with physiological and pathological stiffness; and iii) enables dynamic, fluorescence imaging of cells during mechanical and biochemical perturbations. The design is based on reported equibiaxial strain-generating devices that model *in vitro* cyclic strain in organs such as the lung[97,205]. I further describe hybrid membranes with improved optical properties over commercial silicone. To mimic tissue stiffness, polyacrylamide gels were grafted to the hybrid membranes[186,202]. Time-lapse images of thrombin-treated pulmonary endothelial monolayers on cyclically stretched substrata revealed the dynamics of monolayer disruption and recovery, coordinate protective roles of both physiological CS and substrate stiffness, and their influence on cytoskeletal remodeling.

2.2 MATERIALS AND METHODS

2.2.1 Cell culture and reagents

Human pulmonary artery endothelial cells (HPAECs) were from Lonza (Walkersville, MD), cultured in the recommended endothelial cell growth medium EGM-2 (Lonza) with 10% (v/v) fetal bovine serum (Sigma-Aldrich, St. Louis, MO) in a humidified incubator at 37°C at 5% CO_2.

The third generation self-inactivating lentiviral plasmid for mCherry-LifeAct in a pLV-CMV-IRES-Puro backbone[100] was a gift from Johan de Rooij (UMC Utrecht, The Netherlands). The envelope plasmid PMD2.G and the packaging plasmid psPAX2 were from Didier Trono (Addgene plasmids #12259 and 12260, respectively). Lentivirally transduced HPAECs expressing mCherry-LifeAct were used for all experiments at passages 8-9. Collagen-I (Col-I) from rat tail was obtained from BD Biosciences (San Jose, CA) and human fibronectin (Fn) was from EMD Millipore (Temecula, CA).

2.2.2 Lentiviral transduction of HPAECs

Lentiviral production, concentration, and cell transduction were performed in accordance with established BSL2 protocols, as described previously[204]. HEK293T cells used for lentiviral production were cultured in Dulbecco's Modified Eagle Medium (DMEM, Corning Cellgro) containing 4.5 g/L glucose, 4 mM L-glutamine, and 1 mM sodium pyruvate, with 10% (v/v) FBS and 1% (v/v) penicillin-streptomycin. Virus-harvesting medium consisted of the same DMEM supplemented further with 2 mM L-glutamine, 1 mM sodium pyruvate, 1.1 g/L Bovine Serum Albumin (BSA) and 1% (v/v) non-essential amino acid solution. HEK293T cells at 70% confluence in 100 mm tissue culture dishes were cotransfected with the lentiviral mCherry-LifeAct vector (10 μg/dish) and psPAX2 (7.5 μg/dish) and PMD2.G (5 μg/dish) packaging and envelope plasmids, by calcium phosphate transfection. At 6 hr after transfection, medium was replaced with 5 mL virus harvesting medium per dish. Virus-containing medium was collected at 36 and 72 hr after initial medium replacement, and filtered through a 0.45 μm filter. Lentiviral particles were concentrated 100x by ultracentrifugation (Beckman L8-70 Ultracentrifuge, Brea, CA) and stored at -80^{O}C until use.

For transduction, human pulmonary artery endothelial cells (HPAECs) in the fifth passage were seeded in 6-well plates to reach 80% confluence within ~24 hr. Concentrated lentivirus was diluted 100x into EGM-2 medium with 8 μg/mL polybrene (Santa Cruz Biotechnology, Dallas, TX), and incubated with the HPAECs for 24 hr, after which the cells were washed and expanded further in EGM-2 medium. Transduced cells were cryopreserved at the seventh passage.

2.2.3 Equibiaxial stretcher design

The stretcher is based on a previously reported design[97]. An elastic membrane (see below) is mounted onto a circular membrane-holding ring (MHR, inner diameter 44 mm, anodized aluminum, Fig. 2.1A) using a silicone O-ring (1.864" actual ID, 0.07" actual width, McMaster Carr, Elmhurst, IL) that fits into a groove (1.78 mm width) in the base of the MHR. The MHR stretches the membrane over a fixed indenter ring (IR, outer diameter 41 mm, anodized aluminum, Fig. 2.1B) and exerts equibiaxial strain on the flat section of the membrane. The use of an indenting ring, as opposed to a post, enables membrane imaging with an inverted fluorescence microscope. Because the IR is immobile during strain, there is negligible membrane z-movement, and the membrane remains in the same focal plane (Figs. 2.1C, 2.2E). The MHR is mounted on an aluminum arm with a linear actuator (Anaheim Automation, 11AV102AX06, Anaheim, CA) at one end to move the MHR vertically over the IR (Fig. 2.1C). The other end moves along a Frelon-lined guide rail, ensuring smooth, vertical movement. The edge of the mounted membrane is lubricated with food-grade silicone grease (Refrigeration Technologies, Fullerton, CA) to reduce friction between membrane and IR, during indentation (Fig. 2.2E). The center of the membrane supporting cells is free of lubricant and optically transparent. The stretcher base is designed to mount on the stage of a Zeiss Axiovert 200M epifluorescence microscope for dynamic imaging of

cells subjected to equibiaxial strain (Figs. 2.1C, 2.2E). A programmable driver controls the linear actuator (EZStepper EZ17, Allmotion, Union City, CA). Cyclic strain (CS) is applied in a triangular wave with desired amplitude and frequency, and can be paused at any time or indentation depth for imaging.

2.2.4 Hybrid membrane fabrication

Hybrid membranes were fabricated using medical-grade silicone sheeting (0.01" nominal thickness, SMI silicone, Saginaw, MI) as a scaffold to ensure mechanical durability at the edges where the membranes are mounted onto the MHR. The scaffold experiences significant tensile, compressive and shear forces, during mounting and indentation. A mask was formed by excising a 40 mm diameter circle from the center of a 60 mm x 60 mm silicone sheet. After placing the mask on a glass slab, a thin, transparent PDMS film was cast in the central cut out region, as an optical window, by pouring ~0.63 g of 26:1 (w/w) elastomer base:crosslinker PDMS (Sylgard 184, Dow Corning, Auburn, MI) into the cut out region, with a 1 mm edge overlap with the silicone sheeting (Fig. 2.2A). This assembly was cured for 14-16 hr at 65 °C, and the hybrid membrane was peeled off the glass and placed on an inverted MHR. Holding the membrane under slight tension, the silicone scaffold was fit into the groove of the MHR with the O-ring. Excess silicone was removed (Fig. 2.2B).

The membrane-mounted MHR can be autoclaved and directly used for cell culture. On a 1 cm diameter spot in the center of the membrane, 150 μL of 50 μg/mL Fn or Col-I was incubated for 1 hr at 37 °C. Then, ~25,000 HPAECs expressing mCherry-LifeAct were seeded on the same

spot with 150 μL of medium. After 2 hr, once the cells attached and started spreading, 4 mL medium was added to the MHR.

2.2.5 Grafting polyacrylamide hydrogels on PDMS membranes

To mimic tissue stiffness, polyacrylamide hydrogels were grafted onto hybrid membranes, using benzophenone photochemistry[186,221]. A 10% (w/v) solution of benzophenone in 30:70 (v/v) water:acetone was incubated on the PDMS window of a hybrid membrane for 1 min, rinsed with methanol, and air-dried. Then, 15 μL of a solution containing acrylamide and bis-acrylamide at desired concentrations, 0.05% ammonium persulfate, and 0.5% TEMED (Bio-Rad, Hercules, CA) in PBS was pipetted onto the center of the treated membrane, and a 12 mm glass coverslip was placed over it. The assembly was exposed to UV light (360 nm, 4.4 mW/cm^2, Spectroline XX-15A benchtop UV lamp) for 45 min, to cure the gels and graft them to the PDMS (Fig. 2.2D). To prevent oxygen from diffusing through the thin PDMS membranes (<200 μm) and inhibiting polymerization, a 25 mm glass coverslip was placed on the underside of the membrane. I grafted hydrogels with nominal Young's moduli of 5 kPa (5% acrylamide and 0.15% bis-acrylamide, (w/v)) and 15 kPa (10% acrylamide and 0.3% bis-acrylamide, (w/v)), which are within the respective stiffness ranges for normal and fibrotic lung tissue[133].

After polymerization, the membrane was immersed in PBS, and the coverslips were gently released after 10 min of hydrogel swelling. The hydrogels were twice treated with 0.05% (w/v) Sulfo-SANPAH (ProteoChem, Loves Park, IL) in PBS under 360 nm UV (1.85 J/cm^2 per exposure), with PBS rinses between treatments[169]. Col-I (200 μg/mL in PBS) was covalently linked to the activated hydrogels by incubation for 3 hr at 37 °C. Treated hydrogels were stored

overnight at 4 °C under PBS containing 1% penicillin-streptomycin. The next day, gels were rinsed with warmed medium, and mCherry-LifeAct expressing HPAECs were seeded on hydrogels, as with PDMS membranes (Fig. 2.2E).

2.2.6 Strain characterization

Fluospheres (0.2 μm diameter, 580 nm/605 nm red fluorescent beads; Molecular Probes, ThermoFisher Scientific; Eugene, OR) were added 1:1000 (v/v) to the hydrogel precursor solution. The MHR was inverted during gel grafting to promote bead accumulation at the free surface of the hydrogel. Hybrid membranes with grafted hydrogels were indented incrementally, from the relaxed position. At each step, fluorescent beads at the top surface of the gels and microscopic features in the PDMS membrane directly underneath were imaged, by fluorescence and phase contrast, respectively. At the gel top and PDMS bottom, linear strains were calculated along orthogonal axes. The ratio of strains at the gel top and PDMS bottom determined the strain transfer ratio. Averaging across five independent membranes, the linear strains at the gel surface, and the strain transfer ratios were plotted against indentation depth.

To verify equibiaxial strain, for each of the eight membranes subjected to CS, microscopic features in the PDMS membrane were phase contrast imaged at the relaxed and 5% linear strain positions. A central 'origin' was defined in the relaxed image, four axes offset by 45° were drawn, and two points were chosen per axis on either side of the origin (Figs. 2.4C, 2.4D). Measuring the distances from the origin to each point, before and after indentation, the linear strain along each axis was calculated and averaged across the eight membranes.

2.2.7 Characterization of bulk polyacrylamide moduli and AFM nanoindentation of grafted gels

The bulk Young's moduli of polyacrylamide hydrogels were determined with a material testing system (MTS Insight, MTS Systems Corporation, Eden Prairie, MN). Disks were punched from cast hydrogels, n = 2 per formulation, and equilibrated in PBS overnight. PDMS (26:1 w/w elastomer base:crosslinker) was also cured as described, and two disks were punched out. After determining the diameter and height of the hydrogel and PDMS disks, they were compressed (strain rate = 0.009/min). The slopes of the stress-strain curves between compressive strains of $\varepsilon = \Delta h/h_0 = 0.02$ and 0.05 were used to calculate the average Young's moduli. Compressive testing of the PDMS yielded a Young's modulus of 470±30 kPa, which is 1-2 orders of magnitude stiffer than lung tissue. Comparatively, the Young's moduli of the two compositions of polyacrylamide tested were 3.4±0.5 kPa and 15.0±0.1 kPa.

I also characterized the gel moduli by AFM nanoindentation[133,134]. A 20 μm diameter glass microsphere (Duke Standards, Fremont, CA) was mounted on the cantilever tip (Bruker, Billerica, MA) with thermosetting epoxy. Nanoindentation was performed under PBS with an Asylum MFP-1D AFM (Asylum Research, Santa Barbara, CA). The calibrated spring constant was k = 0.733 nN/nm at room temperature. The cantilever deflection (x) was set to a maximum of 250 nm, and the indentation velocity was 5 μm/s to be able to investigate elastic properties rather than viscoelastic. The Hertz model for a spherical indenter on a flat surface[134] was used to fit the force-displacement data during tip approach:

$$F = \frac{4\sqrt{r}}{3}\frac{\delta^{1.5}}{1-\nu^2}E \quad \ldots (2.1)$$

Here F = k*x = magnitude of force, r = tip radius, δ = indentation depth = z – x = piezo displacement – cantilever deflection, ν = Poisson's ratio ~ 0.46 for polyacrylamide hydrogels[197],

E = Young's modulus. OriginPro v9 (OriginLab, Northampton, MA) was used for non-linear curve fitting to determine the Young's modulus, E. Averaging over n = 9 locations from 3 independent hydrogels of each composition, yielded Young's moduli of 4.1±0.1 kPa and 13.3±0.7 kPa, in agreement with compression tests. The softer and stiffer gels were thus assigned nominal stiffness values of 5 kPa and 15 kPa respectively.

2.2.8 Preconditioning HPAECs to cyclic strain

Cells seeded on membranes were cultured to confluence in the incubator over 2 days. To precondition EC monolayers outside the incubator, a heated enclosure maintained the temperature at 37±1 °C. Cells were cultured in EGM-2 medium, buffered with 25 mM HEPES, 2 mM sodium pyruvate to neutralize HEPES phototoxicity[191] and 1% penicillin-streptomycin. Humidity was maintained by bubbling air through DI water. Under these conditions, cells in tissue culture dishes survived and proliferated for at least 48 hr (not tested further). However, for the cyclic strain experiments, the exposed underside of the thin membrane increases evaporation. Thus during preconditioning, a plastic plug was used with the IR to reduce membrane exposure to air (Fig. 2.1B). Sterile DI water was also periodically added to medium covering monolayers, to maintain osmolarity against evaporation.

The MHR was covered with a 60 mm tissue culture dish cover, sealed with Parafilm (Bemis Company, Neenah, WI), and mounted onto the aluminum arm of the stretcher at the relaxed position (Figs. 2.1C, 2.2E). This static preconditioning lasted 12-16 hr. Subsequently, the medium was replaced, and cells were preconditioned with 8 hr of either 5% linear equibiaxial CS at 15

cycles/min or no CS (static) (Fig. 2.5A). A 5% linear strain approximates physiological levels of strain in lungs[20,205], and 15 cycles/min is within the range of adult human respiration rates.

2.2.9 Live-cell imaging of cyclically stretched monolayers

The plastic plug was removed from the IR, and the stretcher was mounted on a Zeiss Axiovert 200M inverted epifluorescence microscope with a motorized stage and a 20× air objective (NA = 0.50). The microscope was in a heated enclosure. The preconditioned MHR was mounted on the stretcher, CS was applied for 20 min, and 3-4 monolayer locations 1-5 mm apart were chosen for tracking (Fig. 2.4A). Phase contrast and fluorescence images were taken at defined intervals. At 25 min after initiating image acquisition, human α-thrombin (Enzyme Research Laboratories, South Bend, IN) was added at t = 0 min to a final concentration of 0.1 U/mL, and images were acquired for t = 145 min, while continuing CS between acquisition time points. Images were acquired 2 min after pausing CS, to allow system stabilization.

2.2.10 Optical comparison of commercial silicone and PDMS

To quantify background fluorescence from different membranes, five sections each of commercial silicone sheeting and central PDMS window were imaged under identical conditions, with fluorescence filter sets for FITC and Rhodamine channels. Images acquired without illumination accounted for the dark current.

Membrane sections, two of each type, were also incubated with 20 μg/mL fibronectin, seeded sparsely with HPAECs and incubated for 1 day. Cells were fixed with 4%

paraformaldehyde (Fisher), permeabilized with 0.1% (v/v) Triton X-100 (Sigma), blocked with 1% (w/v) BSA, stained with Alexa Fluor 488-phalloidin (Molecular Probes) and mounted on a glass slide. F-actin was imaged through the membranes, under identical conditions.

2.2.11 Image analysis and statistical analysis

For studies of gap dynamics, monolayer images were analyzed with ImageJ v1.50a (NIH). At each location, I compiled a stack of phase contrast images from all time points, to generate a time-lapse movie of the thrombin-treated EC monolayer. Two separate 150 μm x 150 μm fields were randomly chosen per stack, and gaps in the monolayer were outlined and quantified. I thus report average gap areas per 22,500 μm^2 field. Per field, the gap formation rate was also calculated between two consecutive time points t_i and t_{i+1}, and averaged,

$$Gap\ formation\ rate = \frac{Gap(t_{i+1}) - Gap(t_i)}{t_{i+1} - t_i} \quad \ldots (2.2)$$

For monolayers on hydrogels of different moduli, n = 18 fields from three independent experiments were imaged per condition per time point. Because studies involved variations in both stiffness and mechanical strain, at each time point I performed an ANOVA to detect significant effects ($\alpha = 0.05$). The gap areas and formation rates were distributed non-normally, but unimodally. Because variance homogeneity could not be established for the four different conditions, Brown-Forsythe's modification to the two-way ANOVA was preferred[31]. For monolayers on hybrid membranes, I compared n = 14 fields each, from two independent experiments per condition per time point, using a one-tailed Welch's t-test with unequal variances ($\alpha = 0.05$) to identify significant effects of 5% CS. The same test was used in all other comparisons.

To quantify fluorescence background from membranes, in each channel, an image stack was compiled consisting of i) the dark current image, ii) five PDMS section images, and iii) five commercial silicone section images. Per stack, five well-spaced 150 pixel x 150 pixel regions of interest (ROI) were defined, and mean fluorescence intensities (MFI) were measured. For each channel,

$$Background\ MFI_{i,j,k} = MFI_{i,j,k} - Dark\ Current\ MFI_k \quad \ldots (2.3)$$

Here, i = membrane type; j = 1, 2… 5, independent membrane sections; k = 1, 2… 5, ROIs. For each channel, averaging across n = 25 ROIs from five independent sections,

$$Average\ Background\ MFI_i = \frac{\sum_j \sum_k Background\ MFI_{i,j,k}}{5*5} \quad \ldots (2.4)$$

All data are reported as the mean±S.E.M.

2.3 RESULTS

2.3.1 Hybrid membranes exhibit improved image quality and durability

Autofluorescence from the commercial silicone membrane was nearly twice that of the thin PDMS window in the hybrid membranes (Fig. 2.2C). The reduced background from the hybrid membranes was also noticeable in fluorescent images of stained F-actin (Fig. 2.3), and would benefit quantitative comparisons of fluorescence images of cells. The hybrid membranes also sustained continuous 10% linear equibiaxial CS at 15 cycles/min for 24 hr (not tested further) without any evidence of mechanical failure.

2.3.2 Homogeneity of equibiaxial substrate strain

The hydrogel grafting was very robust. After 24 hr of 10% linear, equibiaxial CS at 15 cycles/min, only negligible cracks at the gel-PDMS interface were seen at the gel perimeter, with no bulk damage. The calibration revealed a maximum possible 11±2% linear strain with the current configuration (Fig. 2.4A), but a redesigned MHR or IR could increase the strain limit. The thicknesses of the soft and stiff grafted hydrogels, determined by phase contrast microscopy, were 78±4 μm and 81±6 μm respectively (n = 6 gels each, p = 0.72). This was thick enough for the cells to be unable to feel the stiff PDMS underneath the gels[5]. I further verified that the strain transfer ratio between the PDMS and gels was ~1 (Fig. 2.4B), in agreement with previous reports[186]. At 5% CS, the spatial distribution of the strain profile was essentially homogenous, with a minimum strain of 5.3±0.3% along the 135°-315° direction and a maximum strain of 5.9±0.5% along the 45°-225° direction (p = 0.13) (Fig. 2.4E).

2.3.3 Dynamic imaging reveals the protective effects of cyclic stretch on endothelial monolayers

When EC monolayers on fibronectin-coated hybrid membranes were subjected to eight hours of 5% CS prior to thrombin stimulation, the mechanical stimulation alone induced some gap formation (Fig. 2.5B). Five minutes prior to thrombin treatment, static samples exhibited gap areas of 10±5 μm^2/field, whereas 5% CS samples exhibited substantially larger gaps, 120±30 μm^2/field (Table 2.1, $p = 2.7\times10^{-3}$). Presumably these gaps heal under persistent CS (>8 hr), as cell division replaces dead cells[20,135].

On hybrid membranes, 5 min after thrombin stimulation, the average gap areas in static and stretched samples were nearly identical (Fig. 2.5B). However at 15 min when gap areas

peaked, the gaps in static monolayers (6800±600 μm^2/field) were 144% larger than in 5% CS treated monolayers (2800±400 μm^2/field, $p = 5.0\times10^{-6}$). Lamellipodia were already visible at 15 min, and monolayer recovery was apparent at 25 min (Fig. 2.5B). The gap areas in static and stretched monolayers respectively decreased to 2800±400 μm^2/field and 600±100 μm^2/field ($p = 1.8\times10^{-5}$), *i.e.* 41% and 23% of the respective peak values. At 55 min, gap areas in the static monolayers were 150±80 μm^2/field, which appears greater than the stretched monolayers (40±20 μm^2/field), although statistical significance could not be established ($p = 0.08$). Within 115 min, gap areas in all conditions returned to pre-thrombin levels.

An advantage of this device is the ability to track specific fields over time, enabling reliable calculation of the gap formation rate. In the -5 to 5 min interval, the average gap formation rates (Fig. 2.5C, Table 2.2) for static and stretched samples were comparable, 170±30 μm^2/min-field and 160±30 μm^2/min-field respectively ($p = 0.37$). However, the rate during 5 to 15 min increased to 510±60 μm^2/min-field in static samples, whereas it decreased in stretched samples to 110±30 μm^2/min-field ($p = 1.03\times10^{-5}$), indicating the initiation of monolayer recovery mechanisms in the stretched samples. Over subsequent intervals, the average rate remained significantly more negative for the static samples. I attribute the latter to the larger peak gap area in static samples.

It is worth noting that on Col-I coated hybrid membranes, confluent EC monolayers formed as expected and tolerated 5% CS. However, upon thrombin stimulation, the monolayers peeled off the substrate under both static and 5% CS conditions. I attribute this behavior to delamination of physisorbed collagen because, on hydrogels with covalently bound Col-I, thrombin treated monolayers remained attached to the substrate.

These data demonstrated the protective effect of cyclic stretch on EC monolayers, previously established with fixed monolayers on uniaxially stretched silicone substrates[21]. The

results not only validated the stretcher and hybrid membrane for dynamically imaging cyclically stretched monolayers, but also revealed additional details of gap formation and reannealing.

2.3.4 Substrate rigidity alters thrombin induced gap formation in static and cyclically stretched monolayers

To first assess the impact of substrate rigidity on thrombin-induced gap formation, I compared static EC monolayers on 5 and 15 kPa gels. Fig. 2.6A plots the interendothelial gap area following thrombin stimulation at t = 0 min. At -5 min and 5 min, gap areas in static EC monolayers on 5 and 15 kPa gels were similar, with evident gaps at 5 min (Table 2.3). However, at 15, 25, and 55 min, the gap areas were significantly smaller in monolayers on the softer hydrogels, in qualitative agreement with literature[122]. Substrate stiffness also affected the gap formation rates in static monolayers (Fig. 2.6B, Table 2.4). Between 5 to 15 min, the gap formation rate was higher for the stiff substrate. During recovery, between 25 to 55 min and 55 to 115 min, gap formation rates were more negative in monolayers recovering from larger gaps, *i.e.* on stiff substrates.

To investigate the combined influence of cyclic stretch and substrate stiffness on thrombin-induced gap formation and recovery dynamics, EC monolayers on grafted hydrogels were subject to 5% CS, as above. Prior to thrombin stimulation, the gap areas in 5% CS-treated monolayers, were again significantly larger than in static monolayers, regardless of the matrix stiffness (Fig. 2.6A, Table 2.3). However in all cases, there were prominent stress fibers and F-actin at the cell periphery (Fig. 2.7). Five minutes after thrombin challenge, interendothelial gaps under all four conditions were comparable. The increase in gap areas also coincided with the dissolution of stress fibers, retraction of the cell periphery, and cell-cell junction remodeling.

At 15 min, gap areas peaked across all four conditions (Fig. 2.6A). The gap areas in stretched monolayers on 15 kPa substrates were 3900±400 μm^2/field compared to 2800±400 μm^2/field on 5 kPa – a statistically significant increase of 39% (Table 2.3). Active lamellipodia were visible at 15 min and with cell-cell contacts being re-established, the gaps decreased at 25 min (Fig. 2.7). The protective effects of both softer matrix and CS remained statistically significant during this early recovery stage. In stretched monolayers, the gap areas on 15 kPa substrates (1800±300 μm^2/field) were 79% greater than on 5 kPa substrates (1000±300 μm^2/field). At 55 min (late recovery stage), only the substrate stiffness appeared to have a significant effect on monolayer recovery (Table 2.3). The gap areas on stretched 15 kPa gels (400±100 μm^2/field) were 153% larger than on stretched 5 kPa gels (160±40 μm^2/field). At 115 min, the gaps in EC monolayers under all conditions were minimal and comparable.

In the intervals -5 to 5 min and 15 to 25 min, gap formation rates were comparable across all four conditions (Fig. 2.6B, Table 2.4). However between 5 to 15 min in stretched monolayers, while gap formation rate on 5 kPa gels (60±40 μm^2/min-field) was 55% lower than on 15 kPa gels (130±40 μm^2/min-field), and the effect of substrate stiffness was significant, the error bars do overlap slightly. Between 25 to 55 min and 55 to 115 min, substrate stiffness significantly affected the gap formation rate. In fact between 55 to 115 min, stiffness was the single mechanical parameter affecting the gap formation rate (Table 2.4).

It is worth noting that the peak monolayer gap areas were smallest on stretched 5 kPa gels, and largest on static 15 kPa gels (Fig. 2.6A). The latter were also the only monolayers which showed an increase in the gap formation rate between 5 to 15 min (Fig. 2.6B, 390±50 μm^2/min-field), over the previous time interval (-5 to 5 min, 250±40 μm^2/min-field) – all other conditions showed a reduction in gap formation rates during this interval. This was accompanied by reduced

lamellipodia activity at 15 min in monolayers on static 15 kPa gels, relative to other conditions (Fig. 2.7).

I also observed apparent solvent blisters underneath the EC monolayer (Fig. 2.8), immediately after 3 min of 5% CS on grafted hydrogels. Blisters were typically observed beneath the cell body, and dissipated within ~50 s. They were not observed underneath monolayers on PDMS. Similar behavior was reported in epithelial cell monolayers on hydrogels upon sudden relaxation after single stretch of 5% or greater equibiaxial strain for longer than 1 min[38]. This behavior was attributed to increased solvent pressure at the basal plane due to liquid efflux from porous hydrogels on relaxation, with greater basal solvent pressure on stiffer hydrogels, and thus larger blisters. Thus, CS-treated EC monolayers on hydrogels may also experience additional cyclic hydrodynamic pressure across the monolayer.

2.4 DISCUSSION

I report the development of a live-cell-imaging-capable equibiaxial cell stretcher and hybrid membranes with improved optical properties for use with this device. Results obtained with this platform demonstrated that physiological substrate stiffness and cyclic strain coordinately protect the endothelial monolayer against thrombin-induced disruption.

The described hybrid membranes exhibited uniform equibiaxial strain (Fig. 2.4E), and remained within the focal plane during stretching, enabling live cell imaging during sustained cyclic stretch. These membranes combine the advantages of PDMS and silicone – the PDMS optical window autofluorescence was 50% lower than commercial silicone (Fig. 2.2C). The outer, commercial silicone scaffold provided the necessary durability to withstand stretching while

mounted on the MHR. Hydrogels grafted to the PDMS window enabled greater control over the substrate stiffness, while ensuring 100% strain transfer between the PDMS and hydrogel (Fig. 2.4B).

Treatment with the serine protease thrombin increases cell actomyosin contractility by Rho/Rho kinase-mediated inhibition of myosin light chain phosphatase activity[20,65]. This contractility and associated signaling induces endothelial monolayer gap formation, which is mitigated by factors that reduce RhoA activity[20,122]. Conversely, Rac-mediated cortactin accumulation and actin polymerization at cell periphery and lamellipodia formation enable monolayer recovery, which is attenuated by Rac suppression[21]. The influence of cyclic strain and substrate stiffness on thrombin actuated endothelial disruption and resealing have been studied independently, in the context of endothelial monolayer integrity and barrier function[20,21,23,25,101,122].

Uniaxial cyclic strain influences cell orientation and proliferation in pulmonary endothelial monolayers[20,135]. Relative to static monolayers, 5% uniaxial CS reduced interendothelial gaps observed 50 min after thrombin treatment, but not at 5 min, suggesting faster monolayer recovery in stretched monolayers[21]. The latter behavior was accompanied by increased focal adhesion staining and cortactin accumulation near the cell periphery[21]. Chronic preconditioning with uniaxial 5% CS also reduced RhoA activation 5 min post-thrombin stimulation, and increased Rac1 activity at 50 min, relative to static controls[21]. My live-cell imaging results obtained with hybrid membranes and grafted hydrogels indicate similar gap formation trends for stretched *versus* static monolayers, including the protective effect of CS and the presence of lamellipodia during recovery (Figs. 2.5B, 2.6C, 2.7). My measurements revealed additional differences in monolayer disruption and recovery dynamics at multiple time points. Specifically, the largest gaps were evident 15 min after thrombin, with recovery apparent within 25 min for all conditions. The

imaging capability of this device enabled the dynamic tracking of multiple specific fields per membrane, and thus significantly reduced experimental variability, while enabling visualization of subcellular processes and comparisons of the gap formation rates under different conditions over 3 hr observation time (Fig. 2.5C). Eliminating the need for fixation also increased throughput and avoided potential artifacts associated with fixation and staining.

Studies of static monolayers demonstrated higher Rho-kinase dependent cell contractility on stiff substrata, with corresponding increases in stress fiber formation[25], monolayer forces[122] and leakier junctions[101]. Thus in prior studies, cells cultured on stiff elastomeric membranes likely had elevated levels of active RhoA, relative to cells in pulmonary tissue. Thrombin treatment also increased Rho kinase-dependent stress fiber and gap formation on stiff matrices relative to soft ones[25,122]. My results with static monolayers similarly demonstrated increased gap formation on 15 kPa hydrogels relative to 5 kPa, but I also showed that the effect was mitigated by equibiaxial 5% CS (Fig. 2.6A). Importantly, physiologically relevant substrate stiffness and cyclic stretch together had a greater protective effect against agonist challenge. I further showed that the attenuation in the gap formation rate, indicative of monolayer recovery, was delayed to the 15 to 25 min interval in monolayers on static 15 kPa substrates, relative to other conditions (Fig. 2.6B). Fifteen minutes after thrombin addition, even as gap areas increased, prominent lamellipodia were visible for all conditions, except on the static 15 kPa substrates (Fig. 2.7). Further, at the 55 min time point (Fig. 2.6A), only the softer substrate maintained a significant effect (Table 2.3), suggesting that stretched monolayers on 5 kPa gels completed resealing earlier than on 15 kPa gels (Fig. 2.6A). My results thus establish that both physiological matrix stiffness and physiological cyclic stretch coordinate to protect pulmonary endothelial monolayers against disruption by inflammatory mediators such as thrombin.

These findings suggest that fibrotic lung tissue could augment pulmonary vascular leak triggered by inflammatory mediators and barrier agonists, and delay endothelial barrier recovery relative to healthy tissue. Hypoxia is believed to increase pulmonary tissue stiffness[163], which is associated with disorders such as pulmonary fibrosis[133]. Genetic polymorphisms[2] and aging[101,210] can also contribute to vascular stiffening. The balance between cell-cell and cell-substrate adhesion and cell contractility is complex[65]. However, the device described here provides a platform for investigating their influence on endothelial function, and for interrogating the dynamic, subcellular mechanisms contributing to the mechanical regulation of the vascular endothelium.

2.5 FIGURES

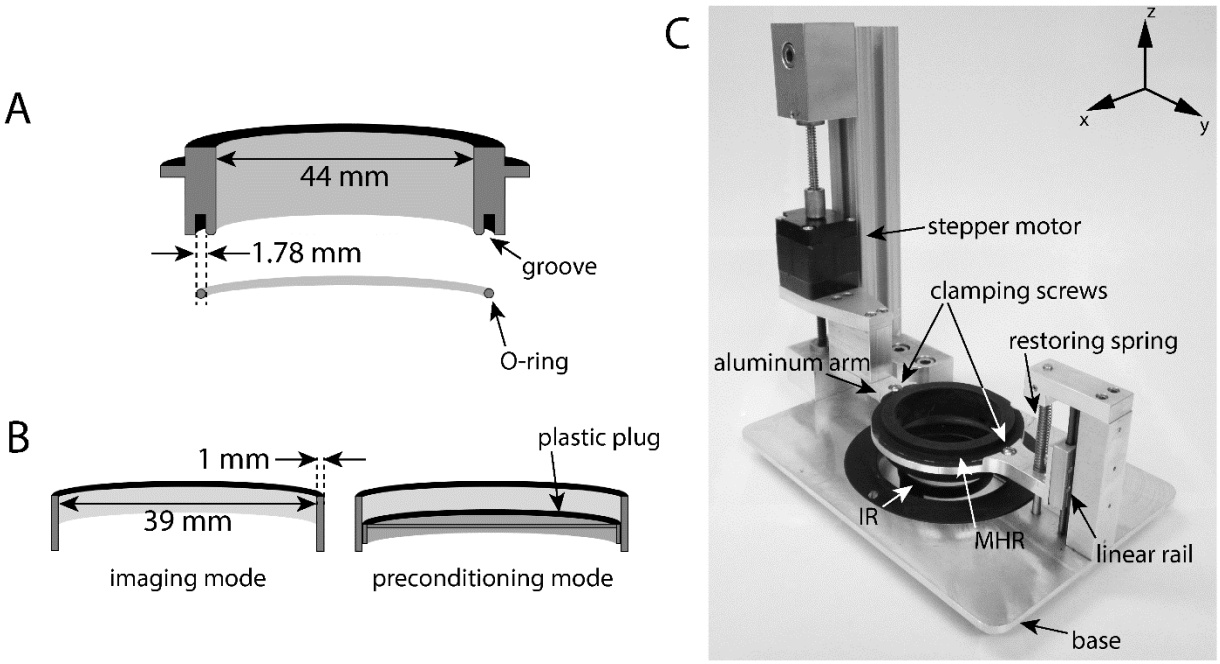

Fig. 2.1: Design of equibiaxial cell stretcher. (A) Cutaway view and dimensions of an anodized-aluminum Membrane-Holding Ring (MHR). An O-ring fits into a groove in the base of the MHR and is used to mount membranes on the MHR. The metal lip on the outside of the MHR is used to clamp the MHR to the aluminum arm of the stretcher with two diametrically opposite screws. (B) Cutaway view and dimensions of the anodized aluminum Indenting Ring (IR). The use of a ring facilitates imaging, as opposed to a cylindrical post, but this configuration increases evaporation losses due to the exposed membrane. Evaporation losses can be reduced using a plastic plug during stretch-preconditioning, in order to reduce membrane exposure to atmosphere. (C) Image of the cell stretcher showing an MHR clamped onto the aluminum arm, and positioned over the IR. On opposite sides of the aluminum arm are the stepper motor driving the arm, and a linear rail which guides the arm. The base of the device is designed to be mounted on a microscope stage.

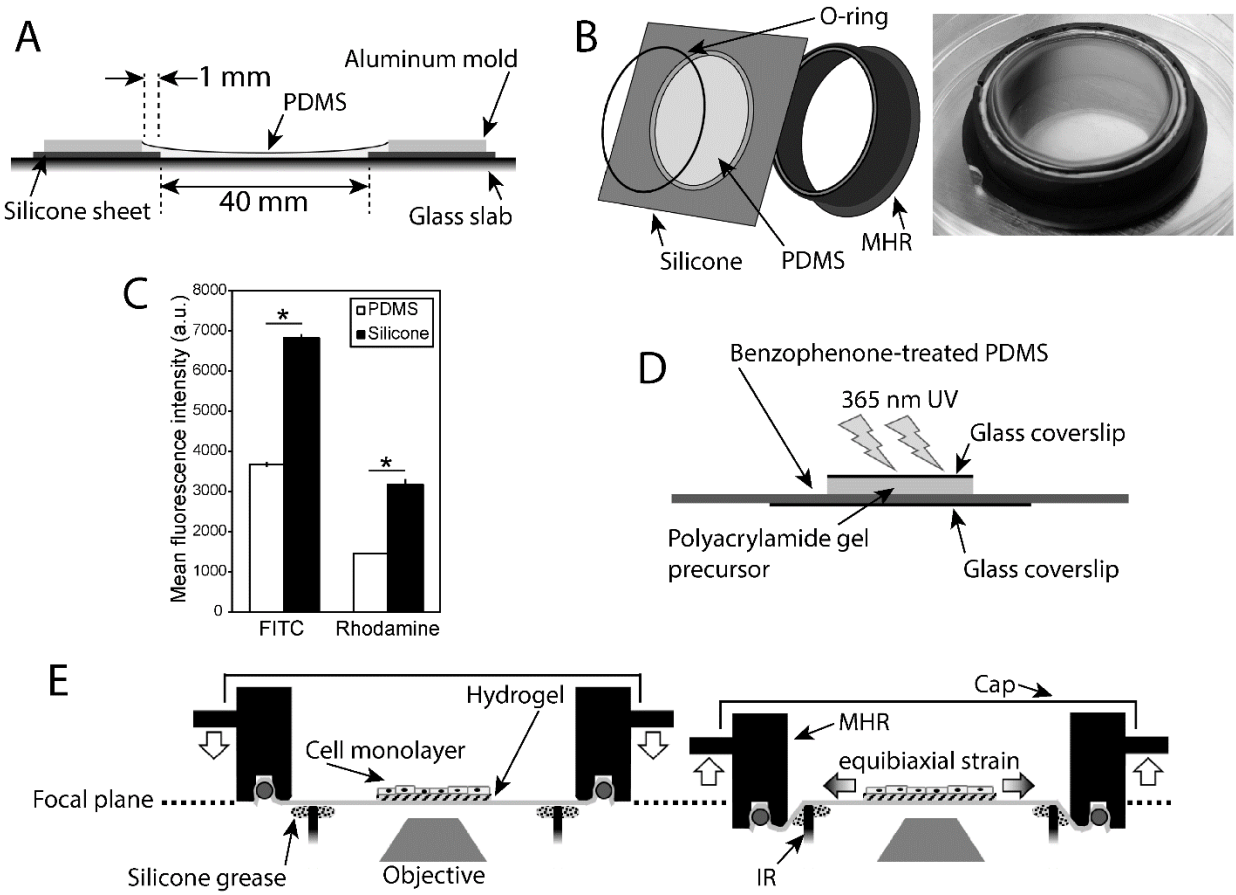

Fig. 2.2: Fabrication and performance of hybrid membrane, gel-grafting, and equibiaxial strain schematic. (A) Hybrid membranes were fabricated by casting polydimethylsiloxane (PDMS) of 26:1 (w/w) elastomer base:crosslinker ratio into the central cutout area of a silicone sheet, against a flat glass slab, confined by an aluminum mold. (B) Hybrid membranes with durable silicone backbones and optically clear, compliant central windows were mounted onto MHRs by O-rings. (C) Under the same imaging conditions, the average background mean fluorescence intensity of the hybrid membrane (PDMS window) and the silicone sheet were quantified using two different filter sets. The hybrid membrane showed half the background intensity of the commercial silicone sheet. Error bars are S.E.M., * represents $p < 5\times10^{-12}$, n = 25 regions of interest from 5 independent membranes. See also Fig. 2.3. (D) During polyacrylamide gel grafting, a glass coverslip backing was necessary to prevent oxygen-inhibition of gel polymerization. (E) During cyclic indentation of the MHR by the IR, the cell monolayer cultured on the hydrogel senses the gel stiffness and the equibiaxial strain. Silicone grease at edge of the membrane reduces friction between the membrane and the IR.

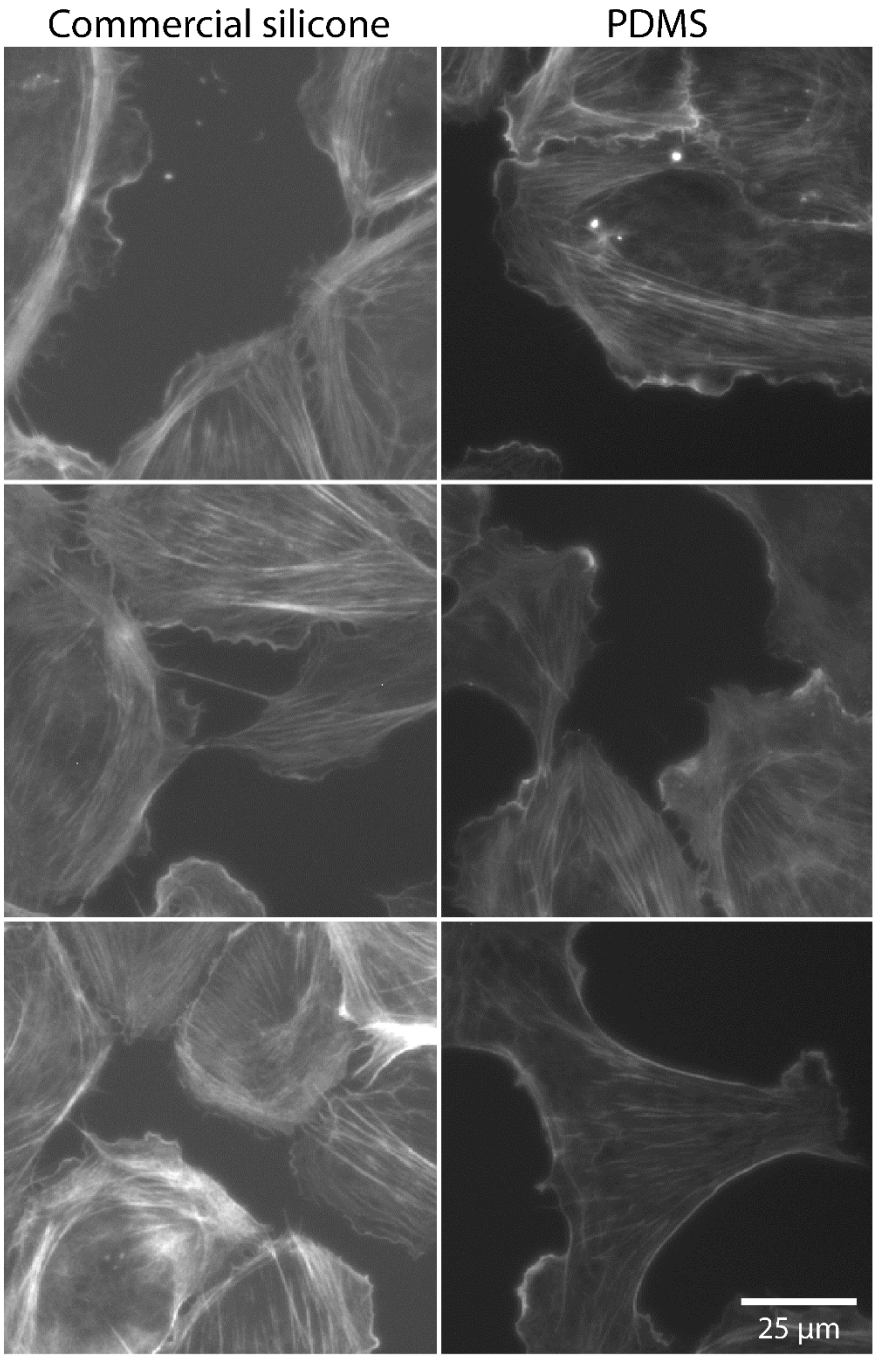

Fig. 2.3: Hybrid membranes reduce background fluorescence. HPAECs were cultured on commercial silicone membranes (left column) and fibronectin-coated hybrid membranes (right column) (n = 2 membranes each), then fixed and stained for F-actin, using Alexa Fluor 488-Phalloidin (1:40). They were then mounted on a glass slide and F-actin was imaged through each membrane, under identical conditions and are shown with identical processing. The lower background fluorescence of the PDMS (hybrid membrane) is evident. This lower background has applications in imaging weak fluorophores, or for imaging fine structures by confocal microscopy. See also Fig. 2.2C.

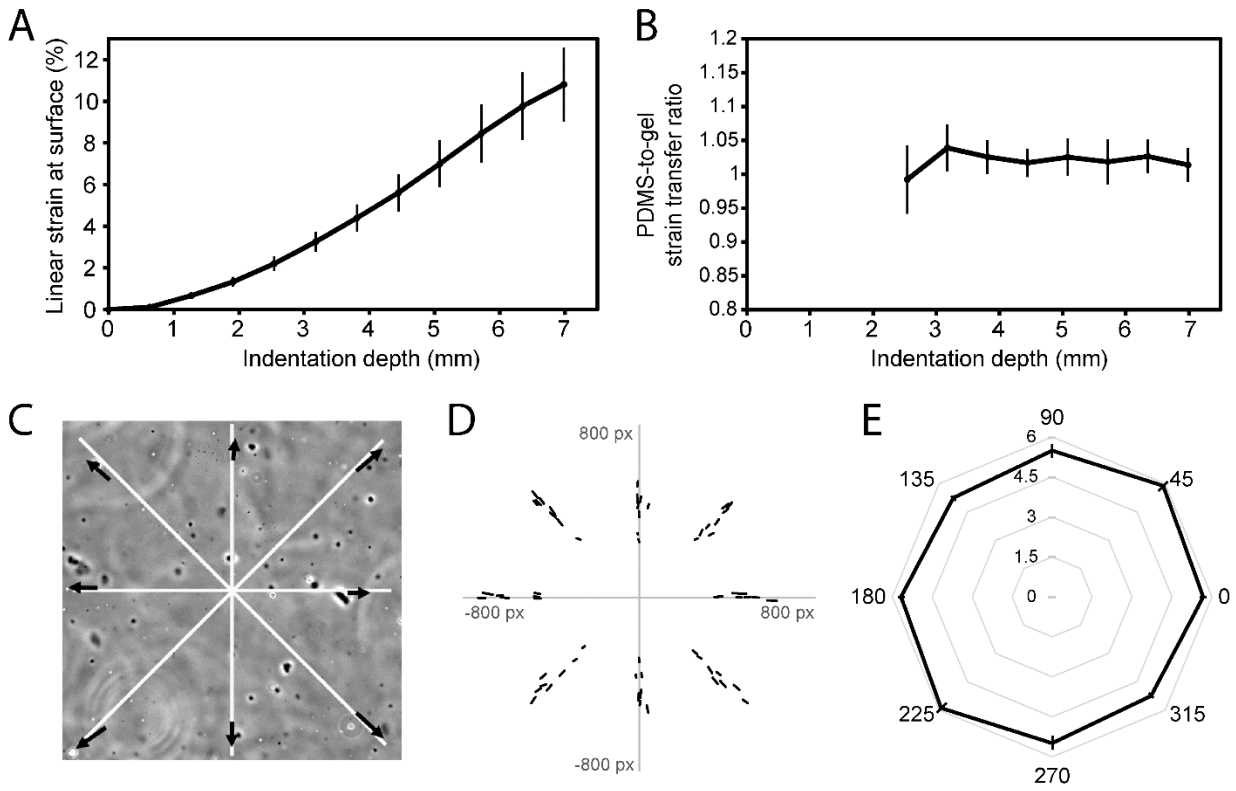

Fig. 2.4: Strain characterization. (A) Fluorescent microspheres near the surface of the hydrogel were imaged at different indentation depths (membrane stretch) to calculate the linear strain averaged along two orthogonal axes. (B) Microscopic features on the PDMS membrane were also imaged and strains calculated. The calculated strain transfer ratio ($\varepsilon_{gel}/\varepsilon_{PDMS}$) was ~1 (at low strains, data were too noisy due to small denominators and are not shown). Data in panels A and B are the pooled average of n = 3 membranes with 5 kPa gels and 2 with 15 kPa gels. (C, D) Microscopic features on the PDMS were tracked along the four indicated axes, in order to determine the strain homogeneity, at the ~5% strain condition. Results from n = 8 membranes are shown in panels D and E. The linear strain varies between 5.9% (45°-225°) and 5.3% (135°-315°), but the difference is not statistically significant. All error bars are S.E.M.

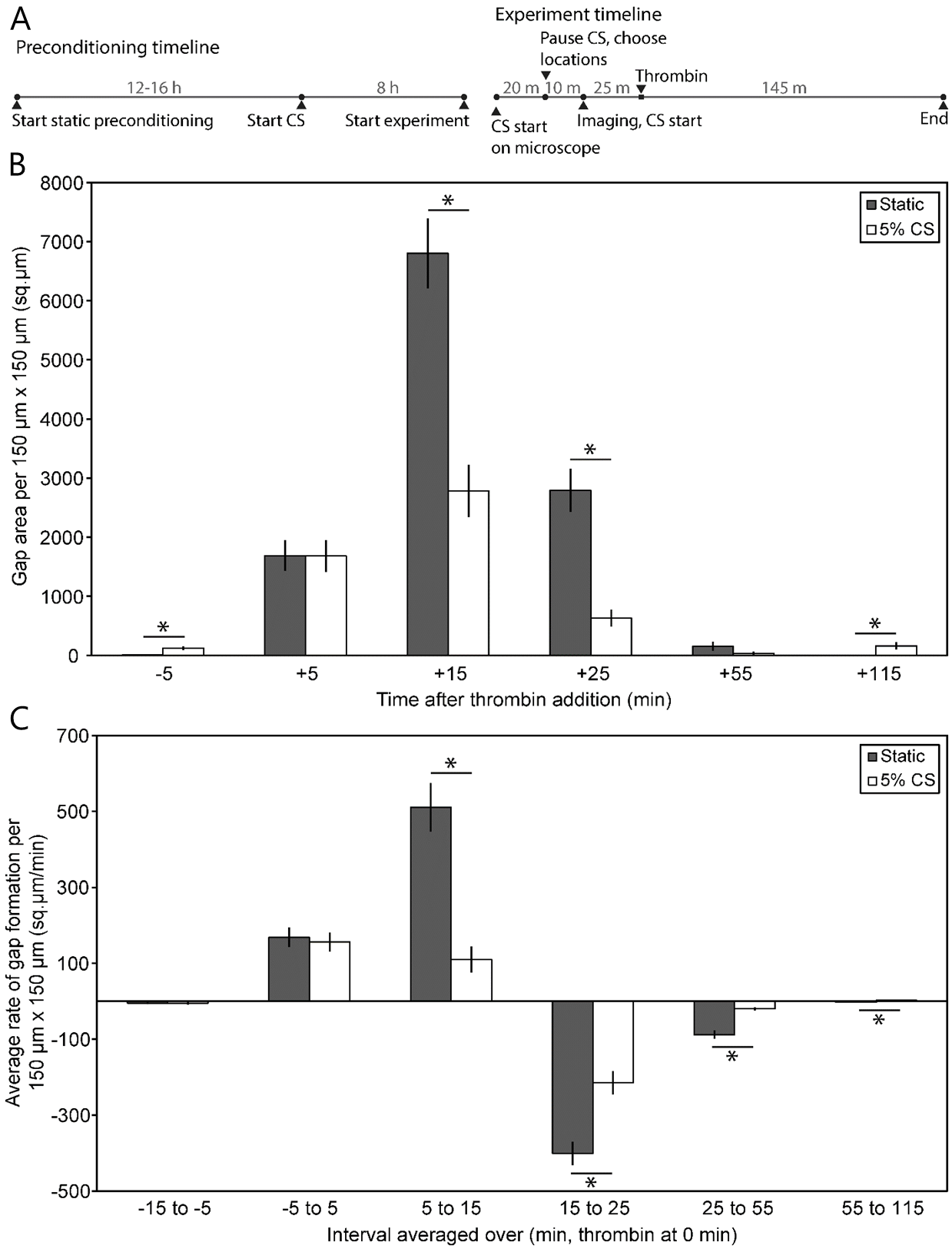

Fig. 2.5: Gap dynamics on fibronectin-coated hybrid membranes after thrombin stimulation. (A) Cell monolayers were preconditioned for culturing outside the incubator for 12-16 hr, before

Fig. 2.5 (contd.): being subjected to 8 hr of equibiaxial 5% CS. After mounting the stretcher with the cell monolayer on the microscope, cells were subjected to CS for 20 min before locating 3-4 positions to track over time. Images were taken every 10-30 min during programmed breaks in cyclic strain application. (B) Average gap area per 150 μm x 150 μm field is plotted as a function of time after thrombin addition to endothelial monolayers cultured on fibronectin-coated hybrid membranes. Gaps are greatest at 15 min. (C) Average gap formation rate in the same fields is presented for different intervals. The gap formation rate falls from the second to the third interval for 5% CS treated monolayers, but rises for static monolayers. For panels B and C, p-values summarized in Tables 2.1 and 2.2 respectively. * represents $p < 0.05$. Per condition, $n = 14$ fields from 2 independent experiments. Error bars are S.E.M.

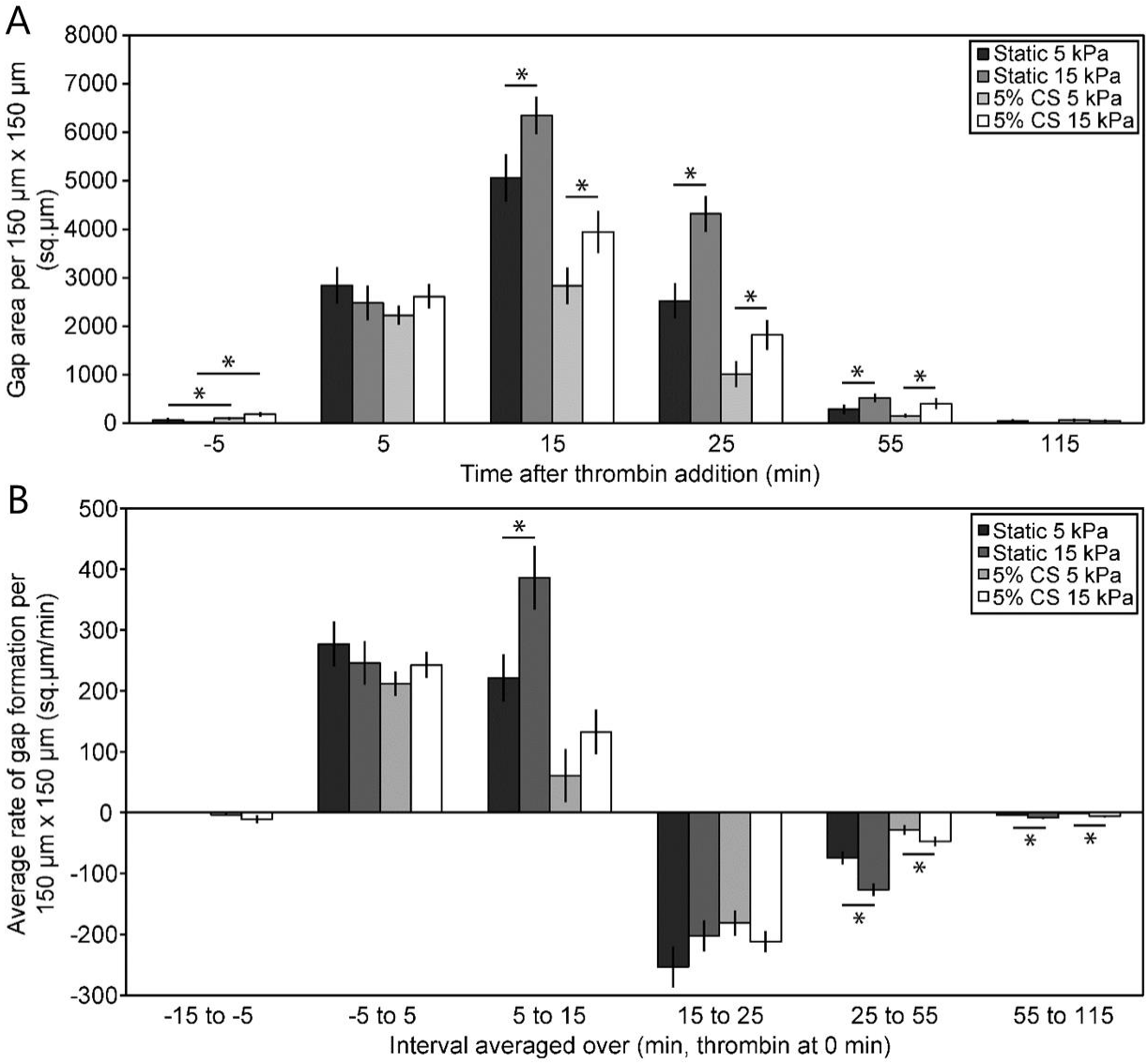

Fig. 2.6: Gap dynamics on collagen-coated soft and stiff hydrogels after thrombin stimulation. (A) Average gap area per 150 µm x 150 µm field is plotted as a function of time after thrombin addition to endothelial monolayers cultured on 5 kPa and 15 kPa Collagen-I coated hydrogels. Gaps are greatest at 15 min. (B) Average gap formation rate in the same fields is presented for different intervals. From the second to the third interval, all gap formation rates fall except for the static, 15 kPa substrate. * indicates only specific significant comparisons described in the text, within individual time points or intervals. Statistical information on effects of matrix stiffness and CS are summarized in Tables 2.3 and 2.4 respectively. Per condition, n = 18 fields from 3 independent experiments. Error bars are S.E.M.

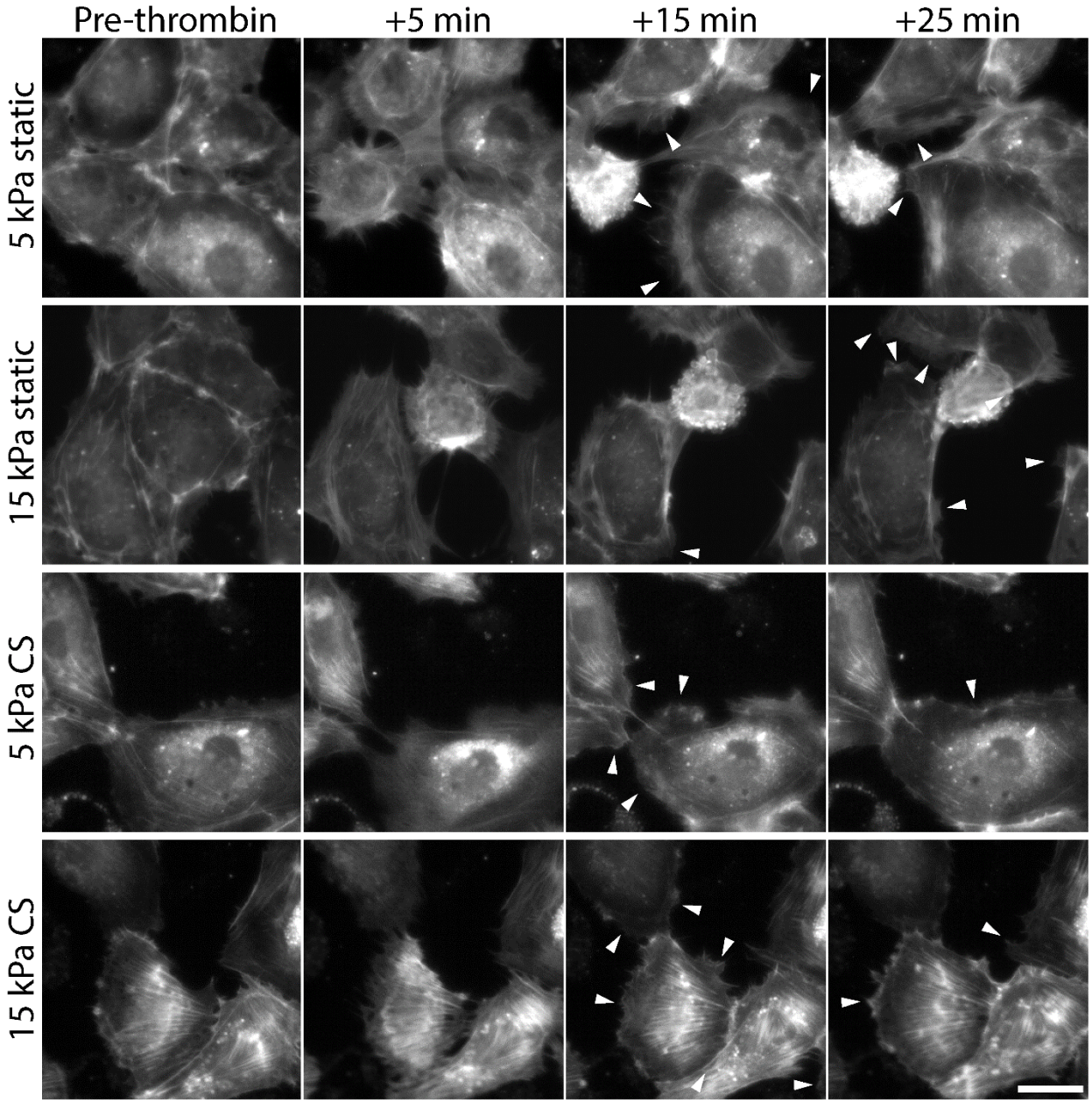

Fig. 2.7: Live cell imaging of actin dynamics as a function of time, relative to thrombin treatment. Representative images of mCherry-LifeAct visualized in HPAEC monolayers shows dissolution of stress fibers at 5 min post-thrombin stimulation, and corresponding retraction of the cell edge. Lamellipodia (white arrows) are apparent at 15 min under most conditions, but this is delayed to 25 min in the static monolayers on 15 kPa gels. Representative images from n = 18 fields from 3 independent experiments per condition. Scale bar 25 μm.

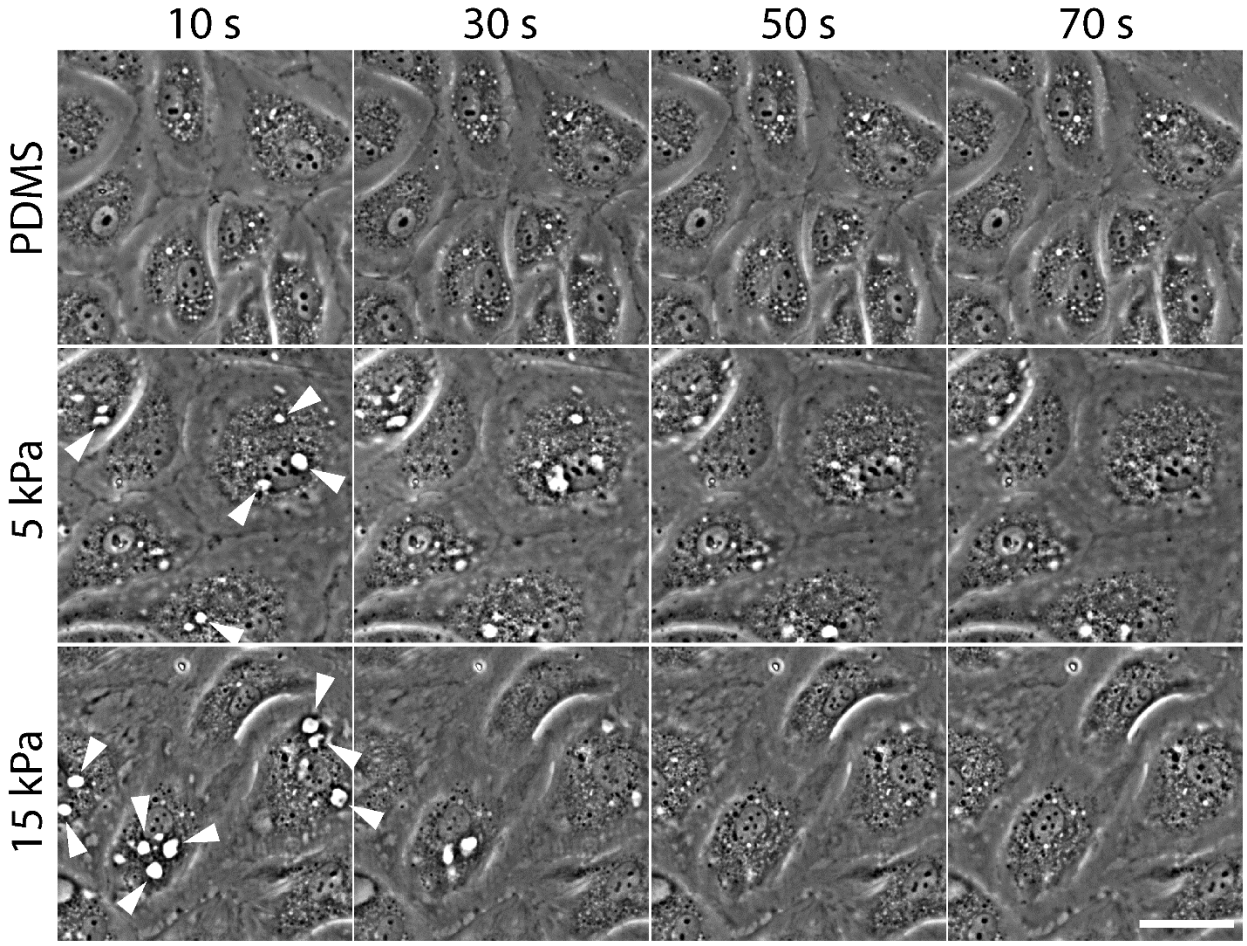

Fig. 2.8: Formation of solvent 'blisters' beneath cells, attributed to porous flow out of hydrogels. HPAEC monolayers were subjected to 3 min of 5% CS at 15 cycles/min, and then immediately imaged by phase contrast microscopy every 10 s for 80 s. In cell monolayers cultured on hydrogels, bright spots beneath cells (white arrows) formed and dissipated over 50 s. These spots do not appear under monolayers cultured on PDMS, which lacks water-permeable pores. Representative images from n = 4 fields from 2 independent experiments per condition. Scale bar 40 μm.

2.6 TABLES

Table 2.1: p-values for the effect of 5% CS at different time points from one-tailed Welch's unequal variance t-test analysis of EC monolayer gap areas on fibronectin physisorbed hybrid membranes. Thrombin was added at t = 0 min.

Time point (min)	p-value for 5% CS
-5 min	2.7E-03
5 min	0.49
15 min	4.991E-06
25 min	1.8E-05
55 min	0.080
115 min	0.013

Table 2.2: p-values for the effect of 5% CS from one-tailed Welch's unequal variance t-test analysis of gap formation rates over different intervals in EC monolayers on fibronectin physisorbed hybrid membranes. Thrombin was added at t = 0 min.

Interval (min)	p-value for 5% CS
-15 to -5 min	0.49
-5 to 5 min	0.37
5 to 15 min	1.03E-05
15 to 25 min	1.2E-04
25 to 55 min	1.5E-05
55 to 115 min	2.0E-03

Table 2.3: p-values for Main effects and Interaction effect at different time points from Brown-Forsythe's modified ANOVA of EC monolayer gap areas on Collagen-I coated hydrogels. Thrombin was added at t = 0 min.

Time point (min)	Calculated df_{Error}	Main Effect Cyclic Strain (C)	Main Effect Matrix Stiffness (M)	Interaction Effect (CM)
-5 min	27.10	0.021	0.39	0.08
5 min	55.89	0.43	0.96	0.22
15 min	64.79	7.6E-07	6.1E-03	0.84
25 min	63.85	7.7E-08	2.0E-04	0.14
55 min	55.44	0.17	9.9E-03	0.93
115 min	52.50	0.33	0.34	0.77

Table 2.4: p-values for Main effects and Interaction effect from Brown-Forsythe's modified ANOVA of gap formation rates over different intervals in EC monolayers on Collagen-I coated hydrogels. Thrombin was added at t = 0 min.

Interval (min)	Calculated df_{Error}	Main Effect Cyclic Strain (C)	Main Effect Matrix Stiffness (M)	Interaction Effect (CM)
-15 to -5 min	21.75	0.035	0.25	0.32
-5 to 5 min	53.70	0.25	0.99	0.30
5 to 15 min	62.71	1.03E-05	8.0E-03	0.29
15 to 25 min	54.41	0.22	0.68	0.11
25 to 55 min	62.87	7.6E-09	3.5E-04	0.079
55 to 115 min	61.46	0.068	1.7E-03	0.99

Chapter 3: Cyclic stretch remodels endothelial junctions and enhances lamellipodia dynamics

3.1 INTRODUCTION

The vascular endothelium is a selectively permeable barrier regulating the transport of fluid, dissolved gases, and nutrients between the blood stream and surrounding tissue. The vasculature is also a mechanically active environment, subjecting the endothelium to mechanical stimuli, including shear stress, hydrostatic forces, and variations in tissue stiffness[86,101]. The pulmonary endothelium in particular regulates the blood-gas barrier between alveoli and surrounding capillaries[65]. Inflammatory mediators can disrupt the endothelial barrier integrity, resulting in increased vascular permeability, leading to pulmonary edema[65,148]. During respiration, the pulmonary endothelium experiences equibiaxial cyclic stretch[205,206] (CS). However, mechanical perturbations due to, for example, mechanical ventilation, can trigger biochemical changes that result in barrier failure and unregulated vascular leakage, which contributes to pathologies such as Ventilator-Induced Lung Injury and Acute Respiratory Distress Syndrome[63,65].

Although excessive mechanical ventilation can trigger barrier dysfunction, physiological CS can also enhance endothelial barrier function. *In vitro* studies show that cyclically stretching endothelial monolayers can activate cytoskeletal reorganization[20], alter gene expression[23], and proliferation[135]. Mechanical stretch is therefore an important design parameter for recapitulating pulmonary endothelial function in tissue engineering applications. In particular, physiological CS has been shown to protect endothelial monolayers against inflammatory mediators by reducing

monolayer disruption and enhancing gap reannealing[21,49]. However, very little is known about the molecular mechanisms underlying this mechanically-induced protection.

Barrier-disrupting agents such as thrombin and histamine trigger intracellular RhoA GTPase signaling[24,65,148]. The resulting increase in Rho-dependent endogenous contractility contributes to endothelial junction failure, and interendothelial gap formation. Previous studies measured Rho activity in physiologically stretched endothelial cell (EC) monolayers as an indicator of thrombin-dependent increase in cell contractility, but found no significant difference in active Rho relative to unstretched monolayers[21]. After gap formation, cells extended sheet-like, actin-rich lamellipodia to close gaps and re-establish cell-cell contacts[49,67,95,189]. The actin-scaffolding protein cortactin enables lamellipodia extensions[34,89,189,227], and Rac1 GTPase facilitates cortactin translocation to the leading edge[90,222]. Physiological CS results in higher Rac1 activation, relative to static controls[21]. Conversely, Rac1 knockdown impairs gap reannealing in cyclically stretched monolayers, after thrombin treatment[21].

I postulated that physiological CS protects intact EC monolayers, by reinforcing the actin cytoskeleton at intercellular junctions, thus protecting junctions against disruption by endogenous contractility or exogenous mechanical forces. However, physiological CS could also activate biochemical signals that enhance interendothelial gap closure, by regulating lamellipodia dynamics. The ability to test these hypotheses has, however, been limited by the challenges of visualizing and quantifying dynamic cellular processes in cyclically stretched endothelia.

I previously reported a device designed to enable dynamic imaging of stretched cell monolayers[49] (Chapter 2). This device enabled quantification of endothelial gap formation and closure dynamics in cyclically stretched monolayers, following thrombin treatment. Results established that 8 h of physiological CS protected against thrombin-induced endothelial disruption,

resulting in reduced gap formation. Specifically, I reported that lamellipodia were apparent earlier than in static monolayers, and appeared to enhance gap closure rates.

This work extends my previous studies to investigate molecular events underlying stretch-dependent protection against endothelial monolayer disruption by inflammatory mediators such as thrombin. I used quantitative immunofluorescence imaging to identify molecular changes underlying the CS-dependent remodeling of endothelial junctions. I focused specifically on cortactin, F-actin, and VE-cadherin because of their demonstrated roles in intercellular adhesion and actin remodeling at cell junctions[87,95]. Studies also quantified the effects of physiological CS on force-dependent activation of the force transducer α-catenin within VE-cadherin complexes. Finally, I exploited the live-cell imaging capabilities of my device, to quantify the impact of physiological CS on endothelial lamellipodia dynamics and collective cell migration. These results indicate that CS activates biochemical processes that both reinforce junctional actin and enhance lamellipodia-dependent recovery dynamics. The results provide important insights into mechanisms by which physiological CS may protect endothelial monolayers against biochemical and mechanical insults *in vivo*.

3.2 MATERIALS AND METHODS

3.2.1 Cell culture and reagents

Primary human pulmonary artery endothelial cells (HPAECs, Lonza) were cultured in endothelial growth medium EGM-2 (Lonza) with 10% (v/v) fetal bovine serum (FBS, Sigma) in a humidified incubator at 37°C with 5% CO_2, and passaged every 3 days. HPAECs between passages 6-8 were used for experiments.

All cyclic stretch experiments were performed in a heated enclosure, with air bubbled through deionized water to maintain humidity. EGM-2 with 10% FBS was supplemented with 25 mM HEPES (Corning) to maintain pH, 2 mM sodium pyruvate (Corning) to reduce phototoxicity[191], and 1% penicillin-streptomycin (Lonza). Evaporation from medium was offset by periodically adding sterile deionized water. Under these conditions, HPAECs could survive and proliferate over 48 h (not tested further). For experiments requiring serum starvation, the medium contained 0.5% (v/v) FBS.

3.2.2 Equibiaxial cyclic stretch of endothelial monolayers

HPAEC monolayers were cyclically stretched with a previously reported custom-built device[49]. Briefly, a circular elastomeric membrane is stretched over a circular indenting ring, to generate equibiaxial strain (Figs. 3.1A, 3.1B). The membrane is an optically transparent substrate onto which cells are seeded. The substrate is cyclically stretched between 0% (relaxed) to 5% (stretched) linear strain, at a frequency of 0.25 Hz to replicate physiological CS[20,49,205]. The device mounts on a microscope stage to enable dynamic imaging of the cultured cells or monolayers during brief pauses between periods of cyclic stretch (Fig. 3.1B).

Human fibronectin (EMD Millipore) at 50 μg/mL was physisorbed to a 1-2 cm^2 central area on the autoclaved membranes for 30 min (Fig. 3.1A). HPAECs were seeded on the treated area and fresh medium was added after cell attachment. The cells were cultured in an incubator for 2 days before use in experiments. Depending on the experimental requirement for single cells, subconfluent (50%) monolayers, or confluent monolayers, initial seeding density was 10,000 cells/cm^2, 20,000 cells/cm^2, or 40,000 cells/cm^2 respectively. Immediately prior to experiments,

cells were rinsed with PBS and the medium was changed to HEPES-buffered EGM-2 with appropriate serum levels.

3.2.3 Antibodies and immunostaining

The following primary antibodies were used: mouse monoclonal anti-cortactin (EMD Millipore), goat polyclonal anti-VE-cadherin (Santa Cruz Biotechnology), rabbit polyclonal anti-α-catenin (Sigma), mouse monoclonal anti-β-catenin (BD Biosciences) (see Table 3.1 for dilutions). The rat anti-α-catenin primary antibody, α18, was a gift from Prof. Akira Nagafuchi (Nara Medical University, Japan), and binds to an epitope on α-catenin that is exposed when the protein undergoes a force-dependent conformation change[234]. When a sample was simultaneously stained for total α-catenin using rabbit polyclonal anti-α-catenin, the pixel-by-pixel measurement of the α18/α-catenin ratio yielded a heat map that represented the distribution of α-catenin in the open, force-activated conformation[234]. Rhodamine-phalloidin (Invitrogen) and DAPI (4',6-diamidino-2-phenylindole, Sigma) were used to stain F-actin and nuclei, respectively. The following secondary antibodies were used: rabbit anti-mouse IgG Alexa Fluor 647 (Invitrogen), rabbit anti-goat IgG FITC (Sigma), donkey anti-rabbit IgG DyLight 550 (Novus Biologicals), goat anti-mouse IgG Alexa Fluor 488 (Invitrogen) and goat anti-rat IgG CruzFluor 647 (Santa Cruz Biotechnology).

HPAEC monolayers were subjected to 8 h of 5% CS, or left unperturbed (static). The cyclically stretched and static monolayers were then immediately fixed with warm 4% (v/v) paraformaldehyde (Fisher Scientific) for 20 min, after which the membrane areas supporting the cells were excised. For samples to be stained with the α18 antibody, warm 1% (v/v) paraformaldehyde was used to fix the cells[234]. Each set of experiments included both 5% CS and

static control monolayers, to compare cells at the same passage and to ensure similar immunostaining conditions.

Immunostaining was performed according to conventional protocols. Cells were permeabilized with 0.1% (w/v) Triton X-100 (Fisher Scientific) for 4 min. Non-specific antibody binding was blocked by 1% (w/v) bovine serum albumin incubation for 1 h. Primary antibody incubation was performed overnight at 4°C, and secondary antibody incubation was performed for 1 h at room temperature (Table 3.1). Membranes supporting the immunostained cells were mounted on slides with Fluoromount G mounting medium (SouthernBiotech). Samples were stored at 4°C until imaging.

3.2.4 Immunostaining analysis

Immunostained samples were imaged on a Zeiss AxioObserver.Z1 epifluorescence microscope with a 40× oil immersion objective (Institute for Genomic Biology, University of Illinois). Under identical imaging conditions for each set of experiments, several multichannel images (312 μm × 250 μm) were captured per sample. Imaging was restricted to the interior regions of the monolayers, to avoid cells at the edge that are at lower density, not contact-inhibited, and able to migrate outward.

Image analyses were performed with ImageJ v1.50i (NIH). Nuclei were counted to estimate cell density. The DAPI channel was thresholded using the Huang method[96]. Overlapping nuclei in the thresholded image were segmented using the watershed algorithm to identify individual nuclei. The ‘Analyze Particles’ tool in ImageJ was used to count all detected nuclei per image, with a minimum size set at 50 μm^2 to exclude any debris.

To quantify the immunostaining intensity at endothelial junctions, images were converted to 8-bit, and a rolling ball background-subtraction was performed. A rolling ball radius of 22 μm (100 px) was chosen, as this was significantly larger than the features of interest at the junctions. Three fields (75 μm × 75 μm) were chosen randomly per image. VE-cadherin was chosen as the reference channel to define the junctions for quantitative analyses of cortactin, F-actin, and VE-cadherin immunofluorescence (Figs. 3.1C, 3.2A). For quantitative analyses of α18 and α-catenin immunofluorescence, β-catenin was used as the reference channel to define the junctions (Fig. 3.3A). To accurately define the junctions and exclude cytoplasmic background, local thresholding was applied on the chosen reference channels using the Phansalkar method[171] (Fig. 3.1C). The 'radius' parameter was manually tuned to optimize junction thresholding and set to 11 μm (50 px). Local thresholding is included in the ImageJ plugin 'Auto Threshold v1.16'. Any remaining cytoplasmic aggregates were cropped out manually, leaving behind only thresholded junctions (Fig. 3.1C). Junction areas were then quantified using the 'Analyze particles' tool in ImageJ.

To isolate junction-specific staining of different proteins, thresholded junctions were used as masks that defined the regions analyzed for the respective cortactin, F-actin, VE-cadherin, α18 and α-catenin immunofluorescence intensities (Fig. 3.1D). The mean fluorescence intensity (MFI) at intercellular junctions could then be computed in each fluorescence channel, for each image field. The immunofluorescence images of α18 and α-catenin in the regions defined by the mask were used to quantify the pixel-by-pixel α18/α-catenin ratio at the junctions (Fig. 3.3A), after which I calculated the average junctional α18/α-catenin ratio for each field.

3.2.5 Kymography analysis

Kymographs of HPAEC lamellipodia were generated to determine the effect of physiological CS on lamellipodia dynamics. In separate experiments, HPAECs at single-cell or subconfluent (50%) densities were serum starved while being preconditioned with 4-7 h of 5% CS or static control. The stretching device was mounted on a Zeiss Axiovert 200M microscope with a 20× air objective and 1.6× Optovar. Images were acquired after pausing cyclic stretch and allowing 5 min for system stabilization. Phase contrast images of the cells were captured every 6 seconds, for 15-17 min.

I also attempted to study the effect of CS on lamellipodia dynamics in thrombin-treated confluent and subconfluent monolayers. However, with confluent monolayers I could not image sufficient lamellipodia protrusion cycles before intercellular gaps closed. In subconfluent monolayers thrombin caused significant disruption of interendothelial contacts, resulting in single (isolated) cells over the period of observation. I instead studied lamellipodia dynamics in single HPAECs treated with 0.1 U/mL human thrombin (Enzyme Research Laboratories) after 7-10 h of serum starvation and 5% CS preconditioning or static control. Stretch was paused 8 min after thrombin addition, and 5 min was allowed for system stabilization. By this time, cells initiate lamellipodia protrusions in thrombin-treated HPAEC monolayers[49]. Timelapse imaging was performed over 17 min, as with untreated cells.

Timelapse stacks were corrected for translational drift by image registration using the StackReg plugin[201] and the Template Matching plugin[207] in Image J. Then, a 1 pixel wide line was drawn perpendicular to the leading edge of the cell in the image stack. Using the 'Reslice' option in ImageJ, the lines from each time point were stacked beside each other, in order to generate kymographs showing the time evolution of the leading edge position (Fig. 3.4A). Only one lamellipodium was analyzed per cell.

Peaks in kymographs represented the lamellipodia protrusion-retraction cycles (Fig. 3.4A). The initial ascending slope represents the ‘protrusion rate’, and the initial descending slope represents the ‘retraction rate’ (Fig. 3.4B). The width of the ascending slope indicates the ‘persistence’, and the peak height indicates the ‘protrusion length’. Only kymographs with a minimum of three peaks, corresponding to three protrusion-retraction cycles, were considered for analysis. Each kymograph was defined by these four parameters averaged across its peaks. Next, these parameters were averaged across the multiple kymographs generated for each treatment.

3.2.6 Collective cell migration

To determine the impact of CS on large wound healing, HPAEC monolayers were subjected to 4 h of either 5% CS or static preconditioning. Multiple scratch wounds were then made in the preconditioned monolayer with a sterile pipette tip, and the stretcher device was mounted on the Zeiss Axiovert 200M microscope for further cyclic stretch and imaging. Multiple locations of the scratch wounds were chosen with a minimum of 3 mm separation, and tracked with a 10× objective every hour for four hours post-wounding, bringing the total experiment duration to 8 h. In between each imaging time point, 5% CS or static treatment was continued for 50 min, allowing an additional 5 min for system stabilization after CS was paused before image acquisition.

Images of the scratch wounds were corrected for translational drift using the Template Matching plugin[207] on ImageJ, and rotated so that the leading edges of the monolayer were parallel to the width of the image. Each leading edge was manually traced on ImageJ, to distinguish the cell areas from the empty areas of the wounds. The change in monolayer area every hour was determined at each leading edge as the scratch wound closed (Fig. 3.6A). The increase in area

covered by cells relative to the baseline (t = 0), divided by the width of the image, indicated the cumulative distance advanced by the leading edge of the cell monolayer, as a function of time. This was used to calculate the effective distance advanced by the leading edge every hour, i.e. the collective cell migration rate as a function of time.

3.2.7 Statistical analysis

Statistical comparisons of cells exposed to 5% CS versus static treatments were performed first by testing equality of variances by the F-test, followed by use of the one-tailed Student's t-test for equal variances or the one-tailed Welch's t-test for unequal variances. For all experiments, $\alpha = 0.05$ was chosen for statistical significance. All data are reported as mean±S.E.M.

Every experiment was performed in duplicate or triplicate. To minimize experiment-to-experiment variability due to staining or imaging conditions in immunostaining experiments with MFI-based readouts, or quantification of α18/α-catenin ratios at junctions, all data points corresponding to each treatment in a particular experiment were normalized to the sample mean of the static (control) treatment for that experiment. The normalized data points obtained for each treatment were then averaged over the independent experiments, prior to statistical analysis.

3.3 RESULTS

3.3.1 Endothelial junction areas decrease under physiological cyclic stretch

HPAEC monolayers subjected to physiological CS for eight hours showed no significant change in cell density, relative to static controls (Fig. 3.2B). Per 312 μm × 250 μm image, static endothelial

monolayers showed 56±2 nuclei whereas stretched monolayers showed 53±2 nuclei ($p = 0.09$). The minor decrease, while not statistically significant, can be explained by cell death seen on initiation of cyclic stretch, even at physiological levels[20,205].

Equibiaxial 5% CS did however lead to a reduction in junction area (Fig. 3.2C) as calculated from thresholded VE-cadherin and β-catenin immunostaining images. Per 75 μm × 75 μm frame, static monolayers showed a junction area of 700±10 μm^2 whereas it reduced to only 580±10 μm^2 in stretched monolayers ($p = 2.3\times10^{-12}$). This 16% decrease in junction area could not be explained by the minor decrease in cell density. The decrease in junction area was also noticeable qualitatively in the immunostaining images (Figs. 3.2A, 3.3A).

3.3.2 F-actin and cortactin are significantly enriched at junctions in cyclically stretched monolayers

The junctional mean fluorescence intensity, normalized to mean values measured under the static condition, revealed significant changes in cortactin, F-actin and VE-cadherin density at junctions (Figs. 3.2A, 3.2D). The actin-scaffolding protein cortactin, plays a critical role in actin polymerization at the leading edge of migrating cells[34,227]. Cortactin is also hypothesized to stabilize cell junctions by scaffolding other F-actin nucleating factors, Arp 2/3 and WAVE2, and directly interacting with cadherin[87].

For static monolayers, normalized junctional cortactin MFI was 1.00±0.03 whereas at junctions in stretched monolayers, this increased to 1.57±0.07 ($p = 8.9\times10^{-11}$) – an increase of nearly 60% (Fig. 3.2D). The normalized junctional F-actin MFI similarly increased from 1.00±0.03 in static monolayers to 1.31±0.03 in stretched monolayers ($p = 1.8\times10^{-11}$). The increased

cortactin and F-actin staining intensity were also noticeable qualitatively in the immunostaining images (Fig. 3.2A). The VE-cadherin intensity at junctions showed the opposite trend, the normalized junctional VE-cadherin MFI decreased from 1.00±0.02 in static monolayers to 0.88±0.02 in stretched monolayers ($p = 5.1\times10^{-6}$).

3.3.3 Cyclic stretch increases tension on endothelial junctions

In order to determine whether physiological cyclic stretch affected the tension on the VE-cadherin complexes at junctions, I focused on α-catenin. α-catenin mechanically links the actin cytoskeleton to the VE-cadherin complex by directly binding to F-actin and β-catenin[234]. α-catenin is also a force transducer, which undergoes a conformational change in response to increased tension at intercellular junctions[116,234]. The antibody α18 specifically binds to an epitope on α-catenin that is exposed only in the 'high-tension' conformation[234].

The normalized total α-catenin MFI at junctions decreased from 1.00±0.02 in static monolayers to 0.72±0.02 in stretched monolayers ($p = 4.3\times10^{-19}$), and the normalized MFI for α18 at junctions simultaneously decreased from 1.00±0.02 under static conditions to 0.86±0.03 on cyclic stretch ($p = 1.5\times10^{-5}$) (Fig. 3.3B). However, the normalized average junctional α18/α-catenin ratio, that indicates the fraction of α-catenin in the 'high-tension' conformation, increased from 1.00±0.01 in static control monolayers to 1.22±0.02 after 8 h of 5% CS ($p = 4.7\times10^{-14}$) (Fig. 3.3C). Thus physiological cyclic stretch in endothelial monolayers leads to a decrease in total junctional α-catenin, but an increase in the tension at VE-cadherin complexes, over the studied timescale.

3.3.4 Endothelial cells under cyclic stretch show enhanced lamellipodia dynamics

In the disrupted endothelium, wound healing occurs by cells extending lamellipodia to close gaps, initiating contacts with adjacent cells and forming new junctions[67,95]. I thus studied the impact of cyclic stretch on lamellipodia dynamics, quantified using four parameters[34,94] (Fig. 3.4B). The initial protrusion rate is the initial speed of lamellipodium extension. Similarly, the initial retraction rate is the initial speed at which the extended lamellipodia retracts. Persistence is the time over which the lamellipodium is extended and remains extended prior to retraction, and protrusion length is the maximum extension length. Generally, increased lamellipodia protrusion rate, persistence and protrusion length would enhance the wound closure rate.

In single cells, which sense cyclic stretch through integrin adhesions, lamellipodia protrusion rate and protrusion length were both significantly higher under physiological CS than in static controls (Fig. 3.4C). The protrusion rate increased from 0.106±0.007 μm/s in static cells to 0.130±0.008 μm/s in 4-7 h stretched cells ($p = 0.010$), and protrusion length simultaneously increased from 2.1±0.1 μm to 2.5±0.1 μm ($p = 0.029$). The retraction rate appeared to increase from 0.148±0.008 μm/s in static single cells to 0.17±0.01 μm/s on cyclic stretch, but statistical significance could not be established ($p = 0.057$). Lamellipodia persistence remained unchanged, 30±2 s in static cells and 29±2 s in stretched cells ($p = 0.44$).

Next, I looked at subconfluent cells (~50% confluence), where cyclic stretch is sensed via both integrin and cadherin adhesions. Compared to single, isolated cells, this approach more closely models the effect of CS on lamellipodia dynamics in disrupted endothelial monolayers. In cyclically stretched subconfluent cells, lamellipodia showed significantly increased persistence and protrusion length than in static controls (Fig. 3.4D). Lamellipodia persistence increased from 24.8±0.9 s in static cells to 29±1 s in 4-7 h stretched cells ($p = 0.0016$), and protrusion length

increased from 1.40±0.08 μm to 1.77±0.09 μm (p = 0.0021). Protrusion rate was unchanged, 0.087±0.007 μm/s in static cells and 0.097±0.007 μm/s on CS conditioning (p = 0.13). Retraction rate was also unchanged, 0.119±0.008 μm/s and 0.121±0.008 μm/s in static and stretched cells respectively (p = 0.43).

Lastly, I quantified the lamellipodia dynamics of single cells recovering after 0.1 U/mL thrombin treatment (Fig. 3.5). Cyclic stretch over 7-10 h resulted in a significant increase in lamellipodia protrusion length, from 1.6±0.1 μm in static control cells to 2.0±0.1 μm in stretched cells (p = 0.014). Protrusion rate was 0.086±0.008 μm/s in static cells and 0.092±0.008 μm/s on stretch conditioning (p = 0.29), and retraction rate was 0.085±0.008 μm/s and 0.101±0.009 μm/s in static and stretched cells respectively (p = 0.11). Lamellipodia persistence was 34±3 s in static cells and 37±3 s in stretched cells (p = 0.18). Thus, cyclic stretch-enhanced lamellipodia dynamics are seen even during recovery from thrombin treatment.

3.3.5 Collective endothelial cell migration is unaffected by cyclic stretch

Scratch wound assays are used to ascertain the effect of various perturbations on cell processes during the healing of large wounds. Collective cell migration is the primary mechanism involved in healing such wounds, and is known to be cortactin-dependent[121]. Because physiological CS resulted in peripheral cortactin localization, enhanced lamellipodia dynamics, and protection against thrombin-induced disruption, I investigated whether CS would protect the EC monolayer against large wounds by enhancing collective cell migration (Fig. 3.6).

At 1 h after scratch wounding the monolayer, the cumulative distance advanced by the leading edges of static control monolayers was 14±1 μm (Fig. 3.6B). This value was slightly higher

than the 11±1 μm advanced by leading edges of stretched monolayers ($p = 0.046$). However this difference was not sustained at longer times. For example, at the 2 h timepoint, the difference between static and cyclically stretched cells was already negligible, with the cumulative distance advanced being 25±2 μm for static monolayers and 23±2 μm for 5% CS monolayers ($p = 0.23$). At 8 h of cyclic stretch, i.e. 4 h after scratch wounding, the leading edges in static monolayers had advanced a total of 41±3 μm compared to 38±2 μm in 5% CS monolayers ($p = 0.25$). There was similarly no significant difference in the hourly averaged collective migration rates, beyond the first hour (Fig. 3.6C).

3.4 DISCUSSION

In this report, I used a previously developed stretcher device[49] to identify subcellular changes induced by prolonged, physiological cyclic stretch that correlate with increased protection against endothelial disruption by inflammatory mediators. Previously reports indicated that physiologically stretched monolayers exhibited smaller interendothelial gaps and increased gap closure rates following thrombin treatment, relative to static monolayers[21,49]. I initially quantify the molecular changes at endothelial junctions that potentially protect against junction disruption. Results show that physiological CS reduced the junction area and increased junctional F-actin and cortactin (Fig. 3.2D). This was accompanied by increased junctional tension, as visualized by the increased α18/α-catenin immunostaining ratio, which reflects increased force-activation of α-catenin in cadherin complexes (Fig. 3.3C). For these analyses, I created thresholded masks of junctions to objectively isolate and quantify immunofluorescence intensities. This improves upon the more common approach of using line-scans – quantification of immunofluorescence intensity along lines drawn orthogonal to junctions – which is subjective and prone to experimenter bias.

Using the live-cell imaging capabilities of my stretcher device, I further established that physiological CS enhanced lamellipodia dynamics, including protrusion length and persistence (Figs. 3.4C, 3.4D, 3.5), which play an important role in the closure of small endothelial gaps[67,95]. Live-cell imaging also revealed that, despite the enhanced lamellipodia dynamics, physiological CS did not alter collective endothelial cell migration in scratch wound assays (Figs. 3.6B, 3.6C). This result suggests that cyclic stretch accelerates the resealing of small gaps by enhancing lamellipodia dynamics, but not the closure rates of large wounds by collective cell migration.

Birukova, et al.[21] showed that, upon thrombin stimulation, both physiologically stretched and static endothelial monolayers show similar Rho GTPase activation. This finding suggested that physiological stretch did not protect against endothelial disruption by modulating Rho-dependent endogenous contractile forces[65,148]. Instead, physiological CS may activate molecular events that both mechanically reinforce cortical actin at endothelial junctions in intact monolayers, and promote gap recovery in disrupted monolayers (Fig. 3.7). My quantitative measurements reveal functional effects of physiological CS on junction remodeling, lamellipodia dynamics, and collective cell migration that contribute to barrier protection.

Quantitative immunostaining revealed F-actin and cortactin accumulation at intercellular junctions in cyclically stretched monolayers (Fig. 3.2D). Physiologically stretched HPAEC monolayers exhibited elevated levels of active Rac1 GTPase[21], which is essential for cortactin phosphorylation and translocation to the leading edge[90,222]. At intercellular junctions, cortactin is hypothesized to associate with cadherin, and reportedly scaffolds Arp2/3 and WAVE2, which regulate actin polymerization and branching[84,87,213]. Knockdowns of Arp3 and WAVE2 reduced myosin IIA and IIB at cell-cell contacts and reduced junctional tension[213]. The Arp2/3 complex also helps maintain endothelial monolayer integrity and barrier function[16,195].

I thus hypothesize that elevated levels of active Rac1 in cells subjected to prolonged (8 h) CS contributes to the observed cortactin accumulation at cell junctions (Figs. 3.2A, 3.2D), accounting for the increased junctional F-actin. The increased junctional tension (Fig. 3.3C) is consistent with increased Arp2/3 scaffolding by cortactin[87]. The basis for the reduction in VE-cadherin (Fig. 3.2D) is unclear. However, under pathological CS, vascular endothelial growth factor receptor 2 (VEGFR2) was activated and dissociated from VE-cadherin, which was then internalized[203]. At the same time VEGFR2 activation also activates Src[187,193], which phosphorylates cortactin[87,89,90,227]. These are possible mechanisms contributing to loss of VE-cadherin and accumulation of cortactin at junctions, but further studies are needed into the role of VEGFR2 in physiologically stretched monolayers.

I also observed a decrease in junction area with CS (Fig. 3.2C). Narrower endothelial junctions correlate with decreased permeability *in vivo* and *in vitro*[101,125]. In previous studies, endothelial monolayers subjected to 5% CS were replated onto transendothelial electrical resistance (TER) electrodes, and exhibited enhanced barrier function in response to thrombin, relative to static controls[20,21]. The baseline permeability of static and physiologically stretched monolayers have not been previously reported, but my results suggest that physiological CS not only protects against thrombin-mediated disruption, but may also enhance baseline barrier function.

Live-cell imaging of lamellipodia dynamics suggested an additional possible basis for the protective effect of physiological stretch. Lamellipodia formation is a critical step in endothelial wound healing, enabling cells to close gaps and establish new intercellular adhesions[49,67,95]. Cortactin enhances lamellipodia protrusion length and persistence[34,89], and scaffolds WAVE2[87] which enhances the protrusion rate[231]. Also, studies reported increased cortactin localization at the

periphery of endothelial cells subjected to physiological CS, 50 min after thrombin treatment[21]. I previously showed that a cortactin polymorphism that is associated with Acute Lung Injury impaired lamellipodia dynamics[42]. Together, the latter studies suggested that physiological CS might enhance gap reannealing[21,49], by regulating lamellipodia dynamics.

I quantitatively demonstrated that physiological CS enhances lamellipodia dynamics in single ECs (Fig. 3.4C). In subconfluent monolayers, which more closely approximate disrupted endothelia, cyclic stretch resulted in increased persistence and protrusion length relative to static controls (Fig. 3.4D). Enhanced lamellipodia dynamics were also observed in isolated endothelial cells following thrombin treatment (Fig. 3.5).

Conversely, dynamic imaging of collective cell migration demonstrated that physiological CS and resulting enhanced lamellipodia dynamics do not enhance the closure of large wounds, even though lamellipodia are a hallmark of collective cell migration[75,176] (Figs. 3.6B, 3.6C). This is not surprising, because several factors control collective cell migration besides lamellipodia formation, including intercellular cohesion[75,176].

In conclusion, my results suggest that the protective effect of physiological CS against endothelial disruption by inflammatory mediators derives from the mechanical reinforcement of junctions by F-actin remodeling, and from enhanced rate of lamellipodia-dependent closure of small gaps (Fig. 3.7). The high-resolution, dynamic imaging capabilities of the stretcher device greatly extends the types of studies possible with cells cultured on flexible substrates, beyond traditional immunofluorescence and Western blotting. As such, this platform enabled the *in situ* measurements of lamellipodia dynamics and collective cell migration studies with cyclically stretched endothelia, permitting the identification of critical phenotypic changes. My findings

provide new insights into mechanisms through which mechanical stimuli both protect against disruption, and enhance reannealing of disrupted endothelia.

3.5 FIGURES

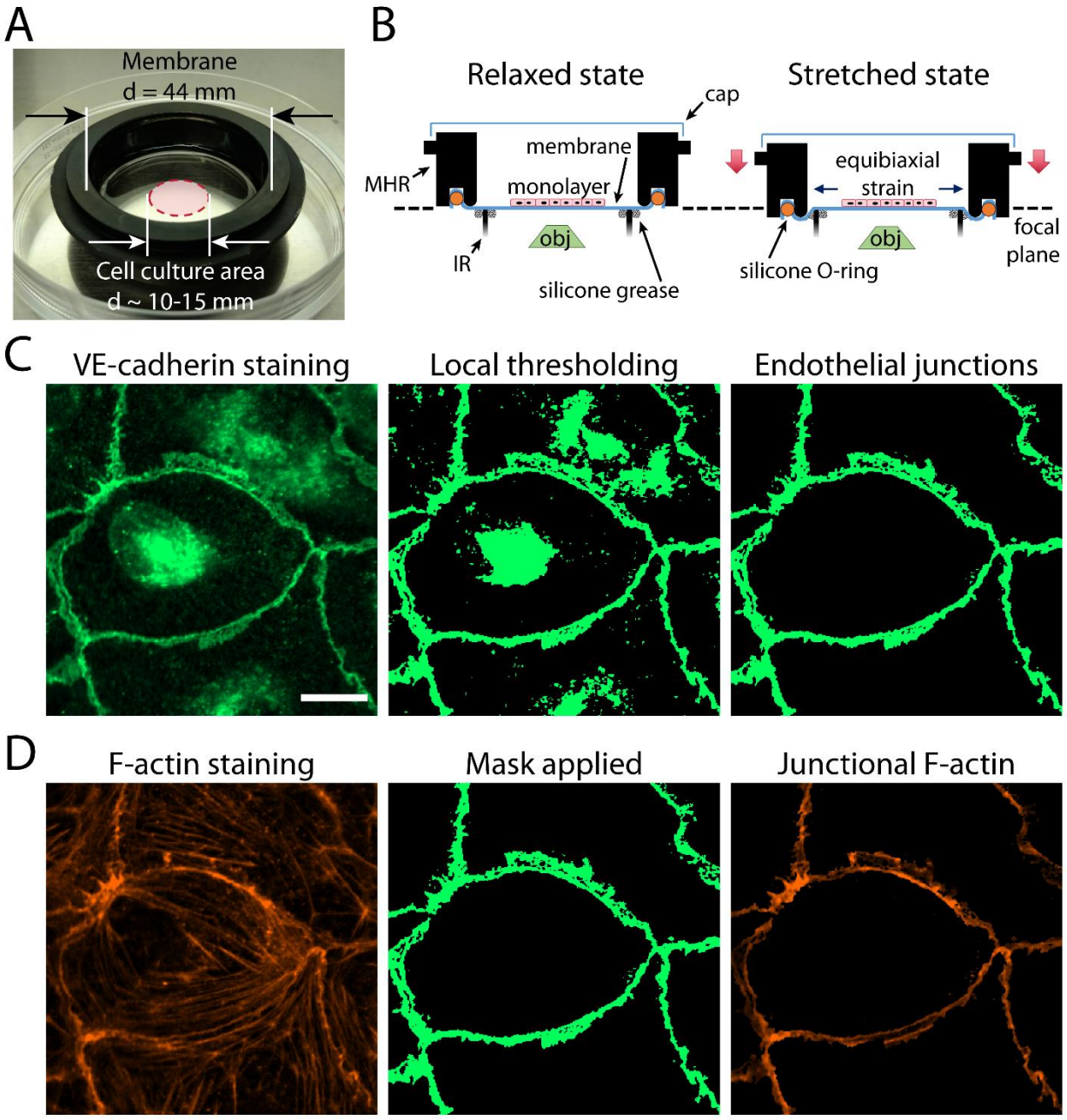

Fig. 3.1: Cyclic stretch treatment and immunofluorescence analysis. (A) An elastomeric membrane is shown mounted on an anodized aluminum membrane holding ring (MHR), and cells are seeded in a fibronectin-treated central area of diameter 10-15 mm. After cell attachment, sufficient medium is added to cover the mounted membrane. (B) Cutaway views of membranes in relaxed and stretched states. A stepper motor moves the MHR down over the indenting ring (IR). The membrane is stretched equibiaxially, and the cells experience strain. Conveniently for live imaging, cells remain in approximately the same plane even when stretched. However in this work

Fig. 3.1 (contd.): all live imaging was performed after pausing cyclic stretch and bringing the membrane back to the relaxed state. (C) To isolate the junctions, local thresholding was performed on the reference channel of interest, shown here as VE-cadherin, and then cytoplasmic aggregates were manually cropped out. The thresholded image could then be used to quantify junction area. (D) The thresholded image could also be used as a mask to isolate junctional staining of other proteins in the same field, e.g. F-actin as shown here. For (C) and (D), scale bar is 15 μm.

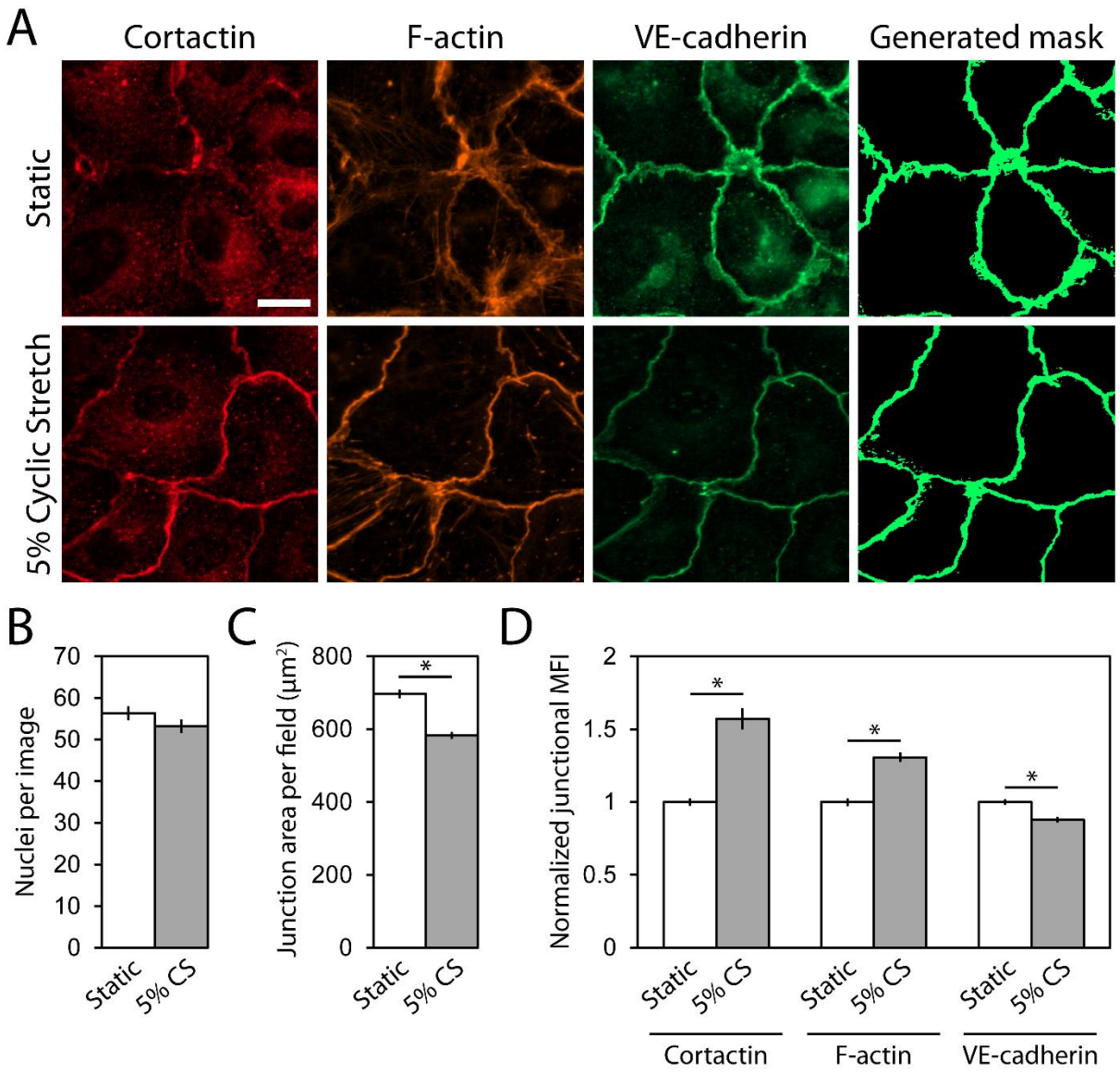

Fig. 3.2: Cyclic stretch reduces junction area and enriches junctional cortactin and F-actin. (A) Representative immunostaining images of HPAEC monolayers reveal changes in junctional localization of cortactin, F-actin and VE-cadherin on 5% CS treatment. VE-cadherin channel was used to generate a mask for the endothelial junctions by local thresholding, which was used to isolate and measure junctional staining intensity. Scale bar is 15 μm. (B) DAPI staining indicates that cell density is unaffected by 5% CS. n = 41 images over 5 experiments, 312 μm × 250 μm image dimensions. (C) Junction area per field, indicative of junction width, decreases upon 8 h of 5% CS. n = 123 fields over 5 experiments. (D) Relative to static control, junctional MFI of cortactin and F-actin increase whereas VE-cadherin decreases after 5% CS treatment. n = 63 fields over 3 experiments. All error bars are S.E.M. * represents $p < 1\times10^{-5}$. For (A), (C) and (D), fields are 75 μm × 75 μm.

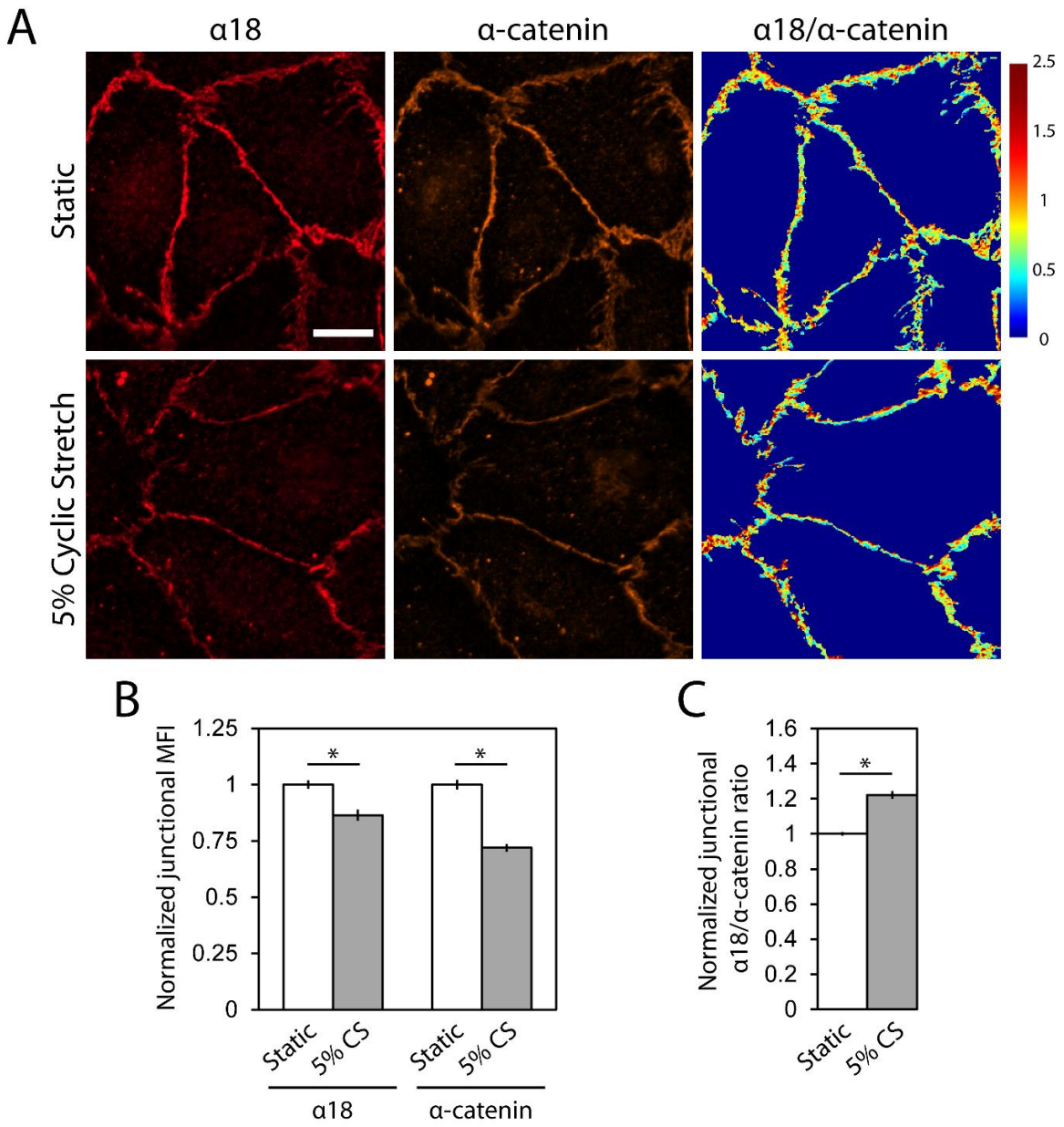

Fig. 3.3: Cyclic stretch leads to increased tension at junctions. (A) Representative immunostaining images of HPAEC monolayers show a decrease in α18 antibody and total α-catenin at junctions on 5% CS treatment. β-catenin channel (not shown) was used to generate a mask to isolate junctional α18 and α-catenin, and the pixel-by-pixel α18/α-catenin ratio was calculated and is shown as a heat map. Scale bar is 15 μm. Colorbar ranges from 0 to 2.5. There are fewer non-zero pixels in the heat map under the 5% CS condition due to reduced junction area, but the pixels on average have a higher value than under the Static condition. (B) Junctional MFI of α18 antibody and total α-catenin both decrease on 5% CS treatment, relative to Static condition. (C) Average junctional α18/α-catenin ratio increases on 5% CS treatment, relative to Static control. All error bars are S.E.M. * represents $p < 5 \times 10^{-5}$. For (B) and (C), n = 60 fields over 2 experiments, fields are 75 μm × 75 μm.

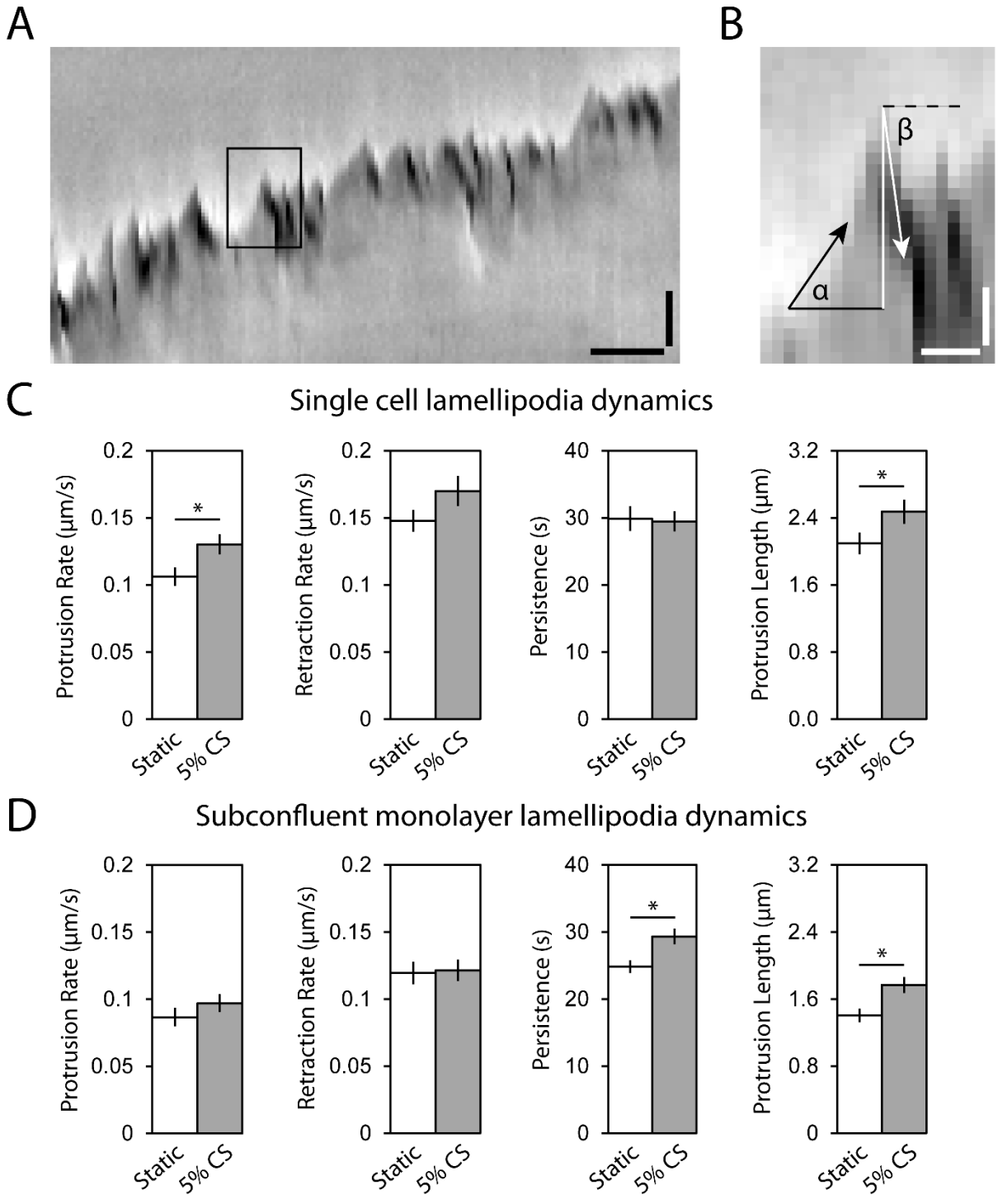

Fig. 3.4: Cyclic stretch enhances endothelial lamellipodia dynamics. (A) Representative kymograph of a single HPAE cell preconditioned to cyclic stretch, showing the position of the leading edge over the imaging time period. Outlined in black is an average and a smaller peak, to show the range of peaks considered for analysis. Horizontal scale bar is 2 min, vertical scale bar is 3 µm. (B) The peaks marked in (A) are shown in higher magnification. The slope of the black

Fig. 3.4 (contd): arrow is the initial protrusion rate, the slope of the white arrow is the initial retraction rate. The solid black line length is the persistence, and the solid white line length is the protrusion length. Horizontal scale bar is 30 s, vertical scale bar is 1 μm. (C) Single cells show increased lamellipodia protrusion rate and protrusion length on 5% CS treatment. n = 37-39 kymographs over 3 experiments, of duration 17 min. (D) Subconfluent cells show increased persistence and protrusion length on 5% CS treatment. n = 40 kymographs over 3 experiments, of duration 15 min. All error bars are S.E.M. * represents $p < 0.05$.

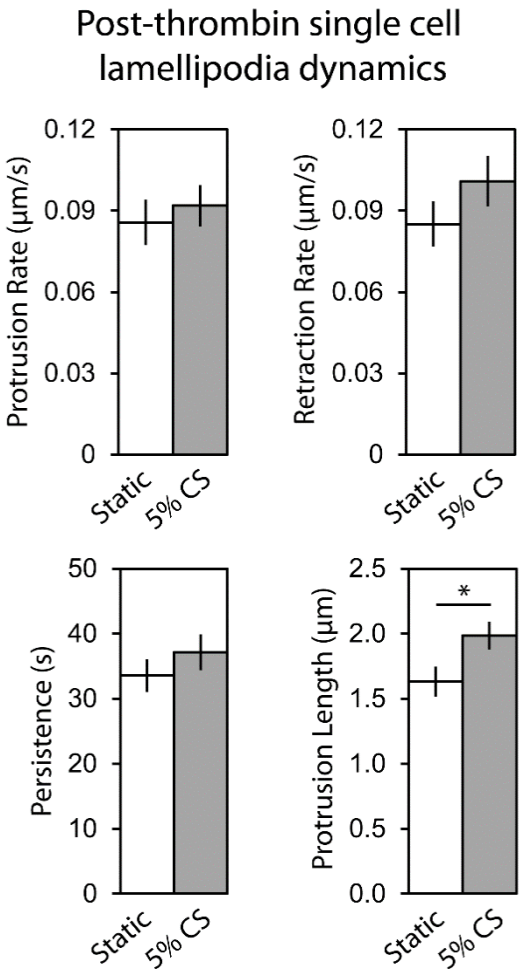

Fig. 3.5: Cyclic stretch enhances lamellipodia dynamics in thrombin-treated single cells. In cells recovering from 0.1 U/mL thrombin insult, 5% CS led to increased lamellipodia protrusion length relative to static treatment. n = 30-38 kymographs over 3 experiments, of duration 17 min. All error bars are S.E.M. * represents $p < 0.05$.

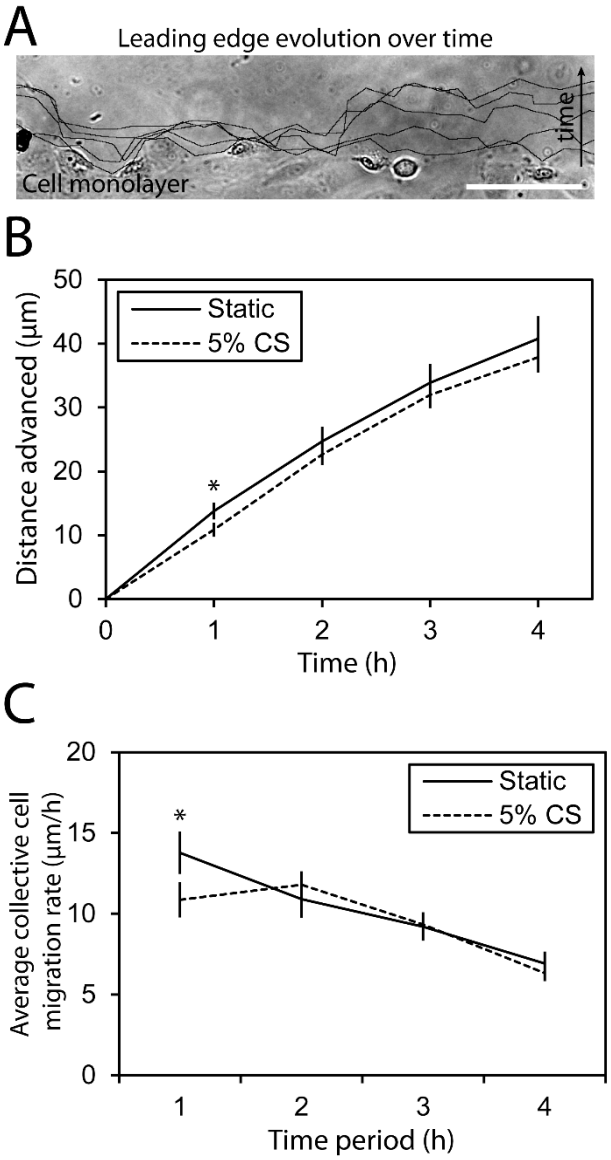

Fig. 3.6: Collective cell migration is unchanged in cyclic stretch-conditioned monolayers. (A) Representative image of collective cell migration of a cyclically stretched cell monolayer, at a leading edge created by scratch wound. The leading edge advances over time, and the positions at t = 0 – 5 h are outlined in black and overlaid on the phase contrast image of the monolayer at t = 0 h. Scale bar is 100 μm. (B) The cumulative distance advanced by the cell monolayer is plotted against time, and (C) the hourly average migration rate is plotted against the corresponding hour. In both (B) and (C), cyclically stretched monolayers behave similar to static control monolayers. n = 34-36 leading edges over 3 experiments. All error bars are S.E.M. * represents $p < 0.05$.

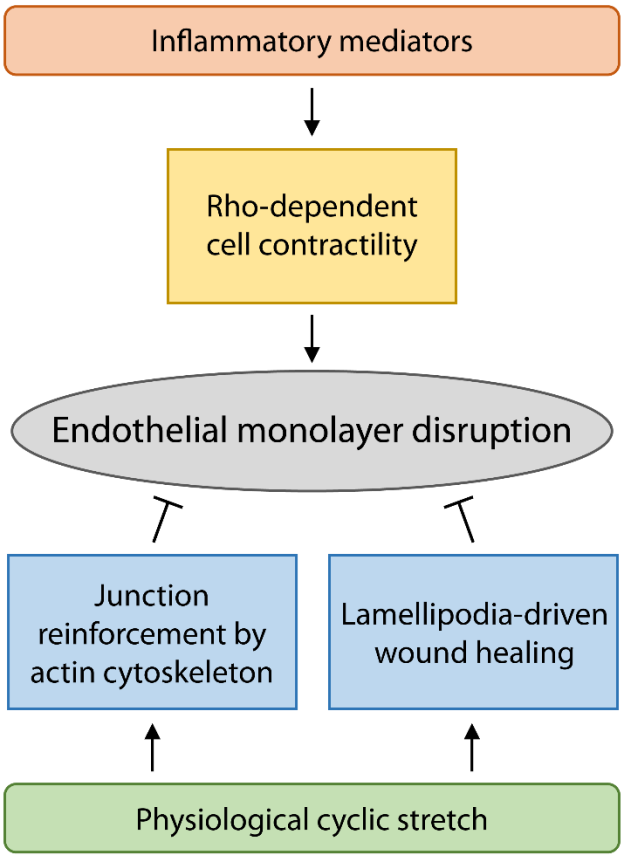

Fig. 3.7: Physiological cyclic stretch protects against endothelial disruption by inflammatory mediators. Inflammatory mediators such as thrombin, histamine, VEGF induce Rho-dependent cell contractility, which leads to endothelial junction failure and monolayer disruption. My results suggest that physiological cyclic stretch induces changes in the monolayer resulting in the reinforcement of endothelial junctions by the actin cytoskeleton, and enhances lamellipodia dynamics which enable closure of small wounds. As a result, physiological cyclic stretch protects against endothelial monolayer disruption by inflammatory mediators.

3.6 TABLE

Table 3.1: List of primary and secondary antibodies, and corresponding dilutions used in immunostaining experiments.

Target	Primary antibody (Source, Clone)	Secondary antibody (Source)
Cortactin	Mouse anti-cortactin (EMD Millipore, 4F11) 1:250 dilution	Rabbit anti-mouse IgG AF 647 (Invitrogen) 1:500 dilution
VE-cadherin	Goat anti-VE-cadherin (Santa Cruz Biotechnology, C19) 1:250 dilution	Rabbit anti-goat IgG FITC (Sigma) 1:250 dilution
'Open' α-catenin	Rat anti-α-catenin, α18 (A. Nagafuchi, Nara Medical University) 1:300 dilution	Goat anti-rat IgG CFL 647 (Santa Cruz Biotechnology) 1:300 dilution
Total α-catenin	Rabbit anti-α-catenin (Sigma) 1:2000 dilution	Donkey anti-rabbit IgG DyLight 550 (Novus Biologicals) 1:500 dilution
β-catenin	Mouse anti-β-catenin (BD Biosciences, 14) 1:150 dilution	Goat anti-mouse IgG AF 488 (Invitrogen) 1:300 dilution

Chapter 4: Elastomeric micropillar arrays as a platform to quantify endothelial junction mechanics

4.1 INTRODUCTION

The vascular endothelium functions as a selectively permeable barrier, regulating the transport fluid, dissolved gases, nutrients, leukocytes, etc. between the blood stream and surrounding tissue[120,212]. There are two primary pathways for transport across the endothelium – transcellular, and paracellular. The transcellular transport pathway is via transcytosis and is primarily vesicle-dependent transport. However, the paracellular transport pathway is through the interendothelial junctions, and is strongly dependent on the integrity of the junctions. Failure of interendothelial junctions leads to formation of gaps in the endothelial monolayer, which in turn leads to edema and further medical complications[65,120,212].

Interendothelial junctions can fail when intracellular contractile forces overcome intercellular adhesive forces[65]. The transmembrane protein VE-cadherin is the primary cell-cell adhesion molecule comprising interendothelial junctions[15,54]. The ectodomains of VE-cadherin molecules in one cell interact with VE-cadherin ectodomains on a neighboring cell to form adherens junctions. The VE-cadherin complex is mechanically linked to the actin cytoskeleton, and experiences actomyosin contractile forces[15,65]. Inflammatory mediators such as thrombin can trigger signaling pathways which result in increased actomyosin contractility[65,148]. VE-cadherin at the cell membrane is also in equilibrium with cytosolic pools of VE-cadherin[214,229], and its stability at the cell membrane and at intercellular junctions may depend on its interaction with several binding partners, such as vascular endothelial protein tyrosine phosphatase[158,160] (VE-PTP). In

order to test the effects of different perturbations on the junction integrity, I needed approaches capable of quantifying their influences on the mechanical properties of interendothelial junctions.

Biological probes previously used to detect the level of tension on the cadherin mechanosensory complex include antibodies[234] and genetically encoded biosensors[44]. However, these probes are limited in their dynamic range, and they report tension on a per-molecule basis as opposed to the entire junction. Further, these conformation-sensitive antibodies and genetically encoded biosensors do not determine the actual force on the protein, but instead report the tension-dependent conformation changes. In comparison, cell-matrix traction forces are more easily quantifiable, by exploiting the elastic properties of various biomaterials suitable as cell culture substrates[56,162,199]. In the latter case, mechanical force balance principles have been used to estimate junction tension or stress in terms of actual mechanical force readouts[122,144,198].

Traction forces measured in cells seeded on polyacrylamide gels are quantified as stresses, and mechanical force balance can be applied to either cell doublets or linear chains of triplets[144], or islands of cell monolayers[6,122,198], to yield an estimate of stress at intercellular junctions. While convenient, polyacrylamide gels suffer from two major drawbacks[232]. Firstly, the polyacrylamide gels are a continuous elastic substrate, such that the contractility of any cell is communicated to its neighboring cell not only through cell-cell adhesions, but also through cell-substrate adhesions[175]. Secondly, the relationship between the displacement field *a(r)* and the traction field *F(r)* is described by the following equation.

$$a_i(r) = \int dr' G_{ij}(r - r') F_j(r') \quad \ldots (4.1)$$

where *G(r-r')* is the tensorial Green's function, representing the displacement at *r* caused by the application of point force at *r'* (i, j = 1, 2, 3). Solving for the unknown traction field *F(r)* using the

known displacement field *a(r)* requires us to invert the above equation. This is a computationally intensive problem, and there is no unique solution. Several constraints must be applied, such as restricting traction forces to cell boundaries, restricting the deformation field of the cell, etc., in order to determine the unique traction field that satisfies all the constraints and also results in the observed displacement map. Further, the traction field can be used to estimate only the stress at the junction, not the actual tension.

Soft lithography has yielded yet another tool to help quantify traction forces[178,199]. Cells can attach and spread on an array of functionalized elastomeric micropillars, and traction forces generated through cell surface receptors deflect the pillar tips from their mean positions. Unlike fiducial marker beads in polyacrylamide gels, each micropillar deflects independently, such that increased contractility in one cell is relayed to its neighboring cell only through cell-cell adhesions and not through the substrate. If the deflections are 'small', such that the deflections are linearly proportional to the force applied on them, knowing the displacement map of pillar tips, the traction force map can be easily calculated. Using mechanical force balance principles as described elsewhere[43] and in the following section, the tension at the junction can be quantified. Immunostaining cell-cell junction components such as VE-cadherin or β-catenin visualizes the junctions. Because endothelial junctions are typically parallel to the substrate, the junction area measured from epifluorescence images corresponds to the actual junction area[53,136]. Knowing the junction tension and area enables calculation of the junction stress.

In this work, I used the micropillar array detector (mPAD) approach to measure junction tension, area, and stress. I studied the effects of various perturbations – biochemical, genetic, matrix composition – to demonstrate the versatility of this approach. Quantifying the effects of

these perturbations on junction mechanics provided important insights into their downstream effects, specifically in relation to junction integrity and barrier function.

4.2 MATERIALS AND METHODS

4.2.1 Cell culture and reagents

Primary human pulmonary artery endothelial cells (HPAECs, Lonza) were cultured in complete endothelial cell growth medium EGM-2 (Lonza) with 10% (v/v) fetal bovine serum (FBS, Sigma) in a humidified incubator at 37°C with 5% CO_2, and passaged every 3 days. HPAECs between passages 6-8 were used for experiments.

Mouse lung microvascular endothelial cells (MLECs) were from Yulia Komarova (University of Illinois, Chicago), isolated from wild-type (WT) or vascular endothelial protein tyrosine phosphatase knockout (VE-PTP KO) C57BL/6 mouse embryos, and cultured in complete mouse endothelial cell medium MECM (Cell Biologics) with 10% (v/v) FBS, in an incubator as described above. MLECs between passages 4-6 were used for experiments.

4.2.2 Photolithographic patterning of silicon mPAD masters

Silicon wafers of diameter 3 inches (University Wafers) were patterned using the positive photoresist AZ1505 (Merck Performance Materials GmbH) at the Micro and Nanotechnology Laboratory (MNTL, University of Illinois). A square chrome-on-sodalime photomask of side 4 inches was designed and fabricated (Applied Image, Inc.) with a clear field pattern consisting of a hexagonal close packed array of dark spots of 2 μm diameter each, and with a 4 μm center-to-

center spacing (Fig. 4.1A). The arrays had flat rectangles around them, to act as supports during protein stamping on the elastomeric mPAD tips[232].

Silicon wafers were cleaned with a standard protocol, consisting of consecutive rinses with acetone, isopropanol, DI water, and finally with isopropanol, prior to blow drying with filtered nitrogen. The sodalime photomask was also cleaned with the same protocol, and allowed to air dry. Wafers were dehydrated on a hotplate at 125°C for 10 min, in order to remove most of the water from the surface, and then cleaned in an oxygen plasma descum chamber (Diener Pico) at 150 mTorr, 500 W, for 3 min. The wafer was mounted on a spin-coater with a vacuum chuck, and 1 mL of hexamethyldisilazane (HMDS, MicroChemicals, MNTL) was pipetted onto it, before starting a spin of 500 RPM for 10 s (spread step), ramping up over 10 s to 4000 RPM, holding for 60 s (dry step), then ramping down over 10 s to 0 RPM. HMDS is an adhesion promoter which bonds to free hydroxyl groups on the dehydrated, hydrophilic silicon wafer. The resulting HMDS-primed surface is hydrophobic, improving the adhesion of photoresist to the wafer, especially positive photoresists. The dehydration bake is necessary for proper HMDS priming of the wafer. Spin-coating is not the preferred approach for HMDS priming of silicon wafers, but an HMDS vapor priming oven was not available. Spin coating HMDS results in a thick HMDS coat on the wafer, which crosslinks the bottom layer of the photoresist during the soft bake and thus prevents complete development[1]. Although this results in photoresist 'scum' that is visible after development, it can be removed with a carefully-controlled oxygen plasma descum process (Fig. 4.1B).

HMDS-primed wafers were coated with the positive photoresist AZ1505. A 2.5 mL volume of the photoresist was pipetted onto the center of the wafer and spun immediately, by ramping up from 0 RPM to 500 RPM in 5 s, holding for 10 s (spread step), ramping up to 2000

RPM in 5 s, holding for 60 s (dry step), followed by ramping down to 0 RPM over 5 s. This results in 0.7 μm thick films, according to the manufacturer's technical datasheet. The minimum film thickness is dictated by the etch selectivity of the inductively coupled plasma – reactive ion etching (ICP-RIE) process. The silicon:photoresist etch selectivity can be tuned to be 100:1 or higher, depending on the process recipe. Because the height of the silicon mPAD masters was to be less than 10 μm, accounting for an etch selectivity ratio of 100:1, the minimum resist thickness must be 0.1 μm. The 0.7 μm film thickness expected by this spin coating protocol is thus appropriate for this application. Thicker positive resist films are unnecessary and not recommended, as obtaining well-defined features during resist development is relatively challenging (Fig. 4.1C).

Coated wafers showed negligible beads at the edge of the wafers, so edge bead removal was not necessary. Coated wafers were soft baked at 100°C for 50 s on a hot plate, after which they were exposed to 18 mJ/cm^2 of i-line radiation from the mercury lamp, in contact mode with the photomask. No post-exposure bake was necessary. The developer was a solution of 1:4 parts AZ400K developer (Merck Performance Materials GmbH) and deionized water, by volume. The wafer was developed in a trough containing the developer solution with gentle, intermittent shaking, for roughly 1 min. Towards the 1 min time point, it was important to rinse off the developer with water, and inspect the developed patterns under the microscope, in order to prevent the overdevelopment of the positive photoresist. Further development, if necessary, can be continued in 5-10 s intervals. To remove any residual photoresist scum, the rinsed wafer was blow-dried, and then subjected to oxygen plasma 'descumming', at 150 mTorr, 500 W, for 3 min, followed by inspection and further descumming in 1 min intervals if necessary. A hard bake at 115°C for 50 s on a hotplate is optional, and it typically helps increase silicon:photoresist etch selectivity.

4.2.3 Replica molding of elastomeric mPADs

Elastomeric mPADs were replica-molded from silicon masters as described[43,232]. I obtained silicon masters from Jianping Fu (University of Michigan, Ann Arbor) with a range of pillar heights, which dictate the bending modulus, or spring constant of the elastomeric mPADs (Table 4.1). When choosing mPADs for a particular application, it is necessary to ensure that the pillars are not soft enough that the traction forces exerted by the cell cause pillar tips to deflect excessively (beyond the linear regime of the force-deflection curves), or contact each other. At the same time, the pillars should not be so stiff that the pillar deflections are barely detected, which depends on imaging magnification and is thus experiment-specific. For HPAECs and MLECs, mPADs #4 with a pillar stiffness of 22 nN/μm met these criteria, and were thus used for all experiments (Table 4.1, Fig. 4.1D). Each silicon master consisted of an array of 9 individual mPAD masters (Fig. 4.2A). The silicon master, of desired pillar height, was silanized by vapor deposition with (tridecafluoro-1,1,2,2-tetrahydrooctyl) trichlorosilane (TFOCS, Gelest), by placing the wafer and 30 μL of the silane inside a dessicator, connected to house vacuum for 4 or more hours. The silanized master was then placed in a 60 mm × 15 mm aluminum weighing dish, with the patterns facing upwards.

A 10:1 (w/w) mixture of Sylgard 184 (Dow Corning) elastomer base and crosslinker, respectively, was prepared to a final weight of 20 g. Once the Sylgard 184 elastomer base and crosslinker were mixed, curing began immediately, and the viscosity of the mixture increased over time. At room temperature, the working time available is 3 h before the solution becomes too viscous to work with. The mixture was stirred vigorously with a toothpick until homogenous, and then degassed under vacuum in a dessicator, until no bubbles were seen. The mixture was then poured onto the silicon master in the aluminum weighing dish, and degassed again, after which

the PDMS was cured in an oven for 15 min, at 110°C. At this point, the aluminum weighing dish could be taken out of the oven and stored indefinitely, with the advantage that the surface of the silicon masters are thus protected from damage. If silicon masters are not stored under cured PDMS, dust can accumulate on the surface, in which case it is recommended to clean the silicon masters with sprays of acetone, isopropanol, DI water, isopropanol again, and finally a nitrogen stream from a nitrogen gun, before silanization. It is recommended to silanize the wafers every 2-3 uses.

The cured PDMS on the silicon master formed a negative mold array of 9 negative molds. The aluminum weighing-dish could be peeled from the PDMS block, which encased the silicon master because PDMS flowed under the wafer during degassing. Using a single-edge razor, the PDMS film under the silicon master was cut from the main PDMS block, and discarded. By pinching the PDMS block between a thumb and a forefinger, on diametrically opposite locations of the circular block, the PDMS could be easily released from a well-silanized master. Using the single-edge razor again, the PDMS negative mold array could then be diced into individual 8 mm × 8 mm negative molds (Fig. 4.2A). The resulting negative molds could also be stored indefinitely.

mPADs were cast from negative molds onto glass coverslips. The PDMS negative molds were activated by air plasma, at high power, 500 mTorr for 2 min (Harrick Plasma, Kenis laboratory, University of Illinois), and silanized with TFOCS as described above, within 30 min of activation. Prior to casting mPADs on glass coverslips, the coverslips were cleaned with sodium hydroxide, detergent, or plasma, and dried by a stream of nitrogen (if the process made drying necessary). Sylgard 184 elastomer base and crosslinker were mixed vigorously in 10:1 (w/w) ratio, and degassed as described above. Using a pipette tip or a toothpick, one drop of the PDMS solution was placed on top of each mPAD negative mold, and spread across the surface. It was important

to avoid touching the silanized mPAD surface directly with the tip or toothpick, as it damages the silane coating and causes the negative mold to bond to the cast mPAD. After spreading the PDMS prepolymer solution over the negative mold surface, the negative molds were degassed for approximately 30 mins, to permit the PDMS to fill the microwells of the negative mold. Then, the negative molds were pressed against the center of the cleaned coverslips, at one mold per coverslip. Gentle pressure was applied to squeeze out excess PDMS, while avoiding excessive pressure or shear that could damage the silane coating. These negative molds pressed against the coverslips could be cured at 110°C in an oven, for 20 h. It was important to keep the curing time constant between runs. Otherwise, the variation in extent of crosslinking led to variation in the stiffness of micropillars. The nominal mPAD stiffnesses reported in Table 4.1 are for the curing time and temperature mentioned above.

The negative molds were released from the cast mPADs on the coverslips, by holding the coverslip down with two fingers, and gripping the negative mold with tweezers. Minimal force was required to thus peel the negative mold from one edge. Negative mold release requires even lesser force when holding the coverslip under an alcohol such as methanol, however, if methanol is used, then it is recommended to either proceed to the critical point drying step within a few hours, or take the mPADs out of methanol and air dry. Dry mPADs can be stored at room temperature for at least 5-7 days before proceeding to 'critical point drying'. Negative molds could be re-used 3-4 times, but re-silanization was required at least after every alternate use. The process of negative mold release typically results in collapsed micropillar arrays, with neighboring pillars contacting each other, and critical point drying is necessary to result in vertical arrays (Fig. 4.2B).

4.2.4 Critical point drying of mPADs

Before proceeding to critical point drying, dry mPADs were immersed into an alcohol such as methanol[232]. It is important that the alcohol that was used throughout the critical point drying process was free of any impurities, including water and particulates. One of the four PDMS walls around the mPAD was scraped off with a single edge razor, preferably in a single, clean motion, which was easier when the mPAD was wetted with methanol. Failing to scrape off the wall cleanly left behind ragged PDMS strips and debris, which can negatively affect the mPAD yield at various subsequent strips. The remaining three walls act as spacers, protecting the mPADs on the coverslips from collapsing when the coverslips are stacked. After scraping off one of the walls, the mPADs were re-immersed in methanol and sonicated for 5 mins. They were then transferred to fresh methanol and sonicated again. After another transfer, the mPADs were transported under methanol for critical point drying (Tousimis Samdri PVT-3D, MNTL). Prior to critical point drying, the mPADs are again transferred and sonicated in fresh methanol. Beyond detaching loose particulates, sonication helps release collapsed posts (Fig. 4.2B). The critical point drying chamber was cleaned with a cleanroom wipe wetted with methanol, then filled to a sufficient level with methanol to immerse all the coverslips. The mPAD coverslips were then quickly transferred into the chamber, with minimal exposure to air. Up to 10 coverslips can be dried at the same time.

The critical point drying was performed according to conventional protocols, provided by the equipment manufacturer. The critical point drying chamber is sealed and cooled to below 0°C, after which liquid CO_2 is allowed to fill the chamber. Due to the different densities of methanol and liquid CO_2, Schlieren lines should be clearly visible inside the chamber. Flooding the chamber with liquid CO_2 with simultaneous purging was continued until there was no trace of methanol in the chamber. The temperature increased during this process, but was not be allowed to go above

10°C, and preferably kept below 0°C. Complete purging of methanol from the chamber could be estimated from the lack of Schlieren lines in the chamber, and lack of methanol in the purge stream, and visible exhaust of dry ice in the same purge stream. As a precaution, the fill and purge process was continued for a while longer, even after all methanol appeared to have been purged. The scraped-off wall enabled methanol and liquid CO_2 to drain easily during critical point drying. Finally, both cooling and the fill-purge cycles were stopped, and heating was switched on to increase the temperature and thus the pressure in the chamber. Doing so took the system through the critical point of CO_2 (1200+ psi, 32 °C), at which point the gas and liquid phases of CO_2 were indistinguishable. The chamber could then be slowly vented to yield the dried mPADs, which could be inspected under a microscope. Proper critical point drying results in mPADs with all pillars standing independently, with minimal number of collapsed pillars (Fig. 4.2B). Warped substrates, or substrates with extensive interpillar adhesion or other obvious defects, were either be discarded or subjected to critical point drying again.

The remaining PDMS walls around the mPAD could then be scraped away cleanly with a single edge razor. The mPAD coverslips were mounted on polystyrene dishes of 35 mm diameter, with a 13 mm central hole in the bottom (Cell E & G). PDMS, Norland optical adhesive, or epoxy was used to mount the coverslips on the dishes (Fig. 4.2A).

4.2.5 Stamp fabrication for microcontact protein printing

To prepare silicon masters for molding of stamps, silicon wafers of diameter 2 inches were patterned with the negative photoresist KMPR 1010. A clear field photomask made of transparency film (FineLine Imaging) carried arrays of dark patterns (Fig. 4.1E). The pattern

consisted of two circles touching at the circumference, to facilitate the formation of cell doublets. The area of each circle was chosen to be 1600 μm^2, which was obtained by imaging a confluent HPAEC monolayer and calculating the average area of an HPAE cell, as 1920±40 μm^2 (n = 75 cells). The patterns were well-spaced (100 μm minimum center-to-center distance), to prevent two cells from neighboring patterns from easily contacting each other.

Wafers were cleaned with successive sprays of acetone, isopropanol, DI water, isopropanol, and finally with a stream of nitrogen. After a dehydration bake on a hotplate at 125°C for 10 min, the wafer was oxygen-plasma cleaned for 3 min at 500 W, 150 mTorr. The negative photoresist KMPR 1010 (Microchem, Micro-Nano-Mechanical Systems cleanroom, UIUC) was then dispensed onto the center of the wafer and immediately spun, ramping up from 0 RPM to 500 RPM in 5 s, holding at 500 RPM for 10 s (spread step), ramping up to 4000 RPM in 5 s, and holding at 4000 RPM for 30 s (dry step), before ramping down to 0 RPM in 5 s. This resulted in a photoresist film thickness of 8 μm, according to the manufacturer's technical datasheet. Edge bead removal was performed with a cleanroom swab soaked in acetone, in radially outward motions at the wafer's circumference. A soft bake was performed at 100°C for 5 min. This was followed by i-line (365 nm) UV exposure, to a dose of 330 mJ/cm^2. Following a post-exposure bake of 2 min 30 s at 100°C, a latent image was visible on the resist. The pattern was developed by submerging the wafer in a trough of propylene glycol monomethyl ether acetate (PGMEA, Sigma), stirring by hand for 30 s, followed by 90 s of sonication. The wafer was then transferred to another trough with fresh PGMEA for 10 s, then sprayed down with isopropanol and dried with a nitrogen gun. Post bake was then performed for 5 min at 150°C.

The patterned wafer (Fig. 4.1F) was then used as a master to cast stamps using Sylgard 184 PDMS. As described earlier, 10:1 elastomer base:crosslinker (w/w) Sylgard 184 was mixed

vigorously, degassed, then poured over the wafer and degassed again, followed by curing at 65°C overnight. The PDMS stamps could then be released from the master and diced into individual stamps (Figs. 4.1G, 4.2C). If patterned cells are not desired on the mPAD tips, flat stamps can be fabricated by curing PDMS against silanized, bare silicon wafer or silanized glass slides, and then dicing the flat PDMS. A notch can be made in the corner of the non-stamping surface with a razor, to distinguish it from the stamping surface.

4.2.6 mPAD functionalization

To facilitate cell attachment, the desired protein was stamped onto the pillar tips[232]. A protein solution in phosphate-buffered saline (PBS) was incubated on the desired number and type of stamps, and the protein physisorbed onto the stamp for 1 h at room temperature (Fig. 4.2C). In all experiments reported here, the stamps used were the ones with two touching circles of 1600 μm^2 each, for formation of cell doublets (Fig. 4.1G), and the mPADs used were #4, with stiffness k = 22 nN/μm. Fibronectin was the typical matrix protein used, and was incubated on the stamps at 50 μg/mL, for 1 h. Following physisorption, the stamps were rinsed in DI water twice consecutively, before being blow-dried under nitrogen.

mPADs in dishes were then activated by treating them with ozone in a UVO cleaner (BioForce Nanosciences ProCleaner Plus, MNTL, UIUC) for 7 min (Fig. 4.2C). Plasma cleaners are not recommended, as they are too harsh and make the surface of PDMS 'glassy' and permanently hydrophilic. UVO cleaners are mild, and the hydrophilicity is temporary. Within 30 min of UVO treatment, the protein coated surface of the stamp was brought into contact with the pillar tips, and gentle pressure was applied on the stamp, using the tweezers. Within 1 min of

contact, the dish was flooded with ethanol and the stamps were peeled or flicked away, whichever was more convenient to avoid collapsing the pillars. The stamps could be reused for stamping the same matrix protein, after sonicating them in ethanol.

The ethanol in mPAD dishes was aspirated and replaced with 70% ethanol for 1 min. Subsequently, three washes were performed with DI water. Vybrant DiI or DiD (Invitrogen, diluted 200 times in water) was incubated over the central area with the mPADs for 1 h, followed by three DI water rinses and 0.2% (w/v) Pluronic F108 (BASF) incubation in PBS for 45 min. After this, the dishes were subjected to two more rinses with DI water, and one rinse with PBS.

In experiments with the Komarova lab (University of Illinois, Chicago) that compared cells on fibronectin versus N-cadherin as a matrix protein for HPAECs, it was necessary to insure that N-cadherin was correctly oriented at the pillar tips, to facilitate cell attachment. Thus, instead of directly stamping N-cadherin, which resulted in poor cell attachment likely due to random N-cadherin orientation, I instead stamped protein A (Sigma), using the same protocol as for fibronectin. The subsequent dye incubation and blocking steps were also the same as with fibronectin. However, following the rinses after Pluronic incubation, N-cadherin-Fc-His (Sino Biological, Komarova lab, UIC) was incubated over the central area with the mPADs at 50 μg/mL in PBS. The Fc tag on the N-cadherin protein bound to the protein A stamped on the micropillar tips, as a result of which the N-cadherin protein was oriented correctly on the surface, and available for cell binding.

Prior to cell seeding, the PBS in the dishes was aspirated, and the central portion with the actual mPADs were left immersed in medium. At all steps, utmost care was required to ensure that the mPADs were not exposed to air, else the pillars could collapse and the mPADs would be unusable for force measurements.

4.2.7 Cell seeding on mPADs and fixation

HPAECs as well as MLECs were trypsinized and seeded on the protein-stamped mPADs. Approximately 20,000 cells in 150-200 μL of their respective complete medium were added to each central mPAD area. Cells were allowed to attach to micropillar tips in the incubator, and observed every 30 min (Fig. 4.2C). When a sufficient number of cells appeared to have attached as doublets, the excess suspended cells were rinsed off with PBS, and fresh medium was added. On N-cadherin substrates, HPAECs did not attach and spread as well as on fibronectin. Instead, cells remained in suspension and formed large clusters prior to settling. As a result, the cell-doublet yield on N-cadherin pillars was significantly lower than on fibronectin pillars, and instead, produced multi-cell clusters.

Cells were incubated overnight. Fixation was then performed using warm 4% paraformaldehyde (Sigma) for 15 min, followed by three rinses with PBS. At this point, if necessary, samples were stored at 4°C in the dark, until immunostaining.

4.2.8 Immunostaining and imaging

Immunostaining was performed according to conventional protocols. Cells were permeabilized by 0.1% (v/v) Triton X-100 in PBS for 4 min, and non-specific antibody binding was blocked by 1% (w/v) bovine serum albumin in PBS for 1 h. Primary and secondary antibody incubations were performed for 1 h each at room temperature. One or more of the following primary antibodies were used: mouse anti-β-catenin (clone 14, BD Transduction, 1:150 dilution), goat anti-VE-cadherin (clone C-19, Santa Cruz Biotechnology, 1:150 dilution). One or more of the following secondary

antibodies were used, with care taken to avoid cross-reactivity: rabbit anti-goat IgG FITC (Sigma, 1:500 dilution), goat anti-mouse IgG Alexa Fluor 488 (Invitrogen, 1:300 dilution), rabbit anti-mouse IgG Alexa Fluor 647 (Invitrogen, 1:500 dilution). Samples were mounted with Fluoromount G and stored at 4°C until imaging.

Samples were imaged on a Zeiss Axiovert.Z1 epifluorescence microscope (Institute for Genomic Biology, UIUC), with a 40× oil immersion objective, and an Axiocam HRm camera with a 2752 px × 2208 px sensor, and 2×2 binning, resulting in 1376 px × 1104 px images. Images were captured of the micropillar tip positions, as well as the endothelial junctions. Occasionally, these were at different focal planes and the focus needed to be adjusted to acquire in-focus images. If the junction morphology varied with the focal plane, multiple images were acquired at different focal planes. Only cell doublets, and cell triplets arranged in a linear chain were imaged, so that mechanical force balance calculations could be done. Further, imaging was restricted to cell clusters (doublets or triplets) where the junction of interest was approximately parallel to the 'neck' of the stamped pattern, i.e. approximately perpendicular to the line joining the two centers of the touching circles (Fig. 4.3A). Imaging was also restricted to cell clusters that had several free columns of pillars on either side of the cluster, cell clusters which had no collapsed pillars and minimal missing pillars underneath, and cell clusters which had not taken up significant amounts of DiI or DiD (i.e. visibility of pillars underneath the cell clusters was not significantly degraded).

4.2.9 Calculation of junction area and cell-generated traction forces

Junction area analysis was performed manually with ImageJ v1.51k (National Institutes of Health). Endothelial junctions typically are flat and parallel to the substrate, as a result the immunostained

intercellular junction area from VE-cadherin or β-catenin staining reflects the actual area of the junction. The junction did appear to gain some 'depth' in some images – such that the junction morphology varied slightly with the focal plane. If the junction morphology variation was 'small', the basal junction immunostaining was used as the reference image. If the junction morphology variation was 'large', a maximum intensity projection of all focal planes was generated, and the resulting image was used as the reference image. The region around the adherens junction was outlined manually, and the threshold was set such that the brightest 15% of pixels in that region were taken to be the AJ area (Fig. 4.3A). The area of the thresholded regions was obtained using the 'Analyze Particles' function of ImageJ. There is scope for improvement in this process to make it more objective – certain local thresholding algorithms might successfully be used to threshold the junction area specifically, when the thresholding parameters are correctly tuned.

Traction force analysis under each cell cluster was performed using a custom MATLAB program written for MATLAB R2007a[43,232]. The code and its accompanying documentation were kindly provided by Christopher Chen (Boston University). The program accepts grayscale '.tif' images of the cell cluster and the micropillar tips (Figs. 4.3A, 4.3B). For a specific combination of microscope, objective, camera, binning, and pillar array structure (square vs. hexagonal array), a configuration file can be created or modified using the program. This configuration file, once produced, can be reused for all mPAD force analyses of images captured using this configuration.

The cell image and pillar tip image were read by the program, and from free pillars in the same row, the images were rotated such that the chosen row and its parallel rows were horizontal. Next, the cell cluster of interest was selected by drawing a box around it, such that it included 2 or more columns or rows of free posts on all sides of the cluster. Next, a free post in the upper left quadrant of the image (outside the selected cluster) was selected, to align the ideal grid of ROIs

from the configuration file, with the grid of posts inside the selected cell cluster. Each ROI in the grid corresponds to one pillar tip. The grid was generated from the pillar spacing calculated and stored in the configuration file. The program allows the user to align the grid such that each free post lies in the center of its corresponding ROI. If the grid of ROIs cannot be aligned with the posts inside the selected box, such that one post corresponds to one ROI, and the center of free posts aligns with the center of their corresponding ROIs, then the configuration file might need to be modified to adjust the pillar spacing.

After adjusting the grid, the program was used to calculate the centroids of the pillar tips after image binarization – i.e. after local thresholding such that dark areas are set to black and bright areas to white. After centroid calculation, post-processing was started, initially by identifying some free pillars as 'alignment' pillars – intended to align the ideal grid of ROIs with the centroids of identified pillar tips. By definition, in the final displacement map these posts will have zero deflection as these posts are reference posts. Next, the ideal grid was displayed superimposed on the centroids, and the user selected at least two, well-spaced free pillars per row of pillars. These free pillars were used to generate best-fit polynomial lines to predict the free positions of all pillars (including attached pillars). As a result, having more than two posts per row was not detrimental. In the final displacement map, the specified free pillars can have non-zero displacements. After this step, the program auto-detected the posts by aligning the pillar tip grid with the ideal grid using the alignment posts specified, then the predicted free-pillar positions were calculated, and actual displacements of each pillar tip from the predicted free-pillar positions were calculated in terms of pixel units. The user can set an auto-detect tolerance in pixel units, such that pillars with displacements larger than the auto-detect tolerance were categorized as 'attached' pillars, and other pillars in the selected box were categorized as 'free' pillars. A high auto-detect

tolerance results in missing small deflections of attached pillars, whereas a low auto-detect tolerance results in a significant number of false positives.

For the experiments that investigated the effect of thrombin on tension at HPAEC junctions, and the effect of VE-PTP knockout on MLEC junctions, an auto-detect threshold of 0.8 pixels was sufficient to detect the majority of attached pillars. With a scale of 0.22 μm/px and a spring constant of 22 nN/μm, this resulted in a minimum force threshold of 3.9 nN per pillar. For studies of HPAE cells on N-cadherin versus fibronectin, an auto-detect threshold of 0.5 pixels was used, as the traction forces generated were significantly lower on both fibronectin and on N-cadherin substrates. The lower auto-detect threshold resulted in a minimum force threshold of 2.4 nN per pillar. The lower tractions observed in the latter experiment was due to use of primary HPAECs from a different source (Komarova lab). Because most cell traction forces are generated at the cell periphery, pillars under the cell body may be incorrectly categorized as free pillars. Similarly, collapsed or missing pillars around the cell can be incorrectly categorized as attached pillars. This incorrect automatic categorization can be manually corrected in the next step.

The MATLAB program has several functionalities to reassign pillar categories. Firstly, a polygon can be traced manually encompassing all pillars attached to the cell. The program sets all pillars detected as ‘attached’, which lie outside the polygon, to ‘ignored’. These pillars are no longer used for force calculations. Next, the program can also accept user input on the fluorescent cell image, differentiating the low-intensity background from the high-intensity fluorescent cell body. Any pillar positions that lie in regions corresponding to high-intensity, are re-categorized to ‘attached’. Lastly, the program also allows the user to manually assign each individual post as ‘attached’, ‘free’, or ‘ignored’.

Further post-processing enables users to automatically or manually change the positions of detected pillar tip centroids. Although using the auto-edit function to correct pillar top positions is always recommended, manual editing can be performed in specific cases, when necessary. The latter is useful when the images are of poor quality, or if there is excess cell body fluorescence due to DiI or DiD pickup by cells, or fluorescent aggregates, etc. In certain cases, the displacement map cannot be reasonably corrected – a common example being cases of substrate warping. Such images cannot be analyzed and must be discarded.

From the final displacement map, the traction force map was easily computed, using beam-bending theory for small cantilever deflections (Fig. 4.3B).

$$\boldsymbol{F} = k * \boldsymbol{x}; k = \frac{3EI}{L^3};\ I = \frac{\pi d^4}{64} \quad \ldots (4.2)$$

where **F** is the force exerted on the free end of the cantilever; k is the spring constant; **x** is the deflection; E is the bulk elastic modulus; I is the area moment of inertia; L is the length of the cantilever; and d is the diameter of the cantilever. Knowing the displacement (**x**) map and the spring constant (22 nN/μm for mPADs #4, Table 4.1), a traction force (**F**) map can be generated.

After the traction forces were quantified, a few post-analysis checks were performed. The program not only outputs the total traction force magnitude exerted by the cell cluster, but also the total 'background' force magnitude, from the 'free' pillar tips. The total force magnitude is calculated by taking the square root of the sums of squares of individual force magnitudes, as with any vector quantity.

$$Total\ traction\ force\ magnitude = \sqrt{\sum_{i=1}^{n} \left|\boldsymbol{F}_{\boldsymbol{i,cell\ cluster}}\right|^2} \quad \ldots (4.3)$$

$$Total\ background\ force = \sqrt{\sum_{j=1}^{m} \left| \boldsymbol{F}_{j,free} \right|^2} \quad \ldots (4.4)$$

where $|\mathbf{F}_{\mathbf{i,cell\ cluster}}|$ is the magnitude of the traction force on the i^{th} pillar attached to the cell cluster (i = 1, 2, 3, …, n); and $|\mathbf{F}_{\mathbf{j,free}}|$ is the magnitude of the 'background' force on the j^{th} free pillar (j = 1, 2, 3, …, m). It should be noted that the 'background' force is not a physical force, rather it is the force-equivalent of noise arising from limitations with centroid detection, which translates to limitations with deflection measurement and thus force measurement. The first post-analysis check involves verifying that the total traction force magnitude is much larger than the total background force magnitude, instead of being comparable. This verifies that the pillars are not too stiff for displacement by the cells.

The second post-analysis check verifies the quasi-steady state assumption. Because the timescale of cell movement is much larger than the timescale of imaging, or even the timescale of cell fixation, a quasi-steady state assumption can be made which states that the cell is stationary and the net force on the cell is zero. Order-of-magnitude calculations show that a 1 nN force imbalance would result in a 10 ng cell accelerating at 100 m/s^2, according to Newton's Second Law of Motion. As a result, the sums of the x- and y-components of the pillar traction forces underneath a cell must ideally each add up to zero. Realistically, due to various imaging and image analysis limitations, it is more reasonable to test that the sums of the x- and y-components of the pillar traction forces underneath a cell must each be below 15% of the total traction force magnitude exerted by the cell. Stricter rules can be applied (10% of total traction force magnitude) if there is sufficient sample size. Cell clusters which do not pass these post-analysis checks were discarded.

4.2.10 Calculation of junction tension and junction stress

Cell clusters with known traction force maps which pass the post-analysis checks, and which have known junction areas, are then used to determine forces and stress at junctions[43,136] (Fig. 4.3B). In cell doublets, there is only one junction to consider. By comparing images of the immunostained cells and the dye-labelled pillars, the traction force from each individual pillar can be assigned to each specific cell, one called the 'cell-of-interest', and the other called the 'rest-of-cluster'. In cell triplets in a linear chain, the cell-of-interest is a cell located at the chain end, such that the cell occupies between 40%-60% of the total cluster area, and the rest-of-cluster comprises the remaining two cells. Cell triplets without a suitable cell-of-interest are discarded.

Since the cell cluster is at rest, under the quasi-steady state assumption, the total traction force underneath the cluster is zero.

$$\sum_{i=1}^{m+n} \boldsymbol{F}_{i,cell\ cluster} = \sum_{j=1}^{m} \boldsymbol{F}_{j,cell-of-interest} + \sum_{k=1}^{n} \boldsymbol{F}_{k,rest-of-cluster} = \mathbf{0} \qquad \ldots (4.5)$$

$$\sum_{j=1}^{m} \boldsymbol{F}_{j,cell-of-interest} = -\sum_{k=1}^{n} \boldsymbol{F}_{k,rest-of-cluster} \qquad \ldots (4.6)$$

where $\mathbf{F}_{\mathbf{i,cell\ cluster}}$ is the traction force on the ith pillar under the cell cluster (i = 1, 2, 3, …, m+n), $\mathbf{F}_{\mathbf{j,cell\text{-}of\text{-}interest}}$ is the traction force on the jth pillar under the cell-of-interest (j = 1, 2, 3, …, m), and $\mathbf{F}_{\mathbf{k,rest\text{-}of\text{-}cluster}}$ is the traction force on the kth pillar under the rest-of-cluster (k = 1, 2, 3, …, n). However, when free-body diagrams are drawn around either the cell-of-interest or rest-of-cluster, the same quasi-steady state assumption permits us to write the following (Fig. 4.3B).

$$\sum_{j=1}^{m} \boldsymbol{F}_{j,cell-of-interest} = -\boldsymbol{F}_{cell-cell,cell-of-interest} \qquad \ldots (4.7)$$

$$\sum_{k=1}^{n} \boldsymbol{F}_{k,rest-of-cluster} = -\boldsymbol{F}_{cell-cell,rest-of-cluster} \qquad \ldots (4.8)$$

$$\boldsymbol{F}_{cell-cell,cell-of-interest} = -\boldsymbol{F}_{cell-cell,rest-of-cluster} \qquad \ldots (4.9)$$

where $\mathbf{F}_{\text{cell-cell,cell-of-interest}}$ is the intercellular tension exerted by the cell-of-interest at the cell junction, and $\mathbf{F}_{\text{cell-cell,rest-of-cluster}}$ is the intercellular tension exerted by the rest-of-cluster at the cell junction.

Thus, to calculate the tension at a cell-cell junction in a given cluster, traction forces underneath the cell-of-interest and rest-of-cluster are summed up to calculate $\mathbf{F}_{\text{cell-cell,cell-of-interest}}$ and $\mathbf{F}_{\text{cell-cell,rest-of-cluster}}$ (Fig. 4.3B). These forces are supposed to be equal and opposite (angle between the forces should be 180°), however due to practical limitations, this is not always true. Thus, two constraints are applied. Firstly, if the magnitudes of the two $\mathbf{F}_{\text{cell-cell}}$ estimates vary by a factor of three or more, the cell cluster is discarded. Secondly, if the smaller angle between the two $\mathbf{F}_{\text{cell-cell}}$ estimates is less than 135°, then also the cell cluster is discarded. In cell clusters which pass these constraints, the junction tension estimate is the average of the two $\mathbf{F}_{\text{cell-cell}}$ estimates. Additionally, knowing the junction area (from immunostaining), the junction stress can be calculated for each specific junction.

$$Stress = \frac{|\boldsymbol{Force}|}{Area} \quad \ldots (4.10)$$

4.2.11 Statistical analysis

As described earlier in this chapter, only one junction is analyzed per acceptable cell cluster. For each junction, the tension, area, and stress are calculated, as required. Further, the total traction force magnitude, number of pillar tips (indicative of cluster area), and traction force per pillar tip are also calculated. Finally, comparisons between conditions are performed by first testing equality of variances by the F-test, followed by Student's one-sided t-test for samples with equal variances

or Welch's one-sided t-test for samples with unequal variances. For all experiments, $\alpha = 0.05$ was chosen for testing statistical significance. All data are reported as mean±S.E.M.

4.3 RESULTS

4.3.1 Thrombin increases tension and stress on endothelial junctions

I studied the impact of the inflammatory mediator thrombin on junction mechanics. HPAECs cultured overnight on fibronectin-stamped mPADs of stiffness 22 nN/μm were treated with 0.9 U/mL human thrombin (Enzyme Research Laboratories) or PBS negative control, for 10 min, after which they were fixed and immunostained (Fig. 4.4A). The total traction force magnitude under each cell cluster was unchanged (Fig. 4.4B), being 2600±200 nN for cells treated with PBS control and 2600±300 nN for cells treated with thrombin ($p = 0.45$). However, there was a drastic reduction in the cell area, as indicated by the reduction in the number of pillars attached to the cell cluster, from 199±8 posts in control cells to 140±10 posts in thrombin-treated cells ($p = 3.0\times10^{-4}$). This resulted in a significant increase in the per-pillar traction force magnitude, which indicates the global cell contractility in the cell cluster, from 8.9±0.5 nN in control cells to 18±1 nN in thrombin-treated cells ($p = 0.0046$).

Thrombin treatment for 10 min also resulted in a slight increase in junction tension (Fig. 4.4C), from 270±20 nN in control cells to 340±30 nN in thrombin-treated cells ($p = 0.043$). However there was a significant decrease in junction area, which decreased from 60±10 μm^2 in control cells to 41±6 μm^2 in thrombin-treated cells ($p = 0.045$). The junction stress increased almost two-fold, from 6±1 $nN/\mu m^2$ in control cells to 10±2 $nN/\mu m^2$ in thrombin-treated cells ($p = 0.040$). These results thus showed that endothelial cell contractility induced by thrombin resulted

in a significant increase in stress at junctions, which could facilitate junction failure and remodeling. Importantly, this result highlights the fact that junctional tension alone is insufficient to fully reveal all of the factors impinging on junction mechanics. In this case, junction area changes resulting from various mechanisms, including possibly thrombin-dependent VE-cadherin internalization, also contribute to the increased stress.

4.3.2 VE-PTP knockout endothelial cells show increased stress at junctions

To study the impact of VE-PTP, which is hypothesized to stabilize VE-cadherin mediated endothelial junctions[158,160], I investigated the impact of knocking out VE-PTP on the interendothelial tension. Either WT or VE-PTP KO mouse lung microvascular endothelial cells (MLECs) were seeded on fibronectin-stamped mPADs of stiffness 22 nN/μm. Quantitative flow cytometry confirmed that the density of VE-cadherin was similar on both cell types, being 95 cadherins/μm^2 for WT MLECs and 81 cadherins/μm^2 for VE-PTP KO MLECs (determined by Vinh Vu). Cells were cultured overnight before fixation and immunostaining (Fig. 4.5A). Cell clusters of WT as well as of VE-PTP KO MLECs showed comparable total traction force magnitudes (Fig. 4.5B) of 1100±100 nN for WT MLECs and 1200±100 nN for VE-PTP KO MLECs ($p = 0.27$). The number of attached pillars per cell cluster was also comparable: 119±9 for WT MLECs and 130±10 for VE-PTP KO MLECs ($p = 0.22$). As a result, the per-pillar traction force magnitude was also comparable, being 8.9±0.5 nN and 8.9±0.4 nN for WT and VE-PTP KO MLECs, respectively ($p = 0.48$).

The junction tension was similar for both cell types (Fig. 4.5C), being 120±10 nN and 140±20 nN for WT and VE-PTP KO MLECs, respectively ($p = 0.22$). However, VE-PTP KO

MLECs suggested a slightly reduced junction area of 49±8 μm^2, relative to 67±8 μm^2 in WT MLECs, although statistical significance could not be established ($p = 0.073$). The junction stress at VE-PTP KO MLEC junctions was thus calculated to be 3.1±0.4 $nN/\mu m^2$, which was higher than the stress at WT MLEC junctions, which was 2.1±0.3 $nN/\mu m^2$ ($p = 0.013$). These results showed that VE-PTP knockout did not affect the traction forces and spread areas, and therefore demonstrated that VE-PTP loss did not affect integrin-mediated tractions at the basal plane. Interestingly, the knockout cells did show increased stress at intercellular junctions, but this appeared to be primarily due to the decrease in junction area.

4.3.3 Endothelial cells on N-cadherin-coated substrates show increased tension at junctions relative to cells on fibronectin

Endothelial cells form homotypic contacts with other endothelial cells via VE-cadherin, and heterotypic contacts with vascular smooth muscle cells and pericytes via N-cadherin[15,157]. To study the impact of N-cadherin adhesion on tension at interendothelial VE-cadherin junctions, HPAECs were seeded on mPADs of stiffness 22 nN/μm tips that were functionalized with either the integrin ligand fibronectin or N-cadherin extracellular domains (referred to as N-cadherin in this text). After overnight culture, the samples were fixed and immunostained (Fig. 4.6A).

Cells attached well to mPAD tips functionalized with fibronectin, primarily as single cells or small clusters. In contrast, cells took significantly longer to adhere to the mPADs functionalized with N-cadherin, and instead remained in suspension and aggregated, such that they formed large enough clusters to settle down and spread on the patterned islands. This was observed by phase contrast microscopy during the initial hours following cell seeding (data not shown). As a result,

the yield of usable cell clusters (doublets or linear triplets) was significantly lower on N-cadherin-coated mPADs than on fibronectin-functionalized mPADs.

Cell clusters on N-cadherin and on fibronectin coated arrays showed comparable total traction force magnitude (Fig. 4.6B): 650±60 nN on fibronectin and 720±80 nN on N-cadherin ($p = 0.23$). The number of attached pillars per cell cluster was also comparable, 190±10 on fibronectin and 193±9 on N-cadherin ($p = 0.43$). The calculated per-pillar traction force magnitude was also comparable, being 3.5±0.2 nN on fibronectin and 3.9±0.6 nN on N-cadherin ($p = 0.26$). However, the calculated tension at junctions between cells on N-cadherin (Fig. 4.6C), 120±10 nN, was significantly higher than that between cells on fibronectin, 86±8 nN ($p = 0.023$). Neither the junction area nor the junction stress could be calculated, as the junction (β-catenin) staining was very diffuse. It should be noted that the forces on fibronectin-functionalized mPADs in this experiment were very different from those determined in the previous negative control experiment, in which cells on fibronectin substrates were treated with thrombin. I attribute this to the HPAECs used in these two different experiments being from different donors and at different passages.

4.4 DISCUSSION

This chapter reports the use of elastomeric cantilever arrays (mPADs), to estimate tension and stress at interendothelial junctions, and to study the impact of chemical perturbations, genetic perturbations, and matrix composition on interendothelial junction mechanics. In this work, I showed that known inflammatory mediators such as thrombin drastically increase endothelial cell contractility and stress at junctions (Fig. 4.4). Such changes may contribute to the failure of endothelial junctions in cell monolayers, and would disrupt the barrier properties of the vascular

endothelium. The vascular endothelial protein tyrosine phosphatase, VE-PTP, is hypothesized to stabilize VE-cadherin adhesions by directly associating with VE-cadherin, and my results show that knocking out VE-PTP increases the stress at endothelial junctions (Fig. 4.5). My results also show that interendothelial junction tension is higher in cell clusters on N-cadherin relative to fibronectin (Fig. 4.6).

A proposed model of endothelial barrier regulation describes a balance between intracellular actomyosin contractile forces, and intercellular adhesive forces[65]. Perturbations to the balance due to increased contractile forces, or destabilization of intercellular adherens junctions, can cause junction failure, leading to paracellular gap formation and increased vascular leakage. In the lung, this results in disruption of the blood-gas barrier and pulmonary edema. Micropillar arrays have been used previously to quantify subcellular traction forces, and also to estimate tension and stress at cell-cell junctions. As a result, micropillar arrays are useful platforms for quantifying the effects of various perturbations on endothelial junctions.

Vasoactive components such as thrombin, histamine, and vascular endothelial growth factor (VEGF) are known to induce cell contractility and to destabilize cell-cell junctions[65]. Thrombin triggers RhoA GTPase signaling in endothelial cells to induce actomyosin contractility[24]. This is known to increase traction forces, reduce the spread area of single cells, and disrupt junctions between endothelial cells[122,136,211]. In their first report demonstrating the use of mPADs to quantify junction tension, Liu, et al.[136] seeded HPAECs on mPADs in bowtie patterns and treated them with thrombin. This treatment resulted in a doubling of the per-pillar traction force, and a reduction in junction area by almost 40%. My results agree with the prior findings (Figs. 4.4B, 4.4C). The prior study reported an eight-fold increase in junction stress upon thrombin treatment, whereas I only observed a two-fold increase. These results can be explained by two

critical differences in the experimental setups. Firstly, Liu, et al.[136] used a bowtie pattern, which restricts the junction area, whereas the neck of the double circle pattern chosen in this work is much wider, permitting the junction area to evolve and adjust naturally between cells on both negative control- and thrombin-treated samples. Secondly, the total bowtie area used by Liu, et al.[136] was 1600 μm^2, which is half the total area of the double circle pattern used in this work. From my measurements of cells in a confluent monolayer, I arrived at an average cell area of 1920±40 μm^2 (n = 75 cells); consequently, cell doublets in the setup described by Liu, et al.[136] were restricted to less than half of the area occupied in a confluent monolayer. The latter conditions could result in low tension at junctions under unstimulated conditions, and a steeper increase in junction tension after thrombin treatment. Regardless of the differences between the two experimental conditions, the general trends of increased contractility, reduced junction area, and increased junction stress are similar in both cases. Increased cell contractility and increased stress at endothelial junctions have also been observed in thrombin-treated endothelial clusters seeded on polyacrylamide gels[122].

I also established the impact of genetic mutations on junction mechanics using mPADs. Specifically, I quantified the effect of VE-PTP on endothelial junction mechanics. VE-PTP associates with VE-cadherin to stabilize cell-cell adhesion, and to regulate phosphorylation state of VE-cadherin[158,160]. The dissociation of VE-PTP from VE-cadherin correlates with increased vascular permeability, and permeability-inducing mediators such as VEGF were shown to trigger this dissociation[158,160]. Conversely, inhibiting the dissociation of VE-PTP and VE-cadherin was shown to restore vascular barrier function[30]. VE-PTP has also been shown to maintain the VE-cadherin phosphorylation state and vascular barrier function independent of its phosphatase activity, whereas absence of VE-PTP was found to result in increased phosphorylation of VE-cadherin[158]. Because VE-cadherin phosphorylation can result in VE-cadherin

internalization[82,147,164,229], one hypothesis was that loss of VE-PTP in the MLECs may promote VE-cadherin internalization, thereby reducing the number of intercellular bonds, and in turn reducing the tension at junctions. However, as reported here, quantitative flow cytometry showed that the VE-cadherin densities on WT and VE-PTP KO MLECs were similar in suspended cells. VE-PTP KO MLECs did show an increase in tension on VE-cadherin complexes, as quantified using a Förster Resonance Energy Transfer (FRET)-based VE-cadherin tension sensor[108,109] (personal communication, Yulia Komarova). However the latter approach does not provide any information about the possible effects of VE-PTP knockout on global cell contractility or basal, integrin-mediated traction forces that could influence interendothelial mechanics. Further, although the junction area can be calculated from the FRET images, it is not possible to calculate the total tension at the junctions, especially considering the limited dynamic range (< 6 pN) of the FRET-based sensors[46]. My results show that knocking out VE-PTP did not cause any significant changes in per-pillar traction forces, indicating that focal-adhesion based tractions were unaffected. Nevertheless, different from the proposed hypothesis but consistent with the FRET experiment, the VE-PTP knockout cells did exhibit increased junction stress (Figs. 4.5B, 5C). The latter was not due to an overall increase in junction tension, but to the reduction in junction area. These results instead suggest that the differences may be due to biochemical processes that regulate the junction area, such as cytoskeletal remodeling.

Lastly, I also performed preliminary studies suggesting that the specific cell surface receptors enabling endothelial cell attachment to substrates, can regulate endothelial junction tension. Endothelial cells *in vivo* can form adhesions with other endothelial cells *via* VE-cadherin, or with matrix proteins such as collagen or fibronectin *via* integrins, or with vascular smooth muscle cells and pericytes *via* N-cadherin[15,157]. The goal of these studies was to determine whether

adhesion to basal N-cadherin could potentially regulate the interendothelial barrier. Results indicated that that the tension between endothelial cells was higher on N-cadherin coated pillars relative to fibronectin, although the cell contractility was not significantly affected, as suggested by the per-pillar traction forces (Figs. 4.6B, 4.6C). This finding suggests that the increased tension on the junctions was not due simply to a redistribution of contractile forces from integrins at the basal plane to cell-cell junctions. This is intriguing, in light of the fact that cells exert similar forces on the pillars, even though they did not initially adhere well to the N-cadherin-coated arrays. Cells were previously shown to sense pillar rigidity through N-cadherin receptors[124]. In addition, prior studies suggested that N-cadherin ligation activates RhoA, which would in turn increase cell contractility and likely increase cell tension[194].

Although the results with N-cadherin coated pillars might suggest the differential regulation of endothelial junction tension by receptor-specific signaling, it should be noted that the micropillar tip functionalization techniques used for fibronectin and N-cadherin were distinct, and the results could also reflect differences in the densities of active receptors, for example. It would be challenging to quantify ligand densities on the micropillar tips, as well as the number of receptor-ligand bonds. Differences in bond density, for example, could also lead to different signal amplitudes. Further studies would be required to identify the basis of the observed differences.

In summary, these results demonstrate that mPADs are a versatile platform for estimating endothelial junction tension and stress, and the effects of biochemical, genetic, and matrix dependent perturbations on those parameters. Although not addressed in this work, varying the height of the micropillars would also tune the matrix stiffness, permitting the investigation of stiffness effects on mechanical forces at endothelial junctions. By providing traction forces and enabling calculation of the actual mechanical tension and stress at the junctions, mPADs provide

significantly more information than biomolecular approaches, such as FRET-based tension sensors, which have a limited dynamic range and only report the tension-dependent conformation of the individual sensor molecules. The simultaneous quantification of basal traction forces and junction areas provides deeper insight into cellular changes that contributes to changes in junction tension and stress. There are also other technical advantages, e.g. transfected cells expressing fusion proteins with fluorescent reporters can be seeded on mPADs, instead of cotransfecting with FRET-based tension sensors, which is challenging from the perspectives of gene delivery as well as spectral overlap for fluorescence imaging. Although not performed in this work, quantitative immunofluorescence can also yield the integrated density of the fluorescence signal at the junctions, in order to quantify the total amount of VE-cadherin or β-catenin at the junctions, instead of merely calculating the junction area. Thus, in this work I used mPADs to explore how different factors implicated in the regulation of endothelial barrier integrity alter both junction tension and junction stresses in ways that might affect barrier function.

4.5 FIGURES

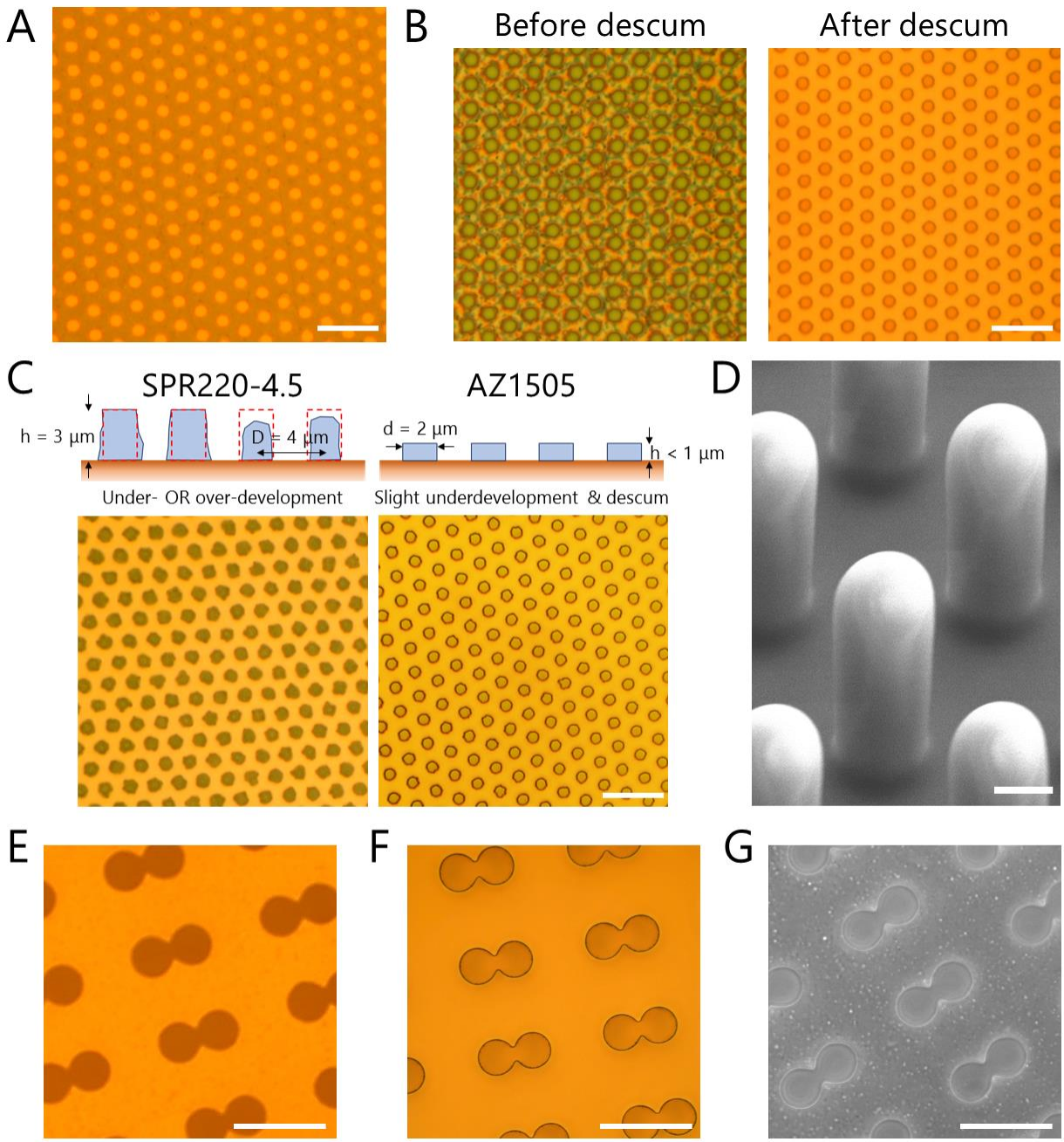

Fig. 4.1: Photolithography for mPAD and stamp fabrication. (A) Clearfield photomask for patterning arrays of circles with a positive photoresist. Diameter of each circle is 2 µm and center-to-center spacing is 4 µm. (B) Spin-coating of HMDS as an adhesion promoter prevents complete development of positive photoresist, leaving behind a layer of 'scum'. Oxygen plasma can be used to descum the slightly underdeveloped wafer, leaving behind a clean array of spots. (C) Positive photoresists show poor tolerance of high aspect ratio structures, leading to overdevelopment or underdevelopment. As a result, the positive resist SPR220-4.5, which can be spun down to a film

Fig. 4.1 (contd.): thickness of 3 μm, did not result in sharp outlines in 2 μm diameter spots. In the side-view schematic, brown gradient represents the wafer, blue represents the photoresist, and red dashed outline reflects desired profile. The positive resist AZ1505, which can be spun down to a film thickness of <1 μm, could be developed with more control and showed sharp outlines for circular spots after descumming. Scale bars for A, B, C are 10 μm. (D) SEM image of PDMS micropillar arrays (mPADs #4) sputtered with gold. Diameter of the micropillars is 2 μm, height is approximately 5.7 μm, resulting in a spring constant of 22 nN/μm. Scale bar is approximately 1 μm. (E) Clearfield photomask for patterning touching circles of area 1600 μm^2 each, with a negative photoresist. (F) Developed wafer showing arrays of touching circles, in a film of KMPR 1010. This is a negative mold, casting PDMS on this mold leads to arrays of raised touching circles. (G) Microscope image of PDMS stamp comprising of arrays of raised touching circles. Scale bars for E, F, G are 100 μm.

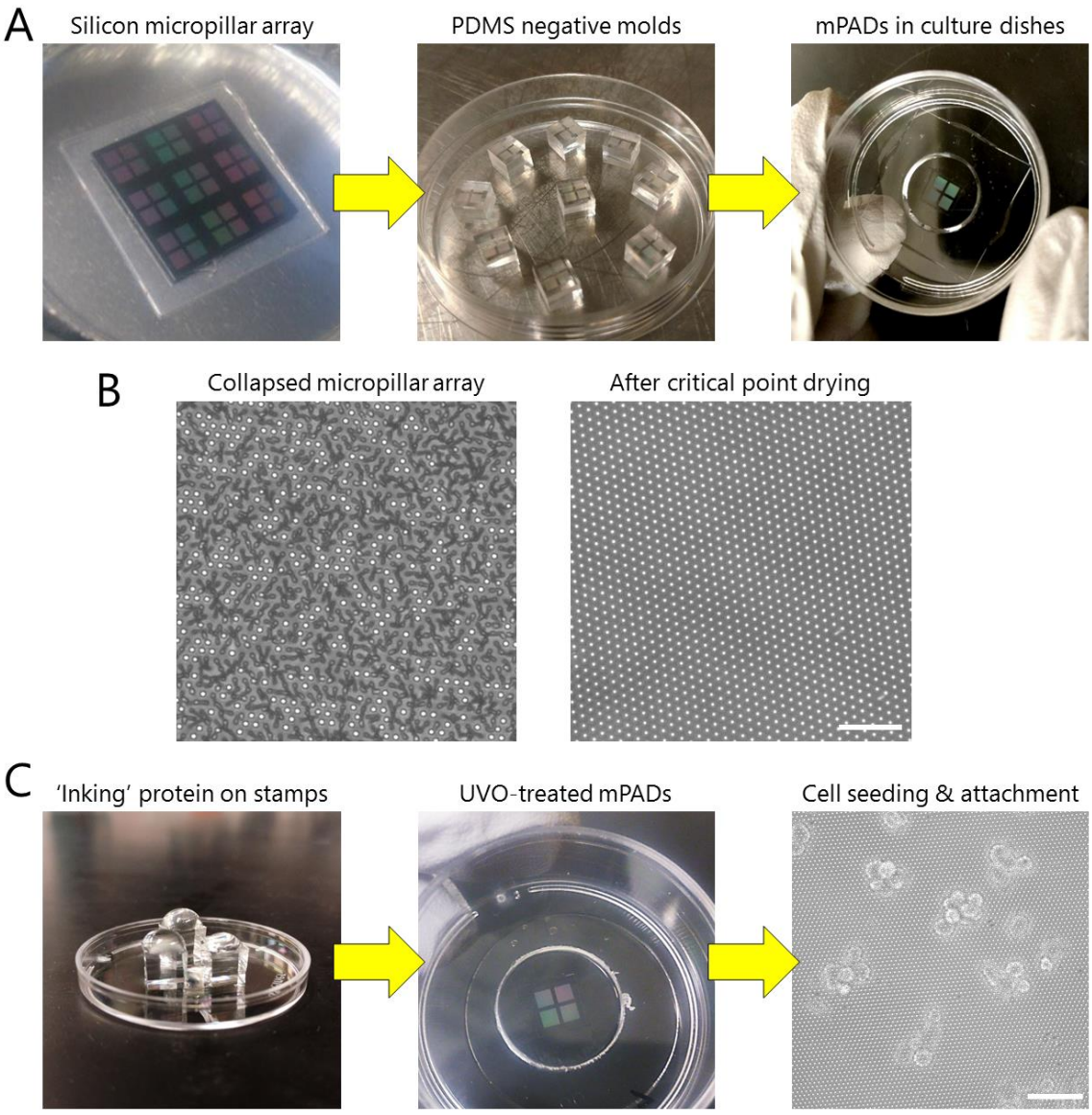

Fig. 4.2: mPAD molding and functionalization. (A) PDMS negative molds are cast from the silicon master with etched micropillar arrays. Negative molds are then used to cast PDMS micropillars on coverslips, which after further processing can be mounted on dishes for cell culture. (B) Microscope images show a collapsed micropillar array and an 'ideal' micropillar array. Immediately after peeling negative molds from cast mPADs on coverslips, the mPADs are typically collapsed due to Van der Waals forces – the tips of neighboring pillars contact each other. Critical point drying yields dry substrates with vertical micropillars. There may be occasional collapsed microposts as shown, which should not significantly impact yield. Scale bar is 25 μm. (C) To functionalize mPADs, the protein of choice is physisorbed to stamps, then the stamps are dried off. mPAD tips are activated by UVO, then the stamps are gently pressed against the mPADs. After dye labeling and blocking non-specific cell attachment, cells can be seeded on the mPADs. The microscope image shows cell clusters shortly after seeding, specifically attached to stamped pillar tips. Scale bar is 50 μm.

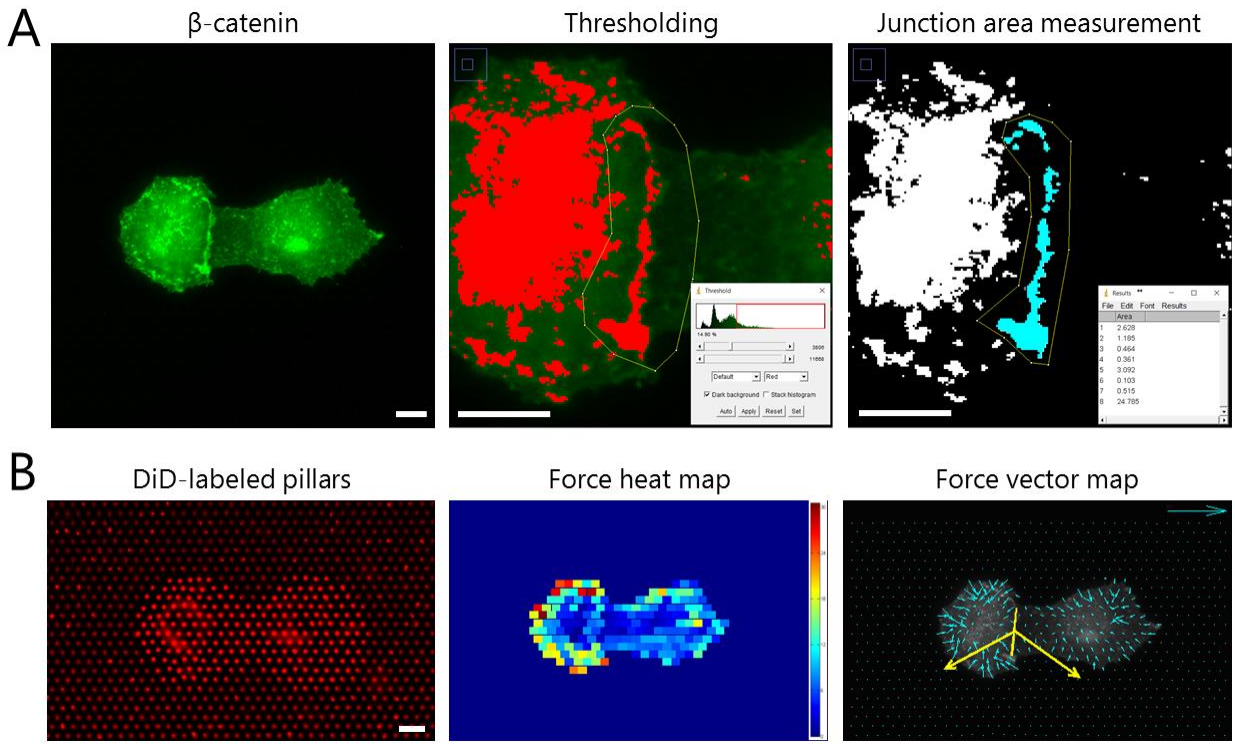

Fig. 4.3: Cell junction area and force analysis. (A) Junction area is quantified by loosely drawing an outline around the junction, excluding most of the cytosolic staining, and thresholding the brightest 15% of pixels. Once thresholded, specific areas corresponding to the junction are selected and the area quantified using the Analyze Particles function in ImageJ. (B) Deflections of micropillar positions can be calculated and converted to a traction force map using a custom MATLAB program. Using the traction force map and free body mechanics, junction tension can be estimated. Scale bars are 10 μm. Color bar is 0 to 30 nN. Scale arrow is 100 nN.

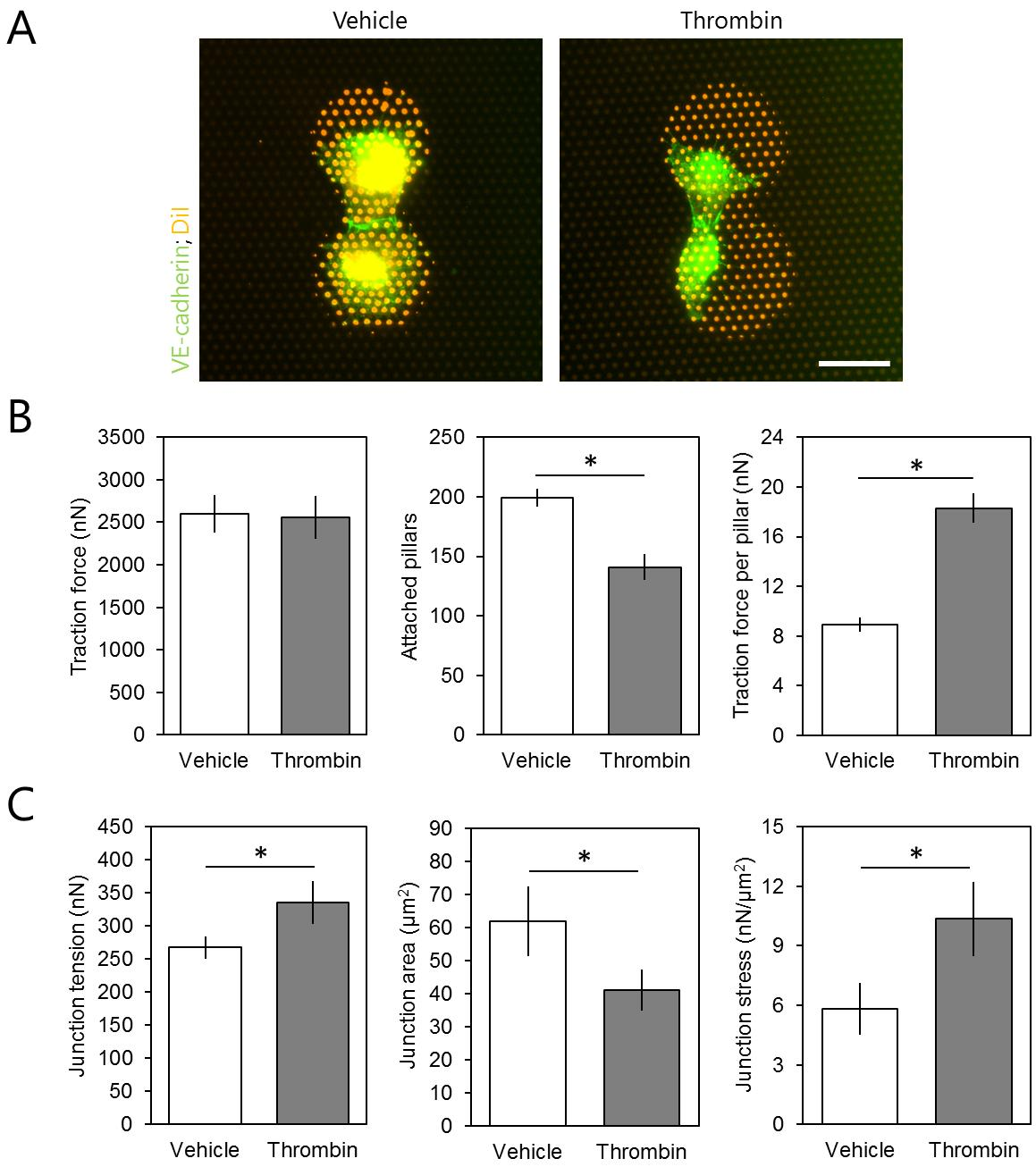

Fig. 4.4: Thrombin induces increased junction tension and stress in endothelial cells. (A) Representative images of HPAECs on mPADs of stiffness 22 nN/μm, treated with vehicle (negative control) or 0.9 U/mL thrombin for 10 min. Scale bar is 25 μm. (B) Total traction force underneath the endothelial cell cluster, number of pillars attached, and traction force per attached pillar, upon treatment with vehicle or 0.9 U/mL thrombin for 10 min. (C) Junction tension, area, and stress, upon treatment with vehicle or 0.9 U/mL thrombin for 10 min. n = 9 clusters (3 doublets, 6 linear triplets) for vehicle. n = 12 clusters (6 doublets, 6 linear triplets) for thrombin. Only one junction analyzed per cluster. * represents $p < 0.05$.

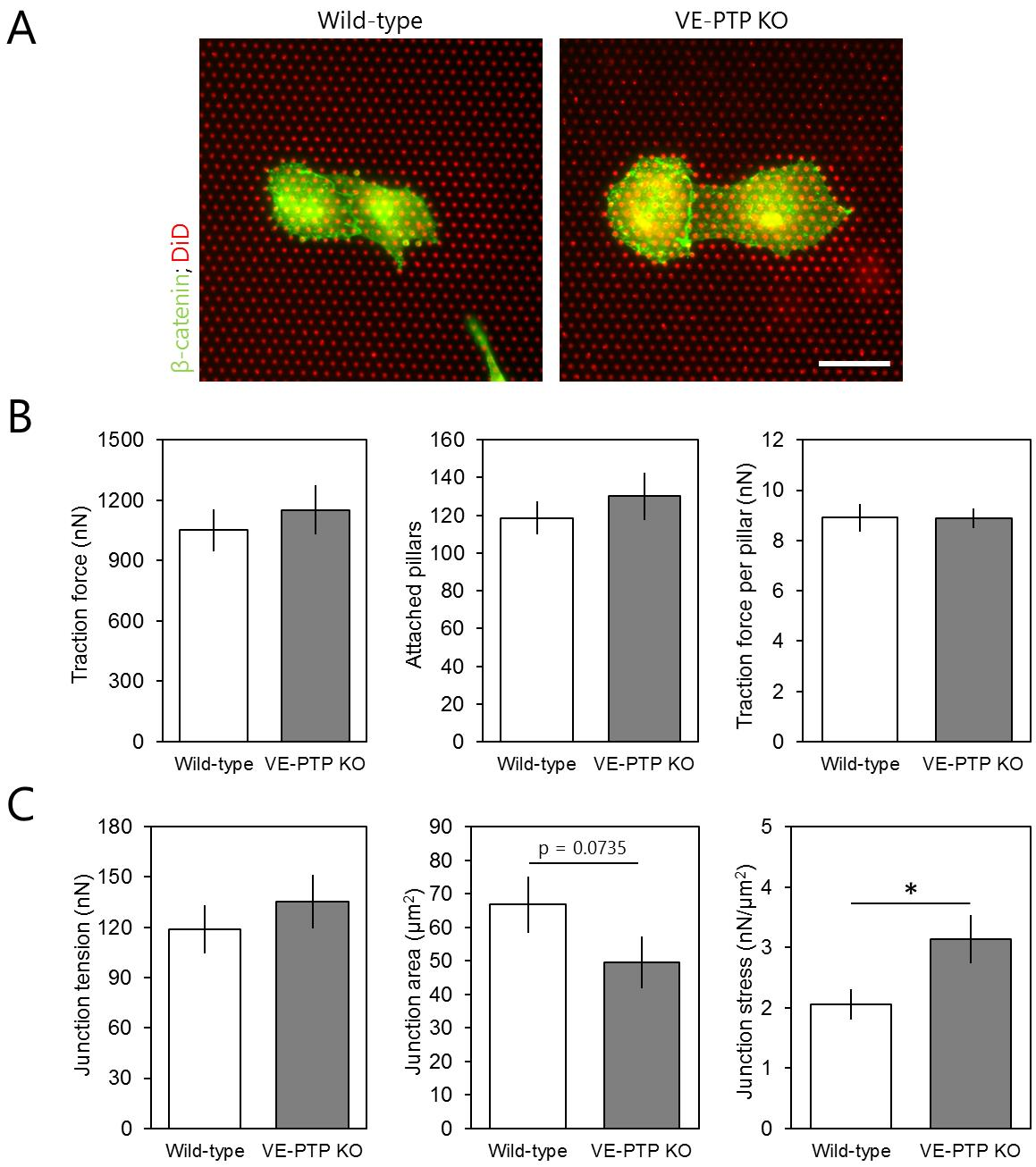

Fig. 4.5: VE-PTP knockout endothelial cells show increased stress at junctions. (A) Representative images of MLECs on mPADs of stiffness 22 nN/μm, wild-type or VE-PTP knockout. Scale bar is 25 μm. (B) Total traction force underneath the endothelial cell cluster, number of pillars attached, and traction force per attached pillar, in wild-type or VE-PTP KO MLECs. (C) Junction tension, area, and stress, in wild-type or VE-PTP KO MLECs. n = 14 clusters (13 doublets, 1 linear triplet) for wild-type MLECs from 3 dishes. n = 12 clusters (10 doublets, 2 linear triplets) for VE-PTP KO MLECs from 2 dishes. Only one junction analyzed per cluster. * represents $p < 0.05$.

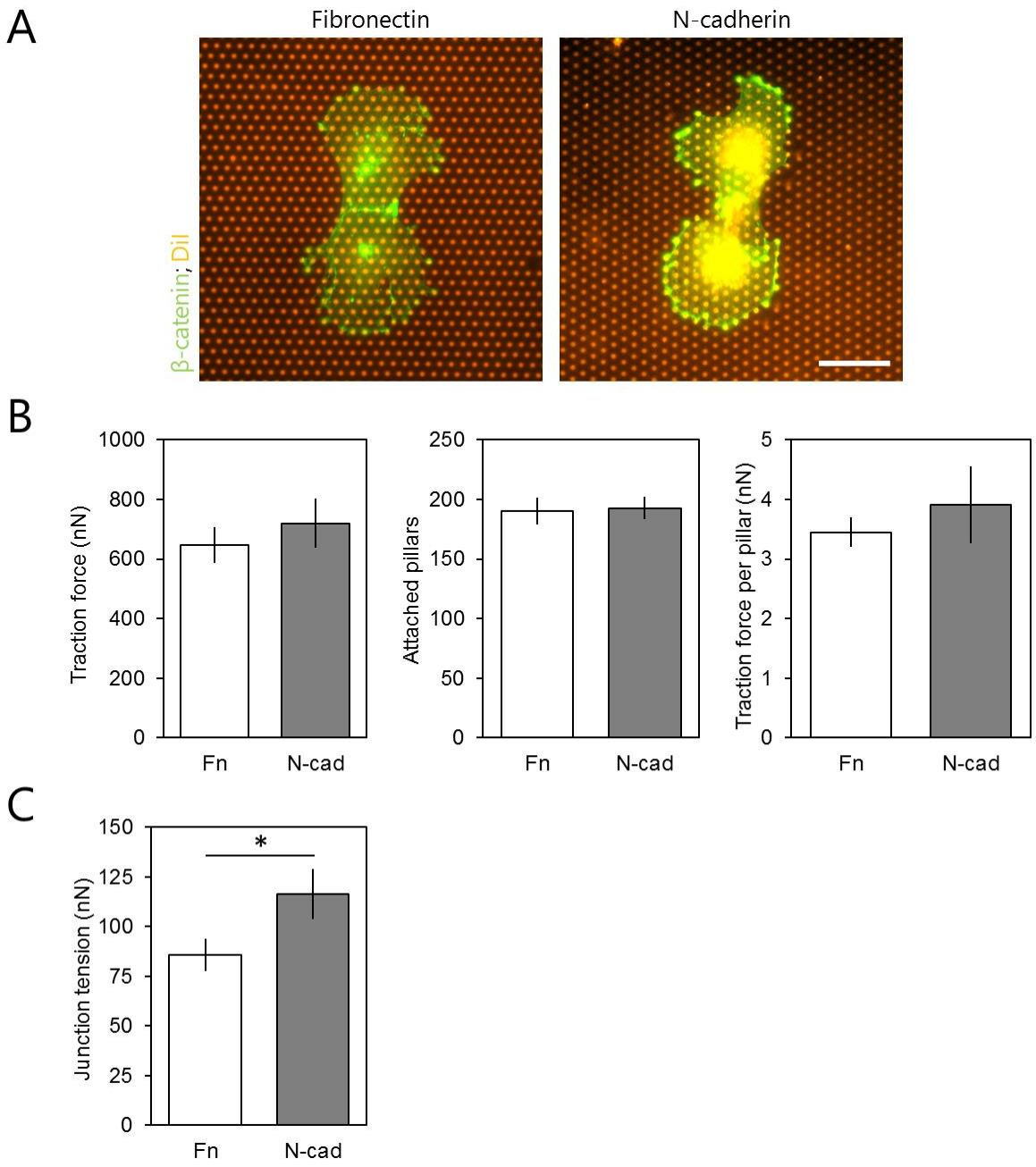

Fig. 4.6: Endothelial cells on N-cadherin show increased junction tension, relative to fibronectin. (A) Representative images of HPAECs on mPADs of stiffness 22 nN/μm, fibronectin or N-cadherin as ECM. Scale bar is 25 μm. (B) Total traction force underneath the endothelial cell cluster, number of pillars attached, and traction force per attached pillar, on fibronectin or N-cadherin. (C) Junction tension, on fibronectin or N-cadherin. Junction area could not be reliably calculated as staining was too diffuse, preventing thresholding. n = 13 clusters (10 doublets, 3 linear triplets) for fibronectin from 2 dishes. n = 9 clusters (7 doublets, 2 linear triplets) for N-cadherin from 3 dishes. Only one junction analyzed per cluster. * represents $p < 0.05$.

4.6 TABLE

Table 4.1: Silicon mPAD masters from Jianping Fu (University of Michigan, Ann Arbor), their nominal heights, and nominal stiffnesses of resulting elastomeric mPADs as reported by them. All mPAD masters are hexagonal close packed micropillar arrays, with nominal pillar diameters of 2 μm, and center-to-center spacing of 4 μm.

mPAD number	Nominal pillar height (μm)	Nominal pillar stiffness (nN/μm)
3	5.0	33
4	5.7	22
5	6.1	18
7	7.1	11
9	8.3	7
11	10.3	4

Chapter 5: Towards an *in vitro* model of the human airway subjected to nanoparticle exposure

5.1 INTRODUCTION

The pulmonary blood-gas barrier facilitates the exchange of oxygen and carbon dioxide between the blood stream and atmosphere, across epithelial and endothelial tissue. The pulmonary epithelium is in contact with air, exhibits a polarized phenotype, and richly differentiated into different cell types based on the position along the respiratory tree[78]. For example, the bronchial epithelium and small airway epithelium consist primarily of goblet cells, which secrete mucins; ciliated cells, each of which possess ~250 cilia beating at approximately 1000 times per minute; club cells, which secrete CC10 protein; and basal cells, which express cytokeratin 19, retain differentiation potential, and aid in wound repair[17,28,181]. Meanwhile, alveolar epithelial cells consist primarily of two cell types, named alveolar epithelial cells type 1 (AE1 or AT1), which comprise most of the alveolar surface area, facilitate gas diffusion, and maintain ion and fluid homeostasis; and alveolar epithelial cells type 2 (AE2 or AT2), which secrete surfactant, retain differentiation potential and perform wound repair[71,73,107]. Because the pulmonary epithelium is in contact with air, it is among the first lines of defense against airborne pathogens and particulate matter[78].

Airborne nanoparticles, in particular, have received attention in recent years, with the increased use of engineered nanoparticles (NPs) in various applications such as cosmetics[174,224] and therapeutics[26,177], in addition to the concern regarding NPs in ambient air as pollutants[151,168]. Inhaled nanoparticles can cross the blood-gas barrier, can have a residence time of days to weeks

in the body, and can even accumulate in specific organs[9,76,80,151]. Efforts are thus underway to develop *in vitro* organ-on-chip models that can replicate the *in vivo* blood-gas barrier, and thus avoid the use of expensive animal models while at the same time enabling easier visualization of cellular responses and nanoparticle transport[17,98,104]. Gold nanoparticles have been extensively used to probe cellular responses to NP exposure, because the inertness of bulk gold ensures that cellular responses reflect the tested size, shape, concentration, and surface chemistry, rather than the core particle chemistry[3,62,154]. Additionally, the plasmonic properties of gold NPs provide an excellent opportunity for visualizing intracellular particle localization and trafficking[3,62,154].

Previous studies have shown the benefits of using differentiated air-liquid interface (ALI) cultures, instead of submerged cultures, for nanoparticle treatment of airway epithelial cells. Air-liquid interface cultures of airway epithelial cells are grown on porous transwell membranes, exposed to air at the apical surface, and cell culture medium at the basal surface, mimicking the physiological environment of these cells. In particular, airway epithelial cells differentiated at the air-liquid interface display higher transepithelial electrical resistance (TEER), which is an indicator of barrier function[48]. Further, airway epithelial cells differentiated at the air-liquid interface show different responses to particulate matter, relative to cells cultured under submerged conditions – although the responses are heavily dependent on cell type, time spent at ALI, method of particle delivery, and particulate size, ranging from microscopic to nanoscopic[81,217]. Assays chosen to study the effects of particle treatment include cytotoxicity assays such as lactate dehydrogenase assay (LDH assay; quantification of cell membrane integrity) and 3-(4,5-dimethylthiazol-2-yl)-2,5-diphenyltetrazolium bromide assay (MTT assay; quantification of cell metabolic activity)[93,106,150,217,230]. RT-PCR quantifies messenger RNA (mRNA) levels of inflammatory and oxidative stress markers such as IL-6, IL-8, HOX1, and COX2[27,81,93,128,217].

Enzyme-linked immunosorbent assays (ELISA) are used to quantify soluble inflammatory markers[27,93,106]. Electron microscopy visualizes and verifies particle uptake and transport[27,93]. Dye-based assays enable quantification of reactive oxygen species generation[106,188,190,230]. Additionally, immunofluorescence is used to visualize differentiation markers and actin[27,93,188,190].

Further in cells cultured at the air-liquid interface, delivery of NPs by aerosolization or by electrostatic precipitation has been found to elicit different cellular responses, relative to NP delivery in solution. Volckens, et al.[217] quantified mRNA expression of IL-8, HOX1, and COX2 in undifferentiated primary cells exposed to coarse atmospheric particulate matter (diameter 2.5 – 10 μm) in solution, and demonstrated a dose-response relationship with cells cultured under submerged conditions. However when they delivered the same coarse particulate matter by electrostatic precipitation to cells cultured at the air-liquid interface, the same fold increase in mRNA expression could be observed with a particulate mass loading that was an order lower than used for solution exposure[217]. This result suggested that cells at the ALI were more sensitive to particulate matter. This observation was confirmed by Lenz, et al.[128], who used zinc oxide nanoparticles either aerosolized onto immortalized cells at the air-liquid interface, or added in solution onto submerged cells. Lenz, et al.[128] reported that mRNA levels of inflammatory markers (IL-6, IL-8, GM-CSF) and oxidative stress markers (HOX1, SOD2, GCS) in submerged cells exposed to nanoparticles in solution was generally significantly lower than the levels in airlifted cells exposed to aerosolized nanoparticles for the same duration[128].

Contrary to above reports, Ghio, et al.[81] found that airlifted cells were less sensitive to atmospheric particulate matter treatment (diameters, $d < 0.1$ μm, $d = 0.1 – 2.5$ μm, $d = 2.5 – 10$ μm) than submerged cells, as quantified by mRNA levels of inflammatory and oxidative stress markers. This difference was observed with differentiated primary airway epithelial cells as well

as with immortalized airway epithelial cells. They were able to successfully show, by culturing cells in normal and hypoxic conditions, that the increased accessibility to oxygen at the air-liquid interface played a significant role in reducing the sensitivity to particulate treatment.

Although there is evidence for both increased and decreased sensitivity of airlifted airway epithelial cultures to NP treatment, relative to submerged cultures, there is a general consensus that airlifted cultures do exhibit different responses compared to submerged cultures. At the same time, there is also evidence of signaling between epithelial and endothelial cells in transwell co-cultures of the two different cell types, which physically separate the two cell types by means of a porous membrane, while enabling exchange of soluble factors. Hermanns, Unger, et al.[92] first established a co-culture on opposite sides of a transwell membrane using the immortalized epithelial cell line, NCI H441, and primary human pulmonary microvascular endothelial cells (HPMECs). These immortalized epithelial cells could not differentiate to form tight junctions, and thus were not cultured at the air-liquid interface. However, dexamethasone was used to induce tight junction formation in the epithelial cells, and consequently increased electrical resistance across the monocultures and co-cultures. Because NCI H441 cells express several of the characteristic markers of primary alveolar type 2 epithelial cells, this was the first co-culture model to mimic the physiological pulmonary epithelial-endothelial barrier, although the epithelial cells were cultured under submerged conditions. Hermanns, Fuchs, et al.[91] later established a second co-culture model, replacing immortalized NCI H441 epithelial cells with primary alveolar type 2 epithelial cells, which differentiate into alveolar type 1 cells and express their respective characteristic markers even in submerged culture. Using this submerged co-culture, they successfully demonstrated communication between the endothelial and epithelial cell types, as

treating endothelial cells on the basal side of the membrane with TNF-α led to an increase in the epithelial expression levels of the interleukin IL-8.

A few studies have treated epithelial-endothelial co-cultures with particulates and further demonstrated communication between the cell types. Snyder-Talkington, et al.[190] used SAECs in a distal co-culture with human microvascular endothelial cells (HMVECs), under submerged conditions. When the apical epithelial cells were treated with multi-walled carbon nanotubes (MWCNTs) in solution, VE-cadherin immunostaining showed disruption of endothelial junctions, despite the fact that the MWCNTs neither directly contacted endothelial cells nor passed through the transwell membranes, as visualized by transmission electron microscopy of the endothelial cells on the basal side of the membrane. This report showed that MWCNT treatment of SAEC monocultures resulted in increased expression of the known endothelial inflammatory mediator vascular endothelial growth factor A (VEGFA), whereas treatment of HMVEC monocultures did not show any such increase. MWCNT treatment of the co-cultures showed the same increase in VEGFA expression, along with increases in soluble intercellular adhesion molecule-1 (ICAM-1 or CD54) and soluble vascular cell adhesion molecule-1 (VCAM-1 or CD106), which were likely responsible for endothelial disruption. MWCNT treatment of SAECs in this co-culture model also induced reactive oxygen species production in HMVECs, as quantified by the dye dihydroethidium (DHE). Sisler, et al.[188] used the same co-culture model with printer-emitted particles (PEPs), performed similar studies, and reported very similar results.

These reports revealed important design criteria for building models of airway epithelial cultures: namely, i) differentiated epithelia behave differently from undifferentiated epithelia, ii) nanoparticle exposure at the air-liquid interface induces different responses in epithelia relative to exposure in solution, iii) epithelial-endothelial co-cultures can replicate communication between

the two different cell types, and iv) treatment of epithelial cells with NP in solution triggers epithelial cell responses that affect the endothelial barrier. These reports thus demonstrate the requirement of a co-culture model to mimic the physiological blood-gas barrier. Establishment of this *in vitro* blood-gas barrier would enable us to model the physiological *in vivo* effects of inhaled airborne NPs.

To replicate the polarization and mucociliary differentiation of the pulmonary epithelium *in vivo*, primary airway epithelial cells are typically cultured at the air-liquid interface (ALI) in the apical chambers of transwells, after removing the medium from the apical chambers, a process known as 'airlift'. However, my goal was to mimic the environment of the lung, particularly the blood-gas barrier, where airway epithelial and endothelial cells are in close contact[28,112], exchange growth factors and cytokines, and enable signaling between the two tissues. An additional goal was to enable aerosolized NPs to settle on the airway epithelial cells at the air-liquid interface on the apical surface of the transwells, in order to study such physiological responses as endothelial monolayer integrity, blood-gas barrier permeability, and NP trafficking across the barrier.

Although there are established protocols for differentiating primary airway epithelial cells at the air-liquid interface[48,181], I needed to establish a co-culture model with endothelial cells. One approach reported by various groups is to culture the endothelial cells in the basal chamber of the transwell and the airway epithelial cells in the apical chamber[190,219] ('distal co-culture', Fig. 5.1A). This approach does not mimic the proximity of the endothelial and epithelial tissues seen *in vivo*, and thus cannot accurately replicate the blood-gas barrier. Another commonly reported approach involves seeding endothelial and airway epithelial cells on opposite sides of an approximately 10 μm thick transwell membrane[91,92,110,118,219] ('proximal co-culture', Fig. 5.1A). Although the distance between the cell types is still significantly higher than *in vivo*, this model is a significant

improvement over the former. However, various previous reports of the latter models either used immortalized cell lines, did not perform airlift and ALI exposure, or performed ALI exposure for very few days (under 5 days), which is insufficient for complete mucociliary differentiation[48,181].

In this work, I established a differentiated airway epithelial-endothelial co-culture model, cultured at the air-liquid interface. The epithelium and endothelium were cultured on opposite sides of a porous transwell membrane. This configuration enables studies of barrier function, signaling between the two cell types, and nanoparticle transport across the barrier. Because the epithelium is at the air-liquid interface, NP can be delivered by aerosolization, and the expression of mucins and other secreted proteins replicate some aspects of protein-nanoparticle interactions before the NPs contact the cells. This well-differentiated macroscale transwell co-culture model also forms the basis for the establishment of well-differentiated co-culture models in microfluidic devices, such as an airway-on-a-chip. I also performed initial evaluations of the cytotoxicity caused by exposure of submerged pulmonary epithelial and endothelial cells to gold nanoparticles in solution. These results provide a basis for future studies of the impact of aerosolized NPs on model airway cultures.

5.2 MATERIALS AND METHODS

5.2.1 Cell culture and reagents

Primary human pulmonary artery endothelial cells (HPAECs, Lonza) were cultured in complete endothelial cell growth medium EGM-2 (Lonza) with 10% (v/v) fetal bovine serum (FBS, Sigma) in a humidified incubator at 37°C with 5% CO_2, and passaged every 3 days. HPAECs between passages 7-9 were used for experiments.

Primary small airway epithelial cells (SAECs, Lonza) were cultured in complete small airway growth medium SAGM (Lonza), in an incubator as described above. This medium is serum-free and any serum used to neutralize trypsin during passaging was removed by centrifugation and washing cells with PBS before replating. Cells at passages 3 and 4 were used for differentiation experiments, and cells at passages 4 and 5 were used for metabolic activity measurements.

5.2.2 Lung epithelial-endothelial co-culture and differentiation

In order to establish a co-culture model with endothelial cells, which also showed mucociliary differentiation and a polarized phenotype, I adopted the general protocol described below. Several aspects of the protocol needed to be modified over time, while troubleshooting the protocol in order to obtain the desired differentiation phenotype. Each variation of the general protocol is detailed in this section as well, and the outcome of each variation is described in the Results section.

The general protocol for the co-culture model is as follows. Transwell membranes were inverted and the basal sides of the transwells were incubated with 20 μg/mL fibronectin (Millipore) for 30 min. HPAECs suspended in EGM-2 were then seeded on the fibronectin-coated basal sides of the transwells. After 1 h, HPAECs were typically attached and well-spread on fibronectin. At this stage, the transwells were put back in their original upright orientation, such that the HPAECs on the basal sides of the membrane were submerged in the basal chambers with EGM-2 (10% FBS). The apical sides of the transwells were kept dry. After overnight culture, the apical sides of the transwell membranes were incubated with 30 μg/mL rat tail collagen-I (Sigma) for 30 min.

SAECs suspended in SAGM were then seeded on the apical sides of the transwell membranes, and allowed to attach and spread over 6 h. Then, the medium in the apical and basal chambers was replaced with a solution of equal parts epithelial medium and endothelial medium by volume ('mixed medium'; see the medium composition for each variation in subsequent paragraphs). Transwells were typically incubated 3-7 days, with the cells cultured in submerged conditions until the SAECs reached confluence. Upon achieving confluence, the 'airlift' procedure was performed on the SAECs, by aspirating medium from the apical chambers, thus leaving the SAECs exposed to air (Fig. 5.1A). Fresh medium was also added to the basal chambers and the plate was maintained in an incubator at 37°C under 5% CO_2. Over the next 3-4 weeks, both apical and basal chambers were rinsed with PBS, and fresh medium was added to the basal chambers every other day. Finally, the cells were fixed with warm 1% paraformaldehyde for 15 min, for immunostaining to assess differentiation. This general protocol could be modified for SAEC monoculture models, by directly seeding SAECs on the collagen-I coated apical sides of transwells.

The initial experiments, performed with 'Variation 1' of the general protocol, were time course experiments to study the expression of differentiation markers over time, for monoculture as well as proximal co-culture models (Fig. 5.1A, Table 5.1, conditions 1 and 4). Variation 1 used polycarbonate transwells (Corning, #3401) with a pore size of 0.4 μm, pore density of 1×10^8 pores/cm^2, and a membrane diameter of 12 mm. The working volume is 0.5 mL for the apical chamber and 1.5 mL for the basal chamber. Next, 50,000 HPAECs and 80,000 SAECs were seeded on each membrane. SAECs were used at passage 4. The polycarbonate membranes are translucent, and did not permit clear visualization of SAEC confluence, which was a drawback. As a precaution, SAECs were maintained in submerged culture for 7 days prior to airlift. The epithelial medium while submerged was S-ALI Growth Medium (S-ALI GM, Lonza). During ALI culture

the epithelial medium consisted of S-ALI Differentiation Medium with the added inducer (S-ALI DM, Lonza) and was used according to manufacturer's protocols, for the monoculture models. For the co-culture models, as described above, a 'mixed medium' was formulated by mixing the appropriate epithelial medium with the endothelial medium, i.e. EGM-2 with 10% FBS, in a 1:1 ratio by volume. It should be noted that there was medium leakage from basal to apical chambers during ALI culture, primarily in monoculture models, but also to a lesser extent in co-culture models. As a result, medium in the basal chamber was reduced to 1 mL during ALI culture, and the leaked medium was pipetted away from the apical chamber every day.

All subsequent experiments were performed to troubleshoot the poor membrane coverage in the monocultures, and the almost non-existent mucociliary differentiation in the co-cultures when using the above conditions, as described in the Results section. The time in ALI culture was fixed at 21 days, which was when the largest number of ciliated cells was seen in monocultures in the above experiments. 'Variation 2' considered four possible conditions (Table 5.1, conditions 1-4). The first condition used a monoculture condition, which was the same as Variation 1. The second condition used SAEC monocultures in mixed medium, instead of in purely epithelial medium. The latter condition tested whether the endothelial growth factors in the mixed medium were responsible for poor SAEC differentiation in co-cultures. The third condition consisted of distal co-cultures in mixed medium, such that HPAECs were cultured in the basal chamber instead of on the basal side of the membrane (Fig. 5.1A). For this condition, 1×10^5 HPAECs were seeded, due to the larger culture area. This scenario tested whether secretory factors from the endothelial cells were responsible for poor SAEC differentiation in co-culture. Finally, the fourth condition consisted of proximal co-cultures on opposite sides of the transwell filter in mixed medium, as described in the general protocol and in Variation 1. In this scenario, HPAECs and SAECs were

on the opposite sides of the same transwell membrane. This condition tested whether the barrier function of the endothelial cells prevented essential nutrients and growth factors from reaching the SAECs, and thus causing poor SAEC differentiation. It should be noted here than in Variation 2 and future transwell experiments, the concentration of FBS in the endothelial medium was reduced from 10% to 2%, such that the final 'mixed medium' had only 1% FBS (reduced from 5% in Variation 1). Because FBS does not have a well-defined composition and may contain unknown factors that could hinder epithelial differentiation, the reduction in FBS was expected to benefit differentiation.

'Variation 3' of the general protocol tested whether SAECs at earlier passages (passage 3 instead of passage 4) showed better differentiation and membrane coverage in monoculture, when using purely epithelial medium as described in Variation 1 or for the first condition in Variation 2 (Table 5.1, condition 1). Thus, the transwells and their working volumes of medium, SAEC seeding protocol, airlift, and the epithelial medium used with submerged and ALI cultures are exactly as described in Variation 1, except for the ALI culture duration, which was fixed at 21 days.

'Variation 4' of the general protocol incorporated major changes, in order to troubleshoot the challenges associated with achieving SAEC monoculture confluence issues and with SAEC co-culture differentiation. Firstly, Variation 4 used polyester transwell membranes (Corning, #3470) with pore sizes of 0.4 μm, a pore density of 4×10^6 pores/cm^2, and a 6.5 mm membrane diameter. Polyester membranes are transparent and enable visualization of SAEC confluence. Further, the pore density is lower by a factor of 25 relative to previous polycarbonate transwell membranes, which could help reduce leakage from the basal chamber during ALI culture. Indeed in these experiments, leakage was completely abolished. The reduced membrane diameter meant

that SAEC cells could be seeded at higher density, which aids differentiation[153,200]. Thus, in Variation 4, the HPAEC cell count during seeding was reduced significantly to 20,000 cells, but the SAEC cell count during seeding was reduced only slightly to 50,000 cells. The working volumes of the apical and basal chambers were 100 μL and 500 μL, respectively. Secondly, SAECs were seeded at passage 3, as described in Variation 3. Thirdly, the epithelial medium for submerged culture was changed to SAGM, and ALI culture was changed to Pneumacult ALI (Stemcell Technologies) supplemented as recommended by the manufacturer. As described earlier, the time spent in the ALI culture was maintained at 21 days, and the endothelial medium used in these experiments contained 2% FBS. 'Mixed medium' was formulated as described above, by mixing equal parts by volume of the epithelial and endothelial media. Five conditions were tested using Variation 4 of the protocol (Table 5.1). The first four conditions were as described in Variation 2, in order to test for the same issues. The fifth condition was a proximal co-culture model using mixed medium during submerged culture and pure endothelial medium, EGM-2 with 2% FBS, during ALI culture. This condition tested whether the epithelial cells could successfully differentiate at the air-liquid interface, based on nutrient transport through, and nutrient secretion by, the endothelial monolayer.

5.2.3 Antibodies and immunofluorescence

The following antibodies were used to identify specific airway epithelial cell types: rabbit anti-acetylated-α-tubulin Lys40 (clone D20G3, Cell Signaling Technology, 1:450 dilution) to identify ciliated cells, rat anti-uteroglobin (uteroglobin also known as CC10, clone 394324, R&D Systems, 1:150 dilution) to identify club cells, and mouse anti-mucin 5AC (clone 45M1, Novus Biologicals, 1:150 dilution) to identify goblet cells. The following secondary antibodies were used: goat anti-

rabbit IgG Cy3 (Abcam, 1:200 dilution), goat anti-rat CruzFluor 647 (Santa Cruz Biotechnology, 1:100 dilution), and goat anti-mouse Alexa Fluor 488 (Invitrogen, 1:200 dilution).

Immunostaining was performed according to conventional protocols. Fixed cells on transwell membranes were in PBS. If they were unnecessary for imaging, the HPAEC monolayers on the basal side of the transwell membranes in co-culture models were scraped off with Kimwipes. Cells were permeabilized by incubating with 0.1% (v/v) Triton X-100 in PBS for 5 min, and non-specific antibody binding was blocked by 1% (w/v) bovine serum albumin in PBS for 1 h. Primary antibody incubation was performed overnight at 4 °C, or at least 2 h at room temperature. Secondary antibody incubation was performed for 1 h at room temperature. Nuclei were labeled by performing a rinse with 1 μg/mL 4',6-diamidino-2-phenylindole (DAPI, Sigma) in PBS for 5 min. Finally, the membranes were excised from the transwell supports, and mounted with Fluoromount G (Southern Biotech) between a glass slide and a coverslip, epithelial side facing upwards, i.e. facing the coverslip.

Epifluorescence imaging was performed either with a Zeiss Axiovert 200M microscope with 10× air and 20× air objectives or with a Zeiss AxioObserver.Z1 microscope with 10× air, 40× oil, and 63× oil objectives. The former microscope was equipped with an Axiocam MRm camera with a 1388 × 1040 pixels sensor, used at 1 × 1 binning. The latter was equipped with an Axiocam HRm camera with a 2752 × 2208 pixels sensor, used at 2 × 2 binning, resulting in 1376 px × 1104 px images. Multiple well-spaced locations were imaged per membrane, keeping the lamp intensity and exposure time constant for different conditions within the same experiment. Image processing was performed using ImageJ v1.51k (National Institutes of Health).

For translucent polycarbonate membranes as well as transparent polyester membranes, the fluorescence from the endothelial side of the membrane could be detected while imaging the

epithelial side, especially at low magnification (10×), where the Depth of Field is relatively large. As a result, scraping away the endothelial cell layer prior to immunostaining is recommended in order to obtain high quality images. Alternatively, confocal imaging may be used to reject out-of-focus fluorescence. If it is desirable to image both sides of a membrane at high magnification, the membrane can be mounted between two coverslips and simply flipped over during imaging, as opposed to mounting the membrane between a coverslip and a glass slide (data not shown). This is especially relevant when using the translucent polycarbonate membranes. On the other hand, polyester membranes are transparent, and cells on both sides could be imaged by confocal z-sectioning, without the need to flip the coverslips, although it is still recommended to do so in order to obtain the best possible images.

5.2.4 Alcian Blue staining of mucins

In initial experiments, Alcian Blue dye staining was performed to confirm production of mucins by secretory cells in differentiated epithelia, in both mono- and co-culture transwell membranes. The medium in the apical chambers was removed, and Alcian Blue solution (Electron Microscopy Sciences, 1% (w/v) Alcian Blue in 3% (w/v) acetic acid, pH 2.5) was incubated with the apical surfaces for 30 s, after which the dye solution was removed by aspiration. Following a PBS rinse, the membranes were excised. Excised membranes were placed on a sheet of paper, apical side facing upwards, and sealed using transparent self-adhesive tape. Alcian Blue staining to detect mucin production is a quick and easy assay to detect differentiation of the airway epithelium, but it was abandoned in favor of immunostaining for later experiments, as described above, due to the wealth of information available from immunostaining.

5.2.5 Nanoparticle library and stabilization

An NP library was generated by Catherine Murphy (University of Illinois, Urbana) for measurements of particle effects on pulmonary endothelial and epithelial cells. Gold nanoparticles were used as model nanoparticles due to their optical properties and tunability of size, shape, surface properties. Further, bulk gold is chemically inert and considered 'safe' for cell culture[3], and any effects observed were therefore not due to the bulk properties of gold, but rather to particle properties such as size, shape and surface chemistry.

Nanoparticle diameters were determined by transmission electron microscopy by Murphy lab. To study the effect of nanoparticle size and concentration on cell viability, citrate-capped gold nanospheres of diameter 18 ± 3 nm, 44 ± 11 nm, and 80 ± 10 nm were used (mean ± S.D., n > 300 NPs each). To study the effects of nanoparticle surface chemistry on cell viability, gold nanospheres of the same diameter were also wrapped consecutively with polyelectrolyte layers, of poly(allylamine hydrochloride) (PAH), polyacrylic acid (PAA), and finally poly(allylamine hydrochloride) again, to yield PAH-PAA-PAH wrapped nanospheres. Stock solutions of all nanoparticles, with known concentrations, were suspended in deionized water and filter sterilized prior to storage and usage.

Exposure of endothelial and epithelial cells to nanoparticles in solution was achieved by incubating cells with medium consisting of a mixture of equal parts of the complete endothelial culture medium (EGM-2, 10% FBS) and complete epithelial differentiation medium, excluding ALI inducer (S-ALI Differentiation Medium, Lonza). This medium is henceforth referred to as '50/50 medium'. Citrate-capped and PAH-PAA-PAH wrapped nanospheres of all sizes were

unstable in 50/50 medium, and tended to aggregate in less than 24 h, as determined by UV-Vis spectroscopy. A protocol was developed by Catherine Murphy's lab to prevent destabilization of the nanoparticles over several days in 50/50 medium. The stock concentration of the nanoparticles (M_1), the final volume of the nanoparticle-containing 50/50 medium for solution exposure (V_2), and the desired final molarity of nanoparticles (M_2) were used to calculate the volume of stock nanoparticles (V_1) required.

$$M_1V_1 = M_2V_2 \quad \ldots (1)$$

This volume of nanoparticles at the stock concentration was then incubated with fatty acid-free bovine serum albumin (BSA-FAF, Sigma, 1.2% (w/v) in HEPES buffer) at room temperature for 45 min, such that the volume of stock BSA-FAF added was 0.5% of the final volume of the nanoparticle-containing 50/50 medium. Next, FBS was added to this volume and incubated at room temperature for 45 min, such that the volume of FBS added was 1% of the final volume of the nanoparticle-containing 50/50 medium. Finally, the remaining volume was made up by adding 50/50 medium, to reach the desired concentration of stabilized nanoparticles, and was used in experiments after at least 1 h. While these prepared nanoparticle solutions are reportedly stable for multiple days, they were used within the same day of preparation for all experiments reported below. This stabilization protocol worked for citrate-capped gold nanospheres of all sizes, and for PAH-PAA-PAH wrapped gold nanospheres of size 44 nm.

5.2.6 Nanoparticle treatment and cell metabolic activity measurements

Lung endothelial and epithelial cells were treated with nanoparticles in solution to study the impact of nanoparticle concentration, size and surface chemistry on the metabolic activity of cells. The

metabolic activity of cells, used as an indicator of cell viability, was quantified using the colorimetric MTT assay. Cells metabolize the yellow tetrazolium dye 3-(4,5-dimethylthiazol-2-yl)-2,5-diphenyltetrazolium bromide (MTT) to the insoluble, purple formazan dye (E,Z)-5-(4,5-dimethylthiazol-2-yl)-2,5-diphenylformazan (formazan), by intracellular NADH-dependent dehydrogenase activity. The insoluble formazan dye can then be solubilized in an appropriate solvent and the absorbance measured using a UV-Vis spectrophotometer or a microplate reader.

HPAECs or SAECs were seeded at a density of 20,000 cells/well in their respective culture medium, in the central 24 wells of a 48-well plate (ThermoFisher, BioLite). Wells at the edge of the plate were excluded for cell-based assays due to temperature-gradient effects on cell viability and metabolism ('edge effects[139]'). Seeded cells were incubated for 2 days prior to nanoparticle treatment, such that the wells were ~80-90% confluent. Then, all the wells were rinsed with phosphate-buffered saline (PBS) to remove dead cells or debris. Stabilized or unstable nanoparticles of desired size and surface chemistry were suspended in 50/50 medium at the desired concentration, and 200 μL of the nanoparticle solution was added per well, in a distributed manner to account for temperature gradients. The plate was incubated immediately for 18 h. MTT stock solution was freshly prepared at a concentration of 5 mg/mL in sterile PBS, and stored at 4 °C in the dark.

The cell medium containing NPs was then aspirated away, and the wells were rinsed once with PBS. Every step henceforth was performed in the dark, until absorbance measurements were complete. MTT stock solution was diluted into phenol red-free Dulbecco's Modified Eagle's Medium (DMEM) with 10% FBS, at 10% (v/v), and 200 μL of this solution was incubated in each well. Meanwhile, a fresh solution of 10% (w/v) SDS in 0.01 M HCl was prepared. After 2 h of MTT incubation, 200 μL of the SDS solution was added to each well to solubilize the formazan

dye and incubated again for 2 h. Finally, the solution in each well was homogenized by pipetting, and a sample of volume 150 μL was pipetted into a well of a 96-well plate. Duplicate samples could be collected if necessary. However, if homogenization was performed correctly, then the variation in absorbance readings in duplicate samplings from the same well was significantly lower than that from nanoparticle-treated replicates from different wells, and thus only single samples were collected per homogenized sample. Absorbance readings were taken with a microplate reader (Tecan Infinite M200 Pro, Chemical and Biomolecular Engineering Shared Facilities, University of Illinois), at 570 nm (A570), which is the peak absorbance for formazan, and 680 nm (A680), which measures the background absorbance. The background subtracted (A570-A680) values were calculated for each well.

It should be noted that the homogenized samples contained nanoparticles, which had been internalized by the cells, adhered to the cell membranes, or adsorbed to the well surface, and could not be washed off during the PBS rinse. These nanoparticles were found to absorb strongly at both A570 and A680, such that appropriate 'blanks' were needed to subtract the contribution of nanoparticles to the MTT absorbance readings, thus insuring that the formazan signal was measured accurately. Thus, for each condition, instead of 2 h MTT incubation, 18 h nanoparticle-treated 'blank' wells were simultaneously treated with 180 μL of phenol-red-free DMEM with 10% FBS for 2 h. Then, 20 μL of the stock MTT and 200 μL of the SDS solution were added to the 'blank' wells and incubated again for 2 h, prior to homogenization and absorbance measurements as described above. Because the cells were lysed immediately after MTT addition, 'blank' wells showed no formazan production, and all absorbance readings at 570 nm and 680 nm were due to nanoparticles only. As described, the background subtracted absorbance $(A570-A680)_{NP\ only}$ in the presence of NPs were calculated for each blank well. Finally, the formazan-only

absorbance signal could be calculated, by subtracting the contribution of the nanoparticles to the absorbance.

$$(A570 - A680)_{formazan\ only} = (A570 - A680)_{formazan+NP} - (A570 - A680)_{NP\ only} \ldots (2)$$

Negative controls for all nanoparticle treatments used an equal volume of the nanoparticle delivery 'vehicle', and cells were treated exactly as the nanoparticle-containing samples. In the case of stabilized nanoparticles, the negative control was similarly incubated with BSA-FAF and FBS, prior to dilution into 50/50 medium. The negative control for citrate-capped nanospheres was water. The polyelectrolyte-wrapped spheres were provided in water, but because the polyelectrolyte layers can desorb, water was not the appropriate negative control. Instead, on the day of the experiment, a known volume of water was added into the stock solution of the polyelectrolyte-wrapped spheres. The spheres were pelleted by centrifugation, and the exact same volume of supernatant was collected by pipetting out before resuspending the stock solution of spheres for use in experiments. Because this collected supernatant contains the same concentration of free polyelectrolyte as the nanosphere solution, this 'PAH-PAA-PAH supernatant' is the appropriate negative control for the PAH-PAA-PAH wrapped nanospheres.

In all MTT experiments, the formazan signal $(A570\text{-}A680)_{formazan\ only}$, which reflects the metabolic activity, was used as an indicator of cell viability. The mean formazan signal for water-treated negative controls was used to normalize the signal from each individual well, such that the mean percentage cell viability for the water-treated negative controls was 100%.

5.2.7 Statistical analysis

Experimental designs for nanoparticle treatments of cells performed on different days included internal negative controls, and treated wells were distributed spatially within the design to cancel any gradient effects due to the geometry of the 48-well plates. Each experiment had multiple treatments, thus significant differences in cell viabilities were analyzed by first performing a one-way ANOVA (Table 5.2), and if the ANOVA detected a difference in the means of the tested conditions, it was followed by a Tukey's Honest Significant Difference (Tukey's HSD) post-hoc test (Tables 5.3 - 5.6). A significance level of $\alpha = 0.05$ was chosen. Unless specified, all data are reported as mean ± S.E.M.

5.3 RESULTS

5.3.1 Establishing an in vitro *co-culture model of the blood-gas barrier*

In order to establish an *in vitro* co-culture model of the pulmonary blood-gas barrier, I cultured primary human small airway epithelial cells and primary human pulmonary artery endothelial cells on opposite sides of transwell permeable supports, as described in the general protocol (Fig. 5.1A). The airlift process was performed to culture the confluent airway epithelial cells at the air-liquid interface for several weeks, during which the airway epithelium differentiated into secretory cells such as goblet cells and club cells, and ciliated cells.

The differentiation of primary airway epithelial cells was first validated using Alcian Blue staining, which stained mucins secreted by goblet cells (Fig. 5.1B). Bare transwell membranes stained uniformly blue, whereas membranes supporting submerged SAEC monocultures showed minimal staining. In contrast, membranes supporting cells cultured at the air-liquid interface for 8

days showed strong Alcian Blue staining. Membranes supporting cells subjected to ALI culture for 20 days showed weak staining. Higher resolution images revealed small clusters (< 1 mm in size) on the membranes, which were stained strongly blue. This suggested that the membrane coverage in the SAEC monocultures was extremely poor at day 20 of ALI culture, but mucin production was still observed. Poor membrane coverage of SAEC monocultures in epithelial medium was confirmed in later immunostained images (see Fig. 5.2, Nuclei, Monoculture, Day 21). In co-cultures with SAECs and HPAECs on opposite sides of the membrane ('proximal' co-cultures), no Alcian Blue staining was observed in cells cultured under submerged conditions, but at day 13 of ALI culture, there was weak mucin staining (Fig. 5.1C).

Immunostaining revealed further details about the epithelial coverage of the membrane and differentiation. When using Variation 1 of the general protocol, the membrane coverage by epithelial cells in the proximal co-cultures was generally good, with cultures starting at 100% membrane coverage under submerged conditions, and decreasing to only about 80% coverage at 28 days of ALI culture, based on visual inspection (Fig. 5.2). However, in monocultures, membrane coverage started at 100% SAEC coverage in submerged cultures, but decreased to only about 20% coverage after 28 days of ALI culture. Results from cell cultures prepared using Protocol Variations 3 & 4, described below, suggested that the most likely cause for this decrease in coverage over time was due to cell senescence and eventual cell death, as passage 3 cells used in Variations 3 & 4 maintained membrane coverage better than passage 4 cells used in Variations 1 & 2.

With Protocol Variation 1, although the co-cultures did show good epithelial coverage, they also showed extremely poor differentiation (Fig. 5.2). In co-cultures, at each time point, only a few cells stained positive for mucin 5AC and CC10, suggesting the presence of some goblet cells

and club cells. However no cells were positive for cilia, indicating that no ciliated cells were present. In contrast, a majority of the viable epithelial cells in monocultures showed differentiation markers for at least one of the three differentiated cell types. Goblet cells and club cells appeared within 7 days of ALI culture, and the fraction of total cells expressing markers for these cell types generally increased until 28 days of ALI culture. Ciliated cells first appeared after around 14 days of ALI culture, and reached a peak by 21 days. Acetylated α-tubulin is present in microtubules that are generally more stable to depolymerization than the remaining cytoplasmic microtubules[173]. Consequently, they are generally present in most cell bodies containing microtubule structures. However, acetylated α-tubulin is significantly enriched in cilia, and the fluorescence signal from cilia in the immunostained samples was significantly higher than the signal from the cell body, making it nearly impossible to mistake the microtubule staining in the cell body staining for cilia. At magnifications of 20× and higher, it was also easy to identify individual cilia, thus confirming the presence of ciliated cells (Fig. 5.3).

Although I demonstrated that the airway epithelial cells could undergo mucociliary differentiation in monoculture in epithelial medium, I was unable to achieve good membrane coverage, which is important for differentiation[153,200]. Further, cells in co-culture seeded at the same time, and at the same passage showed extremely poor differentiation, preventing us from establishing an *in vitro* pulmonary blood-gas barrier.

Protocol Variation 2 thus tested various cell culture conditions to identify a solution to these challenges (Table 5.1), in addition to reducing FBS concentration from 5% (v/v) to 1% (v/v) in mixed medium, as described earlier. The time spent in ALI culture was constant, at 21 days, since ciliated cells were observed at this time point. However, the first condition, i.e. SAEC monoculture in epithelial medium, again revealed poor membrane coverage, with less than 20%

estimated coverage (Fig. 5.4). In this condition, ciliated cells were not observed and very few goblet cells and club cells were observed, in contrast to the results obtained with SAEC monocultures in Variation 1 (Fig. 5.2). These differences suggested a lack of reproducibility. The second, third, and fourth conditions (Fig. 5.4, Table 5.1) – monoculture in mixed medium, distal co-culture, and proximal co-culture – reflected the same trend in differentiation. However these three conditions also showed slightly better membrane coverage, at approximately 50%.

Poor differentiation reproducibility, even in SAEC monocultures in epithelial medium, combined with poor membrane coverage, suggested that the SAEC passage number could influence SAEC differentiation. Accordingly, passage 3 SAECs were used in Protocol Variation 3, instead of the passage 4 cells used in Variations 1 & 2 (Fig. 5.5). In SAEC monocultures in epithelial medium, after 21 days of ALI culture, membrane coverage was improved significantly, with approximately 80% of the membrane area covered with epithelial cells. This result suggested that passage 3 cells resulted in better monolayer coverage outcomes. A sizeable fraction of the cells was positive for cilia. However the morphology of the cilia was significantly different than that seen in monocultures in Protocol Variation 1, because each ciliated cell appeared to have only 1-2 cilia. Further, the fraction of goblet cells and club cells was significantly lower than observed with Variations 1 and 2.

Finally, Protocol Variation 4 introduced major changes to the differentiation process, including changes in the epithelial medium – SAGM and Pneumacult ALI instead of S-ALI GM and S-ALI DM respectively, use of a transparent polyester transwell membrane with reduced pore density, and the use of increased seeding density enabled by the smaller transwell membrane size. In the first condition (Table 5.1), i.e. SAEC monoculture in epithelial medium, membrane coverage was 100%, with some clustering of cells (Fig. 5.6). This was similar to that seen when

using Protocol Variations 1-3. However, epithelial differentiation achieved with this condition was very poor, such that no differentiation markers were observed for any cell type. Conditions 2-4 (Table 5.1) achieved 100% membrane coverage with exceptionally high cell density relative to the first condition, but they also showed extensive mucociliary differentiation and epithelial polarization, with positive staining for secreted mucin 5AC and CC10 (uteroglobin), as well as cilia staining. All differentiation markers showed strongest staining intensity at the apical surface of the epithelial cells, with the nuclei being closer to the basal surface. Representative images for condition 4 are shown in Fig. 5.7. In particular, condition 2 showed that the endothelial growth factors and 1% FBS in the medium did not inhibit SAEC viability or differentiation in monocultures; condition 3 showed that factors secreted by endothelial cells did not inhibit SAEC viability and differentiation in distal co-cultures; and condition 4 showed that an endothelial monolayer on the basal side of membrane did not inhibit SAEC viability and differentiation in co-cultures by restricting nutrient access (Table 5.1). Results obtained with the fifth condition indicated that co-culturing cells in endothelial medium resulted in an estimated 50% membrane coverage, and weak mucociliary differentiation. This result suggested that the epithelial cells did need the epithelial-specific nutrients available in the mixed medium.

These results suggested that airway epithelial-endothelial co-cultures could be established *in vitro,* and that the combination of Pneumacult ALI medium, polyester membrane pore density in transwells, earlier SAEC passages (passage 3 or less), and increased seeding density was important for successful airway epithelial differentiation and viability. When using Protocol Variation 4, it was unclear why the first condition, i.e. SAEC monoculture in epithelial medium, did not result in successful differentiation. The fact that the second condition, i.e. SAEC monoculture in mixed medium, did successfully differentiate suggests that the medium

composition was responsible. It is fortuitous that differentiation of both monocultures and co-cultures was successful, when using the same mixed medium, as this simplifies future experiments where it may be necessary to compare differentiated airway epithelia in monocultures against co-cultures, by removing the medium as a variable.

5.3.2 Dose-dependent effects of NPs on cell viability

Effects on the viability of HPAECs and SAECs due to exposure to gold nanoparticle solutions were assayed using the MTT assay for cellular metabolic activity. Gold nanospheres of diameter 18 nm were used at 0.1 nM and 1.0 nM for dose-dependence studies of cell viabilities (Figs. 5.8A, 5.9A). Stabilized 18 nm gold nanoparticles did not reduce cell viability, even at 1.0 nM (data not shown), and were thus not used in these dose-dependence experiments, or in subsequent size-dependence experiments. In fact, while unstable 18 nm gold nanospheres appeared to cause significant perinuclear aggregates in the cell body of HPAECs and SAECs, stabilized 18 nm gold nanospheres formed significantly fewer perinuclear aggregates in treated cells (Fig. 5.8A).

Despite the extensive perinuclear aggregates observed in the cell body with unstable NPs (Fig. 5.8A), the effects on cell viability were modest (Fig. 5.9A). HPAECs treated with water (negative control) for 18 h showed a normalized viability of 100 ± 2 %, which dropped to 90 ± 1 % with 0.1 nM NPs ($p = 0.0022$ against water), and to 86 ± 2 % with 1.0 nM NPs ($p = 4.2 \times 10^{-5}$ against water). The apparent difference in cell viabilities between cells treated with 0.1 nM versus 1.0 nM NP was not statistically significant (see Table 5.3 for all p-values).

Gold nanospheres of 18 nm diameter had a negligible effect on SAEC viability (Fig. 5.9A). SAECs treated with water for 18 h showed a normalized viability of 100 ± 2 %. However, when

exposed to 0.1 nM gold nanospheres, cell viability was 101 ± 2 %, and at nanoparticle concentrations of 1.0 nM, cell viability was 94 ± 2 %. Statistical significance could not be established for any of the pairwise comparisons (Table 5.3). These results showed that although SAECs and HPAECs appeared to internalize unstable 18 nm gold NPs, their dose-dependent effects on cell viability over an 18 h period were modest to non-existent, depending on the cell type.

5.3.3 Size-dependent effects of NPs on cell viability

In order to study the effects of nanoparticle size on cell viability, unstable gold nanospheres of diameter 18 nm and 80 nm were used. The 80 nm NPs were used at a constant concentration of 0.022 nM, whereas 18 nm NPs were used at 0.022 nM, in order to test size-dependent effects at constant NP concentration, and at 0.44 nM, in order to test size-dependent effects at constant NP surface area.

HPAECs in water-treated control wells showed a cell viability of 100 ± 1 % after an 18 h incubation (Fig. 5.9B), while cells in wells treated with 0.022 nM 18 nm NPs showed a viability of 105 ± 2 % (not significant against water, see Table 5.4 for all p-values). Cell viability when treated with 0.44 nM 18 nm NPs was 98 ± 3 % (not significant against water or against 0.022 nM 18 nm NPs). With the 80 nm NPs used at 0.022 nM, cell viability was 94 ± 3 % ($p = 0.0086$ compared with 0.022 nM 18 nm NPs). This was statistically similar to viability determined after treatment with water or with 0.44 nM 18 nm NPs. Thus, with HPAECs, size-dependent effects of NPs on cell viability could not be established, when maintaining constant total surface area, but differences could be successfully established at constant NP concentration.

In SAECs, the size-dependence of NPs on cell viability exhibited a similar trend as with HPAECs (Fig. 5.9B). After an 18 h incubation, cells in water-treated control wells showed a viability of 100 ± 3 %, while cells in wells treated with 0.022 nM 18 nm NPs showed a viability of 104 ± 4 % (not significant against water). Treatment with 0.44 nM 18 nm NPs resulted in a cell viability of 99 ± 3 % (not significant against water, and against 0.022 nM 18 nm NPs). The larger 80 nm NPs used at 0.022 nM resulted in a cell viability of 87 ± 3 % ($p = 0.042$ against water, $p = 0.0065$ against 0.022 nM 18 nm NPs, not significant against 0.44 nM 18 nm NPs). Thus, with both HPAECs and SAECs, there were no apparent effects of NP size on cell viability following an 18 h exposure at constant total NP surface area with unstable 18 nm and 80 nm gold nanospheres. However, at constant NP concentration, the larger 80 nm gold nanospheres reduced cell viability, relative to 18 nm gold nanospheres at similar concentration.

5.3.4 Effect of NP surface chemistry on cell viability

In order to study the effects of surface chemistry on cell viability, citrate-capped nanospheres were compared against polyelectrolyte-wrapped nanospheres (Figs. 5.8B, 5.10). Unstable as well as stabilized nanospheres were used for cell treatments. The 18 nm and 80 nm polyelectrolyte-wrapped spheres could not be stabilized in 50/50 medium, but 44 nm polyelectrolyte-wrapped spheres were stable. As a result, 44 nm spheres were used for unstable as well as stabilized NP treatment, at a chosen concentration of 0.08 nM.

HPAECs treated with unstable citrate-capped 44 nm nanospheres developed significant perinuclear aggregates, which were significantly reduced in cells treated with stabilized nanospheres (Fig. 5.8B). This response was similar to that seen with unstable citrate-capped 18

nm NPs, suggesting that HPAECs likely internalized unstable nanoparticles as they aggregated and settled on the cells. However, HPAECs treated with PAH-PAA-PAH wrapped nanoparticles showed extensive cell death, when using either unstable or stabilized NPs. Importantly, the PAH-PAA-PAH supernatant also caused visible cell death in the treated wells, suggesting that cell death was due to free polyelectrolyte in the supernatant. SAECs behaved similar to the HPAECs under identical conditions, and exhibited similar perinuclear aggregates and extensive cell death.

HPAECs were treated with 0.08 nM unstable 44 nm nanospheres for 18 h. Control cells in wells treated with water showed 100 ± 5 % viability (Fig. 5.10A), whereas cell viability in wells treated with 0.08 nM unstable citrate-capped NPs was 79 ± 2 % ($p = 1.3 \times 10^{-4}$ against water, see Table 5.5 for all p-values). When treated with 0.08 nM unstable PAH-PAA-PAH wrapped NPs, cells showed significantly lower viability, at 22.1 ± 0.7 % ($p < 1.0 \times 10^{-10}$ against water, $p < 1.0 \times 10^{-10}$ against unstable citrate-capped NPs). However, this drastic drop in cell viability could not be attributed entirely to the PAH-PAA-PAH wrapped nanospheres, as treatment with PAH-PAA-PAH supernatant itself showed a reduced cell viability of 32.6 ± 0.9 % ($p < 1.0 \times 10^{-10}$ against water, $p < 1.0 \times 10^{-10}$ against unstable citrate-capped NPs, $p = 0.040$ against unstable PAH-PAA-PAH wrapped NPs).

SAEC viability showed a slightly different trend from HPAEC viability, when treated with the same unstable NPs. Cells in control wells, treated with water, showed 100 ± 2 % viability (Fig. 5.10A), whereas treatment with 0.08 nM unstable citrate-capped nanospheres resulted in 105 ± 2 % cell viability. Unlike with HPAECs, this difference was not significant, suggesting that these unstable 44 nm citrate-capped nanoparticles did not significantly affect SAEC viability over 18 h of exposure, at 0.08 nM. SAECs treated with 0.08 nM unstable PAH-PAA-PAH wrapped NPs showed a drop in viability to 61 ± 2 % ($p = 9.0 \times 10^{-8}$ against water, $p < 1.0 \times 10^{-10}$ against unstable

citrate-capped NPs), but this drop was not as large as seen with HPAECs. SAECs treated with PAH-PAA-PAH supernatant also showed a drop in viability to 65 ± 4 % ($p = 2.9 \times 10^{-6}$ against water, $p = 5.3 \times 10^{-8}$ against unstable citrate-capped NPs, not significant against unstable PAH-PAA-PAH wrapped NPs). These data suggested that the loss in SAEC viability due to treatment with unstable PAH-PAA-PAH wrapped NPs was almost entirely due to the PAH-PAA-PAH supernatant, which likely contained free polyelectrolyte. Overall, the data from HPAECs and SAECs in wells treated with unstable citrate-capped and polyelectrolyte-wrapped NPs suggested that free polyelectrolytes in the NP supernatant could cause significant cell death, and that the polyelectrolyte-wrapped NPs caused greater loss of HPAEC viability than the supernatant alone. Because this did not similarly affect SAECs, it is possible that the loss of viability due to this particular surface chemistry may be cell type specific.

Stabilized 44 nm nanospheres were also used to treat cells at 0.08 nM for 18 h (Fig. 5.10B). Water-treated control HPAECs exhibited a normalized viability of 100 ± 2 %, whereas treatment with 0.08 nM stable citrate-capped NPs resulted in a viability of 92 ± 1 %. This difference was not significant (see Table 5.6 for all p-values). However, treatment with 0.08 nM stable PAH-PAA-PAH wrapped NPs reduced HPAEC viability to 64 ± 2 % ($p = 2.2 \times 10^{-8}$ against water, $p = 4.7 \times 10^{-8}$ against stable citrate-capped NPs). Meanwhile, HPAEC viability on treatment with 'stable' PAH-PAA-PAH supernatant was 60 ± 2 % ($p = 5.4 \times 10^{-8}$ against water, $p = 1.6 \times 10^{-7}$ against stable citrate-capped NPs, not significant against 0.08 nM stable PAH-PAA-PAH wrapped NPs). Cell viabilities in each experiment reported here are normalized to the water-treated negative controls – keeping in mind this fact, my data show that the stabilization of citrate-capped and polyelectrolyte-wrapped 44 nm NPs led to increased HPAEC viability, relative to the corresponding unstable 44 nm NPs (Figs. 5.10A, 5.10B). Interestingly, the 'stabilized' PAH-PAA-

PAH supernatant – i.e. supernatant treated with BSA-FAF and FBS incubations – also showed an increase in HPAEC viability, relative to untreated supernatant. With unstable 44 nm NPs, the citrate-capped spheres showed a significant loss of HPAEC viability compared to water, and treatment with polyelectrolyte-wrapped spheres also reduced HPAEC viability significantly, compared to supernatant. Whereas upon NP stabilization, both of these comparisons were no longer statistically significant. This suggested that stabilization may protect against the cytotoxic effects of the 44 nm particles of different surface chemistries, as described for 18 nm citrate-capped particles earlier.

SAECs in wells were also treated with 0.08 nM 44 nm nanospheres for 18 h. In control wells treated with water, cell viability was 100 ± 2 % (Fig. 5.10B). Treatment with 0.08 nM stable citrate-capped NPs resulted in a cell viability of 93 ± 2 % in wells. Like HPAECs, the apparent difference was not statistically significant. Stable PAH-PAA-PAH wrapped NPs used at 0.08 nM dropped the cell viability in treated wells to 69 ± 2 % ($p = 2.9 \times 10^{-6}$ against water, $p = 3.0 \times 10^{-6}$ against stable citrate-capped NPs), whereas 'stable' PAH-PAA-PAH supernatant treated wells showed a cell viability of 76 ± 4 % ($p = 7.3 \times 10^{-5}$ against water, $p = 4.1 \times 10^{-4}$ against stable citrate-capped NPs, not significant against 0.08 nM stable PAH-PAA-PAH wrapped 44 nm NPs). Unlike HPAECs, in SAECs, the unstable citrate-capped and polyelectrolyte-wrapped nanoparticles showed no significant cytotoxic effects compared to their respective negative controls, i.e. water and PAH-PAA-PAH supernatant. This data shows that stabilization of nanoparticles also did not change this trend – stabilized nanoparticles still had no cytotoxic effects relative to their respective negative controls. Stabilization of PAH-PAA-PAH wrapped NPs and the supernatant did cause a slight improvement in SAEC viability (normalized to the respective water-treated controls), but the difference was not as drastic as in HPAECs. Surprisingly,

stabilization of citrate-capped spheres led to a slight reduction in cell viability in SAECs but not in HPAECs, although the former was not statistically significant. I cannot currently explain this behavior.

Overall, these results suggested that PAH-PAA-PAH wrapping of nanoparticles had a clear cytotoxic effect that could be distinguished from the effect of the supernatant alone, but only for HPAECs treated with unstable NPs. Further, stabilization only caused a drastic drop in cytotoxicity in HPAECs, but not in SAECs. These results thus demonstrated that the surface chemistry of nanoparticles could influence cell viability in a cell type-specific manner. Interestingly, the stabilization incubations performed on the PAH-PAA-PAH supernatant led to increased cell viability, compared to 'unstable' supernatant, suggesting that the formation of complexes with BSA-FAF and FBS proteins may lower the toxic effects of free polymers, and of free PAH in particular.

5.4 DISCUSSION

In this work, I established an *in vitro* co-culture model that consists of primary airway epithelial and pulmonary endothelial cells that showed rich mucociliary differentiation and a polarized phenotype (Fig. 5.7). The airway epithelial cells and endothelial cells were grown on opposite sides of porous transwell membranes, and the airway epithelial cells were exposed to the atmosphere, to form an *in vitro* model of the pulmonary blood-gas barrier. Further, I established that exposure of airway epithelial cells and pulmonary endothelial cells to nanoparticles in solution influenced cell viability in a dose-dependent, size-dependent, and surface chemistry-dependent manner (Figs. 5.9, 5.10).

I successfully differentiated airway epithelial cells in air-liquid interface co-culture with pulmonary endothelial cells, on opposite sides of a transwell membrane (Fig. 5.7). The differentiated epithelial cells showed the presence of cilia, mucins, and CC10, indicating the presence of all three cell types commonly seen in the small airway – ciliated cells, goblet cells, and club cells respectively[181]. This permits us to perform studies on the permeability of the blood-gas barrier, including transport across the barrier, of nanoparticles delivered to the airway epithelium by aerosolization. Further, these differentiation results can be translated to a lung-on-a-chip system, to incorporate mechanical stimuli such as shear flow and cyclic stretch. The airway epithelium at the air-liquid interface can be exposed to aerosolized nanoparticles, in order to study cellular responses in physiological conditions.

In this work, I performed preliminary studies to quantify the dependence of cell viability on gold nanoparticle dose, size, and surface chemistry. In these preliminary studies, HPAECs and SAECs were exposed to gold nanospheres in solution, instead of by aerosolization. Stabilized, citrate-capped 18 nm spheres did not cause any obvious change to cell morphology (Fig. 5.8). Unstable citrate-capped 18 nm spheres led to formation of significant aggregates inside of both cell types. However they were cytotoxic only to HPAECs, at both 0.1 nM and 1.0 nM concentrations (Fig. 5.9A). This is not surprising – Brandenberger, et al.[27] compiled a list of solution exposure studies performed with gold nanoparticles, on different cell lines, at different NP sizes and concentrations, and found that gold nanoparticles of diameter 20 nm and smaller showed either no cytotoxic behavior, or cytotoxicity at extremely high (micromolar) concentrations. Further, the compiled studies in the prior report suggested that the cytotoxicity was cell type specific.

I also studied the effect of the size of citrate-capped gold nanospheres on cell viability (Fig. 5.9B). When the concentration was adjusted to maintain same total nanoparticle surface area delivered ('size-dependent effects at constant surface area'), I could not observe a significant difference in HPAEC and SAEC viabilities, when comparing the effects of 18 nm and 80 nm gold nanospheres. However, when the concentration was held constant ('size-dependent effects at constant concentration'), I could observe a clear effect of NP size on HPAEC and SAEC viabilities – the larger particles led to a larger drop in cell viability. Previous reports also indicated a size-dependent effect of gold nanosphere treatment at constant concentration on cell viability, but the effect has been described in various reports as either monotonic with smaller particles being more toxic[45,166,183] or less toxic[183,233], or even random[215]. Care should be taken while interpreting these results because assays chosen for evaluating toxicity vary significantly. However, regarding citrate-capped gold nanospheres specifically, it has been shown that higher amounts of citrate on particle surface can affect cell viability significantly, to a greater extent than particle size[74,209]. This parameter was not controlled for, in my study. A greater search of the parameter space thus may be required, in order to evaluate the effects of particle size as well as citrate on the particle surface.

Lastly I investigated the effects of surface chemistry, at constant particle size and concentration. I found that stabilized 44 nm gold nanospheres did not result in significant intracellular aggregates, unlike the results obtained with unstable 44 nm nanospheres (Fig. 5.8B). Further, polyelectrolyte-wrapped nanospheres caused significant cytotoxicity relative to citrate-capped spheres. However, except in the case of HPAECs treated with unstable particles, the toxicity caused by the particle treatment could not be distinguished from the toxicity caused by the vehicle itself, which likely contained free polyelectrolytes. The free polyelectrolytes could be left over in the solution after insufficient washes to remove unbound polyelectrolytes, or could have

desorbed from the wrapped particles during storage. Specifically, free PAH has been found to be extremely toxic relative to free PAA. However, when bound to a surface as part of a polyelectrolyte multilayer (as in this study), the cytotoxicity of PAH was significantly attenuated due to stable polyvalent polycation-polyanion interactions[143]. Even so, the cytotoxicity of PAH-wrapped microspheres and nanospheres has been reported previously[105,179]. Stabilization of particles by sequential incubations in BSA-FAF and FBS led to an increase in cell viability in my studies (Fig. 5.10B). It should be noted that unstable citrate-capped nanospheres are negatively charged (mean zeta potential ζ = -20.6 mV for 44 nm spheres), and the polyelectrolyte-wrapped nanospheres are positively charged (mean ζ = 37.0 mV for 44 nm spheres), whereas after stabilizing incubations, both nanospheres display a relatively small negative charge (mean ζ = -9.9 mV for stabilized citrate-capped spheres and mean ζ = -6.6 mV for stabilized polyelectrolyte-wrapped spheres) (personal communication, Catherine Murphy). Although studies indicated that the surface charge on nanoparticles change anyway after adding to cell media due to adsorption of albumin and serum proteins[4], the stabilization steps prior to addition to cell media reduces particle aggregation immediately after addition to cell media, and helps to attain a uniform, controlled surface coverage of protein on particles instead of random protein uptake from cell media. Surface charge is one of many factors playing a role in determining nanoparticle uptake and toxicity, and thus may help explain the increase in toxicity caused by polyelectrolyte-wrappings as well as the reduction in toxicity caused by nanoparticle stabilization. Cells treated with the vehicle, likely containing free PAH, also showed increased viability with the stabilization incubations. Since PAH and BSA interact to form complexes[12], BSA probably has a role in sequestering free PAH and preventing it from interacting with the cells.

In conclusion, I successfully established a model differentiated pulmonary epithelial-endothelial co-culture *in vitro*. Further, I performed preliminary experiments assaying the viability of HPAECs and SAECs when treated with gold nanospheres for 18 h, and studied the effects of nanoparticle concentration, size and surface chemistry. These results will facilitate the establishment of a well-differentiated lung-on-a-chip model, which incorporates cyclic stretch, as well as shear flow on the endothelial cells, and is capable of live-cell imaging, and will form the basis for studies of aerosolized nanoparticle treatments of differentiated epithelial-endothelial co-cultures in transwell models as well as in lung-on-a-chip models.

5.5 FIGURES

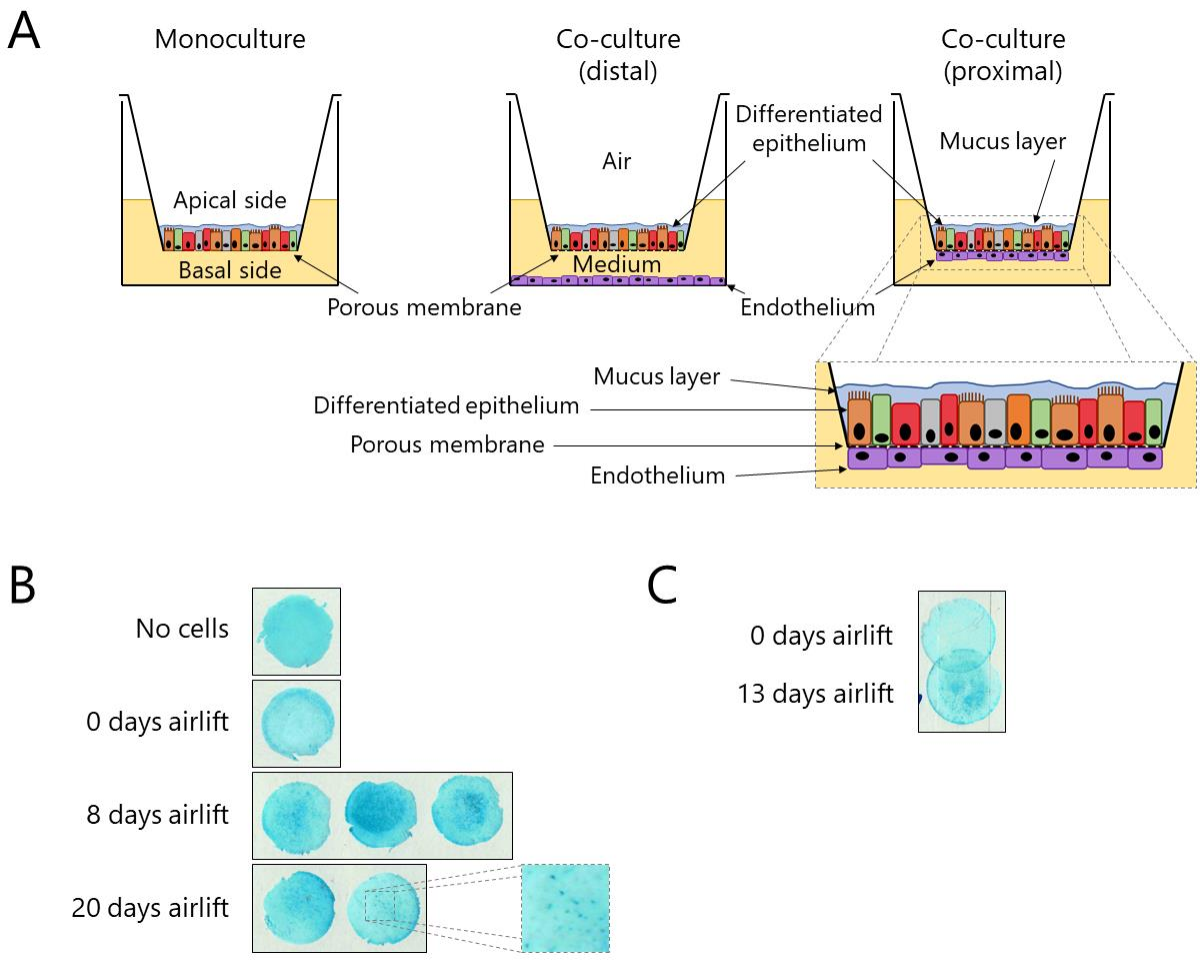

Fig. 5.1: Cultured airway epithelial cells differentiate at the air-liquid interface. (A) Schematic diagram of a transwell setup used for air-liquid interface (ALI) culture of airway epithelial cells (SAECs) in monoculture, or co-culture with pulmonary artery endothelial cells (HPAECs), as described in the general protocol. In co-culture conditions, endothelial cells (purple) are seeded either in the basal chamber, or on the basal side of the membrane, and cultured under submerged conditions throughout. Epithelial cells are seeded on the apical side of the transwell membrane, and cultured to confluence under submerged conditions. The apical side of the transwell, supporting airway epithelial cells, is then exposed to air for several days after 'airlift' – i.e. removing medium from the apical chamber. During this time the epithelial cells undergo mucociliary differentiation and exhibit a polarized phenotype. The polarized epithelium consists of undifferentiated cells (gray), goblet cells (green), ciliated cells (orange), and club cells (red), and is covered by a mucin-rich film. (B) Alcian Blue staining of airway epithelial monocultures on transwell membranes, indicative of mucin production. Bare transwells membranes are stained uniformly blue, whereas membranes supporting SAECs cultured in submerged conditions show weak non-uniform staining despite good epithelial coverage of the membrane, as seen in Fig. 5.2. Membranes supporting SAECs stained 8 days after airlift, showed strong Alcian Blue staining in the central regions of the membrane. Membranes supporting SAECs stained 20 days after airlift

Fig. 5.1 (contd.): showed weaker overall staining, but strong staining in clusters. This is likely a result of poor epithelial coverage of the membrane. (C) Alcian Blue staining of airway epithelial cells on transwell membranes, in co-culture with HPAECs. In submerged conditions, no Alcian Blue staining was seen, suggesting no differentiation, whereas after 13 days of ALI culture, weak staining could be observed. For (B) and (C), the transwell membranes are 12 mm in diameter.

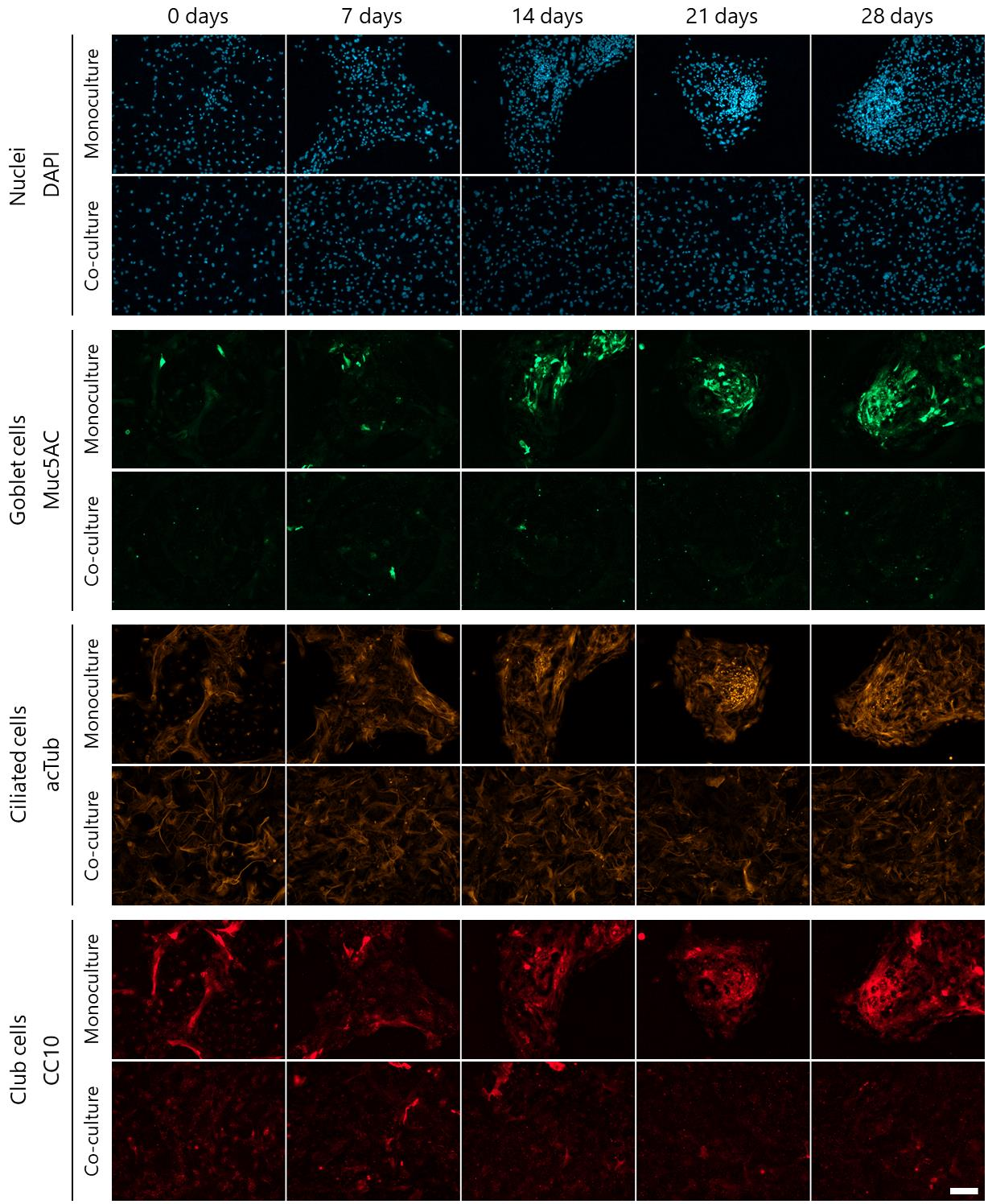

Fig. 5.2: Representative images of airway epithelial differentiation using Variation 1 of the general protocol. In ALI culture, epithelial coverage in SAEC monocultures was poor, ~20-50% for different time points, compared to ~80-90% throughout for SAEC-HPAEC co-cultures. Nuclei were visualized using the DAPI counterstain (blue). SAEC monocultures showed increased staining of mucin 5AC (green), acetylated α-tubulin (orange), and CC10 protein (red) with

Fig. 5.2 (contd.): increased time spent at the air-liquid interface, indicating differentiation of the SAECs into goblet cells, ciliated cells, and club cells respectively. SAEC-HPAEC co-cultures showed minimal staining of these markers over 28 days of ALI culture, suggesting extremely poor differentiation. Scale bar is 200 μm. Two membranes per condition from two experiments. It should be noted that the general cell body staining of acetylated α-tubulin is not a marker of ciliated cells. Rather, individual cilia are stained strongly and visible in the SAEC monocultures at day 21, and to a lesser extent at day 14 and day 28. Another set of images of the SAEC monoculture subjected to 21 days of ALI culture, taken at higher magnification, is available in Fig. 5.3.

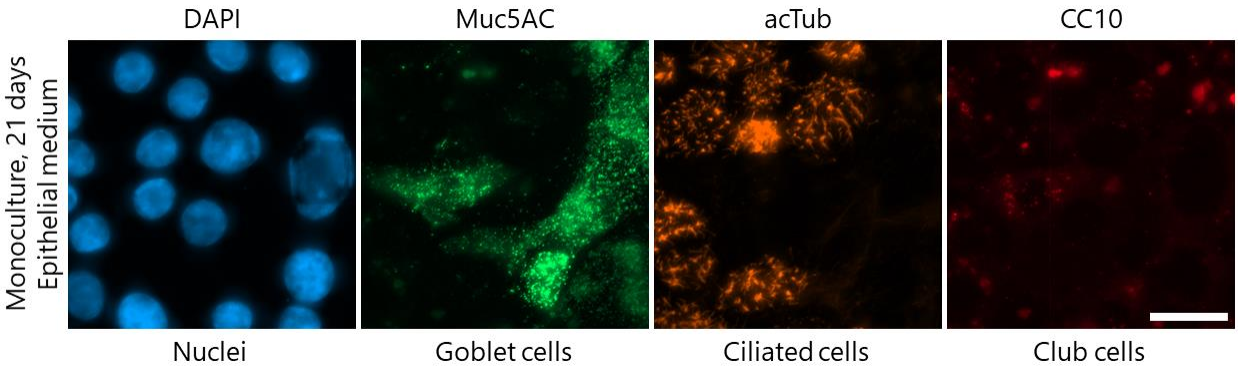

Fig. 5.3: Representative images of SAEC monoculture differentiation using Variation 1 of the general protocol, at 21 days of ALI culture. Cilia stained by acetylated α-tubulin antibody (orange) are clearly visualized in this image, generated by taking regularly spaced images along the z-axis ('z-stack') of the monoculture, performing background subtraction on the z-stack, followed by a maximum intensity projection of the stack. Also visualized are nuclei (blue), and goblet cells (green). Club cell staining (red) was weak at this location. Scale bar is 20 μm. Two membranes for this condition, from two experiments.

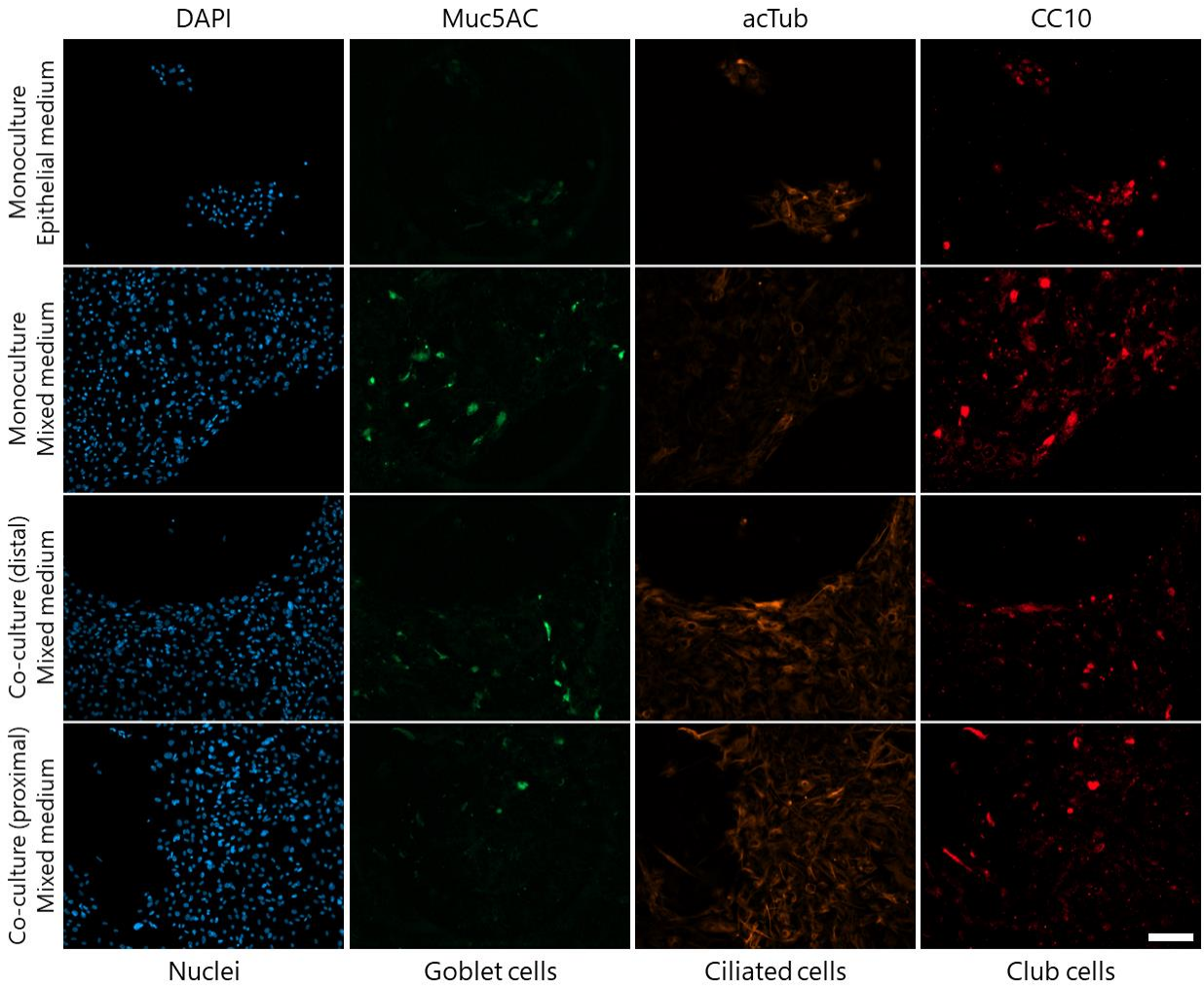

Fig. 5.4: Troubleshooting airway epithelial differentiation using Variation 2 of the general protocol, at 21 days of ALI culture. Representative images show poor mucociliary differentiation of SAECs after 21 days at the air-liquid interface, under all tested conditions (see Materials and Methods for details). Staining for goblet cells (green), ciliated cells (orange), and club cells (red) all showed very few positive cells. Nuclei are in blue. Lack of cilia at the monoculture culture in epithelial medium, compared to presence of cilia seen in Figs. 5.2 & 5.3, shows poor reproducibility. All conditions showed poor membrane coverage by SAECs, ~10% for monoculture in epithelial medium, ~50% for other conditions. Scale bar is 200 μm. Two membranes per condition, from one experiment.

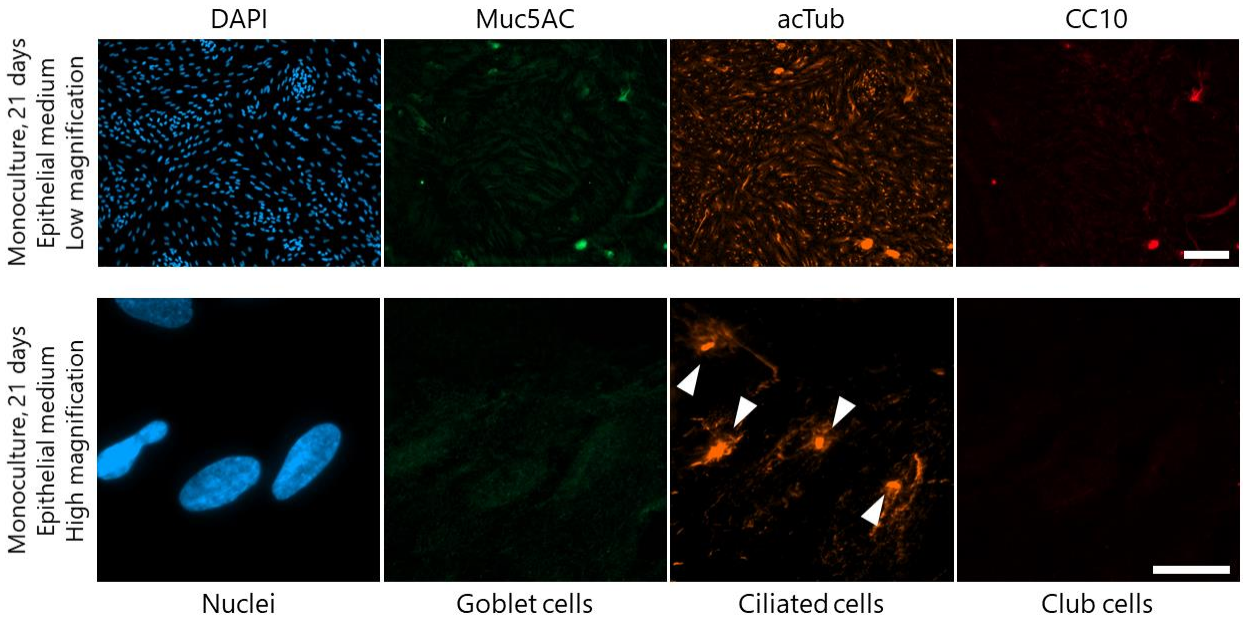

Fig. 5.5: Troubleshooting airway epithelial differentiation using Variation 3 of the general protocol, at 21 days of ALI culture. SAEC monocultures seeded at earlier passages showed better membrane coverage (~80%), and all three differentiation markers, as seen in the top panels. However, at higher magnifications shown in the bottom panels, it became obvious that the ciliated cell phenotype (orange) exhibited significantly fewer cilia than obtained with Variation 1 (Figs. 5.2 & 5.3). Most ciliated cells in this experiment exhibited only 1-2 cilia per cell (white arrows). Scale bars, 200 μm for top panels, 20 μm for bottom panels. Two membranes for this condition, from one experiment.

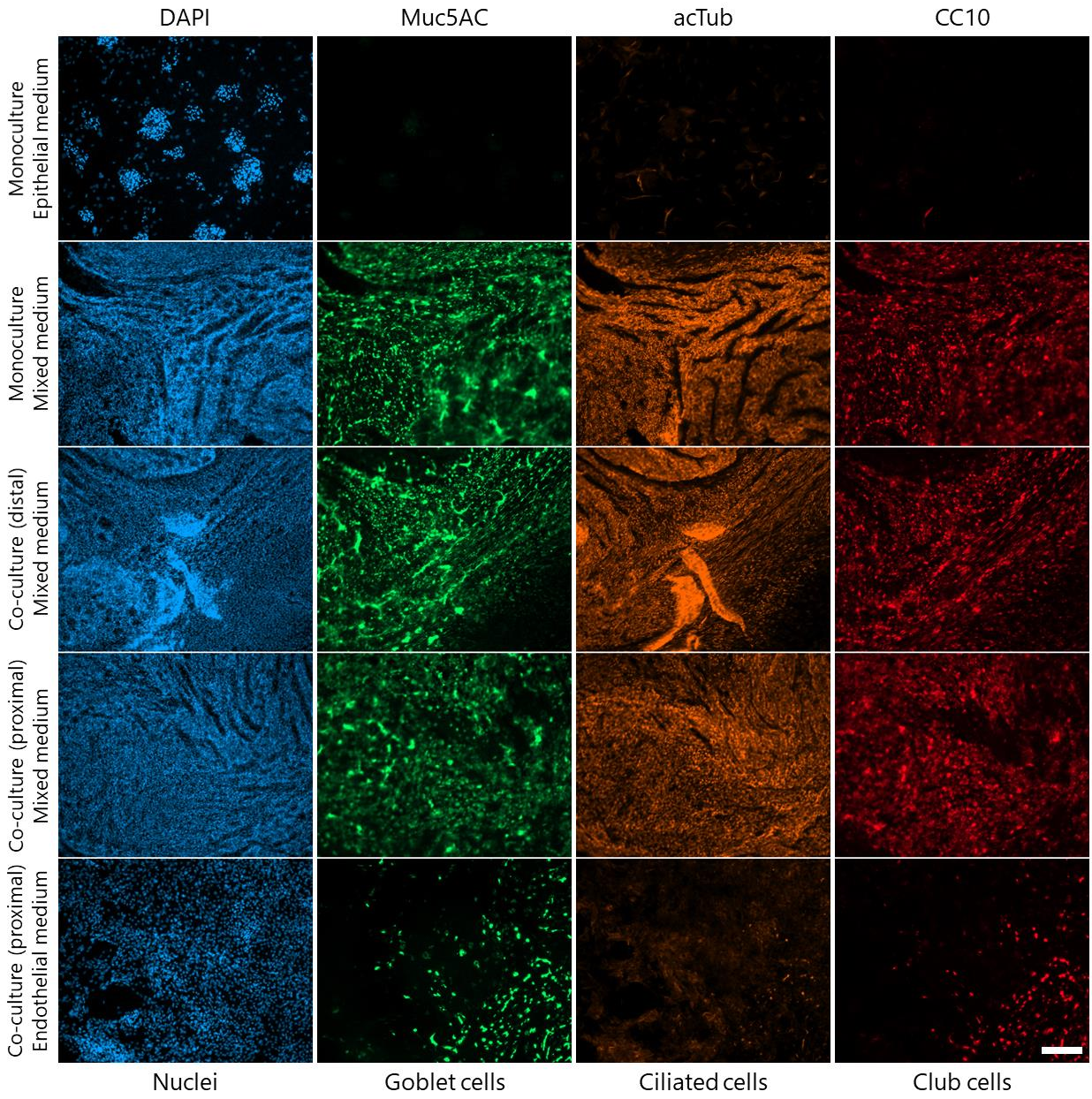

Fig. 5.6: Troubleshooting airway epithelial differentiation using Variation 4 of the general protocol, at 21 days of ALI culture. After 21 days of ALI culture, SAEC monocultures as well as SAEC-HPAEC co-cultures showed rich mucociliary differentiation under specific conditions. SAECs in purely epithelial medium showed poor membrane coverage, as before, as well as poor differentiation. However, SAECs and SAEC-HPAEC co-cultures in mixed medium showed extensive differentiation, with the presence of goblet cells (green), ciliated cells (orange), as well as club cells (red). Scale bar is 200 μm. Two membranes per condition, from one experiment. Fig. 5.7 shows a higher magnification image of the SAEC-HPAEC co-culture on opposite sides of the transwell membrane ('proximal' co-culture).

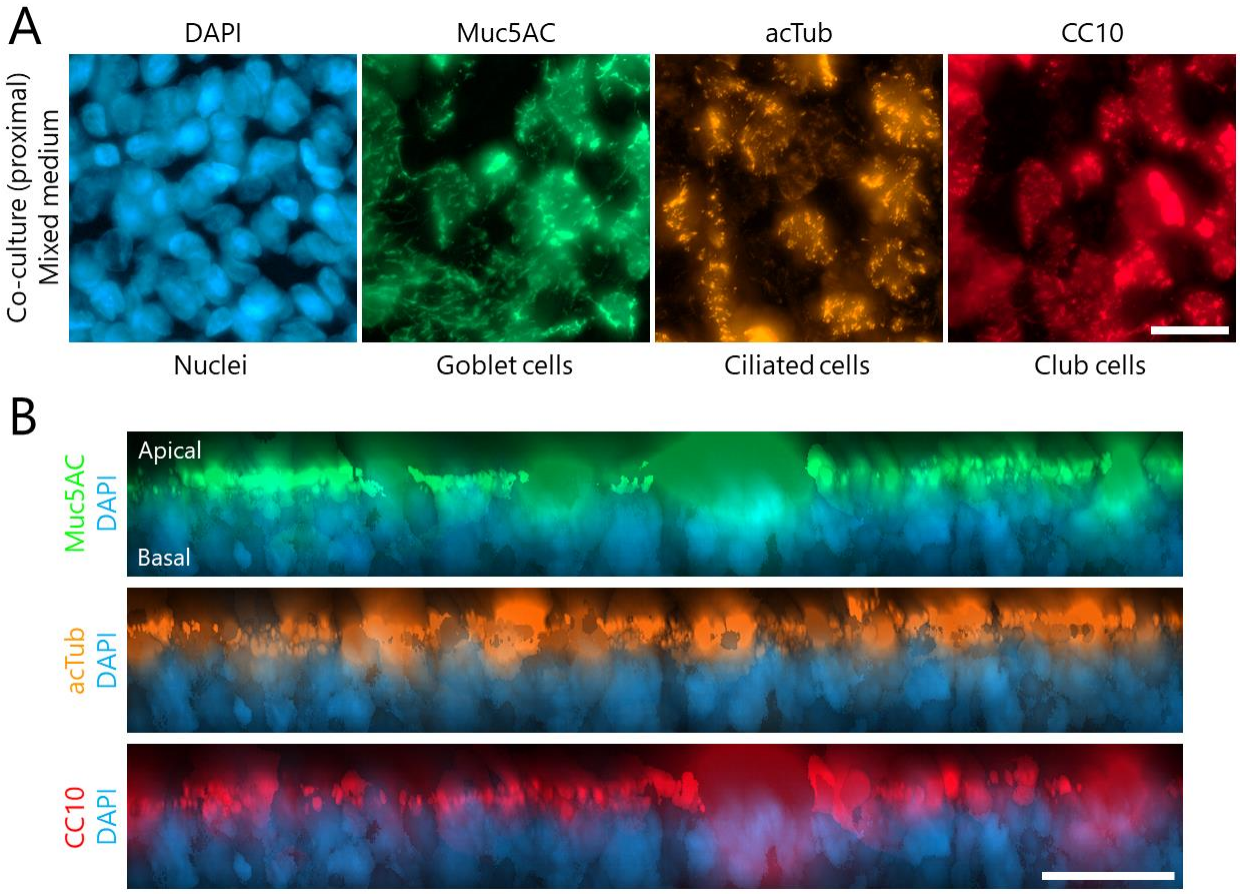

Fig. 5.7: Airway epithelial differentiation in SAEC-HPAEC proximal co-cultures, at 21 days of ALI culture using Variation 4 of the general protocol. (A) SAECs and HPAECs cultured on opposite sides of the same membrane were cultured at the air-liquid interface for 21 days, as described in the general protocol. The epithelial cells underwent mucociliary differentiation and were stained to visualize nuclei (blue), goblet cells (green), ciliated cells (orange), and club cells (red). These images are generated by taking the maximum intensity projection of a background subtracted z-stack, and clearly show the differentiation markers for all three cell types. (B) The background subtracted z-stacks were used to generate a three dimensional model of the fluorescent staining, and the z-variations of the staining intensities were visualized. Mucin 5AC, acetylated alpha tubulin, as well as CC10 protein localized at the apical surface of the epithelial side of the membrane, whereas nuclei were present at the basal surface. This is characteristic of the polarized epithelium. Scale bars are 20 μm. Two membranes for this condition, from one experiment.

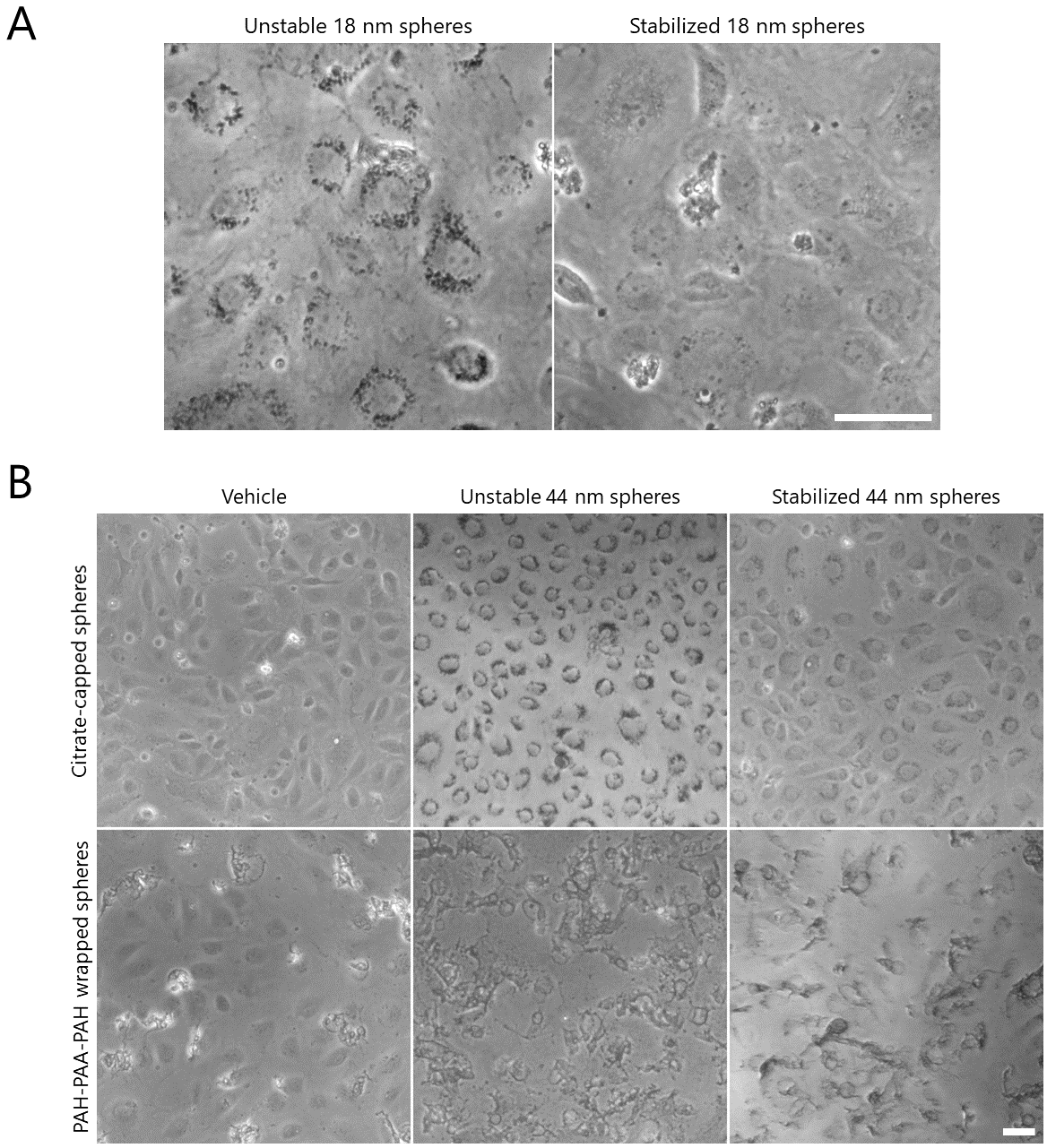

Fig. 5.8: Nanoparticle treatment effects on HPAEC morphology. Representative images of HPAECs treated with nanoparticles in solution for 18 h. The vehicle for citrate-capped spheres is deionized water, and for PAH-PAA-PAH wrapped spheres is 'PAH-PAA-PAH supernatant' as described in Materials and Methods. (A) 18 nm citrate-capped gold nanospheres accumulate in the cell body in the absence of any stabilization treatments, as shown in these images of cells treated with 1 nM particles. However, on particle stabilization, barely any nanoparticle aggregates are seen in the cell body, and there is no detectable change in cell viability (data not shown). (B) 44 nm citrate-capped gold nanospheres behave similarly to 18 nm particles and accumulate in the cell body in the absence of stabilization treatments, even at 0.08 nM, whereas cells treated with stabilized particles show barely any intracellular aggregates. PAH-PAA-PAH wrapped

Fig. 5.8 (contd.): nanospheres disrupt cell morphology drastically, and cell debris is clearly visible when using unstable as well as stabilized NP conditions. Notably, cells treated with the PAH-PAA-PAH supernatant also showed significant cell death, in the absence of nanoparticles. Representative images of at least 6 wells per condition for (A) and (B). Scale bars are 75 μm. SAEC morphology was similar to HPAEC morphology as described above.

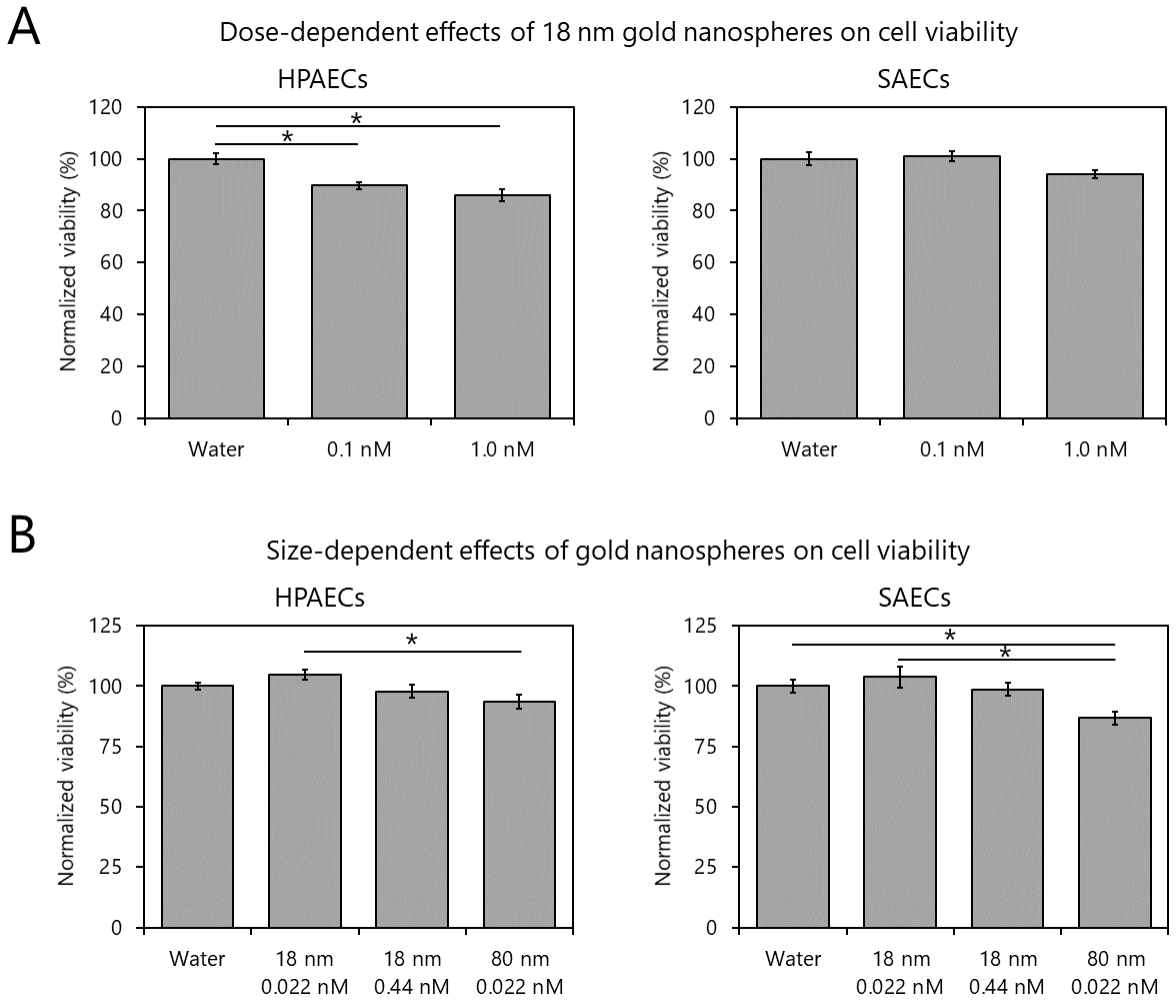

Fig. 5.9: Dose- and size-dependent effects of gold nanospheres on cell viability using MTT assay. HPAECs and SAECs in well-plates were treated with citrate-capped gold nanospheres in 50/50 medium for 18 h. The nanospheres are unstable in the medium and aggregate. The MTT assay for cell metabolic activity was used as an indicator of cell viability in these wells, relative to the control water-treated wells. (A) In HPAECs, increasing the concentration of nanoparticles led to decreased viability, at fixed particle size of 18 nm. However in SAECs, these same particles at the same concentrations did not lead to a significant decrease in viability. n = 12-14 wells per condition. (B) Increasing the size of nanoparticles at the same concentration (0.022 nM) led to a significant decrease in cell viability in both HPAECs as well as SAECs. However, increasing the size of nanoparticles while keeping the total surface area constant (273 m^{-1}) did not lead to a significant drop in cell viability in either HPAECs or SAECs. n = 8-12 wells per condition. * represents $p < 0.05$. See also Fig. 5.8 for perinuclear aggregate formation in treated cells.

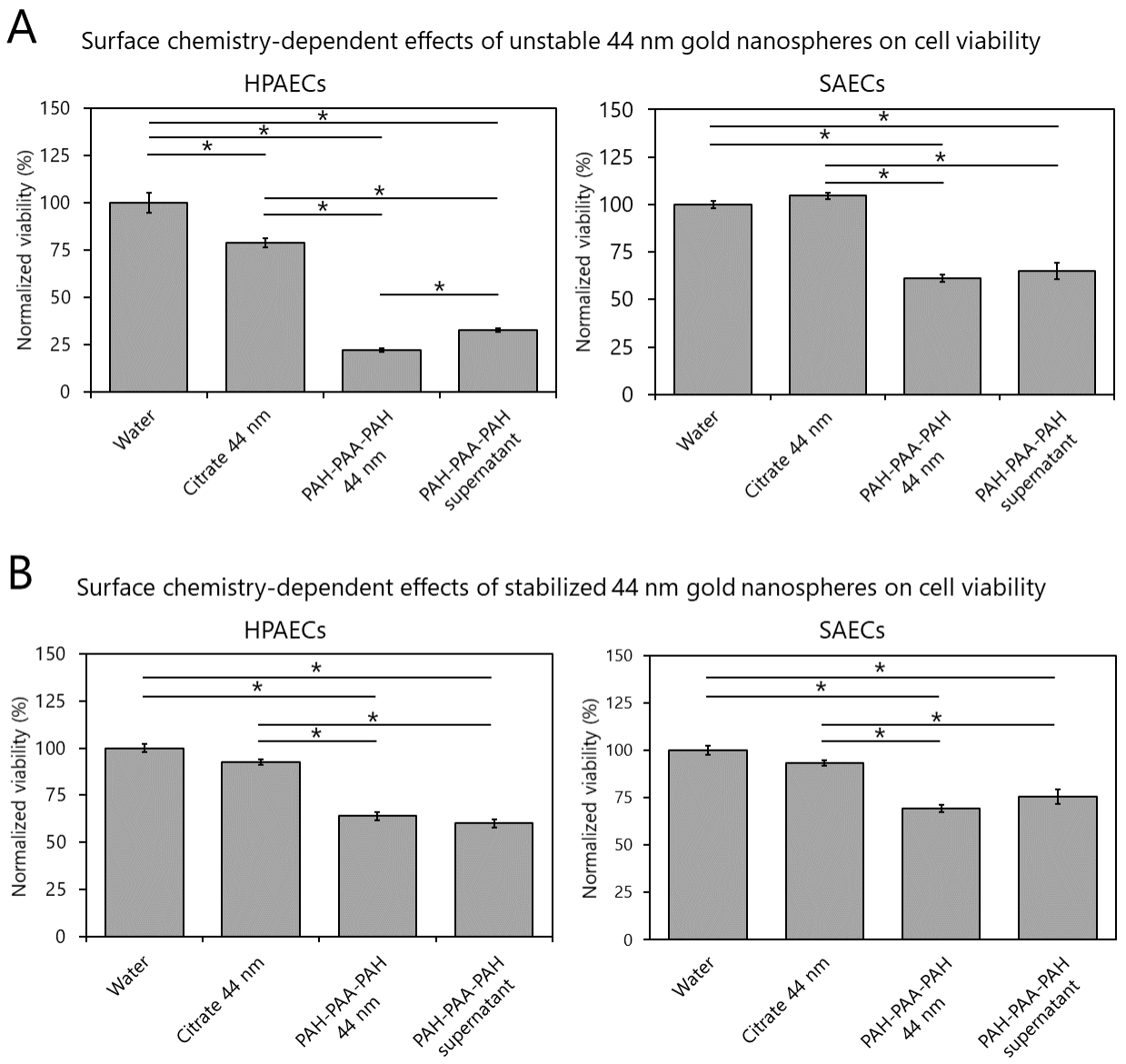

Fig. 5.10: Surface chemistry-dependent effects of gold nanospheres on cell viability using MTT assay. HPAECs and SAECs in well-plates were treated with 0.08 nM citrate-capped, or PAH-PAA-PAH wrapped 44 nm gold nanospheres in 50/50 medium for 18 h. The nanospheres are unstable in the medium and aggregate, or can be stabilized by incubations in BSA-FAF and FBS. The MTT assay for cell metabolic activity was used as an indicator of cell viability in these wells, relative to the control water-treated wells. (A) Without particle stabilization, HPAECs showed significant reductions in cell viability when treated with citrate-capped nanoparticles, and HPAECs and SAECs both showed significant reductions in cell viability with polyelectrolyte-wrapped nanoparticles. However, the loss of viability with PAH-PAA-PAH wrapped nanoparticles could not be completely attributed to the effects of the particles themselves, as the vehicle ('PAH-PAA-PAH supernatant', see Materials and Methods) also caused significant cell death, likely due to the presence of free polymers. (B) With particle stabilization, there was no significant change to cell viability observed with citrate-capped particles, however the PAH-PAA-PAH wrapped nanoparticle solutions still caused significant drops in cell viability. As with the unstabilized

Fig. 5.10 (contd.): particles, the vehicle 'PAH-PAA-PAH supernatant' still caused significant loss of cell viability, such that the effect of the nanoparticles themselves could not be clearly established. Per condition, n = 3 wells for non-nanoparticle treatments, 6 wells for nanoparticle treatments. * represents $p < 0.05$. See also Fig. 5.8 for perinuclear aggregate formation in treated cells.

5.6 TABLES

Table 5.1: Conditions chosen for troubleshooting airway epithelial differentiation and membrane coverage in Variation 2 and Variation 4 of the general protocol for transwell co-cultures

S. No.	Experimental condition	Hypothesis tested
1	SAEC monoculture in epithelial medium	SAECs exhibit complete membrane coverage and rich mucociliary differentiation after 21 days in ALI culture using epithelial medium
2	SAEC monoculture in mixed medium	Endothelial growth factors and serum in mixed medium do not prevent SAEC viability and differentiation
3	'Distal' co-culture in mixed medium: SAECs on apical side of membrane, HPAECs in basal chamber	Factors secreted by endothelial cells does not prevent SAEC viability and differentiation
4	'Proximal' co-culture in mixed medium: SAECs on apical side of membrane, HPAECs on basal side of membrane	Endothelial monolayer does not prevent SAEC viability and differentiation by limiting nutrient access due to its barrier function
5	Proximal co-culture in endothelial medium	Endothelial monolayer generates nutrients and factors needed for SAEC viability and differentiation

Table 5.2: p-values from one-way ANOVAs performed for all MTT assays to study effects of 18 h nanoparticle exposure on HPAEC and SAEC cell viability.

Experiment	Model degrees of freedom, df_{model}	Error degrees of freedom, df_{error}	p-value
Dose-dependence, HPAECs	2	33	4.4×10^{-5}
Dose-dependence, SAECs	2	39	0.045
Size-dependence, HPAECs	3	33	0.014
Size-dependence, SAECs	3	40	0.0093
Surface chemistry-dependence, HPAECs (unstable particles)	3	14	$< 1.0 \times 10^{-10}$
Surface chemistry-dependence, SAECs (unstable particles)	3	14	8.3×10^{-10}
Surface chemistry-dependence, HPAECs (stabilized particles)	3	14	2.4×10^{-9}
Surface chemistry-dependence, SAECs (stabilized particles)	3	14	2.4×10^{-7}

Table 5.3: p-values from Tukey's HSD tests for pairwise comparisons of dose-dependent effects of unstable 18 nm citrate-capped gold nanospheres on cell viability in HPAECs and SAECs.

HPAECs			
	Water	0.1 nM	1.0 nM
Water	×	0.0022	4.2×10^{-5}
0.1 nM		×	0.36
1.0 nM			×

SAECs			
	Water	0.1 nM	1.0 nM
Water	×	0.93	0.12
0.1 nM		×	0.055
1.0 nM			×

Table 5.4: p-values from Tukey's HSD tests for pairwise comparisons of size-dependent effects of unstable citrate-capped gold nanospheres on cell viability in HPAECs and SAECs.

HPAECs				
	Water	18 nm, 0.022 nM	18 nm, 0.44 nM	80 nm, 0.022 nM
Water	×	0.46	0.91	0.23
18 nm, 0.022 nM		×	0.14	0.0086
18 nm, 0.44 nM			×	0.55
80 nm, 0.022 nM				×

SAECs				
	Water	18 nm, 0.022 nM	18 nm, 0.44 nM	80 nm, 0.022 nM
Water	×	0.84	0.99	0.042
18 nm, 0.022 nM		×	0.68	0.0065
18 nm, 0.44 nM			×	0.078
80 nm, 0.022 nM				×

Table 5.5: p-values from Tukey's HSD tests for pairwise comparisons of surface chemistry-dependent effects of 0.08 nM unstable 44 nm gold nanospheres on cell viability in HPAECs and SAECs.

HPAECs				
	Water	Citrate-capped	PAH-PAA-PAH wrapped	PAH-PAA-PAH supernatant
Water	×	1.3×10^{-4}	$< 1.0 \times 10^{-10}$	$< 1.0 \times 10^{-10}$
Citrate-capped		×	$< 1.0 \times 10^{-10}$	$< 1.0 \times 10^{-10}$
PAH-PAA-PAH wrapped			×	0.040
PAH-PAA-PAH supernatant				×

SAECs				
	Water	Citrate-capped	PAH-PAA-PAH wrapped	PAH-PAA-PAH supernatant
Water	×	0.55	9.0×10^{-8}	2.9×10^{-6}
Citrate-capped		×	$< 1.0 \times 10^{-10}$	5.3×10^{-8}
PAH-PAA-PAH wrapped			×	0.74
PAH-PAA-PAH supernatant				×

Table 5.6: p-values from Tukey's HSD tests for pairwise comparisons of surface chemistry-dependent effects of 0.08 nM stabilized 44 nm gold nanospheres on cell viability in HPAECs and SAECs.

HPAECs				
	Water	Citrate-capped	PAH-PAA-PAH wrapped	PAH-PAA-PAH supernatant
Water	×	0.099	2.2×10^{-8}	5.4×10^{-8}
Citrate-capped		×	4.7×10^{-8}	1.6×10^{-7}
PAH-PAA-PAH wrapped			×	0.59
PAH-PAA-PAH supernatant				×

SAECs				
	Water	Citrate-capped	PAH-PAA-PAH wrapped	PAH-PAA-PAH supernatant
Water	×	0.23	2.9×10^{-6}	7.3×10^{-5}
Citrate-capped		×	3.0×10^{-6}	4.1×10^{-4}
PAH-PAA-PAH wrapped			×	0.29
PAH-PAA-PAH supernatant				×

Chapter 6: Conclusions and future work

6.1 CONCLUSIONS

6.1.1 Design of a live-cell imaging capable equibiaxial stretcher device with tunable substrate stiffness

I developed a device to apply equibiaxial cyclic stretch to cells and tissues cultured on an elastomeric membrane (Chapter 2)[49]. The elastomeric membrane had low autofluorescence, enabling imaging of cells transfected with fluorescent reporters. Polyacrylamide hydrogels with various stiffness values could be grafted onto the elastomeric membrane, and cells cultured on these grafted hydrogels could thus be subjected to varying stretch conditions as well as substrate stiffness. The device could be mounted on a fluorescence microscope to enable live-cell imaging of stretched cells and tissues. The device was extensively characterized to determine the calibration curve, homogeneity of the strain field, hydrogel stiffness, and strain transfer ratio from membrane to gel.

6.1.2 Physiological substrate stiffness and cyclic stretch coordinately protect the lung endothelium against inflammatory mediators

The equibiaxial stretcher device was used to precondition lung endothelial monolayers grown on elastomeric membranes, to physiological levels of cyclic strain (Chapter 2)[49]. The inflammatory mediator, thrombin, was used to disrupt endothelial monolayers and form gaps. Cells preconditioned to physiological cyclic stretch showed a smaller peak gap area, as well as faster

restoration of monolayer integrity – including lamellipodia protrusions being observed earlier in cyclically stretched monolayers.

Further, cyclically preconditioned monolayers cultured on hydrogel substrates showed smaller thrombin-induced gap areas and quicker recovery from disruption on soft substrates of physiological stiffness, relative to stiff substrates (Chapter 2). This is extremely interesting, because pulmonary fibrosis is a common consequence of lung injury[36,130,131]. Pulmonary fibrosis is also associated with a reduction in lung compliance and lung volume[85,156]. Thus, in Acute Lung Injury patients who subsequently developed pulmonary fibrosis, lung tissue is stiffer, and also stretches less. My results suggest that pulmonary endothelia under these conditions is more sensitive to disruption by inflammatory mediators. This suggests a feedback loop, such that the first incident of lung injury may result in pulmonary fibrosis, and the relatively stiff, static fibrotic tissue may then be prone to further injury, continuing the cycle. Indeed, outcomes for pulmonary fibrosis patients are typically poor, with a life expectancy of 2 – 6 years after diagnosis[117,228].

6.1.3 Physiological cyclic stretch remodels endothelial junctions and enhances small wound healing

In order to gain some insight into cyclic stretch-induced protection of the lung endothelium, I determined the effects of physiological cyclic stretch on the endothelial junctions, as well as on the dynamics of lamellipodia, which enable healing of small wounds in the endothelium (Chapter 3). Cyclic stretch was found to result in an increase of junctional F-actin, and the actin-scaffolding protein cortactin. Junction areas were reduced on cyclic stretch preconditioning, which is correlated with improved barrier function[101]. Cyclic stretch also resulted in increased tension on

VE-cadherin complexes at the junctions. These cyclic stretch-induced changes may serve to protect and reinforce endothelial junctions against disruption by thrombin.

Physiological cyclic stretch also enhanced lamellipodia dynamics in single cells as well as subconfluent monolayers. These enhancements to lamellipodia dynamics were also observed in thrombin-treated single cells subjected to cyclic stretch preconditioning. However, cyclic stretch did not enhance the collective cell migration rate. Cyclic stretch may thus enhance recovery of endothelial integrity from small gaps, as formed on thrombin treatment, but would likely not protect against large gaps.

6.1.4 An elastomeric micropillar array quantifies changes in endothelial cell mechanics

I used a previously reported platform[43,232], consisting of arrays of microfabricated elastomeric pillars (mPADs), to determine effects of biochemical, genetic, and substrate-based perturbations on endothelial cell mechanics (Chapter 4). Cell-matrix traction forces were calculated from pillar displacements, and mechanical force balance principles were used to calculate the tension at endothelial junctions in cell doublets, and cell triplets arranged linearly. This platform could be used to determine total traction force, per-pillar traction force (indicative of cell contractility), and tension at endothelial junctions. By immunostaining for the cell junction area, stress at endothelial junctions could also be determined. As a result, the platform can be used to study changes in magnitude of cell-generated forces, and redistribution of cell-generated forces between cell-cell and cell-matrix adhesions, under various perturbations.

6.1.5 Development of a primary co-culture model of the pulmonary blood-gas barrier

I developed an *in vitro* co-culture model of the pulmonary blood-gas barrier, using primary airway epithelial and lung endothelial cell monolayers cultured on opposite sides of a transwell membrane. The porous transwell membrane permits exchange of soluble factors while physically separating the cell types. The model is also cultured at the air-liquid interface, such that the epithelial cell monolayer on the apical surface is exposed to air and can undergo mucociliary differentiation and assume a polarized phenotype. The model can be used for studies of nanoparticle uptake and transport across the blood-gas barrier, and effects on the epithelial and endothelial cells, using aerosolized nanoparticles. I also performed preliminary studies of epithelial and endothelial cell viability on exposure to nanoparticles in solution, in order to study the effects of particle concentration, size, and surface chemistry.

6.2 FUTURE WORK

In this dissertation, I have developed engineering tools and techniques, and applied them to studies of the pulmonary blood-gas barrier, with a focus on pulmonary endothelial mechanics. This includes development of an equibiaxial cyclic stretch device, and development of an *in vitro* model of the pulmonary blood-gas barrier.

There are two major challenges to be addressed regarding the cyclic stretch device. First, cell monolayers cultured on the grafted hydrogels experience a previously reported ‘hydraulic fracture’ effect. In brief, aqueous solvent (cell culture media) enters the hydrogel network in stretched hydrogels, swelling the gel, and when the hydrogel is relaxed, the solvent is expelled. When a cell monolayer is cultured over the hydrogels, the solvent cannot be released directly to

the bulk and instead accumulates underneath the monolayer, leading to a rapid increase in the pressure gradient across the monolayer. This pressure is high enough to 'fracture' cell-cell and cell-matrix adhesions. This is not good for long term cyclic stretch (greater than 8 h), as I observed excessive cell death and monolayer breakdown in initial long term studies. The best solution is to use silicones of tunable stiffness, but the greatest challenge is to reach a low enough elastic modulus to be physiologically relevant. One such device combining stretch and substrates of tunable stiffness has been reported[165], where the silicone substrate could be tuned to have a Young's modulus in the range 5 kPa – 1.72 MPa. While this is a viable alternative in many cases, this approach still cannot cover the entire biologically relevant stiffness range, which starts at lower than 0.1 kPa[14,47].

A second challenge is the low throughput of the current stretcher. As a result, only one membrane can be treated at any given time. While this is fine for live-cell imaging, and indeed, this is limited by the area available on the microscope stage, being able to stretch only one membrane at a time is not sufficient for samples to be immunostained, or to be lysed for a Western blot or co-immunoprecipitation. This is also not enough when multiple different drug treatment conditions are to be tried at the same level of cyclic stretch. A second device can be easily designed to stretch four membranes at once, if one is willing to eliminate the live-cell imaging requirement. In this design, the aluminum arm (Fig. 2.1) would be replaced by a square aluminum plate (or equivalent lightweight design) with the stepper motor located at the center of the plate. The linear rail and restoring spring system would be positioned at the four corners of the square. The base itself would be square, and would have four indenting rings positioned along the diagonals, two rings per diagonal, one ring each on opposite sides of the central stepper motor. The membrane holding rings would be mounted on the square aluminum plate attached to the stepper motor,

MHRs being located concentrically above the IRs (as in the current design). A complete characterization of the new device would be necessary.

Regarding the *in vitro* model of the blood-gas barrier, the transwell model is convenient as it is macroscale and easy to use without any specialized equipment, however, it does not capture the mechanical environment of the lung completely – there is no shear flow on the endothelial side, and no cyclic stretch of the tissues. Recent organ-on-chip models[17,98,104] suggest that it should be possible to incorporate shear flow and cyclic stretch in a well-differentiated microfluidic model of the blood-gas barrier. Efforts are underway to develop this model in Prof. Deborah Leckband's laboratory at the University of Illinois, and I anticipate that my work establishing the macroscale transwell model will prove useful in establishing this more sophisticated microfluidic model.

Relating to the biological questions arising from the work with the stretcher showing endothelial junction remodeling upon cyclic stretch – I currently do not have a direct measurement of endothelial barrier function upon cyclic stretch. Thus, it is difficult to conclude whether the cyclic stretch-associated junction remodeling actually enhances barrier function, or whether the increase in junctional F-actin and cortactin just enables rapid re-establishment of the cell junctions to close any gaps that may form. A previously reported dye-based permeability assay may be a useful tool for this assay of barrier effectiveness[64].

References

1. Adhesion Promotion, HMDS, MicroChemicals GmbH, at: http://www.microchemicals.com/products/adhesion_promotion/hmds.html, accessed on 2017/07/08.
2. Agrotis A., The genetic basis for altered blood vessel function in disease: Large artery stiffening, *Vascular Health and Risk Management*, 2005, 1(4):333-344.
3. Alkilany A. M. and C. J. Murphy, Toxicity and cellular uptake of gold nanoparticles: What we have learned so far?, *Journal of Nanoparticle Research*, 2010, 12(7):2313-2333.
4. Alkilany A. M., P. K. Nagaria, C. R. Hexel, T. J. Shaw, C. J. Murphy and M. D. Wyatt, Cellular uptake and cytotoxicity of gold nanorods: Molecular origin of cytotoxicity and surface effects, *Small*, 2009, 5(6):701-708.
5. Amnon B., R. Karthikan, E. X. B. Andre' and E. D. Dennis, How deeply cells feel: Methods for thin gels, *Journal of Physics: Condensed Matter*, 2010, 22(19):194116.
6. Andresen Eguiluz R. C., K. B. Kaylan, G. H. Underhill and D. E. Leckband, Substrate stiffness and VE-cadherin mechano-transduction coordinate to regulate endothelial monolayer integrity, *Biomaterials*, 2017, 140:45-57.
7. Angus G. E. and W. M. Thurlbeck, Number of alveoli in the human lung, *Journal of Applied Physiology*, 1972, 32(4):483-485.
8. Azuma N., S. A. Duzgun, M. Ikeda, H. Kito, N. Akasaka, T. Sasajima and B. E. Sumpio, Endothelial cell response to different mechanical forces, *Journal of Vascular Surgery*, 2000, 32(4):789-794.
9. Bakand S., A. Hayes and F. Dechsakulthorn, Nanoparticles: A review of particle toxicology following inhalation exposure, *Inhalation Toxicology*, 2012, 24(2):125-135.
10. Bakowitz M., B. Bruns and M. McCunn, Acute lung injury and the acute respiratory distress syndrome in the injured patient, *Scandinavian Journal of Trauma, Resuscitation and Emergency Medicine*, 2012, 20:54.
11. Balaban N. Q., U. S. Schwarz, D. Riveline, P. Goichberg, G. Tzur, I. Sabanay, D. Mahalu, S. Safran, A. Bershadsky, L. Addadi and B. Geiger, Force and focal adhesion assembly: A close relationship studied using elastic micropatterned substrates, *Nature Cell Biology*, 2001, 3(5):466-472.
12. Ball V., M. Winterhalter, P. Schwinte, P. Lavalle, J. C. Voegel and P. Schaaf, Complexation mechanism of bovine serum albumin and poly(allylamine hydrochloride), *The Journal of Physical Chemistry B*, 2002, 106(9):2357-2364.
13. Bao G. and S. Suresh, Cell and molecular mechanics of biological materials, *Nature Materials*, 2003, 2(11):715-725.
14. Barnes J. M., L. Przybyla and V. M. Weaver, Tissue mechanics regulate brain development, homeostasis and disease, *Journal of Cell Science*, 2017, 130(1):71-82.
15. Bazzoni G. and E. Dejana, Endothelial cell-to-cell junctions: Molecular organization and role in vascular homeostasis, *Physiological Reviews*, 2004, 84(3):869-901.
16. Belvitch P., M. E. Brown, B. N. Brinley, E. Letsiou, A. N. Rizzo, J. G. N. Garcia and S. M. Dudek, The ARP2/3 complex mediates endothelial barrier function and recovery, *Pulmonary Circulation*, 2017, 7(1):200-210.
17. Benam K. H., R. Villenave, C. Lucchesi, A. Varone, C. Hubeau, H.-H. Lee, S. E. Alves, M. Salmon, T. C. Ferrante, J. C. Weaver, A. Bahinski, G. A. Hamilton and D. E. Ingber, Small

airway-on-a-chip enables analysis of human lung inflammation and drug responses in vitro, *Nature Methods*, 2016, 13(2):151-157.
18. Bernardi L., G. Spadacini, J. Bellwon, R. Hajric, H. Roskamm and A. W. Frey, Effect of breathing rate on oxygen saturation and exercise performance in chronic heart failure, *The Lancet*, 1998, 351(9112):1308-1311.
19. Birukov K. G., Cyclic stretch, reactive oxygen species, and vascular remodeling, *Antioxidants & Redox Signaling*, 2009, 11(7):1651-1667.
20. Birukov K. G., J. R. Jacobson, A. A. Flores, S. Q. Ye, A. A. Birukova, A. D. Verin and J. G. N. Garcia, Magnitude-dependent regulation of pulmonary endothelial cell barrier function by cyclic stretch, *American Journal of Physiology - Lung Cellular and Molecular Physiology*, 2003, 285(4):L785-L797.
21. Birukova A. A., S. Chatchavalvanich, A. Rios, K. Kawkitinarong, J. G. N. Garcia and K. G. Birukov, Differential regulation of pulmonary endothelial monolayer integrity by varying degrees of cyclic stretch, *American Journal of Pathology*, 2006, 168(5):1749-1761.
22. Birukova A. A., N. Moldobaeva, J. Xing and K. G. Birukov, Magnitude-dependent effects of cyclic stretch on HGF- and VEGF-induced pulmonary endothelial remodeling and barrier regulation, *American Journal of Physiology - Lung Cellular and Molecular Physiology*, 2008, 295(4):L612-L623.
23. Birukova A. A., A. Rios and K. G. Birukov, Long term cyclic stretch controls pulmonary endothelial permeability at translational and post-translational levels, *Experimental Cell Research*, 2008, 314(19):3466-3477.
24. Birukova A. A., K. Smurova, K. G. Birukov, K. Kaibuchi, J. G. N. Garcia and A. D. Verin, Role of Rho GTPases in thrombin-induced lung vascular endothelial cells barrier dysfunction, *Microvascular Research*, 2004, 67(1):64-77.
25. Birukova A. A., X. Tian, I. Cokic, Y. Beckham, M. Gardel and K. G. Birukov, Endothelial barrier disruption and recovery is controlled by substrate stiffness, *Microvascular Research*, 2013, 87:50-57.
26. Bogart L. K., G. Pourroy, C. J. Murphy, V. Puntes, T. Pellegrino, D. Rosenblum, D. Peer and R. Lévy, Nanoparticles for imaging, sensing, and therapeutic intervention, *ACS Nano*, 2014, 8(4):3107-3122.
27. Brandenberger C., B. Rothen-Rutishauser, C. Mühlfeld, O. Schmid, G. A. Ferron, K. L. Maier, P. Gehr and A. G. Lenz, Effects and uptake of gold nanoparticles deposited at the air-liquid interface of a human epithelial airway model, *Toxicology and Applied Pharmacology*, 2010, 242(1):56-65.
28. Breeze R. and M. Turk, Cellular structure, function and organization in the lower respiratory tract, *Environmental Health Perspectives*, 1984, 55:3-24.
29. Brieher W. M. and A. S. Yap, Cadherin junctions and their cytoskeleton(s), *Current Opinion in Cell Biology*, 2013, 25(1):39-46.
30. Broermann A., M. Winderlich, H. Block, M. Frye, J. Rossaint, A. Zarbock, G. Cagna, R. Linnepe, D. Schulte, A. F. Nottebaum and D. Vestweber, Dissociation of VE-PTP from VE-cadherin is required for leukocyte extravasation and for VEGF-induced vascular permeability in vivo, *The Journal of Experimental Medicine*, 2011, 208(12):2393.
31. Brown M. B. and A. B. Forsythe, 372: The ANOVA and multiple comparisons for data with heterogeneous variances, *Biometrics*, 1974, 30(4):719-724.
32. Brown T. D., Techniques for mechanical stimulation of cells in vitro: A review, *Journal of Biomechanics*, 2000, 33(1):3-14.

33. Brugués A., E. Anon, V. Conte, J. H. Veldhuis, M. Gupta, J. Colombelli, J. J. Muñoz, G. W. Brodland, B. Ladoux and X. Trepat, Forces driving epithelial wound healing, *Nature Physics*, 2014, 10(9):683-690.
34. Bryce N. S., E. S. Clark, J. M. L. Leysath, J. D. Currie, D. J. Webb and A. M. Weaver, Cortactin promotes cell motility by enhancing lamellipodial persistence, *Current Biology*, 2005, 15(14):1276-1285.
35. Burridge K., W. Chrzanowska and Magdalena, Focal adhesions, contractility, and signaling, *Annual Review of Cell and Developmental Biology*, 1996, 12(1):463-519.
36. Cabrera-Benitez N. E., J. G. Laffey, M. Parotto, P. M. Spieth, J. Villar, H. Zhang and A. S. Slutsky, Mechanical ventilation–associated lung fibrosis in acute respiratory distress syndrome a significant contributor to poor outcome, *Anesthesiology*, 2014, 121(1):189-198.
37. Carter D. R., G. S. Beaupré, M. Wong, R. L. Smith, T. P. Andriacchi and D. J. Schurman, The mechanobiology of articular cartilage development and degeneration, *Clinical Orthopaedics and Related Research*, 2004, (427 Suppl):S69-77.
38. Casares L., R. Vincent, D. Zalvidea, N. Campillo, D. Navajas, M. Arroyo and X. Trepat, Hydraulic fracture during epithelial stretching, *Nature Materials*, 2015, 14(3):343-351.
39. Cheng Z., B. Gang and N. Wang, Cell mechanics: Mechanical response, cell adhesion, and molecular deformation, *Annual Review of Biomedical Engineering*, 2000, 2(1):189-226.
40. Chien S., S. Li and J. Y. J. Shyy, Effects of mechanical forces on signal transduction and gene expression in endothelial cells, *Hypertension*, 1998, 31(1):162-169.
41. Chiquet M., Regulation of extracellular matrix gene expression by mechanical stress, *Matrix Biology*, 1999, 18(5):417-426.
42. Choi S., S. M. Camp, A. Dan, J. G. N. Garcia, S. M. Dudek and D. E. Leckband, A genetic variant of cortactin linked to acute lung injury impairs lamellipodia dynamics and endothelial wound healing, *American Journal of Physiology - Lung Cellular and Molecular Physiology*, 2015, 309(9):L983-L994.
43. Cohen D., M. Yang and C. Chen, Measuring cell–cell tugging forces using bowtie-patterned mPADs (microarray post detectors), In: *Cell-Cell Interactions*, Published by: Humana Press, 2013, pp. 157-168.
44. Conway D. E., M. T. Breckenridge, E. Hinde, E. Gratton, C. S. Chen and M. A Schwartz, Fluid shear stress on endothelial cells modulates mechanical tension across VE-cadherin and PECAM-1, *Current Biology*, 2013, 23(11):1024-1030.
45. Coradeghini R., S. Gioria, C. P. García, P. Nativo, F. Franchini, D. Gilliland, J. Ponti and F. Rossi, Size-dependent toxicity and cell interaction mechanisms of gold nanoparticles on mouse fibroblasts, *Toxicology Letters*, 2013, 217(3):205-216.
46. Cost A.-L., P. Ringer, A. Chrostek-Grashoff and C. Grashoff, How to measure molecular forces in cells: A guide to evaluating genetically-encoded FRET-based tension sensors, *Cellular and Molecular Bioengineering*, 2015, 8(1):96-105.
47. Cox T. R. and J. T. Erler, Remodeling and homeostasis of the extracellular matrix: Implications for fibrotic diseases and cancer, *Disease Models & Mechanisms*, 2011, 4(2):165-178.
48. Damian S., N. Gunther, M. R. Smithhisler and G. J. Klarmann, An air-liquid interface culture system for small airway epithelial cells, Presented at *C74. Acute Lung Injury: Diverse Novel Insights*, 2011, pp. A5231.
49. Dan A., R. B. Huang and D. E. Leckband, Dynamic imaging reveals coordinate effects of cyclic stretch and substrate stiffness on endothelial integrity, *Annals of Biomedical Engineering*, 2016, 44(12):3655-3667.

50. Dasanayake N. L., P. J. Michalski and A. E. Carlsson, General mechanism of actomyosin contractility, *Physical Review Letters*, 2011, 107(11):118101.
51. Davies P. F., Hemodynamic shear stress and the endothelium in cardiovascular pathophysiology, *Nature Clinical Practice Cardiovascular Medicine*, 2009, 6(1):16-26.
52. Davis C. A., S. Zambrano, P. Anumolu, A. C. B. Allen, L. Sonoqui and M. R. Moreno, Device-based in vitro techniques for mechanical stimulation of vascular cells: A review, *Journal of Biomechanical Engineering*, 2015, 137(4):040801.
53. Dejana E., Endothelial cell–cell junctions: Happy together, *Nature Reviews Molecular Cell Biology*, 2004, 5(4):261-270.
54. Dejana E., F. Orsenigo and M. G. Lampugnani, The role of adherens junctions and VE-cadherin in the control of vascular permeability, *Journal of Cell Science*, 2008, 121(13):2115-2122.
55. Dekali S., C. Gamez, T. Kortulewski, K. Blazy, P. Rat and G. Lacroix, Assessment of an in vitro model of pulmonary barrier to study the translocation of nanoparticles, *Toxicology Reports*, 2014, 1:157-171.
56. Dembo M. and Y. L. Wang, Stresses at the cell-to-substrate interface during locomotion of fibroblasts, *Biophysical Journal*, 1999, 76(4):2307-2316.
57. Demeuse P., A. Kerkhofs, C. Struys-Ponsar, B. Knoops, C. Remacle and P. van den Bosch de Aguilar, Compartmentalized coculture of rat brain endothelial cells and astrocytes: A syngenic model to study the blood–brain barrier, *Journal of Neuroscience Methods*, 2002, 121(1):21-31.
58. Dewey J. C. F., S. R. Bussolari, J. M. A. Gimbrone and P. F. Davies, The dynamic response of vascular endothelial cells to fluid shear stress, *Journal of Biomechanical Engineering*, 1981, 103(3):177-185.
59. Diep B. A., L. Chan, P. Tattevin, O. Kajikawa, T. R. Martin, L. Basuino, T. T. Mai, H. Marbach, K. R. Braughton, A. R. Whitney, D. J. Gardner, X. Fan, C. W. Tseng, G. Y. Liu, C. Badiou, J. Etienne, G. Lina, M. A. Matthay, F. R. DeLeo and H. F. Chambers, Polymorphonuclear leukocytes mediate Staphylococcus aureus Panton-Valentine leukocidin-induced lung inflammation and injury, *Proceedings of the National Academy of Sciences of the United States of America*, 2010, 107(12):5587-5592.
60. Discher D. E., P. Janmey and Y.-l. Wang, Tissue cells feel and respond to the stiffness of their substrate, *Science*, 2005, 310(5751):1139-1143.
61. Discher D. E., D. J. Mooney and P. W. Zandstra, Growth factors, matrices, and forces combine and control stem cells, *Science*, 2009, 324(5935):1673-1677.
62. Dreaden E. C., A. M. Alkilany, X. Huang, C. J. Murphy and M. A. El-Sayed, The golden age: Gold nanoparticles for biomedicine, *Chemical Society Reviews*, 2012, 41(7):2740-2779.
63. Dreyfuss D. and G. Saumon, Ventilator-induced lung injury, *American Journal of Respiratory and Critical Care Medicine*, 1998, 157(1):294-323.
64. Dubrovskyi O., A. A. Birukova and K. G. Birukov, Measurement of local permeability at subcellular level in cell models of agonist- and ventilator-induced lung injury, *Laboratory Investigation*, 2013, 93(2):254-263.
65. Dudek S. M. and J. G. N. Garcia, Cytoskeletal regulation of pulmonary vascular permeability, *Journal of Applied Physiology*, 2001, 91(4):1487-1500.
66. Duell B. L., A. W. Cripps, M. A. Schembri and G. C. Ulett, Epithelial cell coculture models for studying infectious diseases: Benefits and limitations, *Journal of Biomedicine and Biotechnology*, 2011, 2011.

67. Ehrlich J. S., M. D. H. Hansen and W. J. Nelson, Spatio-temporal regulation of Rac1 localization and lamellipodia dynamics during epithelial cell-cell adhesion, *Developmental Cell*, 2002, 3(2):259-270.
68. Elliott N. T. and F. Yuan, A review of three-dimensional in vitro tissue models for drug discovery and transport studies, *Journal of Pharmaceutical Sciences*, 2011, 100(1):59-74.
69. Engler A. J., S. Sen, H. L. Sweeney and D. E. Discher, Matrix elasticity directs stem cell lineage specification, *Cell*, 2006, 126(4):677-689.
70. Eyckmans J., T. Boudou, X. Yu and Christopher S. Chen, A hitchhiker's guide to mechanobiology, *Developmental Cell*, 2011, 21(1):35-47.
71. Fehrenbach H., Alveolar epithelial type II cell: Defender of the alveolus revisited, *Respiratory Research*, 2001, 2:33.
72. Fillinger M. F., L. N. Sampson, J. L. Cronenwett, R. J. Powell and R. J. Wagner, Coculture of endothelial cells and smooth muscle cells in bilayer and conditioned media models, *Journal of Surgical Research*, 1997, 67(2):169-178.
73. Flodby P., Y. H. Kim, L. L. Beard, D. Gao, Y. Ji, H. Kage, J. M. Liebler, P. Minoo, K.-J. Kim, Z. Borok and E. D. Crandall, Knockout mice reveal a major role for alveolar epithelial type I cells in alveolar fluid clearance, *American Journal of Respiratory Cell and Molecular Biology*, 2016, 55(3):395-406.
74. Freese C., C. Uboldi, M. I. Gibson, R. E. Unger, B. B. Weksler, I. A. Romero, P.-O. Couraud and C. J. Kirkpatrick, Uptake and cytotoxicity of citrate-coated gold nanospheres: Comparative studies on human endothelial and epithelial cells, *Particle and Fibre Toxicology*, 2012, 9:23.
75. Friedl P. and D. Gilmour, Collective cell migration in morphogenesis, regeneration and cancer, *Nature Reviews Molecular Cell Biology*, 2009, 10(7):445-457.
76. Fröhlich E. and S. Salar-Behzadi, Toxicological assessment of inhaled nanoparticles: Role of in vivo, ex vivo, in vitro, and in silico studies, *International Journal of Molecular Sciences*, 2014, 15(3):4795-4822.
77. Galbraith C. G. and M. P. Sheetz, A micromachined device provides a new bend on fibroblast traction forces, *Proceedings of the National Academy of Sciences of the United States of America*, 1997, 94(17):9114-9118.
78. Ganesan S., A. T. Comstock and U. S. Sajjan, Barrier function of airway tract epithelium, *Tissue Barriers*, 2013, 1(4).
79. Geiger B. and A. Bershadsky, Assembly and mechanosensory function of focal contacts, *Current Opinion in Cell Biology*, 2001, 13(5):584-592.
80. Geiser M. and W. G. Kreyling, Deposition and biokinetics of inhaled nanoparticles, *Particle and Fibre Toxicology*, 2010, 7:2.
81. Ghio A. J., L. A. Dailey, J. M. Soukup, J. Stonehuerner, J. H. Richards and R. B. Devlin, Growth of human bronchial epithelial cells at an air-liquid interface alters the response to particle exposure, *Particle and Fibre Toxicology*, 2013, 10:25.
82. Giannotta M., M. Trani and E. Dejana, VE-cadherin and endothelial adherens junctions: Active guardians of vascular integrity, *Developmental Cell*, 2013, 26(5):441-454.
83. Goers L., P. Freemont and K. M. Polizzi, Co-culture systems and technologies: Taking synthetic biology to the next level, *Journal of the Royal Society Interface*, 2014, 11(96).
84. Goley E. D. and M. D. Welch, The ARP2/3 complex: An actin nucleator comes of age, *Nature Reviews Molecular Cell Biology*, 2006, 7(10):713-726.

85. Gross T. J. and G. W. Hunninghake, Idiopathic pulmonary fibrosis, *The New England Journal of Medicine*, 2001, 345(7):517-525.
86. Hahn C. and M. A. Schwartz, Mechanotransduction in vascular physiology and atherogenesis, *Nature Reviews Molecular Cell Biology*, 2009, 10(1):53-62.
87. Han S. P., Y. Gambin, G. A. Gomez, S. Verma, N. Giles, M. Michael, S. K. Wu, Z. Guo, W. Johnston, E. Sierecki, R. G. Parton, K. Alexandrov and A. S. Yap, Cortactin scaffolds Arp2/3 and WAVE2 at the epithelial zonula adherens, *The Journal of Biological Chemistry*, 2014, 289(11):7764-7775.
88. Harris A. K., P. Wild and D. Stopak, Silicone rubber substrata: A new wrinkle in the study of cell locomotion, *Science*, 1980, 208(4440):177-179.
89. He Y., Y. Ren, B. Wu, B. Decourt, A. C. Lee, A. Taylor and D. M. Suter, Src and cortactin promote lamellipodia protrusion and filopodia formation and stability in growth cones, *Molecular Biology of the Cell*, 2015, 26(18):3229-3244.
90. Head J. A., D. Jiang, M. Li, L. J. Zorn, E. M. Schaefer, J. T. Parsons and S. A. Weed, Cortactin tyrosine phosphorylation requires Rac1 activity and association with the cortical actin cytoskeleton, *Molecular Biology of the Cell*, 2003, 14(8):3216-3229.
91. Hermanns M. I., S. Fuchs, M. Bock, K. Wenzel, E. Mayer, K. Kehe, F. Bittinger and C. J. Kirkpatrick, Primary human coculture model of alveolo-capillary unit to study mechanisms of injury to peripheral lung, *Cell and Tissue Research*, 2009, 336(1):91-105.
92. Hermanns M. I., R. E. Unger, K. Kehe, K. Peters and C. J. Kirkpatrick, Lung epithelial cell lines in coculture with human pulmonary microvascular endothelial cells: Development of an alveolo-capillary barrier in vitro, *Laboratory Investigation*, 2004, 84(6):736-752.
93. Herzog F., M. J. D. Clift, F. Piccapietra, R. Behra, O. Schmid, A. Petri-Fink and B. Rothen-Rutishauser, Exposure of silver-nanoparticles and silver-ions to lung cells in vitro at the air-liquid interface, *Particle and Fibre Toxicology*, 2013, 10:11.
94. Hinz B., W. Alt, C. Johnen, V. Herzog and H.-W. Kaiser, Quantifying lamella dynamics of cultured cells by SACED, a new computer-assisted motion analysis, *Experimental Cell Research*, 1999, 251(1):234-243.
95. Hoelzle M. K. and T. Svitkina, The cytoskeletal mechanisms of cell–cell junction formation in endothelial cells, *Molecular Biology of the Cell*, 2012, 23(2):310-323.
96. Huang L.-K. and M.-J. J. Wang, Image thresholding by minimizing the measures of fuzziness, *Pattern Recognition*, 1995, 28(1):41-51.
97. Huang L., P. S. Mathieu and B. P. Helmke, A stretching device for high-resolution live-cell imaging, *Annals of Biomedical Engineering*, 2010, 38(5):1728-1740.
98. Huh D., B. D. Matthews, A. Mammoto, M. Montoya-Zavala, H. Y. Hsin and D. E. Ingber, Reconstituting organ-level lung functions on a chip, *Science*, 2010, 328(5986):1662-1668.
99. Humphrey J. D., M. A. Schwartz, G. Tellides and D. M. Milewicz, Role of mechanotransduction in vascular biology, *Circulation Research*, 2015, 116(8):1448-1461.
100. Huveneers S., J. Oldenburg, E. Spanjaard, G. van der Krogt, I. Grigoriev, A. Akhmanova, H. Rehmann and J. de Rooij, Vinculin associates with endothelial VE-cadherin junctions to control force-dependent remodeling, *The Journal of Cell Biology*, 2012, 196(5):641-652.
101. Huynh J., N. Nishimura, K. Rana, J. M. Peloquin, J. P. Califano, C. R. Montague, M. R. King, C. B. Schaffer and C. A. Reinhart-King, Age-related intimal stiffening enhances endothelial permeability and leukocyte transmigration, *Science Translational Medicine*, 2011, 3(112):112ra122.

102. Ingber D., Mechanobiology and diseases of mechanotransduction, *Annals of Medicine*, 2003, 35(8):564-577.
103. Ingber D. E., Cellular mechanotransduction: Putting all the pieces together again, *The FASEB Journal*, 2006, 20(7):811-827.
104. Jain A., R. Barrile, A. D. van der Meer, A. Mammoto, T. Mammoto, K. De Ceunynck, O. Aisiku, M. A. Otieno, C. S. Louden, G. A. Hamilton, R. Flaumenhaft and D. E. Ingber, A primary human lung alveolus-on-a-chip model of intravascular thrombosis for assessment of therapeutics, *Clinical Pharmacology & Therapeutics*, 2017.
105. Jayant R. D., M. J. McShane and R. Srivastava, Polyelectrolyte-coated alginate microspheres as drug delivery carriers for dexamethasone release, *Drug Delivery*, 2009, 16(6):331-340.
106. Jing X., J. H. Park, T. M. Peters and P. S. Thorne, Toxicity of copper oxide nanoparticles in lung epithelial cells exposed at the air–liquid interface compared with in vivo assessment, *Toxicology in Vitro*, 2015, 29(3):502-511.
107. Johnson M. D., J. H. Widdicombe, L. Allen, P. Barbry and L. G. Dobbs, Alveolar epithelial type I cells contain transport proteins and transport sodium, supporting an active role for type I cells in regulation of lung liquid homeostasis, *Proceedings of the National Academy of Sciences of the United States of America*, 2002, 99(4):1966-1971.
108. Juettner V., A. Dan, D. Leckband, Y. Komarova and A. Malik, The role of VE-PTP scaffold in stabilizing the adherens junction, *The FASEB Journal*, 2017, 31(1 Supplement):1065.1062-1065.1062.
109. Juettner V. V., A. Dan, D. Leckband, Y. Komarova and A. Malik, The role of VE-PTP in stabilizing VE-cadherin adhesion, *The FASEB Journal*, 2016, 30(1 Supplement):lb520-lb520.
110. Kasper J. Y., L. Feiden, M. I. Hermanns, C. Bantz, M. Maskos, R. E. Unger and C. J. Kirkpatrick, Pulmonary surfactant augments cytotoxicity of silica nanoparticles: Studies on an in vitro air–blood barrier model, *Beilstein Journal of Nanotechnology*, 2015, 6:517-528.
111. Kasper J. Y., M. I. Hermanns, R. E. Unger and C. J. Kirkpatrick, A responsive human triple-culture model of the air–blood barrier: Incorporation of different macrophage phenotypes, *Journal of Tissue Engineering and Regenerative Medicine*, 2017, 11(4):1285-1297.
112. Kierszenbaum A. L. and L. L. Tres, Respiratory system, In: *Histology and Cell Biology: An Introduction to Pathology*, 3e Published by: Elsevier/Mosby, 2012, pp. 387-412.
113. Killian M. L., L. Cavinatto, L. M. Galatz and S. Thomopoulos, The role of mechanobiology in tendon healing, *Journal of Shoulder and Elbow Surgery*, 2012, 21(2):228-237.
114. Kim D.-H., P. K. Wong, J. Park, A. Levchenko and Y. Sun, Microengineered platforms for cell mechanobiology, *Annual Review of Biomedical Engineering*, 2009, 11(1):203-233.
115. Kim J. B., Three-dimensional tissue culture models in cancer biology, *Seminars in Cancer Biology*, 2005, 15(5):365-377.
116. Kim T.-J., S. Zheng, J. Sun, I. Muhamed, J. Wu, L. Lei, X. Kong, Deborah E. Leckband and Y. Wang, Dynamic visualization of α-catenin reveals rapid, reversible conformation switching between tension states, *Current Biology*, 2015, 25(2):218-224.
117. King T. E., A. Pardo and M. Selman, Idiopathic pulmonary fibrosis, *The Lancet*, 2011, 378(9807):1949-1961.
118. Klein S. G., T. Serchi, L. Hoffmann, B. Blömeke and A. C. Gutleb, An improved 3D tetraculture system mimicking the cellular organisation at the alveolar barrier to study the potential toxic effects of particles on the lung, *Particle and Fibre Toxicology*, 2013, 10:31.

119. Kohn Julie C., Dennis W. Zhou, F. Bordeleau, Allen L. Zhou, Brooke N. Mason, Michael J. Mitchell, Michael R. King and Cynthia A. Reinhart-King, Cooperative effects of matrix stiffness and fluid shear stress on endothelial cell behavior, *Biophysical Journal*, 2015, 108(3):471-478.
120. Komarova Y. and A. B. Malik, Regulation of endothelial permeability via paracellular and transcellular transport pathways, *Annual Review of Physiology*, 2010, 72(1):463-493.
121. Kowalski J. R., C. Egile, S. Gil, S. B. Snapper, R. Li and S. M. Thomas, Cortactin regulates cell migration through activation of N-WASP, *Journal of Cell Science*, 2005, 118(1):79-87.
122. Krishnan R., D. D. Klumpers, C. Y. Park, K. Rajendran, X. Trepat, J. van Bezu, V. W. M. van Hinsbergh, C. V. Carman, J. D. Brain, J. J. Fredberg, J. P. Butler and G. P. van Nieuw Amerongen, Substrate stiffening promotes endothelial monolayer disruption through enhanced physical forces, *American Journal of Physiology - Cell Physiology*, 2011, 300(1):C146-C154.
123. Kumar S. and V. M. Weaver, Mechanics, malignancy, and metastasis: The force journey of a tumor cell, *Cancer and Metastasis Reviews*, 2009, 28(1-2):113-127.
124. Ladoux B., E. Anon, M. Lambert, A. Rabodzey, P. Hersen, A. Buguin, P. Silberzan and R.-M. Mège, Strength dependence of cadherin-mediated adhesions, *Biophysical Journal*, 2010, 98(4):534-542.
125. Lampi M. C., C. J. Faber, J. Huynh, F. Bordeleau, M. R. Zanotelli and C. A. Reinhart-King, Simvastatin ameliorates matrix stiffness-mediated endothelial monolayer disruption, *PLoS ONE*, 2016, 11(1).
126. Leckband D. E., Q. le Duc, N. Wang and J. de Rooij, Mechanotransduction at cadherin-mediated adhesions, *Current Opinion in Cell Biology*, 2011, 23(5):523-530.
127. Lee J., M. Leonard, T. Oliver, A. Ishihara and K. Jacobson, Traction forces generated by locomoting keratocytes, *The Journal of Cell Biology*, 1994, 127(6 Pt 2):1957-1964.
128. Lenz A.-G., E. Karg, E. Brendel, H. Hinze-Heyn, K. L. Maier, O. Eickelberg, T. Stoeger and O. Schmid, Inflammatory and oxidative stress responses of an alveolar epithelial cell line to airborne zinc oxide nanoparticles at the air-liquid interface: A comparison with conventional, submerged cell-culture conditions, *BioMed Research International*, 2013.
129. Levesque M. J. and R. M. Nerem, The elongation and orientation of cultured endothelial cells in response to shear stress, *Journal of Biomechanical Engineering*, 1985, 107(4):341-347.
130. Ley K. and A. Zarbock, From lung injury to fibrosis, *Nature Medicine*, 2008, 14(1):20-21.
131. Li H., S. Du, L. Yang, Y. Chen, W. Huang, R. Zhang, Y. Cui, J. Yang, D. Chen, Y. Li, S. Zhang, J. Zhou, Z. Wei and Z. Yao, Rapid pulmonary fibrosis induced by acute lung injury via a lipopolysaccharide three-hit regimen, *Innate Immunity*, 2009, 15(3):143-154.
132. Li L.-F., S.-K. Liao, C.-C. Huang, M.-J. Hung and D. A. Quinn, Serine/threonine kinase-protein kinase B and extracellular signal-regulated kinase regulate ventilator-induced pulmonary fibrosis after bleomycin-induced acute lung injury: A prospective, controlled animal experiment, *Critical Care*, 2008, 12(4):R103.
133. Liu F., J. D. Mih, B. S. Shea, A. T. Kho, A. S. Sharif, A. M. Tager and D. J. Tschumperlin, Feedback amplification of fibrosis through matrix stiffening and COX-2 suppression, *The Journal of Cell Biology*, 2010, 190(4):693-706.
134. Liu F. and D. J. Tschumperlin, Micro-mechanical characterization of lung tissue using atomic force microscopy, *Journal of Visualized Experiments*, 2011, (54):e2911.
135. Liu W. F., C. M. Nelson, J. L. Tan and C. S. Chen, Cadherins, RhoA, and Rac1 are differentially required for stretch-mediated proliferation in endothelial versus smooth muscle cells, *Circulation Research*, 2007, 101(5):e44-e52.

136. Liu Z., J. L. Tan, D. M. Cohen, M. T. Yang, N. J. Sniadecki, S. A. Ruiz, C. M. Nelson and C. S. Chen, Mechanical tugging force regulates the size of cell–cell junctions, *Proceedings of the National Academy of Sciences of the United States of America*, 2010, 107(22):9944-9949.
137. Lo C.-M., H.-B. Wang, M. Dembo and Y.-l. Wang, Cell movement is guided by the rigidity of the substrate, *Biophysical Journal*, 2000, 79(1):144-152.
138. Lu D. and G. S. Kassab, Role of shear stress and stretch in vascular mechanobiology, *Journal of the Royal Society Interface*, 2011, 8(63):1379-1385.
139. Lundholt B. K., K. M. Scudder and L. Pagliaro, A simple technique for reducing edge effect in cell-based assays, *Journal of Biomolecular Screening*, 2003, 8(5):566-570.
140. Mammoto A., T. Mammoto, M. Kanapathipillai, C. Wing Yung, E. Jiang, A. Jiang, K. Lofgren, E. P. S. Gee and D. E. Ingber, Control of lung vascular permeability and endotoxin-induced pulmonary oedema by changes in extracellular matrix mechanics, *Nature Communications*, 2013, 4:1759.
141. Mammoto T. and D. E. Ingber, Mechanical control of tissue and organ development, *Development*, 2010, 137(9):1407-1420.
142. Mammoto T., A. Mammoto and D. E. Ingber, Mechanobiology and developmental control, *Annual Review of Cell and Developmental Biology*, 2013, 29(1):27-61.
143. Martinez J. S., T. C. S. Keller and J. B. Schlenoff, Cytotoxicity of free versus multilayered polyelectrolytes, *Biomacromolecules*, 2011, 12(11):4063-4070.
144. Maruthamuthu V., B. Sabass, U. S. Schwarz and M. L. Gardel, Cell-ECM traction force modulates endogenous tension at cell–cell contacts, *Proceedings of the National Academy of Sciences of the United States of America*, 2011, 108(12):4708-4713.
145. Matute-Bello G., G. Downey, B. B. Moore, S. D. Groshong, M. A. Matthay, A. S. Slutsky and W. M. Kuebler, An official American Thoracic Society workshop report: Features and measurements of experimental acute lung injury in animals, *American Journal of Respiratory Cell and Molecular Biology*, 2011, 44(5):725-738.
146. McCain M. L., H. Lee, Y. Aratyn-Schaus, A. G. Kléber and K. K. Parker, Cooperative coupling of cell-matrix and cell–cell adhesions in cardiac muscle, *Proceedings of the National Academy of Sciences of the United States of America*, 2012, 109(25):9881-9886.
147. Mège R.-M., J. Gavard and M. Lambert, Regulation of cell–cell junctions by the cytoskeleton, *Current Opinion in Cell Biology*, 2006, 18(5):541-548.
148. Mehta D. and A. B. Malik, Signaling mechanisms regulating endothelial permeability, *Physiological Reviews*, 2006, 86(1):279-367.
149. Mierke C. T., D. Rösel, B. Fabry and J. Brábek, Contractile forces in tumor cell migration, *European Journal of Cell Biology*, 2008, 87(8):669-676.
150. Mihai C., W. B. Chrisler, Y. Xie, D. Hu, C. J. Szymanski, A. Tolic, J. A. Klein, J. N. Smith, B. J. Tarasevich and G. Orr, Intracellular accumulation dynamics and fate of zinc ions in alveolar epithelial cells exposed to airborne ZnO nanoparticles at the air–liquid interface, *Nanotoxicology*, 2015, 9(1):9-22.
151. Miller M. R., J. B. Raftis, J. P. Langrish, S. G. McLean, P. Samutrtai, S. P. Connell, S. Wilson, A. T. Vesey, P. H. B. Fokkens, A. J. F. Boere, P. Krystek, C. J. Campbell, P. W. F. Hadoke, K. Donaldson, F. R. Cassee, D. E. Newby, R. Duffin and N. L. Mills, Inhaled nanoparticles accumulate at sites of vascular disease, *ACS Nano*, 2017, 11(5):4542-4552.
152. Moore J. E., E. Bürki, A. Suciu, S. Zhao, M. Burnier, H. R. Brunner and J.-J. Meister, A device for subjecting vascular endothelial cells to both fluid shear stress and circumferential cyclic stretch, *Annals of Biomedical Engineering*, 1994, 22(4):416-422.

153. Mou H., V. Vinarsky, Purushothama R. Tata, K. Brazauskas, Soon H. Choi, Adrianne K. Crooke, B. Zhang, George M. Solomon, B. Turner, H. Bihler, J. Harrington, A. Lapey, C. Channick, C. Keyes, A. Freund, S. Artandi, M. Mense, S. Rowe, John F. Engelhardt, Y.-C. Hsu and J. Rajagopal, Dual SMAD signaling inhibition enables long-term expansion of diverse epithelial basal cells, *Cell Stem Cell*, 2016, 19(2):217-231.
154. Murphy C. J., A. M. Gole, J. W. Stone, P. N. Sisco, A. M. Alkilany, E. C. Goldsmith and S. C. Baxter, Gold nanoparticles in biology: Beyond toxicity to cellular imaging, *Accounts of Chemical Research*, 2008, 41(12):1721-1730.
155. Murrell M., P. W. Oakes, M. Lenz and M. L. Gardel, Forcing cells into shape: The mechanics of actomyosin contractility, *Nature Reviews Molecular Cell Biology*, 2015, 16(8):486-498.
156. Nava S. and F. Rubini, Lung and chest wall mechanics in ventilated patients with end stage idiopathic pulmonary fibrosis, *Thorax*, 1999, 54(5):390-395.
157. Navarro P., L. Ruco and E. Dejana, Differential localization of VE- and N-cadherins in human endothelial cells: VE-cadherin competes with N-cadherin for junctional localization, *The Journal of Cell Biology*, 1998, 140(6):1475-1484.
158. Nawroth R., G. Poell, A. Ranft, S. Kloep, U. Samulowitz, G. Fachinger, M. Golding, D. T. Shima, U. Deutsch and D. Vestweber, VE-PTP and VE-cadherin ectodomains interact to facilitate regulation of phosphorylation and cell contacts, *The EMBO Journal*, 2002, 21(18):4885-4895.
159. Ng M. R., A. Besser, J. S. Brugge and G. Danuser, Mapping the dynamics of force transduction at cell-cell junctions of epithelial clusters, *eLife*, 2014, 3:e03282.
160. Nottebaum A. F., G. Cagna, M. Winderlich, A. C. Gamp, R. Linnepe, C. Polaschegg, K. Filippova, R. Lyck, B. Engelhardt, O. Kamenyeva, M. G. Bixel, S. Butz and D. Vestweber, VE-PTP maintains the endothelial barrier via plakoglobin and becomes dissociated from VE-cadherin by leukocytes and by VEGF, *The Journal of Experimental Medicine*, 2008, 205(12):2929-2945.
161. Ochs M., J. R. Nyengaard, A. Jung, L. Knudsen, M. Voigt, T. Wahlers, J. Richter and H. J. G. Gundersen, The number of alveoli in the human lung, *American Journal of Respiratory and Critical Care Medicine*, 2004, 169(1):120-124.
162. Oliver T., K. Jacobson and M. Dembo, Traction forces in locomoting cells, *Cell Motility and the Cytoskeleton*, 1995, 31(3):225-240.
163. Ooi C. Y., Z. Wang, D. M. Tabima, J. C. Eickhoff and N. C. Chesler, The role of collagen in extralobar pulmonary artery stiffening in response to hypoxia-induced pulmonary hypertension, *American Journal of Physiology - Heart and Circulatory Physiology*, 2010, 299(6):H1823-H1831.
164. Orsenigo F., C. Giampietro, A. Ferrari, M. Corada, A. Galaup, S. Sigismund, G. Ristagno, L. Maddaluno, G. Young Koh, D. Franco, V. Kurtcuoglu, D. Poulikakos, P. Baluk, D. McDonald, M. Grazia Lampugnani and E. Dejana, Phosphorylation of VE-cadherin is modulated by haemodynamic forces and contributes to the regulation of vascular permeability in vivo, *Nature Communications*, 2012, 3:1208.
165. Palchesko R. N., L. Zhang, Y. Sun and A. W. Feinberg, Development of polydimethylsiloxane substrates with tunable elastic modulus to study cell mechanobiology in muscle and nerve, *PLoS ONE*, 2012, 7(12):e51499.
166. Pan Y., S. Neuss, A. Leifert, M. Fischler, F. Wen, U. Simon, G. Schmid, W. Brandau and W. Jahnen-Dechent, Size-dependent cytotoxicity of gold nanoparticles, *Small*, 2007, 3(11):1941-1949.
167. Parekh D., R. C. Dancer and D. R. Thickett, Acute lung injury, *Clinical Medicine*, 2011, 11(6):615-618.

168. Paur H.-R., F. R. Cassee, J. Teeguarden, H. Fissan, S. Diabate, M. Aufderheide, W. G. Kreyling, O. Hänninen, G. Kasper, M. Riediker, B. Rothen-Rutishauser and O. Schmid, In-vitro cell exposure studies for the assessment of nanoparticle toxicity in the lung - A dialog between aerosol science and biology, *Journal of Aerosol Science*, 2011, 42(10):668-692.
169. Pelham R. J. and Y.-l. Wang, Cell locomotion and focal adhesions are regulated by substrate flexibility, *Proceedings of the National Academy of Sciences of the United States of America*, 1997, 94(25):13661-13665.
170. Pelham R. J. and Y.-l. Wang, High resolution detection of mechanical forces exerted by locomoting fibroblasts on the substrate, *Molecular Biology of the Cell*, 1999, 10(4):935-945.
171. Phansalkar N., S. More, A. Sabale and M. Joshi, Adaptive local thresholding for detection of nuclei in diversity stained cytology images, Presented at *2011 International Conference on Communications and Signal Processing*, 2011, pp. 218-220.
172. Phillip J. M., I. Aifuwa, J. Walston and D. Wirtz, The mechanobiology of aging, *Annual Review of Biomedical Engineering*, 2015, 17(1):113-141.
173. Piperno G., M. LeDizet and X. J. Chang, Microtubules containing acetylated alpha-tubulin in mammalian cells in culture, *The Journal of Cell Biology*, 1987, 104(2):289-302.
174. Raj S., S. Jose, U. S. Sumod and M. Sabitha, Nanotechnology in cosmetics: Opportunities and challenges, *Journal of Pharmacy & Bioallied Sciences*, 2012, 4(3):186-193.
175. Reinhart-King C. A., M. Dembo and D. A. Hammer, Cell-cell mechanical communication through compliant substrates, *Biophysical Journal*, 2008, 95(12):6044-6051.
176. Rørth P., Collective cell migration, *Annual Review of Cell and Developmental Biology*, 2009, 25(1):407-429.
177. Rosi N. L. and C. A. Mirkin, Nanostructures in biodiagnostics, *Chemical Reviews*, 2005, 105(4):1547-1562.
178. Roure O. d., A. Saez, A. Buguin, R. H. Austin, P. Chavrier, P. Siberzan and B. Ladoux, Force mapping in epithelial cell migration, *Proceedings of the National Academy of Sciences of the United States of America*, 2005, 102(7):2390-2395.
179. S. Bozich J., S. E. Lohse, M. D. Torelli, C. J. Murphy, R. J. Hamers and R. D. Klaper, Surface chemistry, charge and ligand type impact the toxicity of gold nanoparticles to Daphnia magna, *Environmental Science: Nano*, 2014, 1(3):260-270.
180. Schaffer J. L., M. Rizen, G. J. L'Italien, A. Benbrahim, J. Megerman, L. C. Gerstenfeld and M. L. Gray, Device for the application of a dynamic biaxially uniform and isotropic strain to a flexible cell culture membrane, *Journal of Orthopaedic Research*, 1994, 12(5):709-719.
181. Schamberger A. C., C. A. Staab-Weijnitz, N. Mise-Racek and O. Eickelberg, Cigarette smoke alters primary human bronchial epithelial cell differentiation at the air-liquid interface, *Scientific Reports*, 2015, 5:srep08163.
182. Schwartz M. A. and D. W. DeSimone, Cell adhesion receptors in mechanotransduction, *Current Opinion in Cell Biology*, 2008, 20(5):551-556.
183. Shang L., K. Nienhaus and G. U. Nienhaus, Engineered nanoparticles interacting with cells: Size matters, *Journal of Nanobiotechnology*, 2014, 12:5.
184. Shikata Y., A. Rios, K. Kawkitinarong, N. DePaola, J. G. N. Garcia and K. G. Birukov, Differential effects of shear stress and cyclic stretch on focal adhesion remodeling, site-specific FAK phosphorylation, and small GTPases in human lung endothelial cells, *Experimental Cell Research*, 2005, 304(1):40-49.
185. Shulman M. and Y. Nahmias, Long-term culture and coculture of primary rat and human hepatocytes, *Methods in Molecular Biology*, 2013, 945:287-302.

186. Simmons C. S., A. J. S. Ribeiro and B. L. Pruitt, Formation of composite polyacrylamide and silicone substrates for independent control of stiffness and strain, *Lab on a Chip*, 2013, 13(4):646-649.
187. Simons M., E. Gordon and L. Claesson-Welsh, Mechanisms and regulation of endothelial VEGF receptor signalling, *Nature Reviews Molecular Cell Biology*, 2016, 17(10):611-625.
188. Sisler J. D., S. V. Pirela, S. Friend, M. Farcas, D. Schwegler-Berry, A. Shvedova, V. Castranova, P. Demokritou and Y. Qian, Small airway epithelial cells exposure to printer-emitted engineered nanoparticles induces cellular effects on human microvascular endothelial cells in an alveolar-capillary co-culture model, *Nanotoxicology*, 2015, 9(6):769-779.
189. Small J. V., T. Stradal, E. Vignal and K. Rottner, The lamellipodium: Where motility begins, *Trends in Cell Biology*, 2002, 12(3):112-120.
190. Snyder-Talkington B. N., D. Schwegler-Berry, V. Castranova, Y. Qian and N. L. Guo, Multi-walled carbon nanotubes induce human microvascular endothelial cellular effects in an alveolar-capillary co-culture with small airway epithelial cells, *Particle and Fibre Toxicology*, 2013, 10:35.
191. Spierenburg G. T., F. T. J. J. Oerlemans, J. P. R. M. van Laarhoven and C. H. M. M. de Bruyn, Phototoxicity of N-2-Hydroxyethylpiperazine-N′-2-ethanesulfonic acid-buffered culture media for human leukemic cell lines, *Cancer Research*, 1984, 44(5):2253-2254.
192. Stroka K. M. and H. Aranda-Espinoza, Endothelial cell substrate stiffness influences neutrophil transmigration via myosin light chain kinase-dependent cell contraction, *Blood*, 2011, 118(6):1632-1640.
193. Sun Z., X. Li, S. Massena, S. Kutschera, N. Padhan, L. Gualandi, V. Sundvold-Gjerstad, K. Gustafsson, W. W. Choy, G. Zang, M. Quach, L. Jansson, M. Phillipson, M. R. Abid, A. Spurkland and L. Claesson-Welsh, VEGFR2 induces c-Src signaling and vascular permeability in vivo via the adaptor protein TSAd, *The Journal of Experimental Medicine*, 2012, 209(7):1363.
194. Tabdili H., A. K. Barry, M. D. Langer, Y.-H. Chien, Q. Shi, K. J. Lee, S. Lu and D. E. Leckband, Cadherin point mutations alter cell sorting and modulate GTPase signaling, *Journal of Cell Science*, 2012, 125(14):3299-3309.
195. Taha A. A., M. Taha, J. Seebach and H.-J. Schnittler, ARP2/3-mediated junction-associated lamellipodia control VE-cadherin–based cell junction dynamics and maintain monolayer integrity, *Molecular Biology of the Cell*, 2014, 25(2):245-256.
196. Takahashi K., Y. Kakimoto, K. Toda and K. Naruse, Mechanobiology in cardiac physiology and diseases, *Journal of Cellular and Molecular Medicine*, 2013, 17(2):225-232.
197. Takigawa T., Y. Morino, K. Urayama and T. Masuda, Poisson's ratio of polyacrylamide (PAAm) gels, *Polymer Gels and Networks*, 1996, 4(1):1-5.
198. Tambe D. T., C. Corey Hardin, T. E. Angelini, K. Rajendran, C. Y. Park, X. Serra-Picamal, E. H. Zhou, M. H. Zaman, J. P. Butler, D. A. Weitz, J. J. Fredberg and X. Trepat, Collective cell guidance by cooperative intercellular forces, *Nature Materials*, 2011, 10(6):469-475.
199. Tan J. L., J. Tien, D. M. Pirone, D. S. Gray, K. Bhadriraju and C. S. Chen, Cells lying on a bed of microneedles: An approach to isolate mechanical force, *Proceedings of the National Academy of Sciences of the United States of America*, 2003, 100(4):1484-1489.
200. Tata P. R., H. Mou, A. Pardo-Saganta, R. Zhao, M. Prabhu, B. M. Law, V. Vinarsky, J. L. Cho, S. Breton, A. Sahay, B. D. Medoff and J. Rajagopal, Dedifferentiation of committed epithelial cells into stem cells in vivo, *Nature*, 2013, 503(7475):218-223.
201. Thevenaz P., U. E. Ruttimann and M. Unser, A pyramid approach to subpixel registration based on intensity, *IEEE Transactions on Image Processing*, 1998, 7(1):27-41.

202. Throm Quinlan A. M., L. N. Sierad, A. K. Capulli, L. E. Firstenberg and K. L. Billiar, Combining dynamic stretch and tunable stiffness to probe cell mechanobiology in vitro, *PLoS ONE*, 2011, 6(8):e23272.
203. Tian Y., G. Gawlak, J. J. O'Donnell, A. A. Birukova and K. G. Birukov, Activation of vascular endothelial growth factor (VEGF) receptor 2 mediates endothelial permeability caused by cyclic stretch, *The Journal of Biological Chemistry*, 2016, 291(19):10032-10045.
204. Tiscornia G., O. Singer and I. M. Verma, Production and purification of lentiviral vectors, *Nature Protocols*, 2006, 1(1):241-245.
205. Tschumperlin D. J. and S. S. Margulies, Equibiaxial deformation-induced injury of alveolar epithelial cells in vitro, *American Journal of Physiology - Lung Cellular and Molecular Physiology*, 1998, 275(6):L1173-L1183.
206. Tschumperlin D. J., J. Oswari, Margulies and S. Susan, Deformation-induced injury of alveolar epithelial cells, *American Journal of Respiratory and Critical Care Medicine*, 2000, 162(2):357-362.
207. Tseng Q., E. Duchemin-Pelletier, A. Deshiere, M. Balland, H. Guillou, O. Filhol and M. Théry, Spatial organization of the extracellular matrix regulates cell–cell junction positioning, *Proceedings of the National Academy of Sciences of the United States of America*, 2012, 109(5):1506-1511.
208. Tzima E., M. Irani-Tehrani, W. B. Kiosses, E. Dejana, D. A. Schultz, B. Engelhardt, G. Cao, H. DeLisser and M. A. Schwartz, A mechanosensory complex that mediates the endothelial cell response to fluid shear stress, *Nature*, 2005, 437(7057):426-431.
209. Uboldi C., D. Bonacchi, G. Lorenzi, M. I. Hermanns, C. Pohl, G. Baldi, R. E. Unger and C. J. Kirkpatrick, Gold nanoparticles induce cytotoxicity in the alveolar type-II cell lines A549 and NCIH441, *Particle and Fibre Toxicology*, 2009, 6:18.
210. Ungvari Z., G. Kaley, R. de Cabo, W. E. Sonntag and A. Csiszar, Mechanisms of vascular aging: New perspectives, *Journals of Gerontology Series A: Biological Sciences and Medical Sciences*, 2010, 65A(10):1028-1041.
211. Valent E. T., G. P. van Nieuw Amerongen, V. W. M. van Hinsbergh and P. L. Hordijk, Traction force dynamics predict gap formation in activated endothelium, *Experimental Cell Research*, 2016, 347(1):161-170.
212. Vandenbroucke E., D. Mehta, R. Minshall and A. B. Malik, Regulation of endothelial junctional permeability, *Annals of the New York Academy of Sciences*, 2008, 1123(1):134-145.
213. Verma S., S. P. Han, M. Michael, G. A. Gomez, Z. Yang, R. D. Teasdale, A. Ratheesh, E. M. Kovacs, R. G. Ali and A. S. Yap, A WAVE2–Arp2/3 actin nucleator apparatus supports junctional tension at the epithelial zonula adherens, *Molecular Biology of the Cell*, 2012, 23(23):4601-4610.
214. Vestweber D., VE-cadherin, *Arteriosclerosis, Thrombosis, and Vascular Biology*, 2008, 28(2):223-232.
215. Vijayakumar S. and S. Ganesan, Size-dependent in vitro cytotoxicity assay of gold nanoparticles, *Toxicological & Environmental Chemistry*, 2013, 95(2):277-287.
216. Vlaar A. P. J. and N. P. Juffermans, Transfusion-related acute lung injury: A clinical review, *The Lancet*, 2013, 382(9896):984-994.
217. Volckens J., L. Dailey, G. Walters and R. B. Devlin, Direct particle-to-cell deposition of coarse ambient particulate matter increases the production of inflammatory mediators from cultured human airway epithelial cells, *Environmental Science & Technology*, 2009, 43(12):4595-4599.

218. Wang J. H. C. and J.-S. Lin, Cell traction force and measurement methods, *Biomechanics and Modeling in Mechanobiology*, 2007, 6(6):361.
219. Wang L., R. Taneja, W. Wang, L.-J. Yao, R. A. W. Veldhuizen, S. E. Gill, D. Fortin, R. Inculet, R. Malthaner and S. Mehta, Human alveolar epithelial cells attenuate pulmonary microvascular endothelial cell permeability under septic conditions, *PLoS ONE*, 2013, 8(2):e55311.
220. Wang X. and T. Ha, Defining single molecular forces required to activate integrin and notch signaling, *Science*, 2013, 340(6135):991-994.
221. Wang Y., H.-H. Lai, M. Bachman, C. E. Sims, G. P. Li and N. L. Allbritton, Covalent micropatterning of poly(dimethylsiloxane) by photografting through a mask, *Analytical Chemistry*, 2005, 77(23):7539-7546.
222. Weed S. A., Y. Du and J. T. Parsons, Translocation of cortactin to the cell periphery is mediated by the small GTPase Rac1, *Journal of Cell Science*, 1998, 111(16):2433-2443.
223. West J. B. and O. Mathieu-Costello, Structure, strength, failure, and remodeling of the pulmonary blood-gas barrier, *Annual Review of Physiology*, 1999, 61(1):543-572.
224. Wiechers J. W. and N. Musee, Engineered inorganic nanoparticles and cosmetics: Facts, issues, knowledge gaps and challenges, *Journal of Biomedical Nanotechnology*, 2010, 6(5):408-431.
225. Wirtz D., K. Konstantopoulos and P. C. Searson, The physics of cancer: The role of physical interactions and mechanical forces in metastasis, *Nature Reviews Cancer*, 2011, 11(7):512-522.
226. Wong V. W., M. T. Longaker and G. C. Gurtner, Soft tissue mechanotransduction in wound healing and fibrosis, *Seminars in Cell & Developmental Biology*, 2012, 23(9):981-986.
227. Wu H. and J. T. Parsons, Cortactin, an 80/85-kilodalton pp60src substrate, is a filamentous actin-binding protein enriched in the cell cortex, *The Journal of Cell Biology*, 1993, 120(6):1417-1426.
228. Wynn T. A., Integrating mechanisms of pulmonary fibrosis, *The Journal of Experimental Medicine*, 2011, 208(7):1339-1350.
229. Xiao K., J. Garner, K. M. Buckley, P. A. Vincent, C. M. Chiasson, E. Dejana, V. Faundez and A. P. Kowalczyk, p120-catenin regulates clathrin-dependent endocytosis of VE-cadherin, *Molecular Biology of the Cell*, 2005, 16(11):5141-5151.
230. Xie Y., N. G. Williams, A. Tolic, W. B. Chrisler, J. G. Teeguarden, B. L. S. Maddux, J. G. Pounds, A. Laskin and G. Orr, Aerosolized ZnO nanoparticles induce toxicity in alveolar type II epithelial cells at the air-liquid interface, *Toxicological Sciences*, 2012, 125(2):450-461.
231. Yamazaki D., S. Suetsugu, H. Miki, Y. Kataoka, S.-I. Nishikawa, T. Fujiwara, N. Yoshida and T. Takenawa, WAVE2 is required for directed cell migration and cardiovascular development, *Nature*, 2003, 424(6947):452-456.
232. Yang M. T., J. Fu, Y.-K. Wang, R. A. Desai and C. S. Chen, Assaying stem cell mechanobiology on microfabricated elastomeric substrates with geometrically modulated rigidity, *Nature Protocols*, 2011, 6(2):187-213.
233. Yen H.-J., S.-H. Hsu and C.-L. Tsai, Cytotoxicity and immunological response of gold and silver nanoparticles of different sizes, *Small*, 2009, 5(13):1553-1561.
234. Yonemura S., Y. Wada, T. Watanabe, A. Nagafuchi and M. Shibata, α-Catenin as a tension transducer that induces adherens junction development, *Nature Cell Biology*, 2010, 12(6):533-542.
235. Zaidel-Bar R., G. Zhenhuan and C. Luxenburg, The contractome – a systems view of actomyosin contractility in non-muscle cells, *Journal of Cell Science*, 2015, 128(12):2209-2217.

236. Zhao S., A. Suciu, T. Ziegler, J. E. Moore, E. Bürki, J.-J. Meister and H. R. Brunner, Synergistic effects of fluid shear stress and cyclic circumferential stretch on vascular endothelial cell morphology and cytoskeleton, *Arteriosclerosis, Thrombosis, and Vascular Biology*, 1995, 15(10):1781-1786.